(5)

Flexible Fabrication of Structural Roof Panels: Process Layout and Assembly Equipment Development

by

DAVID LYNN PHILLIPS

B.S., Mechanical Engineering
The University of Texas at Austin
1992

Submitted to the Department of
Mechanical Engineering
in Partial Fulfillment of the Requirements
for the Degree of

MASTER OF SCIENCE
in Mechanical Engineering
at the

MASSACHUSETTS INSTITUTE OF TECHNOLOGY

September 1994

Signature of Author _____
Department of Mechanical Engineering
September 1994

Certified by _____
Dr. Andre Sharon
Thesis Supervisor

Accepted by _____
Professor Ain A. Sonin
Departmental Committee on Graduate Studies
Department of Mechanical Engineering

Flexible Fabrication of Structural Roof Panels: Process Layout and Assembly Equipment Development

by

David Lynn Phillips

Submitted to the Department of Mechanical Engineering on June 6, 1994 in partial fulfillment of the requirements for the Degree of Master of Science in Mechanical Engineering

ABSTRACT

The use of structural panels in residential roof systems increases architectural design flexibility, provides usable space beneath the roof, reduces field assembly time, increases energy efficiency, and potentially reduces overall cost substantially, provided that the panels can be manufactured in a flexible and cost-effective manner. This document describes the conceptual design of a cost-effective, flexible manufacturing process capable of producing 160 panels per day with minimal material waste.

Because of the large variation in panel geometry, the process of attaching end caps to the panels was identified as one of the most challenging tasks in the system and was hence given detailed design consideration. Emphasizing simplicity, the solution employs a manually operated manipulator to position the end caps and a servo-controlled, three-axis mechanism to fasten them to the panel ribs. The nailing mechanism was completely designed, including its control system, and nonlinearly simulated to evaluate its performance. Conservative results indicate a 14-second cycle time for fastening an end cap, well within the system requirements.

Thesis Supervisor: Dr. Andre Sharon
Title: Executive Officer, MIT Manufacturing Institute

Acknowledgments

This endeavor has left me with much more debt than what I owe on my student loans. I feel as though I have accumulated an enormous personal debt to so many who have helped me along the way, especially to those who came through when I really needed them.

First of all, my adviser, Dr. Andre Sharon, gave me professional and personal advice that I will carry with me for a long time. I know his advice is good; it has already been proven. He once told me never to take a girlfriend (or spouse) skiing for her first time. I understood his point, but I thought he was exaggerating. Well, I learned the hard way when I took my girlfriend Erika, who is now my wife, skiing for her first time. Not only did she hurt her knee, but she still complains about my less-than-perfect instructional techniques.

Andre provided me with exactly the type of project for which I was searching, and then he pushed me to achieve without looking over my shoulder. For these I am grateful.

I must also thank the people who encouraged me to come to MIT, people such as Professor Neville Hogan. Professor Warren Seering, and Leslie Regan. Their enthusiasm and willingness to talk to a faceless newcomer made a difference.

I appreciate the support of the Building Technology Group, who responded to all of my exhaustive questions about their roof system. I particularly want to thank Professor Morse-Fortier, whose door and mind were always open.

My lab mate and partner on this project, Susie Ward (Ryerson), deserves most of the credit for driving this project forward. Her energy and positive attitude never failed to inspire solutions to the design problems we faced together.

Possibly the best part of graduate school is the interaction with other grad students. In the mostly informal setting of the lab, the exchange of ideas flourishes. So many times, a fresh look at a problem by a colleague jump-starts research and development that

has begun to drag. My lab mate and good friend Frank Pennisi was the best at that. No matter how short the notice I gave him was, he always came up with valuable suggestions. I have matured professionally because of Frank, but our adventures outside of work have kept me from getting old.

Other lab residents Eric, Wayne, Miguel, Tiina, Moris, and Brandon draw my praise as well. Specifically, Wayne for his patience in answering my endless number of MacQuestions, Tiina for her wit and candor, Moris for his constant willingness to share his knowledge, and Brandon for those late-night debates.

Finally, I extend my deep gratitude to family and friends, particularly to Mom and Dad, who have always encouraged me to do my best, to my grandfather, who has unwittingly inspired me, and my loving wife, Erika, who has endured much to see the completion of this document.

Table of Contents

List of Figures

List of Tables

Chapter 1
Introduction

In his 1918 article, "Art and Machine", J.J.P. Oud wrote, "for the modern artist the future line of development must lead inevitably to the machine" [Rowe, 1993]. As the article continued, Oud voiced his belief in the potential benefit of manufacturing not only to architectural expression, but to the growing need for inexpensive housing.

Several prominent architects of the time shared his vision. Frank Lloyd Wright, one of the most important architects in U. S. history, argued for mass production as a way to raise the standard of living [Rowe, 1993]. Walter Gropius, of Germany, worked diligently to make the dream a reality. Seeing prefabrication as a way to lower housing costs and improve housing quality, he designed a number of complete house systems whose components were factory built and assembled on site with precision and efficiency [Herbert, 1984].

Today, use of manufactured housing continues to gain in popularity and importance, not only for providing affordable housing, but also for addressing the increasing demands for energy efficiency and environmental consideration. Broad acceptance, however, depends on the ability of prefabricated systems to meet these demands without ignoring the aesthetic consciousness people have of their living space.

1.1 Manufactured Housing: Historical Overview

The use of prefabrication in housing dates back to the nineteenth century, when the Early Industrial Revolution was bringing on urbanization and dramatic changes in family life style and social organization [Herbert, 1984]. Housing design was profoundly influenced by these changes and by the same technological advancement that drove the movement itself—the development of new production techniques and materials, as well as vast improvements in transportation [Fish, 1979].

Advances of the period found their way into the construction of housing from two distinct directions. One is the logical extension of industrialization to the construction industry: the manufacture of traditional building materials and components [Herbert, 1984]. The other vision challenged convention fundamentally, leading to the revolutionary concept of the factory-built house.

After a century of sporadic enterprises, government and industry began a concerted effort in the early 1900s to develop "cheap, durable, attractive housing for industrial production" [Herbert, 1984]. Formally, architects joined forces with manufacturers for the first time in 1907, when a German organization entitled the Deutscher Werkbund was founded to encourage the 'fruitful cooperation of art, industry and craft' [Rowe, 1993]. However, the rapid progress and renowned success that typified other businesses, such as the automobile industry, did not ensue for prefabricated housing.

In spite of the devoted efforts of brilliant architects and numerous laborers, in spite of the large expenditures for the cause (one estimate made in the 1930s, before markets for mass-produced housing had even opened up, put the total at one billion dollars), and in spite of the outward enthusiasm generated in trade shows and press conferences, commercial failures far outnumbered the successes [Herbert, 1984]. Public skepticism toward industrialized housing, spawned by sentiment toward the traditional home and resistance to change, combined with the multitude of over-restrictive building codes and the conservative policies of lenders to blunt the impact of developments [Fish, 1979]. Yet, enthusiasm and large-scale experimentation persisted throughout the 20th century, and prefabrication slowly pushed its way into the housing industry.

At the turn of the century, houses were typically custom-built by local workers under the direction of the prospective owner [Fish, 1979]. Constructed with local materials, these structures were often large and extravagant. However, mass relocation of people to urban areas, brought on by industrialization, created a rising demand for inexpensive single-family housing. The urgency for low-cost solutions heightened during the depression, when millions were without jobs, and housing production had dropped by 84% from the average in the 1920s [Herbert, 1984].

The Federal Housing Act, signed in 1934 by Franklin Delano Roosevelt, completely changed the structure of the housing industry [Mason, 1982]. Revolutionizing finance with its long-term amortized mortgage, the act encouraged the success of prefabrication innovators such as E.F. Hodgson of Boston, founder of the oldest

prefabrication firm in the United States (established in 1892), during what is known as the heroic period of prefabrication. By 1941, Hodgson had produced 100,000 units of his bolt-together system, which he had created in the early 1930s. The use of stressed skin plywood panels, which were produced on a hot press with waterproof adhesives, also began in this period. Foster Gunnison, who pioneered the panels, sold more than 5,000 homes during World War II and expanded further after the war.

The second world war boosted the prefabricated house industry in the U. S., as the war effort left materials in short supply [Mason, 1982]. In 1942, the Defense Housing Division of the Federal Works Administration introduced a $153 million program to build 70,000 prefabricated homes in one year. As has happened many times in this industry, however, exciting plans met disappointment in the field. The program failed to even come close to achieving this goal. On the other hand, the funds did stimulate development, and more than 200,000 prefabricated homes are reported to have been built during the war, although much negativism towards prefab housing is attributed to these structures.

Research and development continued and expanded in the 50s and 60s. The Research Institute, operated by the National Association of Home Builders, led the way in the 50s with their lab research on new building products and experiments on delivery and installation [Mason, 1982]. From their efforts came the standardization of dimensions in housing construction.

In the 60s, collaboration of researchers, builders, and manufacturers produced the "greatest technological housing

advances in U. S. history" [Mason, 1982]. The industry tested and applied novel products such as foam-core sandwich panels, pre-finished roof panels, plastic plumbing, and baseboard wiring. The progress of the decade was exemplified dramatically in 1968 by the construction of the San Antonio Hilton hotel. The building, completed in only nine months, was put together with pre-cast concrete modules lifted into place with a huge crane. Each module came complete with carpeting, curtains, and pictures on the wall.

Prefabrication gained more widespread use in the 1970s. About half the U. S. homes being built in 1969 contained prefabricated components [Fish, 1979]. Usage spread to nearly all new homes by 1979. The prosperity of the housing market helped encourage this growth, as 17.8 million houses were built in the U. S., the largest amount in any decade in U. S. history [Mason, 1982].

Perhaps more important to the prefabrication industry, however, were political changes that occurred during this time. Raised awareness of the increasingly detrimental effects of industrialization on the natural environment and public health gave rise to the environmentalist movement. The immediate effect on the housing industry was a tremendous rise in land and development costs that caused millions of builders to go out of business [Mason, 1982]. On the other hand, the movement has opened the way for new, innovative businesses, such as producers of engineered wood products. Today, Trus Joist MacMillan Corporation, the first to offer wood I-joists to replace traditional lumber, has a 70% share of its market [Crowley and others, 1992].

Finally, the oil embargo of 1973, which raised gasoline prices from 38 cents to $1.30 by the end of the 70s, made the U. S. suddenly aware of its wasteful usage of energy [Mason, 1982]. As the cost of heating and cooling homes rose, the industry searched for ways to conserve energy. The U. S. Department of Energy (DOE) got involved, providing funding for six prefabricated, panelized houses, six modular-type houses, four mobile homes, two precut-type houses, and one prefabricated log house. The DOE now plays an important role in fostering research aimed at low-cost, energy-efficient housing.

1.2 MIT Construction Technology Research

Mason [1982] attributes the technological success of the 1960s to the fact that, for the first time, researchers, builders, and manufacturers worked together. Keeping with their precedent, MIT established the Innovative Housing Construction Technology Program (IHCTP) in 1988, with sponsorship from key members of the building industry (Table 1-1). The research effort also cuts across departmental lines at MIT, including the following:

- Department of Architecture and Planning
- Department of Civil Engineering
- Department of Mechanical Engineering
- Laboratory for Manufacturing and Productivity

Table 1-1
Industry Participants in the
Innovative Housing Construction Technology Program

Major Sponsors	Advisory Board
ALCAN International	Acorn Structures
Certainteed	Atlas Industries
Dow Chemical	Gebhardt Industries
GAF Corporation	Maison Bouygues
General Electric	MiTek Industries
Hoerchst Celanese	Mykonos Corporation
Illinois Tool Works	Ryan Homes
MacMillan Bloedel	The Ryland Group
Mobay Chemical Corporation	Winchester Homes
United States Gypsum Corporation	Winter Panel Corporation
Weyerhaeuser	Wood Structures

Through advances in materials, design, and manufacturing, this program seeks to develop new technology for energy-efficient and affordable housing. Among the research topics emphasized are advanced insulation materials and systems. The group has studied the major mechanisms of heat transfer, particularly radiation, through closed-cell foams and fiberglass. By finding ways to reduce the heat transfer, this research promises to aid the transition to insulation foams that do not use chloro-fluorocarbon (CFC) blowing agents [Crowley and others, 1992]. (CFCs are the substances believed to contribute to ozone depletion.) Other work includes studies of the

aging phenomena of foams and development of vacuum panels, which can reduce insulation thermal conductivity by an order of magnitude.

One of the program's most comprehensive accomplishments, to date, has been the development of a panelized roof system. In the early 1980s, as the demand for more attractive and varied housing styles rose, builders returned to the more complex roof designs that had all but disappeared since World War II [Crowley and others, 1993]. The supply of skilled carpentry laborers, however, was scant, and on the decline. Furthermore, truss technology was inadequate for many of these designs. As a result, defects in home insulation and ventilation have become more common.

Recognizing the potential market value, MIT decided that the roof is an excellent subject for the focus of innovative housing research. The result was a complete, prefabricated roof system that offers improved thermal performance over conventional roof structures, at a lower installed cost.

1.3 The Roof System

MIT's panelized roof system comprises two primary elements: insulated structural panels and triangular-truss ridge beams. Constructed with an inexpensive wood composite called Oriented Strand Board (OSB), the roof panels fit together like pieces of a puzzle to form the roof enclosure. They are supported at the ridge by the ridge beams, which are composed of standard lumber and OSB

sheathing. Figure 1-1 shows how the panels fit together to form the roof enclosure.

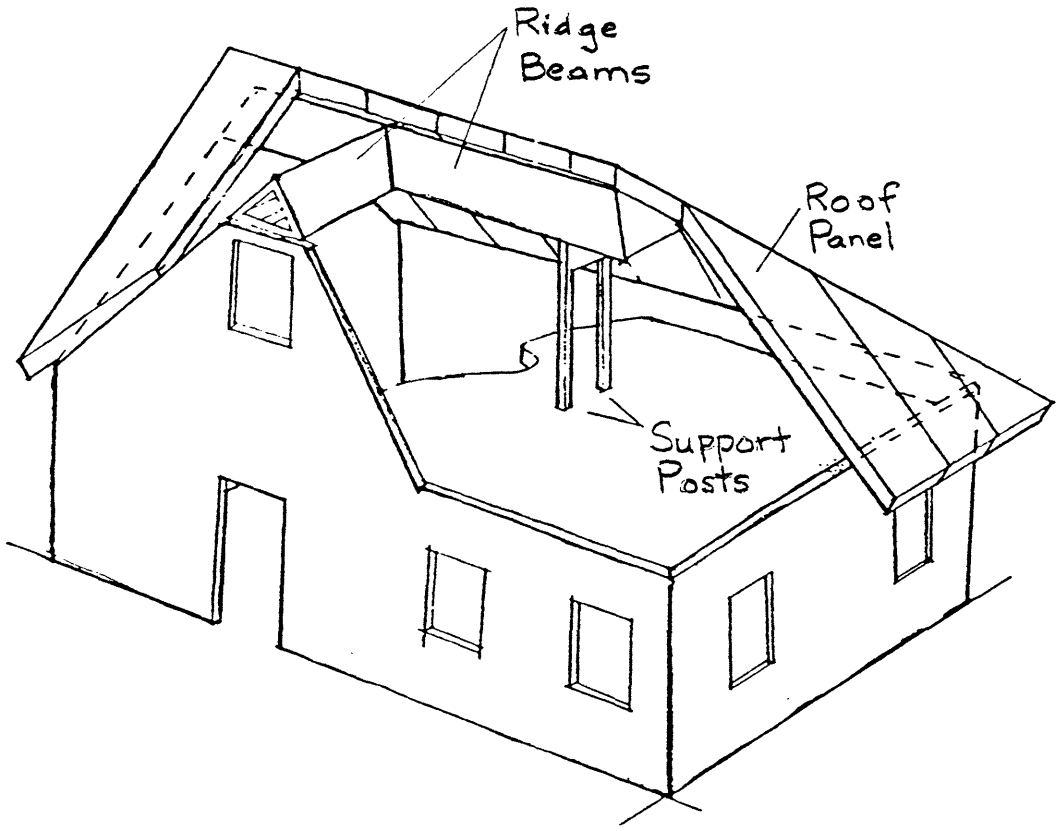

Figure 1-1. Sketch of a proof-of-concept structure that was built in Acton, Massachusetts [courtesy of the MIT Building Technology Group]. The roof panels and the ridge beams make up the MIT roof system.

These components are manufactured in advance and shipped to the construction site, ready for assembly. First, the ridge beams are erected and supported through end walls, interior walls, or posts. A small crane then hoists the panels into place, one by one. Most of the panels span from the ridge to the eave and are fastened at both ends with metal strapping. Other panels, which terminate at a hip, valley, or dormer, attach directly to adjoining panels, again with metal strapping. After all the panels are in place, spline connectors, made

from foam, and associated fasteners are installed between adjacent panels. In three to four hours, a crew of four and a crane operator can easily assemble a 1700 square foot roof. (A team of MIT researchers achieved a rate of about five minutes per panel in building a full-scale proof-of-concept structure.)

The MIT roof system offers several significant advantages over conventional roof construction. We have already mentioned that many of the complex roof designs that are gaining in popularity exceed the capacity of truss technology. Use of trusses also takes away the possibility of using the volume directly underneath the roof. Rafter construction has neither of those limitations, but it increases assembly time and cost. In addition, rafter roofs have a shorter allowable span than truss roofs. So, while rafter roofs may be able to accommodate more complexity, they do so potentially at the expense of the structure's size.

The MIT roof system permits a high degree of design flexibility without the drawbacks of rafter construction. Although this point may not be the system's most concrete advantage, it is perhaps one of the most important for the system's acceptance. Mason [1982] alludes to the monotony of typical manufactured housing in his explanation for the industry's modest commercial success (compared to other industries). He makes the point that each building site is unique because of its natural surroundings and the local customs. Furthermore, consider the recent success of the Japanese auto industry. In architect Peter Rowe's [1993] words, it is due to the "well-timed diversity, individuality, and reliability" of the products.

The design benefits of the panelized system are not nearly enough to justify introducing it as a product, however. The system must offer more tangible returns to be successful in this industry, which is historically resistant to change. Together, rafter and truss roofs account for 99% of the roofing market (foam panels account for the other 1%) [Crowley and others, 1993]. Nevertheless, with the promised benefits summarized here, the MIT roof system does possess a strong potential to succeed in this market.

- Lower installed cost for complex roofs
  - Less than 50% of the cost of an equivalent installed rafter roof
  - About a $1,020 savings compared to a truss roof of moderate complexity (direct substitution basis)
- Lower cost per unit area than trusses
  13% savings on a typical townhouse
- 83% reduction in roof assembly time
- Higher energy efficiency
  Good design and tight tolerance control in the factory process reduce thermal defects
- Lower value wood composites used in place of old-growth timber
- 60% reduction in wood fiber consumed
- Reduced number of on-site skilled laborers
- Design flexibility
- Space under the roof enclosure
- Reduced time between product order and delivery

This last point deserves further attention. The net-shape approach of the system (panels fitting together like puzzle pieces),

plus the absence of any express limitations on roof design, necessarily requires a high degree of flexibility in the manufacture of the roof panels. At the same time, the MIT roof system possesses a consistency in design that encourages automation in both planning and production. Computer aided design and manufacturing (CAD/CAM) software can automatically convert a customer sketch or architectural plan into a complete set of dimensional data for all the required roof components—in about an hour for a moderately complex roof [Crowley and others, 1992]. As a result, builders will be able to gain more precise control over scheduling and reduce their carrying cost.

1.4 Roof Panel Design

Integrating insulation, ventilation, and structure into a single unit, the roof panel essentially constitutes the entire roof. Once the panels and their connectors are fastened in place, all that remains in completing the roof is the interior and exterior finishing.

The panel's basic structure consists of a top face (exterior), a bottom face (ceiling), and two, three, or four ribs that separate the two faces (Figure 1-2). The faces and ribs, cut from 7/16" (inch) OSB stock, are glued together with an industrial wood adhesive and fastened with staples. (The staples clamp the parts together while the adhesive cures.) Near the center of the panel, a block of polyurethane foam bridges the gap between two ribs, up to about 1.5 inches from the top face. This block adds lateral support to the

structure. Insulation fills the remaining space of the channels formed by adjacent ribs, but also leaves a 1.5 inch gap at the top. Along with semi-circular cuts made at the tops of the ribs, this gap permits ventilation of the panel, which occurs along and across the panel, and between adjacent panels. Finally, end caps, also cut from 7/16" OSB, are glued and nailed to the ribs at both ends of the panel.

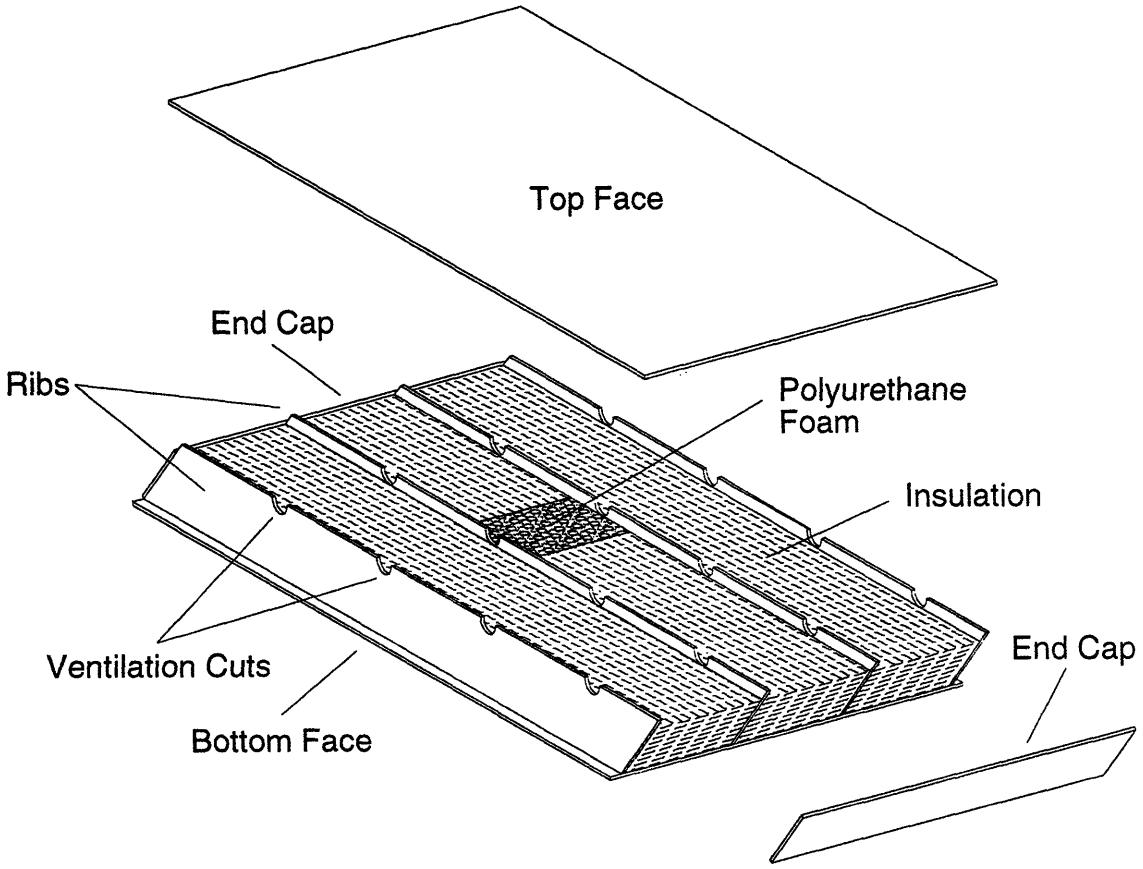

Figure 1-2. Roof panel structure. The ribs, end caps, and faces are made of Oriented Strand Board.

The roof panel stands out as the most important component in the roof system, and it represents the greatest challenge in making the system available commercially. Although the benefits promised

by this system are good reason for optimism, they cannot be realized without efficient, cost-effective fabrication of the product.

This thesis describes the development of an automated process for mid-volume manufacture of the roof panels. The level of automation prescribed, which is notably greater than the norm for this industry, reflects the particular importance of tight tolerance control. Unlike many housing construction products, this system is designed to need no field modification. Any dimensional mistakes could take away the system's thermal performance advantage, which it theoretically obtains through a reduction in construction variability and defects. The ease with which those inaccuracies can occur was observed firsthand in the construction of panels for a proof-of-concept structure. Furthermore, hand building the panels is time consuming. A team of four people needed an average of one hour to build one panel. With practice, the crew achieved a rate of thirty minutes per panel, but it is nowhere near the speed necessary for profitable production.

Chapter 2 begins by explaining some of the broad issues that define the design scope of the manufacturing process. Later, the chapter moves into a piece-by-piece discussion of the process, offering conceptual solutions along the way, and culminates in a presentation of the complete, conceptual process layout. The focus of the thesis then narrows to one specific part of the assembly process.

In Chapter 3, the conceptual design of the subsystem responsible for attaching the end caps is developed further, and in Chapter 4, the principal machine in that subsystem—the end cap

nailing mechanism—is described in detail. Chapter 5 presents critical load analysis that was the basis for several design features and component selections.

Although a prototype of this mechanism was not built, its design was validated through computer simulation. Chapter 6 recounts the derivation of the model's dynamic equations; Chapter 7 shows how the simulation was used to design the mechanism's control system. In the conclusion, recommendations are made for future work on both the end cap station and other parts of the production line.

Chapter 2
Process Design

Automating the tasks of design and construction calls for simplification and standardization. Yet, the aim of the MIT technology is to provide custom-built roofing, tailored to the needs and preferences of the designer and the customer. As a result, the MIT roof panel demands considerable flexibility from the process that produces it. The most influential factor in the design of the process layout was this demand.

This chapter explains the conceptual development of an automated manufacturing process for the OSB roofing panels. Much of the discussion relates to the critical issues for success of the line. Not all aspects of the process are specifically addressed. Important topics such as production order, material storage and distribution, and computer networking are left for future work. The emphasis of this thesis is on the development of automated machinery.

Along the way, the chapter discusses redesign work that was done on the panel to make it more suitable for automated manufacture. A categorical discussion of the major tasks of the manufacturing process follows, with concepts that address the issues raised. Finally, the individual concepts are combined into an overall layout, which is described step by step, and one part of the process is singled out for further development.

2.1 Broad Design Issues

Before making a serious attempt to generate design solutions, one must establish the scope and limitations of the project. The designer must have a clear understanding of the design goals, which may actually conflict with one another, and the constraints imposed by any specifications given. Often, the designer must also make decisions up front to narrow the scope of possible solutions. Following is a discussion of important issues and assumptions that help define the requirements of the roof panel production line.

2.1.1 Flexibility. The bends that are present in all but the simplest roofs create the need for panels with non-rectangular faces. When a panel meets a hip joint (convex part of a turn) or a valley joint (concave part of a turn), its end must be cut at an angle, as shown in Figure 2-1. This geometry is compounded by the additional cut that allows panels to butt against one another flush along their depth. To further complicate matters, these cut angles change for different roof pitches and for turns of magnitudes other than 90°.

The cut angles vary on a continuous scale. As a result, much of the manufacturing equipment, such as cutting machines and fixturing devices, cannot be designed with discrete position settings. Such equipment must have effectively infinite adjustment within its range of operation.

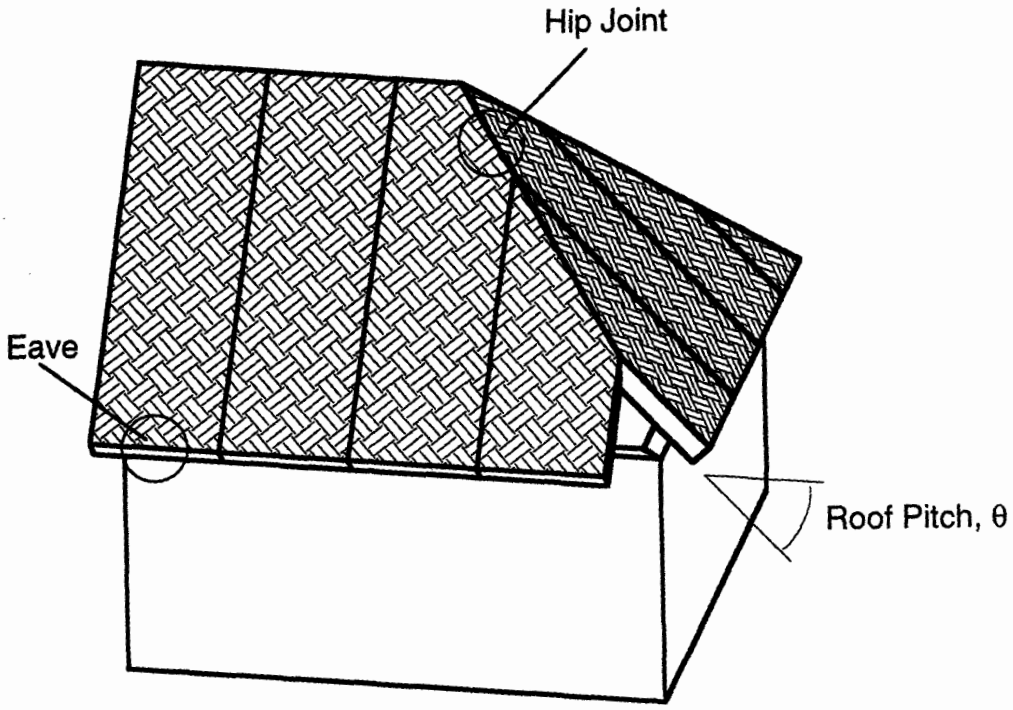

Figure 2-1. Net-shape panelized roof system. The panels that meet at hip joints and valley joints (not shown) have compound cut angles at their adjoining ends.

The result of all this variability is that the roof panel manufacturing process must handle and assemble components with a wide range of dimensions. The panels may be as long as twenty four feet and perhaps as short as twenty one inches. The faces may be rectangular, trapezoidal with one or two angled ends, five-sided, or even triangular. Figure 2-2 illustrates how most of these shapes fit into a typical roof design. Not shown in the roof layout is the panel with two angled ends, which is only necessary in the relatively rare case where a panel meets a hip at one end and a valley at the other. This panel appears in Figure 2-4, along with another five-sided panel, which is sometimes used to join the ridge to the top of a dormer. The automated assembly process described in this thesis does not address this special five-sided panel. (See Chapter 3.)

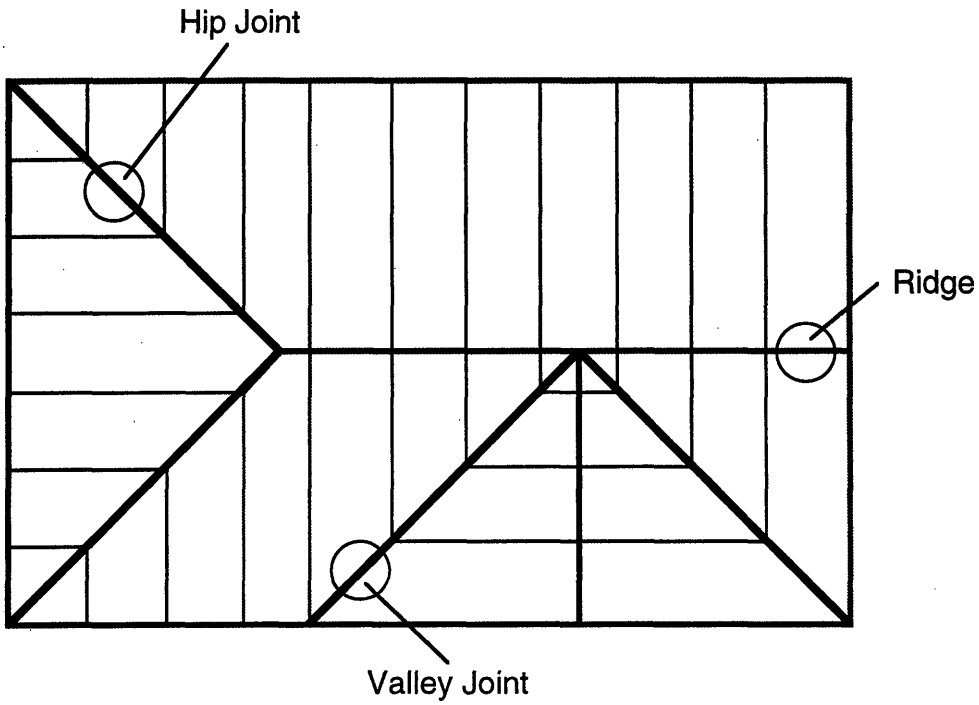

Figure 2-2. Top view of a typical roof, showing the layout of the panels.

The ribs always have at least one angled end and may have two. Furthermore, some of the ribs are so small, their longest edge is actually the end rather than the top or bottom edge (Figure 2-3). These particular ribs significantly increase the complexity of the rib handling equipment.

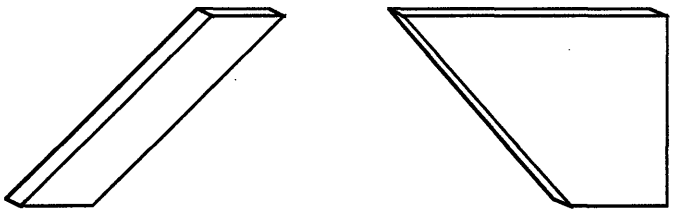

Figure 2-3. Geometries of small ribs. These ribs, which would go into a triangular panel, require special equipment for manipulation.

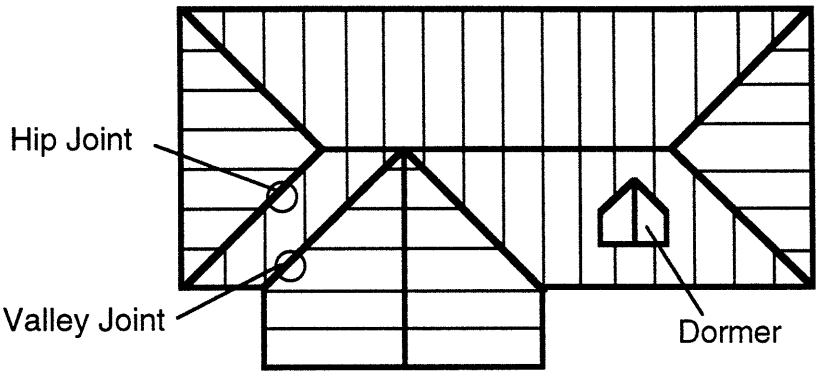

Top View

Front View

Figure 2-4. Top and front views of a house with a slightly more complex roof. This design requires some panel shapes that represent only a small percentage of the panels that will be produced.

2.1.2 Component Form. The assumption was made that the OSB components would be cut to their final shape first and then assembled. The alternative, assembling more basic components and then cutting the panel to the desired size and shape would greatly simplify assembly and material handling, as all components would be rectangular and of standard sizes. However, this alternative was rejected because it would generate a very large amount of material waste, including glue, fasteners, and insulation, as well as OSB. Moreover, recycling that waste would be difficult. The fasteners

would have to be removed from the OSB. The adhesive, on the other hand, cannot be separated from the wood; the affected regions would have to be cut off and discarded.

2.1.3 Knowledge Form. Another question that heavily influenced design concepts is how the machinery receives and manipulates these non-uniform components. Because the line is intended to be mostly automated, many of the machines must have geometrical information on the components with which they are working. This information could be obtained by sensors and processors incorporated into each machine, or it could be programmed ahead of time and distributed in instructions to the equipment as needed.

The second approach makes more sense in this case. All the geometrical information is already available in CAD/CAM data from the panel design software. This software, which automatically generates the panel layout and dimensions according to the roof design, may be modified to create the panel production order as well. All this information could be used by a computer system to drive the manufacturing process. Therefore, the process was developed under the assumption that the data is available for use at any point in the process.

2.2 Panel Redesign for Manufacture

Today, designers realize the benefit of seriously addressing manufacturing issues early in product design. With this practice, products, particularly new ones, reach the market faster and with better quality. Often, changes can be made to product concepts that significantly improve manufacturing without degrading performance. These improvements may be manifested in costs, production rate, or simply convenience. The use of snap-together fasteners in place of screws, for instance, greatly simplifies the manufacture of many products.

Although the net-shape roof panel was designed with production in mind, several features of its initial design were not well suited for automated assembly. This realization, which was reached during the initial search for assembly solutions, prompted two major changes to the original panel.

2.2.1 Panel Connections. The original panel design included one-inch by six-inch (1×6)* strips of lumber laid along the inside of the bottom face to provide reinforcement at the roof assembly joints. These strips were eliminated from the panel, and as a result, an entire subsystem of feeders, saws, and handling mechanisms was eliminated from the line. However, the method of attaching the panels during roof assembly also had to be altered. The reinforcement strips were a necessary part of using screws as the

* Lumber is typically designated by the dimensions of its cross section, in inches. The abbreviation shown is used hereafter in the thesis.

fasteners, so the screws had to be eliminated as well. After testing several solutions, we modified the design such that the panels could be fastened to the house and to each other with metal strapping, without any reinforcement of the panels themselves. Figure 2-5 shows how this change affects the panel connection at the exterior wall.

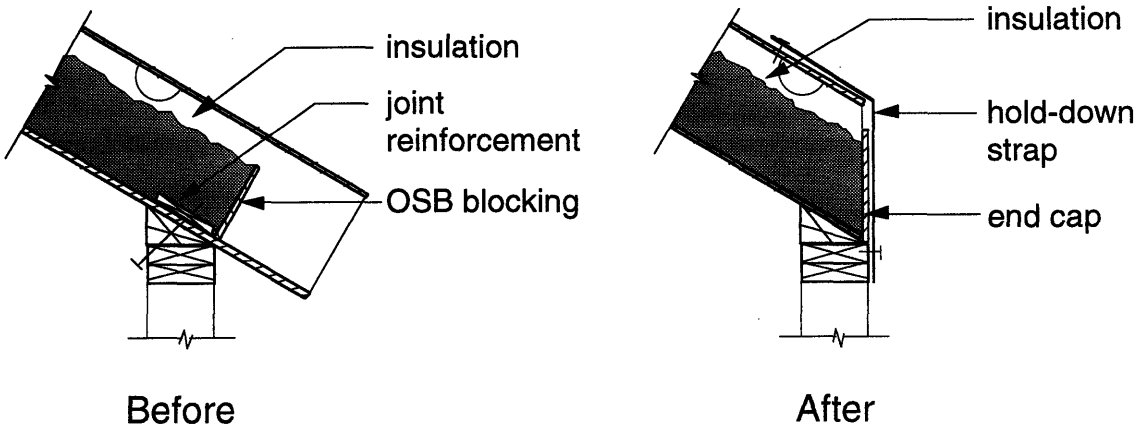

Figure 2-5. Eave condition modification [courtesy of Mike McCormick]. Panel attachment at the eave is achieved using a metal hold-down strap that extends from the top face of the panel down the face of the exterior wall. This arrangement requires an additional piece that attaches to the end of the panel (not shown), but provides the opportunity for customization of the eave.

These modifications simplify field installation as well as manufacturing [Crowley and others, 1993]. In addition, the new arrangement offers more freedom to the builder. Because the panel stops at its junction with the exterior wall, as shown in Figure 2-5, the roof system does not dictate what eave type the house must have. The builder can choose from a wide variety of conventional designs and available prefabricated products.

2.2.2 Blocking. The original panel design also included blocking made from 7/16" OSB and inserted between the ribs. This blocking serves to prevent lateral collapse of the panel. However, the need for extra saws, conveyors, and mechanisms to produce and install the blocking inspired a search for alternatives, as structural tests and analyses indicated that the panels do need additional support between the ribs. End caps alone will not prevent the panels from collapsing in extreme shipping and storage situations.

In the end, a block of polyurethane foam was substituted for the OSB blocking. The foam can simply be sprayed directly into place between the ribs—a much more efficient procedure. Further tests confirmed that a foam block sprayed in the center of a panel adds the necessary stability to the panel. In addition, the foam is a good insulator; so it will not compromise the heat resistance of the panel. Polyurethane foam creeps when loaded for extended periods, but the blocking will only experience significant loading for a short length of time. Once the roof is assembled, the panels are no longer subjected to large lateral stresses. Even in the event of an earthquake, the panel is already stable enough without the blocking to withstand the lateral stresses it would experience.

2.3 Design Criteria

The overall objective of this research was to devise an automated approach to the panel manufacture that is cost-effective. As such, the criteria given the strongest consideration during

development and evaluation of concepts were capital cost, throughput, and reliability.

The residential housing industry has traditionally been scattered. At one time, an estimate reported more than 110,000 builders in the U.S., most of whom produced fewer than twenty five units per year; and most of the units were single-family houses rather than apartment buildings or other multi-family units. Compared to the companies found in a number of other industries, most home builders have a modest amount of capital to invest. Yet, this investment promises to be worthwhile, as market penetration is projected at about 40% [Crowley and others, 1993]. Volume is therefore an additional priority. Crowley [1992a] established a target production rate of about 2300 roofs per year to meet anticipated demand.

These circumstances make reliability especially important. The production requirements do not allow for much down time, and process redundancy is not economically feasible. The line must operate smoothly for long periods of time, without jams or equipment breakdowns.

2.4 Major Subsystem Functions and Concepts

Conceptual development began at a basic level in which subprocesses were treated individually, although their interaction with one another was considered as well. This approach encouraged

a broad range of possible solutions by keeping the fundamental operations in focus.

Fabrication process topics that are addressed here include the form and method of input of the raw materials (OSB, insulation, foam) and the manipulation of OSB components for assembly. OSB-component cutting, stapling, and gluing, and other less emphasized subprocesses, are not discussed.

2.4.1 OSB Supply. Oriented strand board dominates the makeup of the roof panel, as the faces, ribs, and end caps are all cut from 7/16" stock. The matter of introducing this stock into the production line raises two distinct issues. One concerns the physical process of separating individual sheets from the supply and transporting them onto the line. The other issue concerns the material supply's form, which affects the first issue. For instance, the size and arrangement of the OSB stock influences how the sheets should be fed.

OSB typically comes as four foot by eight foot (4×8)* sheets, stacked on a pallet. Though the width is invariable, OSB can be bought in other lengths as well, usually at higher unit cost. In the panel production line, the sheets are removed one by one from the stack and placed onto a conveyor. Methods considered for this process are characterized by one of two basic approaches: taking from the top and taking from the bottom.

* When it is clear that the material being discussed is in the form of sheets, this abbreviation designates the width and length of the sheets, in feet.

Removing the uppermost sheet is the most obvious approach. An overhead suction lifter could pick the top sheet from the stack and set it gently onto a conveyor. This lifter might be operated automatically or manually. In addition, the stack itself may be mobile or stationary. If the stack were placed on a platform that could raise it, the lifter could be somewhat simple, needing only a small range of motion vertically. In the other case, the lifter would need much greater range, and essentially continuous movement within that range. The top sheet could also be slid off the stack, perhaps by rollers. In this case, a mechanized platform is necessary. This system would be much simpler than the lifter. However, because of the role that friction plays, it could also be less reliable.

Another concept employs a tray on which the stack rests. An actuator pushes the tray, carrying with it one OSB sheet, out from under the stack. Rollers slide this sheet off the tray and onto the conveyor, and then the next sheet drops onto the tray as it retracts. The single advantage to this approach is that more OSB could be added to the supply without interfering with the feed operation. On the other hand, friction forces between the bottom two sheets would be very large. The surface of OSB is rough and irregular, and this shearing action could mar it. The problem may, however, be alleviated some by tilting the stack, which lowers the friction forces.

The approach best suited for the production line is the top feed. The method chosen for transferring the top sheet, however, does not employ an automatic mechanism as was discussed. Instead, a human operator slides the sheet off the stack, which rests on a mechanized platform that is tilted to assist the operator. This solution results in

the least amount of difficulty and cost, as people are needed anyway to oversee operations of the production line.

A human can be expected to handle an eight foot long sheet effectively with this setup. However, we have said that the panels may be up to twenty four feet long. This dilemma brings us to the second issue involved in feeding the OSB. What size should the stock material be?

The maximum panel length would seem to indicate that the sheets must be at least twenty four feet long. Or more reasonably, the supply could comprise more than one sheet size, with the appropriate size selected according to individual panel length. In either case, however, panel production would generate a very large amount of OSB waste.

Consider the making of an angled-end panel for a roof pitch of 12/12 (45°). In the best case, the length of the supply sheet would exactly match the final panel length. Depicted in Figure 2-6, the section cut from one face sheet and discarded would have an area of 11 $ft.^2$. Doubling that figure and multiplying by the unit price of OSB ($\$0.37/ft.^2$, as reported by Somerville Lumber [1992]) reveals that in making two faces for this one panel, $8.48 worth of undamaged material becomes scrap.

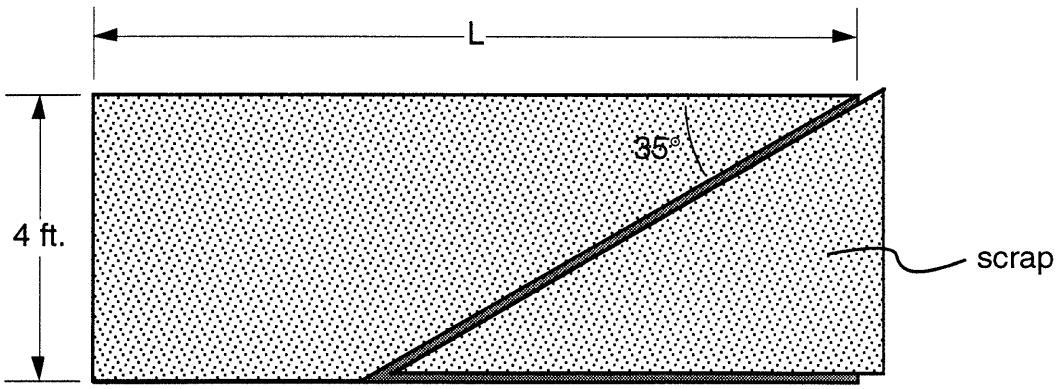

Figure 2-6. An example of potential material waste. The scrap produced in making this single face for an angle-end panel would cost more than $4.

Now consider the production of an entire roof—the roof of the first proof-of-concept structure that MIT built. The scrap produced from the OSB faces, if we again assume the supply sheets are exactly the right size, would total $218. Moreover, because the sheets will generally be longer than they need to be, this estimate is conservative.

The problem of scrap generation can be minimized, however, if the sheets are first joined to one another end to end. This practice effectively produces a continuous supply of material, from which the exact length needed for a given component can be cut. Furthermore, judicious choice of production order allows the problem exemplified in Figure 2-6 to be avoided. Components with a common cut angle will be cut in succession. In this way, one end of each component will be made with one cut, and no scrap will result. Figure 2-7 illustrates the idea. This strategy drastically reduces the overall amount of waste produced because all the panels on a given hip or valley line share common cut angles. In fact, for the majority of

roofs, which do not have multiple roof pitches or multiple turn angles, all the angled-end panels have the same cut angles.

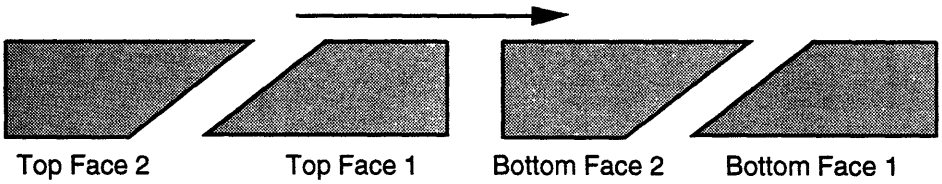

Figure 2-7. An example of how trapezoidal faces might be cut. Panel 1 and Panel 2 share common cut angles on both ends. Therefore, only five cuts are needed to produce the four faces shown. Besides the sawdust produced in making the cuts, no material is wasted.

On the other hand, in practice the end caps will also be cut from the face supply. The rectangular end caps for the panels in Figure 2-7, for instance, might be cut directly before Bottom Face 1. The caps for the angled ends might be cut between the two bottom faces. Because the latter caps have slightly different cut angles from the faces, a small amount of scrap would be produced.

Reducing the amount of scrap produced lowers material cost and environmental effect. In the long run, these benefits outweigh the costs of installing and maintaining the equipment required to join the OSB. (Material cost represents over 65% of the projected selling price of the roof panels.) Furthermore, our dilemma over the OSB supply is solved. The stock can be completely made up of standard 4×8 sheets.

2.4.2 OSB Preparation: End-jointing. Wood components may be fused together end to end through a process known as end-jointing. The joint linking two sections is formed by cutting their

ends in a particular pattern, gluing the mating ends together, and clamping the joint while the glue cures.

Although the manufactured building industry splices a variety of wood products this way, our research did not find anyone end-jointing thin OSB sheets in particular. Using a finger-type joint, Georgia-Pacific had tried and failed to end-joint 7/16" sheets. Because of the flaky structure of OSB and the lack of material in the thin sheets, the joint fingers had had no integrity [McCullough, 1993].

However, research did indicate that the endeavor is possible. Ray Bender [1993] of Indspec has successful experience end-jointing 1 1/2" OSB with a simpler joint known as a scarf joint. (Refer to Figure 2-8.) This joint, which is made with a single, angled cut at each mating end, provides a large surface area for the adhesive bond to form. For 7/16" OSB, Charlie Vick of the Forest Products Lab in Madison recommends that the length of the joint, ℓ, be six inches [1993].

Because OSB contains voids, Bender [1993] suggests that gap filling adhesives be used to form a strong bond. Potential candidates include melamines, melamine ureas, and phenol resourcinals [Vick, 1993]. Of these, the phenol resourcinals require the least amount of time to cure and are considered to be the best in the flakeboard industry. In addition, the melamine ureas, which are isocyanates, are dangerous. Odorless and colorless, these substances can, over time, cause industrial asthma [Bender, 1993].

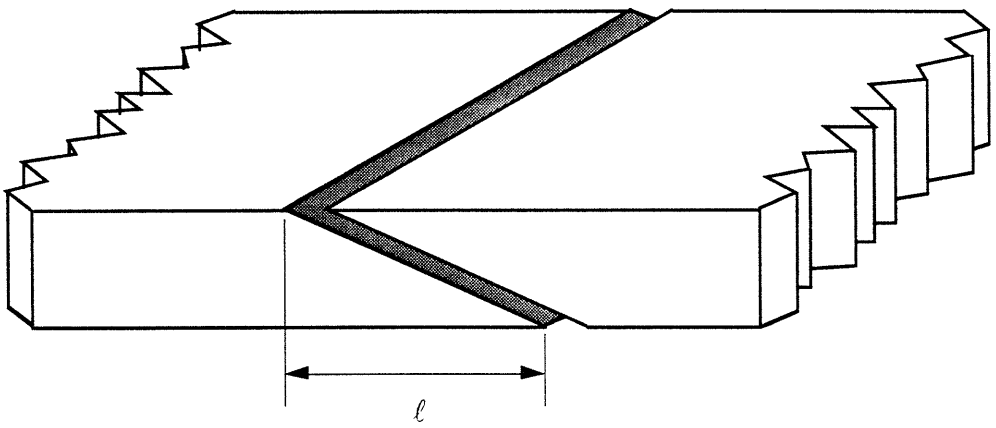

Figure 2-8. A sketch of a scarf joint. This glued joint can be used to splice the OSB sheets end to end—a process that would significantly reduce production of material waste

On the panel production line, cure time is especially critical. The joint must completely cure, at least on the surface (outer 1/8"), before the sections can continue to the next step in the process [Vick, 1993]. Otherwise, microcracks can form, which significantly weaken the joint. Phenol resourcinals cure at room temperature in about thirty minutes; this time diminishes to only a few minutes if the joint's temperature is elevated to 225 °F. However, to meet the panel production goal, the joint must cure in no more than half a minute. The only way to achieve this demand is to subject the joint to radio frequency (RF) energy. According to Mann-Russell Electronics, a producer of scarf joint gluing systems, the curing process, including closing and opening of the press, takes less than thirty seconds if a twenty kilowatt RF generator is employed [Knutson, 1991].

This technology is expensive, however. For example, a Mann-Russell two-line scarf-joint gluing system, which includes a main press with a twenty kilowatt RF generator, press infeed conveyors, stationary cut-off saw, outfeed conveyors with an overhead measurement device, and an Allen-Bradley motor control center,

sells for $200,000 [Knutson, 1991]. This price does not even include the equipment that cuts the scarf joints. A machine that simultaneously cuts the joints on both mating ends of 4×8 sheets, available from Mereen-Johnson, costs an additional $217,000.

Another alternative is to use a completely different type of adhesive. Hot melt adhesives cure rapidly at room temperature, within thirty seconds [Crowley, 1992a]. However, because the hot melt is a thermoplastic, it would creep during a fire, with possibly disastrous results. Thermoset adhesives, which are based on formaldehyde, do not creep, but they require six to seven hours to cure. The ideal adhesive would combine properties of both types—a quick setting substance that maintains its form and strength in high heat.

Evidence suggests that such an adhesive may be available in the near future. Polyurethane reactive hot melt (PURHM) adhesives, which are based on a chemical reaction of a polyol with an isocyanate, cure in a two stage process ["Reactive", 1992]. The adhesive is applied in a molten state, and as it cools, an initial bond forms that is strong enough for handling. Exposure to moisture in the air and in the OSB initiates a further reaction that causes the substance to form a thermoset polymer. This polymer has heat resistance against prolonged exposure to 230 °F and short term exposure to 300 °F. The polymer also boasts water resistance, solvent resistance, and cold temperature resistance (-40 °F).

Nevertheless, this new PURHM technology may not be ready for end-jointing the OSB components. Larry Cerkanic [1993] of Henkel Adhesives Corp., a supplier of PURHM adhesives, says that

the polymer is only a virtual cross-link thermoset, and that his company is not willing to endorse its use in roofing panels. Independent testing must be done to establish whether this technology is suitable for the application. So for now, we assume that the manufacturing line must incorporate RF curing equipment.

2.4.3 OSB Components Assembly. What is the simplest, cheapest, most efficient, and most reliable way to bring the components together? The vagueness of the phrase *bring the components together* in this question alludes to how difficult focusing on a problem is when designing an assembly process. The question is really composed of numerous other questions about the movements of the components: which components move and which are stationary, in what order are the components connected, how many at a time, what are their orientations, and how do these orientations change in the process.

To minimize complexity and assembly time (as well as floor space used), the moves should be as short in distance and as few in number as possible. From the first part of this guideline, we can say that, where possible, the components should be transferred along their widths rather than their lengths. Consider, for example, aligning a twenty-four foot rib for attachment to the bottom face. Moved along the width of the face, the rib might be aligned in a distance as short as two inches, if we assume the rib is initially positioned just outside the perimeter of the face. On the other hand, the rib would have to travel no less than twenty four feet if moved along the length of the face.

We also have constraints for handling the OSB components. All but the smallest faces and ribs, and many of the end caps, are highly flexible; the longer they are, the more flexible they are. Therefore, during assembly, these objects must be positively grasped at many points to ensure proper alignment. In addition, some rib edges will be coated with adhesive. This glue must not contact anything except the mounting surfaces, and it must not be smeared. In other words, the joints must be formed without the parts sliding relative to one another.

Before assembly, the faces, ribs, and end caps are all lying flat, so they must be rotated into the proper relative orientation. Several approaches are possible, but the most practical one is to leave the faces as they are and orient the ribs and end caps accordingly. Once the ribs are aligned parallel to the length of the faces, they are simply rotated 90°. The end caps, on the other hand, require two independent rotations whose magnitudes are determined by the roof geometry.

Just as the ribs and end caps are cut at different stations, they are handled by different subsystems. Likewise, we break our discussion into two parts here.

2.4.4 Rib Manipulation. After the ribs are cut, they are transported to an assembly area. The most cost-effective way to get them there is on a standard conveyor. However, in the process, they will undoubtedly shift out of alignment, and the shift may be exaggerated for the very small ribs, like those in Figure 2-3.

So, in addition to being rotated 90° for assembly, these ribs must also be reoriented. For the longer ribs, this task is simple. They are simply put on an incline, and gravity does the work. But for the odd ribs of Figure 2-3, much more is involved.

From this need grew the concept of a rib orienting mechanism that accepts any rib in any orientation (within reasonable expectations) and performs the realignment and rotation automatically. Ward [1994] designed, built, and tested a prototype for such a mechanism. This device, which employs two servo-controlled paddles to realign the odd ribs, succeeded in handling ribs of all shapes and initial orientations.

Also conceived was a transport device that grabs the oriented ribs, one by one, and carries the load (along the direction of the ribs' thickness) into position above the bottom face. This overhead transport mechanism (OTM), whose conceptual design appears in Ward's thesis [1994], then presses the ribs onto the bottom face while they are fastened from underneath by automatic staplers. Finally, the top face is added later (after the insulation is applied) by a lifter that moves width-wise, in a manner similar to the OTM.

2.4.5 End Cap Manipulation. After the ribs are stapled to the bottom face, end caps are affixed to the rib ends. Capping the ribs before their union with the bottom face was considered, but no clear advantage was apparent. In contrast, fastening the ribs to the bottom face first, which is a straightforward operation, creates a more rigid subassembly and thereby reduces the likelihood of trouble during the end cap attachment.

The end caps must be rotated about two independent axes to achieve proper orientation for attachment to the rib ends. This manipulation is inherently more complex than orienting the ribs. Furthermore, like the ribs, the end caps come in a variety of shapes and sizes (although in this case, all the shapes are parallelograms). As it turns out, automation was determined not to be cost-effective for this task, but the end cap will be fastened with a servo-controlled nailing mechanism. Chapter 3 covers this subject in greater detail.

2.4.6 Insulation and Blocking. Making insulation an integrated part of the roof panel adds considerable value to the roofing system. It not only reduces on-site labor, but also improves quality control of the roof's thermal characteristics, compared to those of conventional roofs. Defects such as insulation gaps, blocked ventilation passages, and thermal bridges are common in site-built roofing [Crowley, Dentz, and others, 1992]. Shifting responsibility to the factory enhances the likelihood that these defects will no longer inflate the energy bills of homeowners.

For the purpose of maintaining comfortable house temperature, the form of the insulation does not matter, only that the insulation provides the necessary thermal resistance and does not interfere with proper ventilation. The roof system design specifies that the roof panel must have an overall R-value of 31 or greater and that a gap of at least one inch is left between the insulation and the top face [Crowley and others, 1992].

Batt or blown-in insulation would serve this purpose equally well, but their methods of installation set them apart. Insulation

batts work well in assembly by hand. They are simply cut to size with a utility knife and laid in place. An automated process, too, would easily cut the batts to proper size; it could do so, in fact, with much greater precision. However, the inappropriateness of these batts in an automated production line becomes apparent when the issues of storage and handling are considered. In the extreme, a panel is twenty-four feet long and has three channels to fill. A batt roll with enough insulation for just one channel would be about five feet in diameter, and such large rolls would constantly have to be retrieved and spooled to keep up with the production volume of the line.

Insulation that is made to be blown, sprayed, or poured is much better suited for automated panel production. The insulation material is stored efficiently in one or more large vessels and dispensed through a hose or similar apparatus. Furthermore, the process can be controlled with good accuracy. If fiberglass insulation is used, for instance, a typical level accuracy achieved with, say, a four inch hose is ±0.25 inches [Crowley, 1992a]. The application can be further refined by adding a watered-down binder to the insulation so that it will spread out. This practice reduces the need for mobility in the hose. Finally, blown-in insulation possesses the additional advantage over batts that recycled material may be, and often is, used in its production. (As part of the Innovative Housing Construction Technology Program, MIT is considering the feasibility of alternative insulation materials derived from newspaper and other waste paper and plastic products.)

The production speed at which this line will be operating, however, reduces the potential of some insulation spray systems as solutions. To meet production rate demand, the material flow rate must be high compared to what is common for this type of equipment [Ward, 1993]. The swift-moving material could bounce off the panel surfaces, failing to fill the panel accurately, as well as making a mess.

One promising method comes from Ark·Seal, a company based in Denver. An adaptation of their Blow-in-Blanket System (BIBS) would employ a cover to control the level of the insulation [Kuta, 1993]. One or more nozzles would automatically mix a binder with the insulation material and spray the mixture into an open-top panel subassembly. The system would control the applied insulation's density, and hence R-value, by regulating the amount of material dispensed according to the pressure exerted on the cover. According to Jesse Aragon [1993] at Ark·Seal, the large version of their system, with three nozzles, could completely insulate a twenty-four foot panel in two minutes. This system with two nozzles (standard) sells for about $25,000. (Price for the machine with an extra nozzle was not available.)

At this same station, before the insulation is applied, a block of polyurethane foam is deposited near the center of the panel subassembly, which is formed by the bottom face, the ribs, and the end caps. This block, bonding to the ribs and the bottom face, adds structural stiffness and strength to the roof panel.

The foam is stored under pressure in fluid form until application. Once it is deposited, a blowing agent in the material

causes it to expand, and in seconds, the foam begins to harden. After about five seconds, the foam would be firm enough to be covered, at which time the insulation subprocess would begin [Moore, 1993].

The most widely used blowing agents today are HCFC 141B and carbon dioxide (CO_2). Although HCFC 141B is one tenth chloro-fluorocarbon (CFC), this blowing agent should be chosen over the CO_2 because of its superior thermal performance. With CO_2 , the foam has an R-value density of only 2.8 per inch of thickness. A block 7 3/4" deep (up to the bottom of the ventilation scallops) therefore has a total R-value of only 22, well out of specification. Expanded with the HCFC agent, the block's R-value would exceed 50.

The amount of CFC released into the atmosphere would be negligible. Furthermore, HCFC 141B, a class two substance, will be phased out (replaced) by the year 2015.

Off-the-shelf dispensing equipment will likely be suitable for the production line. Available through Foam Enterprises in Minneapolis, for example, is a portable machine capable of depositing one-cubic-foot blocks, one at a time. The price of this machine falls within the range of $20,000-$25,000 [Farmer, 1993]. Sold in fifty-five gallon drums, the foam itself costs about $1.25 per pound.

2.5 Manufacturing Process Layout

We have explored some of the defining design issues for the major duties of the roof panel production process. Resulting machine concepts include the OSB feeder, the end-jointer, the assembly

devices for the faces, ribs, and end caps (overhead transport mechanism, rib orienter, end cap nailing mechanism), and the insulation and foam dispensers. In general, the subjects of material waste, production rate, and capital investment directed the search for solutions, with investment cost often being included indirectly through the assessment of complexity. Consolidating the stations into a complete manufacturing process, too, is governed by cost, speed, and efficiency.

This section presents the overall process layout of the production line. In an effort to follow guidelines for efficient material handling—optimize material flow, use minimum space, keep it simple, to name a few—numerous layouts were generated and refined. In Figure 2-9, the end result is depicted in a generic, simplistic flowchart that emphasizes the division of operations and the physical relation they have to one another. Figure 2-10, which immediately follows, depicts the process in a more informative schematic.

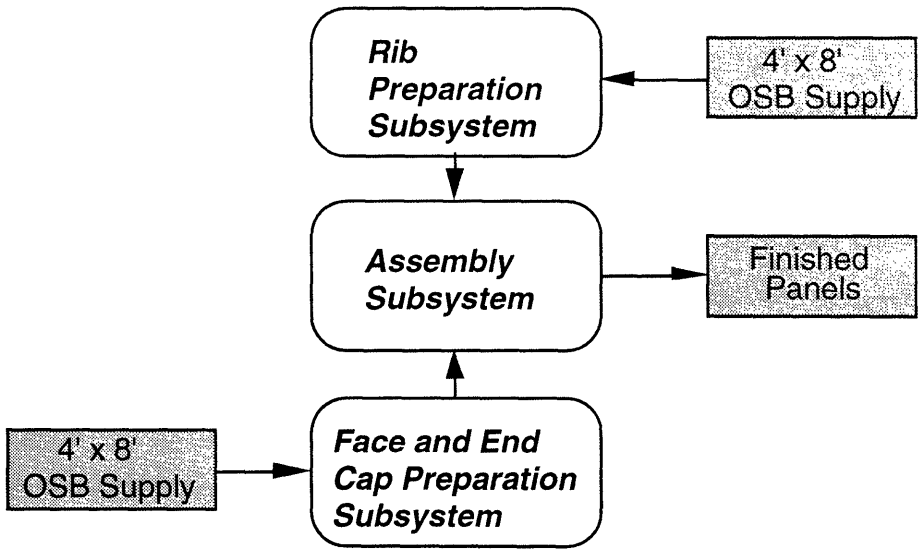

Figure 2-9. Simple schematic of the manufacturing line. The layout of the blocks in the diagram reflects the true arrangement of the facility.

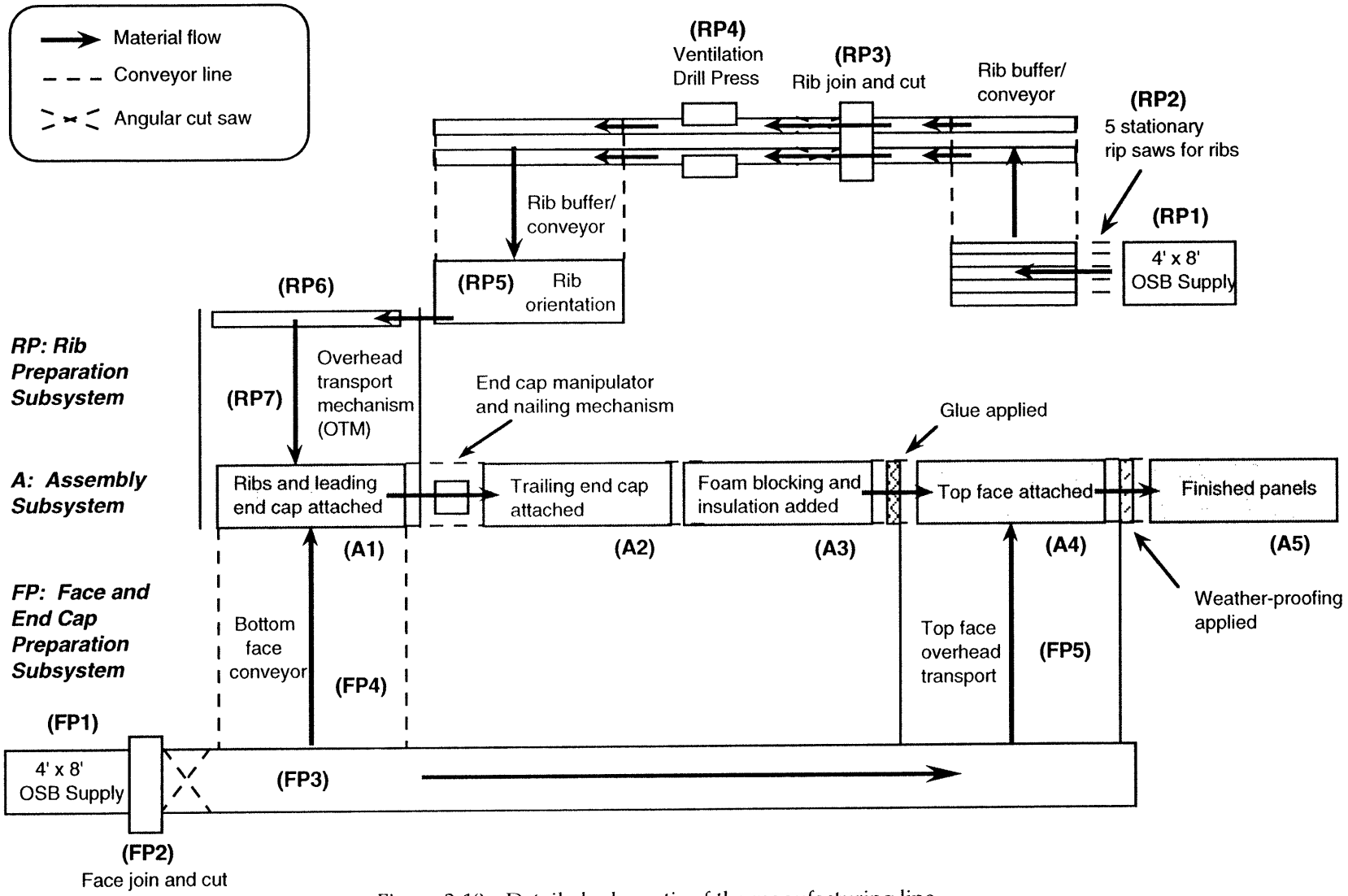

Figure 2-10. Detailed schematic of the manufacturing line.

The following steps, labeled in Figure 2-10, describe the process in greater detail.

Rib Preparation

(RP1) Using a mechanized lifter, an operator feeds sheets of OSB, used for rib production, onto a conveyor.

(RP2) The rib supply sheets are cut into strips.

(RP3) The strips are spliced with a glued scarf joint and cut into ribs by an angular cut-off saw.

(RP4) Ventilation scallops are cut at the top of the ribs, which are lying flat, by a drill press.

(RP5) A rib is rotated 90° onto its bottom edge, and its ends and bottom edge are glued as the rib is moved toward the overhead transport mechanism.

(RP6) The rib is positioned lengthwise and picked up by the overhead transport mechanism. RP5 and RP6 are repeated until the overhead mechanism has collected all the ribs for one panel.

(RP7) The ribs are moved to the assembly subsystem by the overhead transport mechanism.

Face and End Cap Preparation

(FP1) Using a mechanized lifter, an operator feeds sheets of OSB, used for face and end cap production, onto a conveyor.

(FP2) The sheets are spliced (with the same process used in rib preparation) and cut into top faces, bottom faces, and end caps by an angular cut-off saw.

(FP3) A face conveyor and buffer system delivers top and bottom faces to their respective transfer locations.

(FP4) The bottom face moves from the face preparation subsystem to the assembly subsystem on a connecting conveyor.

(FP5) The top face is moved from the face preparation subsystem to the assembly subsystem by an overhead transport lifter.

Assembly

(A1) A bottom face is conveyed from the face preparation area and secured. Ribs, transported from the rib preparation area, are held in place by the overhead mechanism as they are stapled to the face from below by translating staplers. Afterwards, an operator positions an end cap at the leading end of the panel, and the nailing mechanism fastens the end cap. (Refer to Figure 2-11 for a three dimensional schematic of the assembly subprocess.)

(A2) An end cap is affixed in the same manner to the trailing end of the panel.

(A3) A block of foam is sprayed into the space between the inner ribs, and insulation is sprayed into the channels formed by the ribs.

(A4) The top-face transport lifter sets the top face on the panel and staples it to the ribs.

(A5) After weather proofing is applied to the top face, the panel is stacked onto a pallet for shipment to the work site.

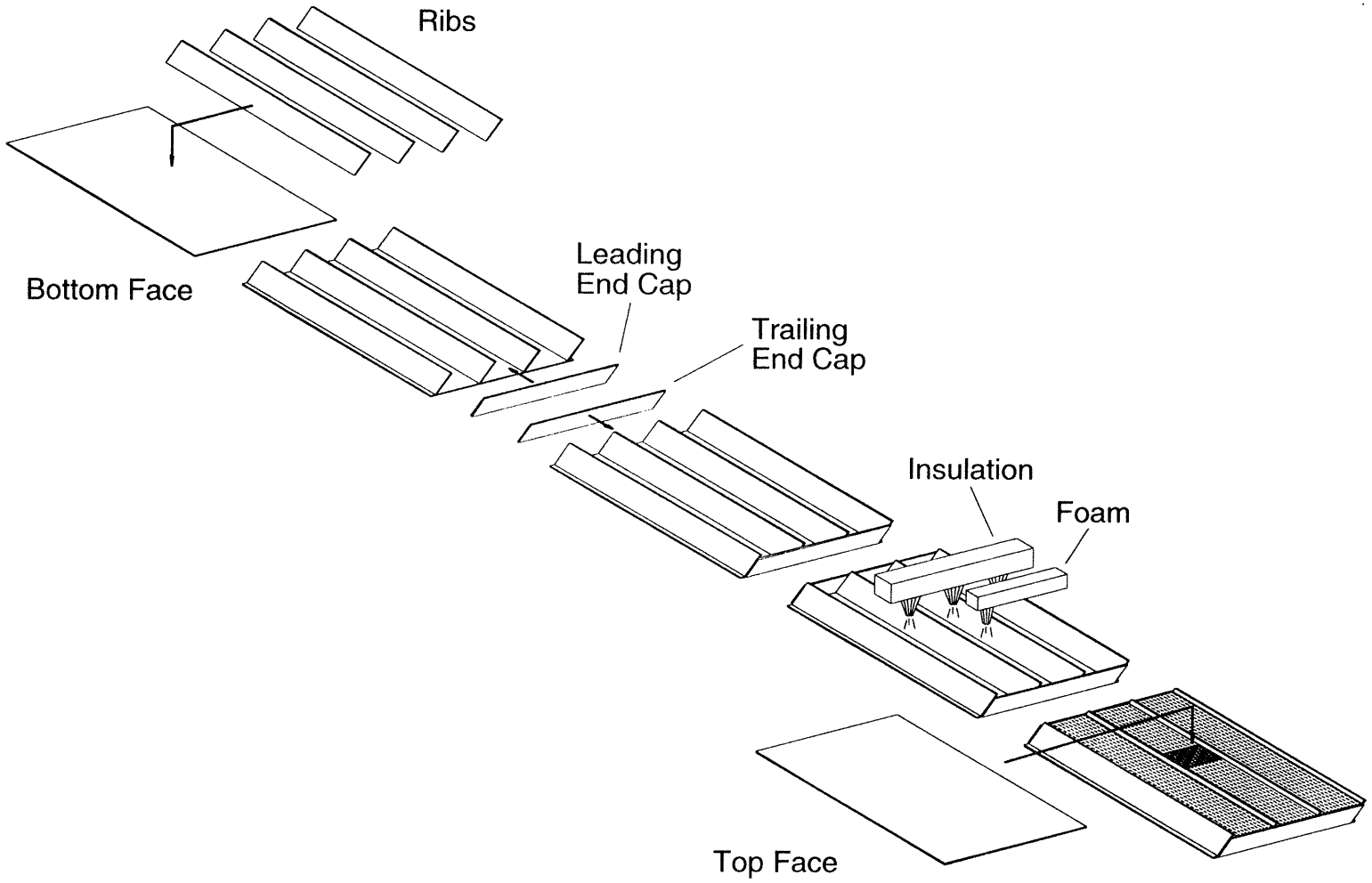

Figure 7-11. Schematic of the panel assembly process.

2.6 Production Capacity

One key motivation for development of the MIT roof system was the demand for reduced time lag between the design of complex roofs and installation. Developers aimed to shorten the completion time of every aspect of the roof construction process—design, specification, manufacture, delivery, and installation. They further planned to provide the product at a lower cost than wood truss and rafter roofs.

These goals, combined with knowledge of market acceptance of truss technology, led to the expectation that within fifteen years of the product's introduction, the MIT roof can capture about 40% of the complex-design roof market. Using this prediction, Crowley [1992] established a target daily output for the roof panel production line: 10,000 ft^2 of roof per eight hour shift. If the panel dimensions are 12 ft. by 4 ft. on average, the line would be producing about 208 panels in every eight hour period of operation.

The time to complete one panel equals the time to progress through the longest station multiplied by the number of stations operating in parallel. In contrast, the cycle time, the time that elapses between completions of the panels, simply equals the time consumed at the longest station. To meet the production goal, the fabrication process must have a cycle time of 138 seconds, or 2.3 minutes.

The process was decomposed into its fundamental operations and the time to complete each was estimated. These operations were

then combined in Gantt charts, which appear in Appendix A, to gain an understanding of how the timing of the process may work and to predict the actual cycle time. Based on conservative estimates, the cycle time is 180 seconds; the line would produce 160 panels per day, 77% of the target rate. However, the estimate is not so far off the goal that it cannot be reached. Instead, the timing analysis provides insight that should be used in refining the process further.

2.7 Further Development

With an understanding of the major subprocesses and a concept of how they come together, the design may proceed beyond the conceptual. At this point, the focus shifts from a comprehensive view of production to a confined look at the individual tasks that must be performed.

For this thesis, the end cap station was identified for detailed design because of the technical challenges it poses. Capping the panels is not a simple task to automate. The surface formed by spanning the ends of the ribs, which must be matched by the end cap, is described by two rotational degrees of freedom; the only reference is the location of the end cap's bottom edge within the plane of the conveyor surface. The dimensions of the end cap itself vary with the change in its destined orientation. The design problem is further compounded by the flexibility of the larger end caps, which makes them awkward to handle.

For this reason, we explored the possibility of eliminating end caps from the panel design. What we found is that the end caps make essential contributions to the design, and we were unable to generate a

better alternative. The end caps serve three basic functions: containment of the insulation, assistance in roof assembly, and structural rigidity.

Because the spray type insulation flows until the adhesive in it cures, the insulation material has to be contained as it is being sprayed into the channels formed by the ribs. End caps provide that function by closing the ends of the channels. The end caps also protect the insulation from objects that might otherwise penetrate the ends of the panels during shipping and handling. In addition, shifting of the insulation that could occur during transport and throughout the use of the panel is limited.

By covering the rib ends, the end caps act as smooth bumpers during roof assembly. As a result, the construction workers have a much easier time aligning the mating ends of panels at a hip or valley line. This revelation was discovered during assembly of the first proof-of-concept structure when end caps were not a part of the panel design.

Finally, the end caps help prevent collapse of the panels by bracing the rib-face joints.

Chapter 3
Conceptual Design of the End Cap Station

The end cap station must handle end caps of numerous sizes and geometry, and it must place, hold, and fasten them in a variety of orientations in space. The key challenge, therefore, in automating the attachment of end caps lies in the need for flexibility.

This chapter describes the extent of this variability and states what is required to properly affix an end cap. Several approaches are explored, and one is chosen for refinement. Finally, the chapter gives a brief but thorough explanation of how the proposed designs work, including a step-by-step account of the end cap attachment procedure.

3.1 Specifications

At each end of every panel, the rib-end surfaces uniquely define a plane. The orientation of that plane depends on whether the end in question is part of the ridge, the eave, or a hip or valley line. It also depends on the local roof pitch, and for some panel ends, on the local turn angle of the house.

The end caps, which rest flush against these rib-end surfaces, may be shaped as rectangles or non-rectangular parallelograms. The rectangular caps come in three lengths to go on the straight ends of

one-, two-, and three-bay panels: 15.25", 30.06", and 44.87". In contrast, the non-rectangular caps, which fit the angled-end panels, have an infinite number of possible lengths, ranging from 15.25" to over seven feet. Finally, the widths of the end caps, as well, have infinite variation within a certain range.

Precise alignment of the end cap on the panel is not critical. The only requirements are that the cap completely covers each rib end to ensure good contact at the joints and that the cap's bottom edge leaves as small a gap between itself and the bottom face as possible. A gap there would allow insulation to escape as the panel is being filled. However, a small gap can be tolerated because the binder in the insulation would quickly plug the gap and prevent leakage. Figure 3-1 illustrates details of the end caps' proximal relationship to the face and rib corners.

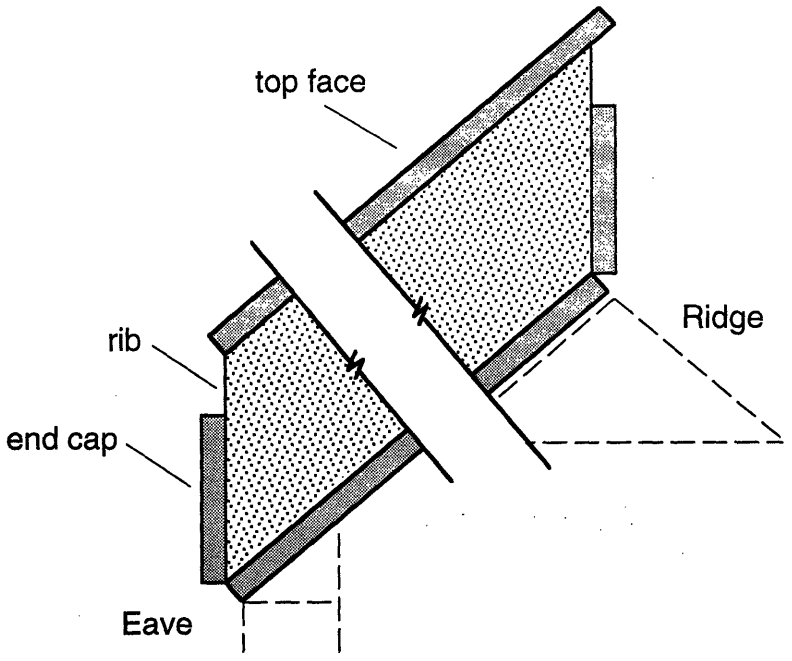

Figure 3-1. Side view schematic of a roof panel. The thickness of the end caps and ribs is exaggerated to highlight details of how they adjoin.

At last, two ring-shank nails at each rib end fasten the end caps to the ribs. These nails provide the clamping that is necessary to ensure good adhesive bonds. The requirements for where these nails should be driven appear in Figure 3-2.

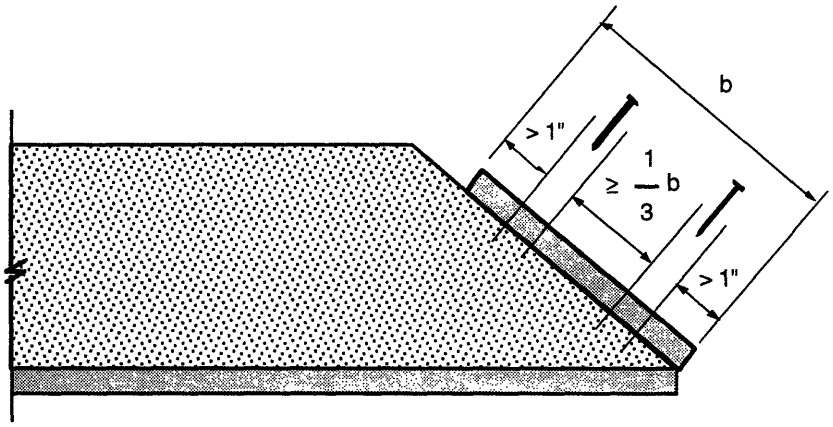

Figure 3-2. End cap nailing specifications. Two nails are driven through the end caps at each rib. Exactly where is not important, but the nails should be adequately separated and not too close to the edges.

3.2 Approaches

After an end cap has been cut to size, its attachment to the panel can be viewed as a three-part process. The cap is transferred to the end cap station, where it is then oriented and placed on the end of a panel. Once in place, it is fastened to the ribs with nails. Conceivably, these tasks could all be completely automated—performed by several independent, specialized devices or one integrated apparatus. As with all the stations in the fabrication

process, we wanted to automate as many tasks as technically and economically feasible. Our efforts produced three different approaches with distinct levels of automation.

3.2.1 Standard General Purpose Robot. In the process layout defined in Chapter 2 (Figure 2-10), the physical distance separating the end cap station from the cutting station effectively eliminates the possibility of one mechanism doing everything. A more reasonable approach would be to transfer the end cap on a conveyor and have a robot do the rest. This robot would need at least five degrees of freedom (DOF), three to position the end cap and two to orient it.

We considered implementing one of a number of industrial robots and equipping it with an end effector specifically designed to handle the long, flexible end caps. For example, an end effector that possesses a wrist joint could be affixed to the AdeptOne SCARA robot, which has four DOF, to provide the extra rotational axis needed to orient the end cap. Other robots, such as the GMF M-100 material handling robot, which has five DOF, and the six DOF Cincinnati Milacron T3-646 would only require modification for gripping the end cap. However, all of these robots are expensive. New, the GMF M-100 and the T3-646 both sell for over $70,000 [Marshall, 1993]. At $55,000 new, the AdeptOne is somewhat less expensive, but also requires more modification.

In addition, the robot could not be expected to simultaneously nail the end caps to the ribs. That task would require an additional robotic device.

3.2.2 Specialized Robotic Apparatus. Another approach considered was to develop an automated fixturing apparatus, somewhat similar in principle to some truss fabrication tables in use today. The servo-controlled apparatus would configure itself according to the current panel end, and an operator would place the appropriate end cap in its grasp. It would then translate to the final destination and attach the end cap.

The design conceived for this device consists of three linear tracks, along which nodes translate independently of one another. Their differential displacement, which defines either one or two lines, would set one angular position of the end cap (or caps) being attached. (The two-line configuration is for compound-end panels, such as those that adjoin a dormer or the vertex of two hips and the ridge.) The other angle would be achieved through rotation of joints at each node.

In spite of the promise this approach has for rapid end-cap maneuvering that gives up nothing in flexibility, it was abandoned because it threatened to be costly and difficult to implement.

3.2.3 Hand Manipulation with Robotic Fastening. In place of a robotic fixturing apparatus, a passive mechanical manipulator can be employed. As before, an operator would deliver an end cap into the device's grasp. This time, however, the operator would adjust the device to orient and position the end cap. Leaner and much less expensive, this device would be inherently less likely to interfere with other equipment, including a robotic nailing mechanism that would travel from rib to rib, firing nails into each.

3.3 Evolution and Justification of Approach

Separating the tasks of manipulating and fastening makes sense because their directions of action are inherently independent. Orienting the end cap requires rotation about some line in the x-z plane, a line whose own orientation within the plane varies with the roof pitch. (Refer to Figure 3-3.) Orienting the fasteners is more straightforward. Although the fasteners are rotated about the z-axis to match the roof pitch, they are always driven into the ribs within the planes of the ribs (parallel with the x-y plane).

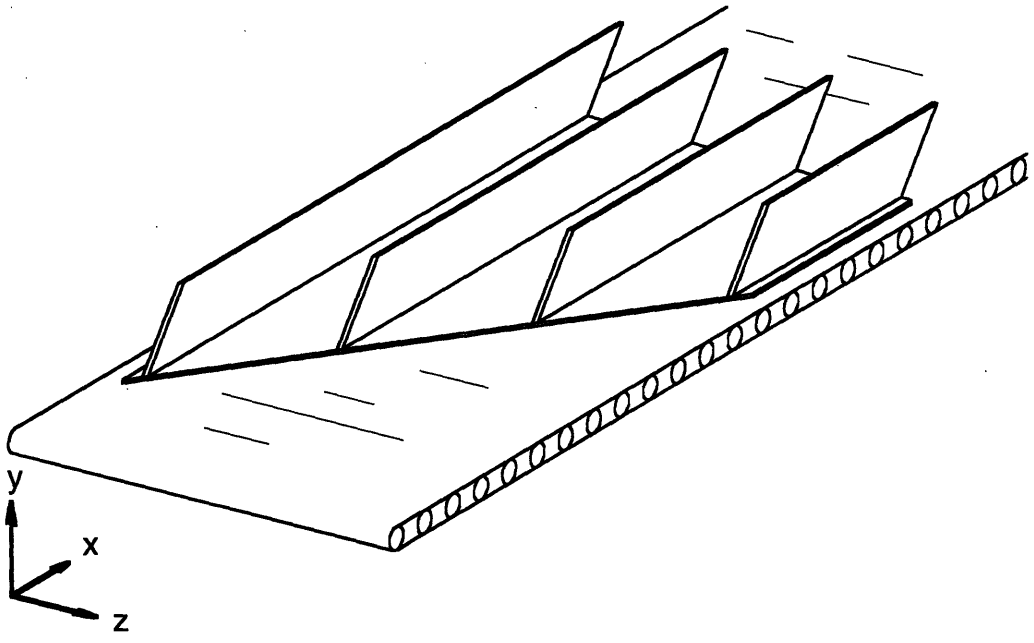

Figure 3-3. Rib and bottom face subassembly. The end caps butt against the ends of the ribs, and the nails are driven straight into the thickness of the ribs.

3.3.1 Manipulating. In this particular fabrication process, manipulation is not well suited for full automation. True, a robot can

achieve higher accuracy in positioning and orienting objects than a person can. Yet the accuracy actually needed for positioning the end caps can easily be achieved by a person. In fact, in this case, a person can do the job more reliably and more quickly. Precise alignment of the end cap on the panel end is not critical, but the end cap must contact each rib over most of its end surface area for the end cap to be fastened properly. This task is much easier for a human than for a robot, which would likely need a complex arrangement of feedback sensors. Moreover, in spite of the advantages of robots, they have difficulty handling large, awkward payloads.

The mechanical fixturing device is essential, however. One person cannot adequately orient and apply the longer end caps by hand without being directly in front of the panel end (the longer caps, which may be seven feet or longer, are very flexible). Either the worker would have to be in line with the flow of the process or the panel would have to be taken off line. Although two people could easily do the job, we could not justify committing two people to attaching end caps. Furthermore, having anyone hold the end caps for an automatic nailing mechanism presents a potential safety hazard. Safeguards could be put in place, but avoiding the danger altogether is the best solution.

3.3.2 Fastening. Experience in building two proof-of-concept structures testifies that fastening is a process that calls for automation [Morse-Fortier, 1993]. The ribs are only 7/16 of an inch thick, and they are hidden by the faces and end caps that are being

attached to them. For a person, driving nails or staples directly into the ribs is very difficult under these circumstances, particularly with the end caps, where the surface being contacted is not always perpendicular to the action of the fastener.

A robotic device could drive the fasteners with high repeatability, as the ribs would always have the same alignment. Moreover, automating this task makes the process much safer. Staplers and nailers can be dangerous and are frequent causes of injury.

3.4 How the End Cap Station Works

The mechanical fixturing device allows the operator to easily manipulate the end cap into its proper orientation. As shown in Figure 3-4, the manipulator has two rotational axes that allow the holding frame to match the orientation of any panel end. It also has two translational axes, one for moving the end cap toward the panel, and one for retracting the manipulator out of the panel's path.

Once the end cap is set in place on the panel, the overhead transport mechanism takes over. Holding the ribs with motorized clamps, the mechanism pushes the panel, along with the fixturing device, into the workspace of the fastening mechanism. These clamps, which move along guides on the mechanism's structure, are mechanically opened by cams when they reach the end of the structure. So, row by row, the clamps release the ribs as the panel

moves along the rollers. (For more details on the overhead transport mechanism, refer to Ward [1994].)

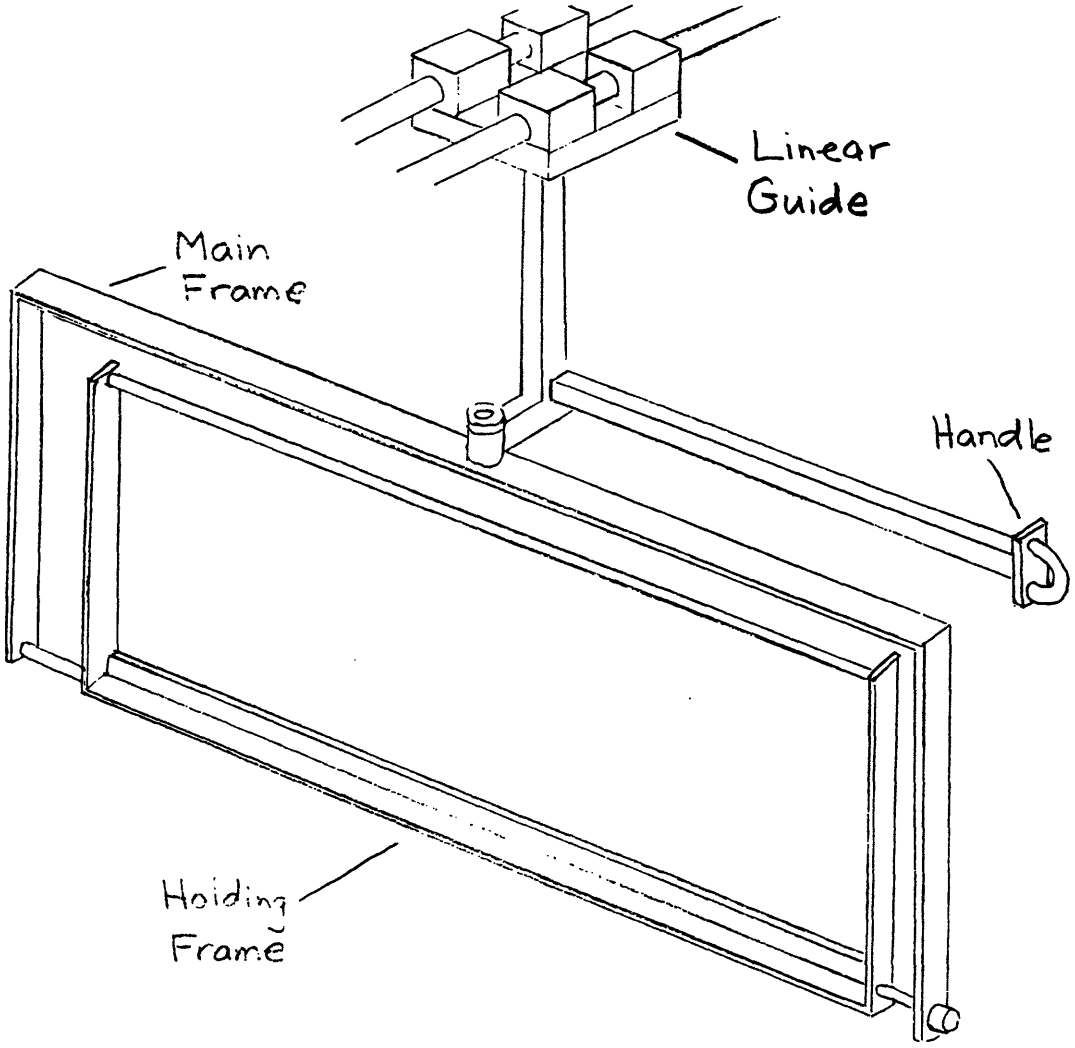

Figure 3-4. A sketch of the mechanical end-cap manipulator concept. Not shown are the manipulator's fourth axis, which allows the device to be lifted out of the way of a passing panel, and the suction holders.

With the end cap still secure in the fixturing device, the robotic nailing mechanism fastens the end cap to the ribs. The following list describes the steps of the end cap attachment process in detail:

(1) Observing the current panel subassembly on the line, the operator swings the main frame into an orientation that

corresponds roughly to the end of the panel and rotates the holding frame into a convenient orientation—perhaps almost parallel with the conveyor surface.

(2) The operator takes an end cap from the cutting station, carries it to the end cap station, and slides it onto the holding frame.

(3) Moving the manipulator in toward the panel subassembly, the operator makes course adjustment of the main frame and the end cap.

(4) The operator turns on the suction holders and flips the holding frame into position. He or she then makes final adjustments to align the ends of the end cap with the edges of the panel, presses the end cap against the ribs, and locks the holding frame.

(5) The operator activates the overhead transport mechanism, which pushes the subassembly and manipulator toward the nailer.

(6) On contact with the end cap, the nailer drives a nail into the end cap and rib, and then repositions itself to fire the next nail. After shooting two nails into every rib, the nailing mechanism retreats beneath the conveyor rollers,

and air to the nailer is cut off. The subassembly then stops, if it is not already at rest.

(7) The operator releases the manipulator from the end cap and raises the manipulator out of the way.

(8) The operator restarts the overhead transport mechanism, which then pushes the subassembly onto powered rollers. The powered rollers move the subassembly forward until the trailing edge of the panel has moved beyond the nailing mechanism's workspace.

(9) The end cap attachment process is repeated for the trailing edge of the subassemby, this time the powered rollers driving the subassembly.

Chapter 4
Detailed Design of the Nailing Mechanism

The end caps are fastened to the panels automatically by a robotic nailing mechanism. Matching the primary slant of the rib ends, as in Figure 4-1, this mechanism fires two nails into each rib—in many cases, while the panel is moving. Panel production goals require the device to move swiftly. At the same time, the shock loads induced by this action call for sturdy construction.

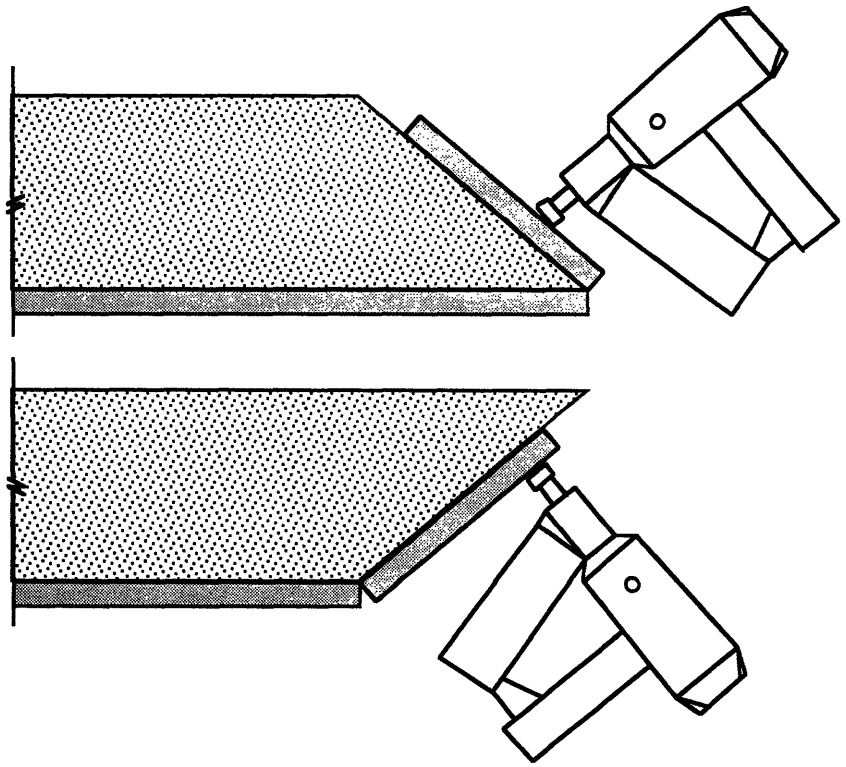

Figure 4-1. Side views of panel subassembly and nailer. The angle of the primary rib slant determines the orientation of the nailer and the arm.

This chapter explains how the parts of the mechanism work together to meet the requirements of fastening end caps to the panels. Following an overview of the basis for the design, the discussion breaks the mechanism down into its components and describes the relevant attributes and specifications. Where appropriate, justification is provided.

4.1 Operating Principle

The nailing mechanism comprises a commercially available, pneumatic nail gun mounted at the end of a servo-controlled arm, which is, in turn, mounted on a linear guide assembly (Figure 4-2). (Appendix B contains a detailed layout and mechanical design drawings, and Appendix C is a list of major parts to be purchased.)

In all, the mechanism has three degrees of freedom (DOF)—two in the x-y plane and one along the z-axis. One rotational axis is used to control the nailer's orientation; the other one is used to move the nailer in the x-y plane. Just two degrees of freedom are not enough, however, to define both position and orientation in a two dimensional space. For the nailer to reach a target position with the proper orientation, the arm must be coordinated with the panel's translation along the conveyor. Together, the nailer's orientation, the arm's angular position, and the panel's position determine where in a particular rib each nail is driven.

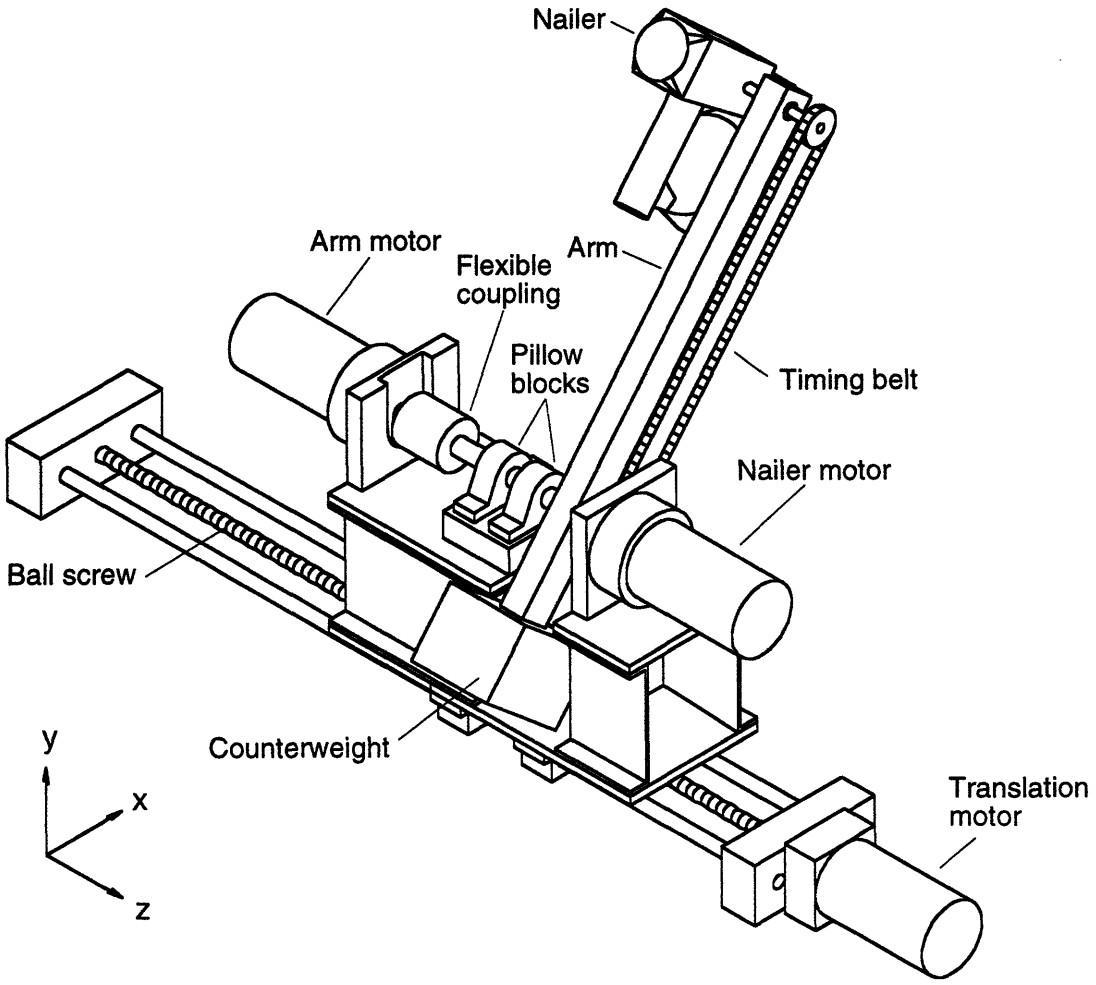

Figure 4-2. Layout of the 3-DOF end-cap nailing mechanism. The concentricity of the arm and nailer motors kinematically decouples the nailer's rotation from the arm's.

The translation axis, provided by the linear guide, allows the mechanism to move from one rib to the next. To prevent the mechanism from colliding with the surrounding conveyor structure, this movement is only allowed to take place when the arm is in certain positions. The arm must either be vertical such that it can move uninhibited along the conveyor gap, or below horizontal such that the nailer can pass underneath the roller support brackets.

Figure 4-3 depicts these positions relative to a possible configuration for the conveyor's structure. The first position is used when the panel end faces upward as shown. When the end faces downward (Figure 4-1), the mechanism must retreat below the conveyor surface to continue to the next rib.

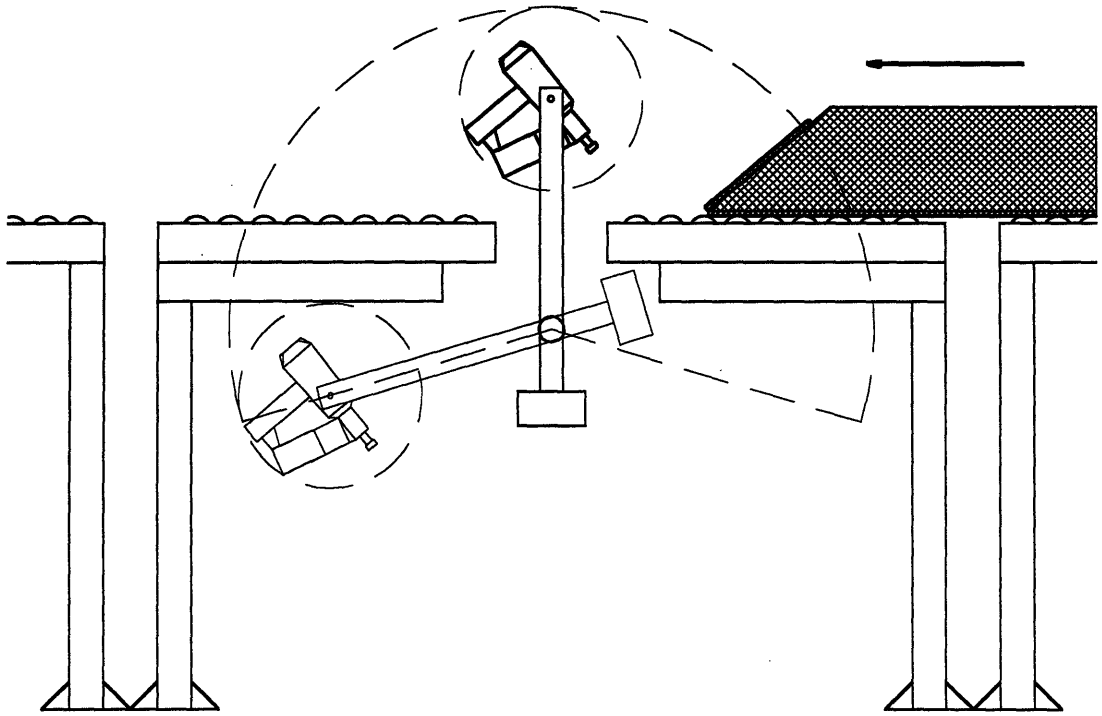

Figure 4-3. Side view of nailer and arm showing their workspaces and relation to the panel conveyor. The conveyor must be cantilevered as shown to allow the nailer to move between ribs.

The timing belt and pulleys link the nail gun with its actuator. The axis of this actuator, hereafter referred to as the nailer motor, is directly in line with the arm's axis of rotation. As a result, the angular position of the arm and the orientation of the nailer are effectively decoupled kinematically. In other words, if the nailer motor shaft were locked, the nailer would maintain the same

orientation in space as the arm rotated. This configuration is ideal for the end cap fastening operation because the nailer's orientation must simply match the panel's roof pitch angle.

4.2 Nailer

The fasteners are driven by a standard, hand-held-type nail gun. Held in position by the servo system, the nailer waits for the panel subassembly, and upon contact with the end cap, the nailer fires one nail. This contact mode of operation is standard on commercial nailers. With the trigger held, compression of the spring-loaded tip opens a valve, releasing air to propel the nail-driving piston. For this application, however, the tip must be modified slightly. (Refer to Chapter 5.)

The mechanism prototype was designed and analyzed with the assumption that the nail gun to be used is a model N50 coil nailer, produced by Stanley-Bostitch, Inc. The nailer's compactness makes it suitable for the limited space between conveyor tracks, while its light weight allows for rapid maneuvering. Space and speed aside, however, any other nailer would work just as well, as long as it accommodated the 2" ring-shank nails used for the end caps. (The ring shank helps provide the clamping necessary for the glued joint.)

The N50 has a 300-nail capacity, the largest among Stanley-Bostitch's hand-held coil nailers. In the panel production line, this nailer would have to be changed or reloaded, at most, once every 37

panels. During an eight-hour shift in which 160 panels are produced, the nailer would have to be changed or reloaded only three times.

A nailer was chosen over a staple gun, although staples would otherwise be preferred for the OSB joints. In general, staples provide superior clamping for the glued joints and are less likely to split the ribs. An additional degree of freedom would have to be added to the system, however, if a stapler were used. Because the staples are packed side by side in straight-line clips, the stapler would have to be oriented such that its magazine sticks out to one side of the rib. As a result, the stapler would have to be flipped 180° from time to time to avoid interference with the panel ends.

Finally, a signal must be sent to the controller after each nailer discharge so the computer can update the mechanism's position command. A pressure sensor placed inside the nailer to measure the pressure drop in one of the air chambers would accomplish the task at little cost.

4.3 Nailer Mount

In Figure 4-2 and Appendix B, the nailer is shown mounted rigidly to the shaft that permits its rotation relative to the arm. However, because of the dynamic loading inherent in the mechanism's operation, compliance must be integrated into the system. The solution recommended here is inserting a device between the nailer and its shaft that allows the nailer to translate with respect to the arm.

The action of this mount is modeled in computer simulation, and criteria for the key characteristics of the mount, stiffness and damping, are obtained. Both the analysis of Chapter 5 and the simulation results presented in Chapter 7 address the requirements of the device. Ultimately, however, the simulation is used to establish the maximum allowable stiffness, 1200 N/m, and maximum damping coefficient, 100 kg/sec, which are based on allowable torsion loads on the arm shaft.

4.4 Arm and Counterweight

Constructed of aluminum, the arm is designed to keep the weight and rotational inertia of the mechanism low. Contrary to the simplified drawing of Figure 4-2, the actual arm has a non-uniform cross section—a consequence of the confined space in which the mechanism must work. The arm narrows near its end so that the mechanism can move freely between the conveyor roller tracks. The thicker dimension near the base boosts stiffness to limit side-to-side vibration of the nailer.

If the arm is modeled as a massless cantilever beam (grounded at the rotation axis) with a lumped mass at the end, a conservative estimate of its fundamental frequency of vibration is 28 Hz. (See Appendix D.)

By balancing the mechanism, the steel counterweight reduces the nonlinear effect of gravity on the mechanism and thereby improves its performance. With its mass center spaced 7.65 inches

from the arm's pivot, the 31 pound weight reduces the maximum static torque on the arm motor to about 14 in.-lb. (1.6 N-m). The variation comes from rotation of the nailer, whose mass center is offset from its rotational axis.

4.5 Arm Drive

The drive system for the arm consists of a DC servo motor with a gear reducer, a pillow-block mounted shaft, and a flexible coupling.

4.5.1 Motor. The nailing mechanism makes only short, quick maneuvers during its operation. To drive this motion, which is characterized by low speed and high acceleration, a brushed DC servo motor was chosen. Stepper motors cost less, but they are better suited for applications where the dynamic requirements and external loads are not so high.

For this intermittent application, peak torque rating supplies the basis for motor size selection. The motor must accelerate and decelerate a large inertia without overshooting the destination, but demand on the motor lasts for very short periods of time. The mechanism's speed is particularly important when the panel end is of the angled type. In this case, the panel translates at a constant speed, and the mechanism must settle at each nailing position before the panel passes through that point.

We can find a minimum torque requirement by estimating the accelerations required to move the arm to each of these points within

the time allowed. Using the assumptions and data listed in Table 4-1, we find that the motor must output a peak torque of at least 9.3 N-m.

Table 4-1
Information for Sample Motor-torque Estimate

Assumptions	Data
roof pitch: 30° (worst case)	critical rotation: 10.5°
panel speed: 3.0 in./sec.	time allowed: 0.64 sec
trapezoidal velocity profile: 2/3 acceleration, 1/3 max. velocity	motor inertia: 2.36e-4 kg·m^2
	load inertia: 1.85 kg·m^2

However, the discharge of the nail gun puts an even greater demand on the arm motor, which must bring the resulting response under control. Computer simulation, covered in the following chapters, provided insight into this event, and ultimately led to the final choice: a motor with a peak output-torque rating of 192 N-m (1699 in.-lb.) and a continuous rating of 77 N-m (681 in.-lb.). In addition, the transmission ratio of the gearing is 100:1. Selected from the available standard reductions, this ratio approaches the optimal ratio of 89, obtained by impedance matching the inertias. Park and Kim [1989] show how this optimal ratio, defined explicitly in Equation 4-1, minimizes heating of the motor.

$$n_{opt} = \sqrt{\frac{I_L}{I_M}} \qquad (4\text{-}1)$$

where

$I_L \equiv$ *mass moment of inertia of the load*

$I_M \equiv$ *mass moment of inertia of the motor*

The motor also has a built-in optical encoder and a tachometer for measuring the arm's position and velocity, which are employed in the mechanism's control system (Chapter 7). For safety, the motor has a built-in brake that automatically engages if power is lost.

4.5.2 Shaft and Bearing Layout. The arm shaft transmits torque between the motor and the arm, and supports the arm in a cantilevered arrangement. Two pillow blocks carry the radial and axial loads exerted on the shaft by the arm, which is press-fit and bolted onto a square section of the shaft.

A flexible coupling, available through Zero-Max, Inc., connects the arm shaft and the arm-motor shaft. This particular coupling fits the application well because it takes up a large amount of misalignment (3° angular, 0.015" parallel, 0.09" axial) without sacrificing the high torsional stiffness necessary for a responsive system.

The drive-system components carry large, dynamic loads from the nailer's action. Depending on the orientation of the nailer with respect to the arm, these loads may be mostly torsional or mostly radial. Analysis of both situations was performed to ensure proper selection of shaft, coupling, and bearings. Chapter 5 investigates the

radial loading analytically, whereas the torsion loading is revealed by computer simulation (Chapter 7). The component selections based on this analysis are summarized as follows:

- a 1 1/8" arm shaft, made from AISI 1050 cold-drawn steel (S_{ut} =100 kpsi, S_y =84 kpsi)
- a single flex, composite disc coupling: Zero-Max, model 6A45 (peak torque rating of 564 N-m, safety factor of 2.5)
- Dodge pillow blocks with SC bearing inserts (static load capacity of 2250 lb.)

4.6 Nailer Drive

Like the arm, the nail gun is driven by a gear-reduced DC servo motor. A timing belt links the nailer to the nailer-motor shaft, which adjoins the arm shaft through a radial bearing.

4.6.1 Motor. The nailing mechanism's operation is much less demanding on the nailer motor. Because of the kinematic decoupling from the arm, the position command remains constant during the process. Also, this subsystem has relatively low inertia, and the offset of the nailer's mass center from the recoil's line of action is small (about 1.75").

The nailer motor, also equipped with an encoder and tachometer, has a peak output-torque rating of 23.3 N-m (207 in.-lb.)

and a gear reduction ratio of 20:1, compared to the optimal ratio of 24.

4.6.2 Shaft and Bearing Layout. The input-end timing pulley attaches directly to the nailer-motor shaft; no flexible coupling is included. In addition, the nailer-motor shaft is pressed into a bearing located in a bore in the arm shaft. This connection of the two shafts ensures concentricity between the two axes so that the center-to-center distance between the pulleys remains constant as the arm rotates. Furthermore, the bearing carries part of the load from the tension in the belt and thereby reduces wear on the nailer motor.

4.7 Linear Guide Assembly

Translation along the width of the panel is provided by an integrated, double-shaft ball-screw assembly produced by Thomson Industries. Size selection (shaft diameter) was based on the maximum travel rate of the carriage, which is limited by the system's natural frequencies of vibration. For this system, which has an overall length of 66", a 1" shaft diameter allows for an acceptable rate. Taking 72% of the system's critical speed and assuming the translation velocity follows a trapezoidal profile (2/3 acceleration, 1/3 maximum speed), we obtain an estimate of 1.64 sec for the time to travel from one rib to the next (14.81"). Based on a lead of 1" per revolution, an estimate of the torque required for this movement is 0.5 N-m (4.4 in.-lb.).

Once again, the subsystem employs a DC servo motor with encoder and tachometer feedback. The motor's continuous torque rating is 1.32 N-m, leaving a 164% margin over the acceleration requirement.

Chapter 5
Load Analysis and Design Justification

Unlike most robotic devices, the end cap nailing mechanism is regularly and purposely subjected to shock loads. Those loads come from two events: the discharge of the nailer and the collision of the panel with the nailer. These external forces on the nail gun generate reaction forces throughout the nailing mechanism. The critical reactions are those carried by the bearings, which are essential for smooth and accurate operation.

This chapter details some important analysis used to justify parts of the mechanical design of the end cap nailing mechanism. Reaction forces on the arm shaft bearings resulting from the nail gun's recoil and from the panel's impact with the nail gun were estimated and applied to component selection. Moreover, this analysis led to several additions to the design.

5.1 Static Reaction Force Equations

The recoil force on the nailer is always collinear with the path of the nail. The loads transmitted to the arm shaft bearings, as a result, are purely radial. On the other hand, the impact force between the panel and the nailer has a component along the arm shaft's axis when the panel has an angled end. The relative magnitude of this component depends on the roof pitch.

With the schematic shown in Figure 5-1, the forces and moments at the joint where the arm meets the arm shaft are found as a function of these external forces:

$$F_x = -f_N \cos\theta_T - f_P \cos\varphi \cos\theta_T \pm \mu f_P \sin\theta_T \qquad (5\text{-}1)$$
$$\left\{\begin{matrix} +: & \theta_T \text{ in quadrant II or IV} \\ -: & \theta_T \text{ in quadrant I or III} \end{matrix}\right\}$$

$$F_y = -f_N \sin\theta_T - f_P \cos\varphi \sin\theta_T \pm \mu f_P \cos\theta_T \qquad (5\text{-}2)$$
$$\left\{\begin{matrix} +: & \theta_T \text{ in quadrant I or III} \\ -: & \theta_T \text{ in quadrant II or IV} \end{matrix}\right\}$$

$$F_z = \pm f_P \sin\varphi \qquad (5\text{-}3)$$

$$M_x = -f_N e \sin\theta_T - f_P d \cos\varphi \sin\theta_T + f_P \sin\varphi\left(L_A \sin\theta_A + L_N \sin\theta_T\right) \pm \mu f_P d \cos\theta_T \qquad (5\text{-}4)$$
$$\left\{\begin{matrix} +: & \theta_T \text{ in quadrant I or III} \\ -: & \theta_T \text{ in quadrant II or IV} \end{matrix}\right\}$$

$$M_y = f_N e \cos\theta_T + f_P d \cos\varphi \cos\theta_T - f_P \sin\varphi\left(L_A \cos\theta_A + L_N \cos\theta_T\right) \pm \mu f_P d \sin\theta_T \qquad (5\text{-}5)$$
$$\left\{\begin{matrix} +: & \theta_T \text{ in quadrant I or III} \\ -: & \theta_T \text{ in quadrant II or IV} \end{matrix}\right\}$$

where

$\mu \equiv$ *coefficient of friction between the nailer tip and the OSB*

$d \equiv$ *offset of the contact point from the nailer - tip axis*

$\theta_A \equiv$ *angle of the arm with respect to the x - axis*

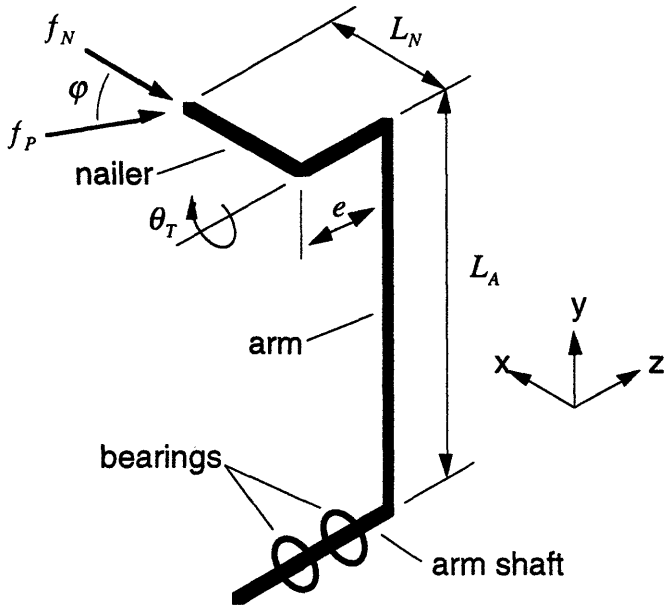

Figure 5-1. Schematic of the nailing mechanism, showing the external loads on the nailer.

Now, Figure 5-2 depicts the arm shaft with these joint forces and moments, as well as the reaction forces on the bearings. We solve for these reactions in the static equilibrium equations:

$$R_{1x} = \frac{F_x(b-a) + M_y}{a} \tag{5-6}$$

$$R_{1y} = \frac{F_y(b-a) + W(a-b) - M_x}{a} \tag{5-7}$$

$$R_{2x} = \frac{-F_x b - M_y}{a} \tag{5-8}$$

$$R_{2y} = \frac{(W - F_y)b + M_x}{a} \tag{5-9}$$

$$R_A = \frac{-F_z}{2} \tag{5-10}$$

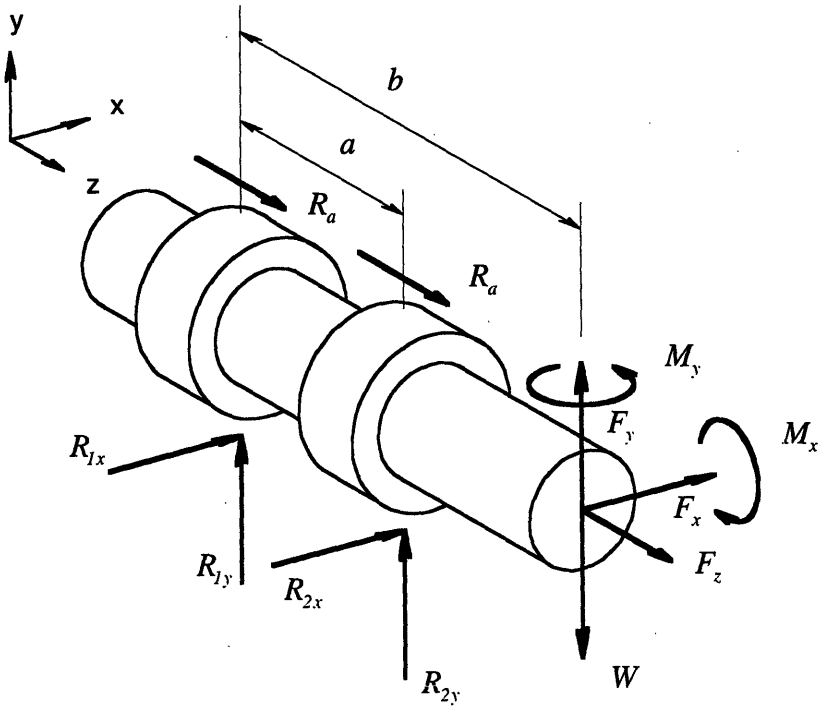

Figure 5-2. Free body diagram of arm shaft and bearings.

5.2 Dynamics

Because the forces on the nailing mechanism are dynamic, they are not easily obtained. However, making good assumptions and using experimental results, we can produce conservative estimates. This section develops simple models of the nailing mechanism to estimate the maximum dynamic loads on the arm shaft bearings. Much of the analytical effort goes into deriving model stiffnesses, but the application of these values is quite simple. The results are used to specify a mount for the nailer that absorbs the shock loads.

5.2.1 Nailer Recoil. Experiments performed by Stanley-Bostitch show that the N50 coil nailer can output a maximum driving force of 7000 pounds [Valley, 1994]. This force corresponds to the peak of a time varying force that occurs as a nail is driven into a material. The actual force function (and maximum force) depends on the hardness of the material and the stiffness of its structure. For softer, more compliant workpieces, the maximum driving force is actually lower than 7000 pounds.

If the nailer recoil were static, the 7000 pounds of force would be transmitted to the bearings and amplified according to Equations 5-1 through 5-10. However, because the force function lasts only for a short period, the resulting reactions are significantly lower. (Valley [1994] reports that the shock lasts for about 800 microseconds.)

5.2.2 Panel Impact. The panel moves along the conveyor at a constant speed as the nailer waits in position. Contact between them triggers the nail gun. Although the speed of the panel is low (3 to 4 inches per second), it is enough to consider the contact as an impact. In addition, when the panel has an angled end, this impact knocks the nailer to the side as well as backward.

Predicting exactly what will happen when an angled-panel contacts the tip of the nailer is difficult. How elastic will the collision be? How much time will elapse after the tip reaches full compression before the nailer actually fires and begins to retreat?

Assuming the collision is perfectly elastic, the panel and nailer are free bodies, and contact between them is frictionless, we find the

velocities of the two bodies after the collision from the following equations for kinetic energy and momentum.

kinetic energy:

$$\frac{1}{2}m_P v_P^2 = \frac{1}{2}m_P v_P'^2 + \frac{1}{2}m_N v_N'^2 \tag{5-11}$$

where

$m_P \equiv$ *mass of the panel*
$m_N \equiv$ *effective mass of the nailer*
$v_P \equiv$ *initial velocity of the panel*
$v_P' \equiv$ *panel velocity after impact*
$v_N' \equiv$ *nailer velocity after impact*

momentum:

$$x: \quad m_P v_P = m_P v_P' \cos\theta_1 + m_N v_N' \cos\theta_2 \tag{5-12}$$

$$y: \quad 0 = m_P v_P' \sin\theta_1 + m_N v_N' \sin\theta_2 \tag{5-13}$$

Because the contact is frictionless, $\theta_2 = \varphi$ (Figure 5-1). Solving for the velocity of the nailer after impact, we get

$$v_N' = \frac{2m_N v_P \cos\varphi}{\frac{m_N^2}{m_P} + m_N} \tag{5-14}$$

As with the nailer recoil, the contact force function alone does not reveal the reactions at the bearings. In fact, in this case, the force function during impact does not need to be considered. The relevant information from this analysis is the kinetic energy of the nailing mechanism just after the impact.

5.2.3 System Model. The overall mass and stiffness of the mechanism determine how much force the bearings actually experience as the result of shock forces on the nail gun. However, if the bearing support structure is assumed to be perfectly rigid, only the load path between the tip of the nailer and the bearings needs to be considered. Although the load path is continuous, the system can then be modeled as a lumped mass at the end of a fixed, massless spring, as shown in Figure 5-3.

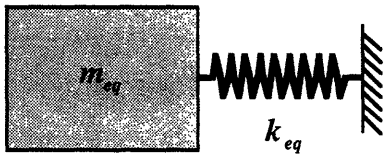

Figure 5-3. Simple mass-spring system.

In this model, the mass is assumed to be equal to the mass of the nailer plus one fourth the mass of the arm (excluding the counterweight, which is not in the load path). The stiffness of the spring is composed of the relevant individual stiffnesses of the elements along the load path, and it depends on the configuration of the mechanism. Because we want to know what the largest forces on the bearings will be, only the stiffest configuration is considered for each type of shock.

5.2.4 Stiffness Resisting Nailer Recoil. If the tip of the nail gun points in a direction perpendicular to the arm's long axis, the recoil from the gun's discharge will cause the arm to rotate. The

dominant stiffness resisting this motion is the effective servo stiffness of the actuator. On the other hand, if the nail gun is directed along the arm's long axis (straight outward or straight inward), the actuator will experience no load at all. The shock will be absorbed solely by the structure, which is much stiffer than the actuator. The relevant analysis for determining maximum bearing loads corresponds to the second extreme.

We begin by obtaining a partial stiffness matrix for the structure depicted in Figure 5-4 that will give us the equivalent stiffness opposing the recoil. (A simple, step-by-step example of how to derive the stiffness matrix of a one dimensional system appears in Appendix E.) In this derivation, the corners of the structure are assumed to be perfectly rigid [Thomson, 1988]. In other words, the vertex between two beam elements always maintains a 90° angle. We also assume the axial displacements of the beams are small compared to the lateral (bending) displacements.

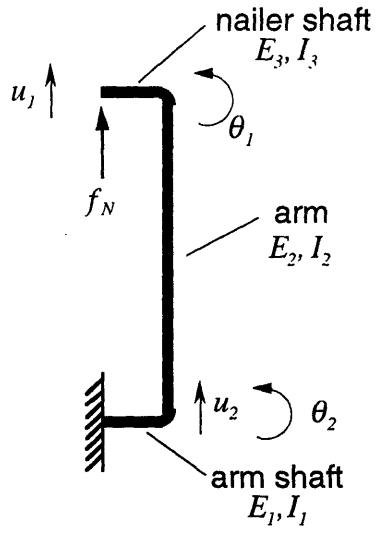

Figure 5-4. Beam model of the nailing mechanism in its worst-case configuration for firing a nail.

Making use of the standard solutions for beam element displacements (see Thomson [1988]), we obtain the following stiffness matrix:

$$\underline{\underline{K}}_N = \begin{bmatrix} \frac{3E_3I_3}{l_3^3} & \frac{-3E_3I_3}{l_3^3} & \frac{3E_3I_3}{l_3^2} & 0 \\ \frac{-3E_3I_3}{l_3^3} & \frac{3E_3I_3}{l_3^3} + \frac{12E_1I_1}{l_1^3} & \frac{-3E_3I_3}{l_3^2} & \frac{-6E_1I_1}{l_1^2} \\ \frac{3E_3I_3}{l_3^2} & \frac{-3E_3I_3}{l_3^2} & \frac{3E_3I_3}{l_3} + \frac{4E_2I_2}{l_2} & \frac{2E_2I_2}{l_2} \\ 0 & \frac{-6E_1I_1}{l_1^2} & \frac{2E_2I_2}{l_2} & \frac{4E_2I_2}{l_2} + \frac{4E_1I_1}{l_1} \end{bmatrix} \tag{5-15}$$

(The derivation of this matrix appears in Appendix F.) We know that under static loading,

$$\underline{f} = \underline{\underline{K}}\,\underline{x} \tag{5-16}$$

where

$f \equiv$ *force in the spring (structure)*
$x \equiv$ *deflection of the spring (structure)*

Multiplying through by the inverse of $\underline{\underline{K}}$, we get

$$\underline{x} = \underline{\underline{K}}^{-1}\,\underline{f} \tag{5-17}$$

where $\underline{\underline{K}}^{-1}$ is also known as the compliance matrix. Expanding this equation gives

$$\begin{bmatrix} u_1 \\ u_2 \\ \theta_1 \\ \theta_2 \end{bmatrix} = \begin{bmatrix} C_{11} & C_{12} & C_{13} & C_{14} \\ C_{21} & C_{22} & C_{23} & C_{24} \\ C_{31} & C_{32} & C_{33} & C_{34} \\ C_{41} & C_{42} & C_{43} & C_{44} \end{bmatrix} \begin{bmatrix} f_N \\ 0 \\ 0 \\ 0 \end{bmatrix} \tag{5-18}$$

The symbol f_N corresponds to the reaction force on the nail gun due to the recoil, and this force is the only external force on the structure—as the zeros in the remaining elements of the vector indicate. Therefore,

$$u_1 = C_{11} f_N \tag{5-19}$$

Rearranging, we get

$$f_N = \frac{1}{C_{11}} u_1 \tag{5-20}$$

which gives us the equivalent stiffness we are looking for:

$$k_{eqN} = \frac{1}{C_{11}} \tag{5-21}$$

Inserting the data summarized in Table 5-1 into Equations 5-15, 5-18, and 5-21, we find that

$$k_{eqN} = 10965 \frac{lb.}{in.} \tag{5-22}$$

Table 5-1
Parameters of the Nailing Mechanism's
Structural Models

Beam	E (10^6 psi)	I (in.^{4})	l (in.)
1	30	0.049	2.5
2	10	0.56	21.5
3	30	0.0031	2.8

5.2.5 Stiffness Resisting Side Impact from Panel. Using the same mass-spring model of Figure 5-3, we derive the equivalent stiffness of the structure that resists the side impact from the moving panel (Figure 5-5).

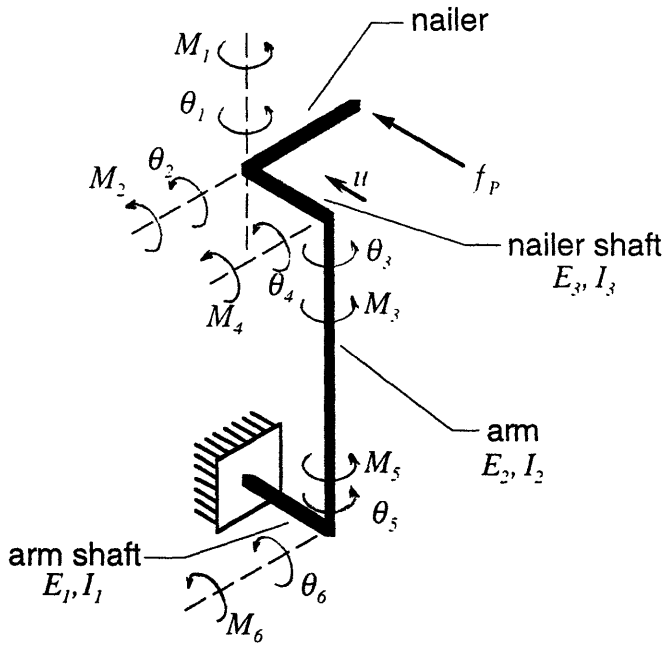

Figure 5-5. Beam model of the nailing mechanism in its worst-case configuration for a collision with the panel. The beam that represents the nailer in this model is assumed to have infinite stiffness because the nailer's stiffness is much greater than the stiffnesses of the other elements.

In this case, the relevant partial stiffness matrix is

$$\underline{\underline{K}}_P = \begin{bmatrix} \frac{12E_2I_2}{l_2^3} & 0 & 0 & 0 & \frac{-6E_2I_2}{l_2^2} & 0 & \frac{-6E_2I_2}{l_2^2} \\ 0 & \frac{4E_3I_3}{l_3} & 0 & \frac{2E_3I_3}{l_3} & 0 & 0 & 0 \\ 0 & 0 & \frac{4E_3I_3}{l_3} & 0 & \frac{2E_3I_3}{l_3} & 0 & 0 \\ 0 & \frac{2E_3I_3}{l_3} & 0 & \frac{GI_p}{l_2}+\frac{4E_3I_3}{l_3} & 0 & \frac{-GI_p}{l_2} & 0 \\ \frac{-6E_2I_2}{l_2^2} & 0 & \frac{2E_3I_3}{l_3} & 0 & \frac{4E_2I_2}{l_2}+\frac{4E_3I_3}{l_3} & 0 & \frac{2E_2I_2}{l_2} \\ 0 & 0 & 0 & \frac{-GI_p}{l_2} & 0 & \frac{GI_p}{l_2}+\frac{4E_1I_1}{l_1} & 0 \\ \frac{-6E_2I_2}{l_2^2} & 0 & 0 & 0 & \frac{2E_2I_2}{l_2} & 0 & \frac{4E_1I_1}{l_1}+\frac{4E_2I_2}{l_2} \end{bmatrix} \tag{5-23}$$

This time,

$$\underline{x} = \underline{\underline{K}}_P^{-1}\,\underline{f} \tag{5-24}$$

yields

$$\begin{bmatrix} u \\ \theta_1 \\ \theta_2 \\ \theta_3 \\ \theta_4 \\ \theta_5 \\ \theta_6 \end{bmatrix} = \left[\underline{\underline{C}}\right] \begin{bmatrix} f_P \\ M_1 \\ 0 \\ 0 \\ 0 \\ 0 \\ 0 \end{bmatrix} \tag{5-25}$$

Thus,

$$u = C_{11} f_P + C_{12} M_1 \tag{5-26}$$

$$\theta_1 = C_{21} f_P + C_{22} M_1 \tag{5-27}$$

But $C_{12} = C_{21} = 0$, so

$$u = C_{11} f_P \tag{5-28}$$

$$\theta_1 = C_{22} M_1 \tag{5-29}$$

The total deflection at the tip of the nailer is

$$\Delta = u + L_N \theta_1 \tag{5-30}$$

Substitution of (5-28) and (5-29) into (5-30), with $M_1 = L_N f_P$, yields

$$\Delta = \left(C_{11} + L_N^2 C_{22}\right) f_P \tag{5-31}$$

Therefore,

$$\underline{\underline{k}}_{eqP} = \frac{1}{C_{11} + L_N^2 C_{22}} \tag{5-32}$$

Finally, with the data in Table 5-1,

$$\underline{\underline{k}}_{eqP} = 1165 \frac{lb.}{in.} \tag{5-33}$$

5.2.6 System Response. The shock loads impart kinetic energy to the nailing mechanism and cause it to deform. At the point of maximum deformation, the reactions are at their greatest. Therefore, we set the initial kinetic energy of the mechanism equal to the potential energy stored in its structure at maximum deformation.

$$\frac{1}{2}m_{eq}v^2 = \frac{1}{2}k_{eq}x^2 \tag{5-34}$$

Refer again to the schematic of Figure 5-3. The stiffness k_{eq} relates the deflection of the spring to the reaction force at the base:

$$x = \frac{f}{k_{eq}} \tag{5-35}$$

Substitution of (5-35) into (5-34) reveals that

$$f = v\sqrt{m_{eq}k_{eq}} \tag{5-36}$$

We find the two external loads on the mechanism, f_N and f_P (Figure 5-1) by substituting specific quantities into (5-36).

For f_N, the velocity in question is that of the nailer just after its discharge. However, the nailer is not a free body in space; it is connected to the arm, which contributes some inertia. So the equivalent mass is set equal to the mass of the nailer plus one fourth the mass of the arm. If we assume that all of the energy from the discharge is given to the nailer, we find that

$$f_N = 1671\ lb. \tag{5-37}$$

If we use the result of Equation 5-14 to find the velocity for computation of f_P, we obtain a relatively small load, about 25 pounds. However, let us assume instead that the collision is inelastic. Then the equivalent mass will have a dominant contribution from the panel. The velocity, in this case, is essentially the initial velocity of the panel. We find a more conservative estimate of the load from the panel:

$$f_P = 112\ lb. \tag{5-38}$$

Finally, to obtain the reactions at the bearings, we enter f_N and f_P into Equations 5-1 through 5-5, and enter the results into Equations 5-6 through 5-10.

$$R_1 = 63.5\ lb. \tag{5-39}$$

$$R_2 = 1782\ lb. \tag{5-40}$$

These forces do not exceed the static capacity of the arm shaft bearings (2250 lb.). However, R_2 is very large, and the safety factor is only 1.3. The system should be modified to reduce these loads.

5.2.7 Shock Absorbing Mount. Introducing a compliant medium into the mechanism's structure decreases its equivalent stiffness, and thereby diminishes the reaction forces. The best place

to install this device is between the nailer and the arm; the response induced by the shock loads will be minimized as a result.

The bearings selected for the arm shaft have a static capacity of 2250 pounds. Including a safety factor of 2.5, the allowable load on the bearings is 900 lb. By iteratively entering values for f_N and f_P in Equations 5-1 through 5-5 and checking the resulting bearing reactions, we can establish minimum stiffnesses for the mount in the relevant directions.

However, a dilemma arises when one tries to specify the stiffness to resist the side impact. Decreasing the stiffness reduces the loads, but it also reduces the nailer's accuracy where it is needed the most. Without further modification, the nailer cannot achieve the required ±1/16 inch accuracy in the z-direction if the stiffness is lowered to bring the loads down to an acceptable level.

5.2.8 Nailer Tip Modification. This problem was circumvented by adding a toothed ring onto the nailer tip. When the panel makes contact with this tip, the teeth dig into the OSB end cap. As a result, the direction of the contact force is now always along the panel's direction of motion. The nailing mechanism no longer experiences any appreciable side load. Figure 5-6 illustrates the new load conditions.

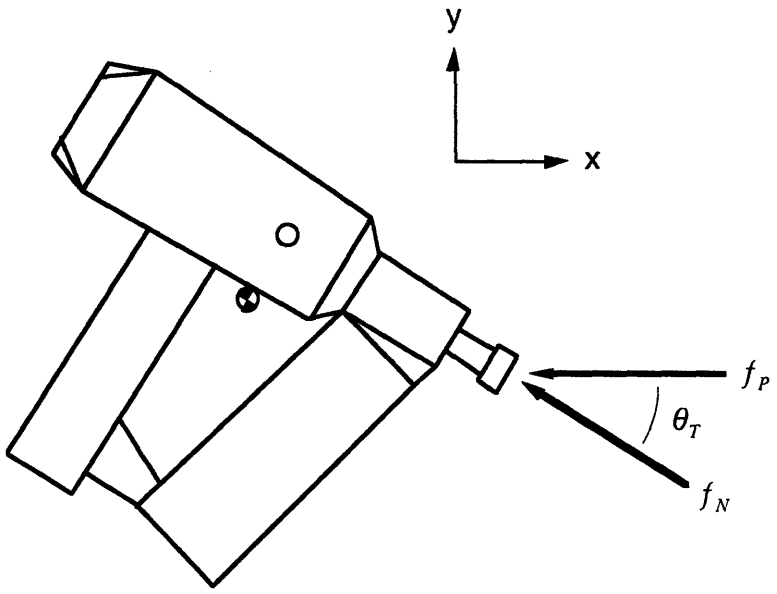

Figure 5-6. External forces on the nail gun with its tip modification.

The static force and moment equations (beginning with Equation 5-1) simplify to the following:

$$F_x = -f_N \cos\theta_T \pm f_P \qquad (5\text{-}41)$$

$$\begin{Bmatrix} +: & \theta_T \text{ in quadrant II or III} \\ -: & \theta_T \text{ in quadrant I or IV} \end{Bmatrix}$$

$$F_y = -f_N \sin\theta_T \qquad (5\text{-}42)$$

$$M_x = -f_N e \sin\theta_T \qquad (5\text{-}43)$$

$$M_y = f_N e \cos\theta_T \pm f_P d \qquad (5\text{-}44)$$

$$\begin{Bmatrix} +: & \theta_T \text{ in quadrant I or IV} \\ -: & \theta_T \text{ in quadrant II or III} \end{Bmatrix}$$

However, the contact trip, which upon deflecting half an inch causes the gun to fire, must also be altered. If it were left unchanged, contact with the panel would cause the nailer to rotate immediately. At best, the nail would be fired in an undetermined direction. Most likely, the nail would not fire at all.

Simply shortening the spring-loaded tip may solve the problem. Otherwise, the tip must be clamped in the compressed position, and an alternative contact sensor must be integrated into the tip ring. Perhaps a load cell could be used so that a contact force above a certain minimum will cause the gun to fire. This solution might provide an acceptable level of safety, as the gun will not fire as a result of simply touching the tip. On the other hand, another mechanical trip may be better; a false signal to the controller could cause a nail to fire into the air.

Chapter 6
Dynamic Simulation

In industry, simulation is seldom used in the design of manufacturing machines [Slocum, 1994]. Typically, designers rely mostly on experience. Problems, which may arise from lack of understanding or may simply be oversights, are eliminated through a process of trial and error, in which prototypes are built and tested.

Often these designs can be refined at much lower cost and the problems avoided if a little extra effort is put into design analysis. Dynamic modeling and simulation provide insight into how a system will respond to any number of situations and could expose unforeseen complications before the system is built. Also, one can easily obtain estimates of informing quantities, such as loads and accelerations, that may be rather difficult to measure experimentally.

Simulation further encourages system optimization. Once the simulation is built, it affords the opportunity to experiment with the characteristics of the system efficiently, without wasting money and material. Finally, developing a good dynamic model is essential for proper control system design. With the simulation, one can evaluate controller gain settings quickly by inspection or with well-defined performance measures.

This chapter presents modeling and computer simulation of the end cap nailing mechanism. After explaining the idea behind our approach to the simulation, the text derives the equations of motion for the system model. In nonlinear and linearized form, these

equations are implemented on a computer workstation with a general purpose software program called MATLAB. At the end, motions of the mechanism predicted by the simulation are evaluated to confirm the model's validity.

6.1 Simulation Strategy

The best model of a system is the simplest one that captures the system behavior at a level that is needed. Often a simpler model provides more insight into the system. In addition, more tools are available for extracting the information. For instance, responses of all linear systems have a closed form solution, whereas only a few special cases of nonlinear systems do. Among the linear systems, analytical expressions for performance criteria, such as overshoot and settling time, are in common usage for prototype first and second order systems—but not so for more complex systems [Kuo, 1991]. In general, as the order of the system increases, so too does the effort needed to compute responses.

Separately, the translation subsystem and the arm and nailer orientation subsystems can all be completely modeled as linear systems (if gravity is ignored). Furthermore, the mechanism's translation can be modeled independently because it has only secondary effects on the other movements. The nailer and arm, however, are coupled dynamically, and that coupling is nonlinear. The resulting set of motion equations consists of linear and nonlinear equations that are coupled.

To take advantage of the wealth of analysis techniques and tools available for linear systems, the nonlinear equations were linearized. The linearized model is valid only for small motions about a specific position, so it generally cannot be used to simulate the nailing mechanism's rotations. Instead, the linear model was used for the design of the control system (Chapter 7). Afterwards, the nonlinear model was combined with the controller model to simulate the operation of the end cap nailing mechanism.

6.2 The Model

The nailing mechanism was modeled with discrete mass, spring, and damping elements. Figure 6-1 depicts the translation subsystem model, Figure 6-2 the arm and nailer rotation model.

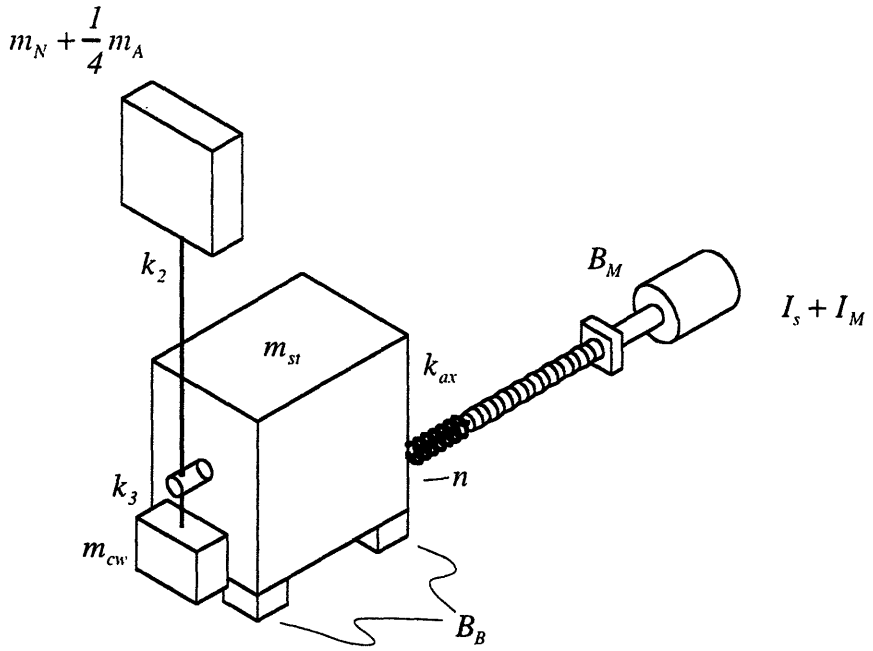

Figure 6-1. Model of the nailing mechanism's translation subsystem.

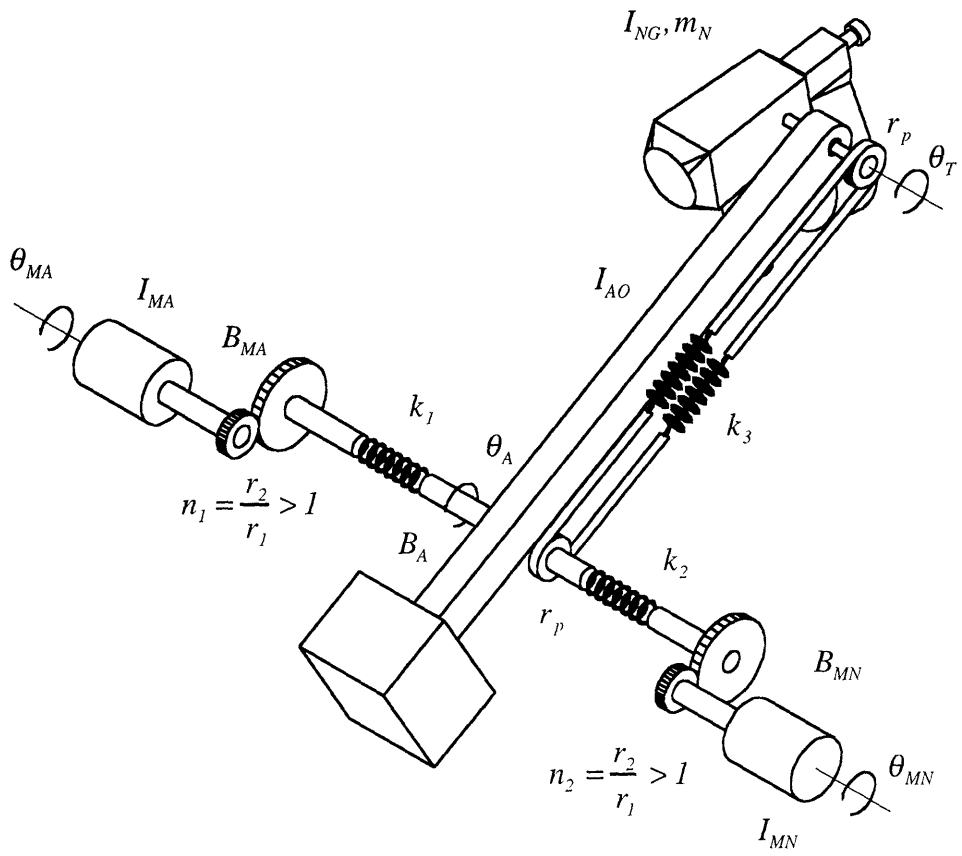

Figure 6-2. Model of the arm and nailer rotation subsystems.

6.3 Equations of Motion

In this section, equations describing the motion of each subsystem are derived with the help of bond graphs (for the linear equations) and Newton's Second Law (for the nonlinear equations). (Bond graphing is a compact, systematic technique for deriving equations of motion for linear systems. For detailed instruction on the use of the technique, refer to System Dynamics: A Unified

Approach [Karnopp and others, 1990].) These equations were arranged in state-space form, which is represented compactly by the following matrix equation:

$$\dot{\underline{x}} = \underline{\underline{A}}\underline{x} + \underline{\underline{B}}\underline{u} \tag{6-1}$$

where

$\underline{x} \equiv$ *the state vector*

$\underline{u} \equiv$ *the input vector*

$\underline{\underline{A}}, \underline{\underline{B}} \equiv$ *matrices embodying the physical parameters of the system*

6.3.1 Translation (z-axis) State Equations. Converting the model of Figure 6-1 into bond graph form produces the representation shown in Figure 6-3.

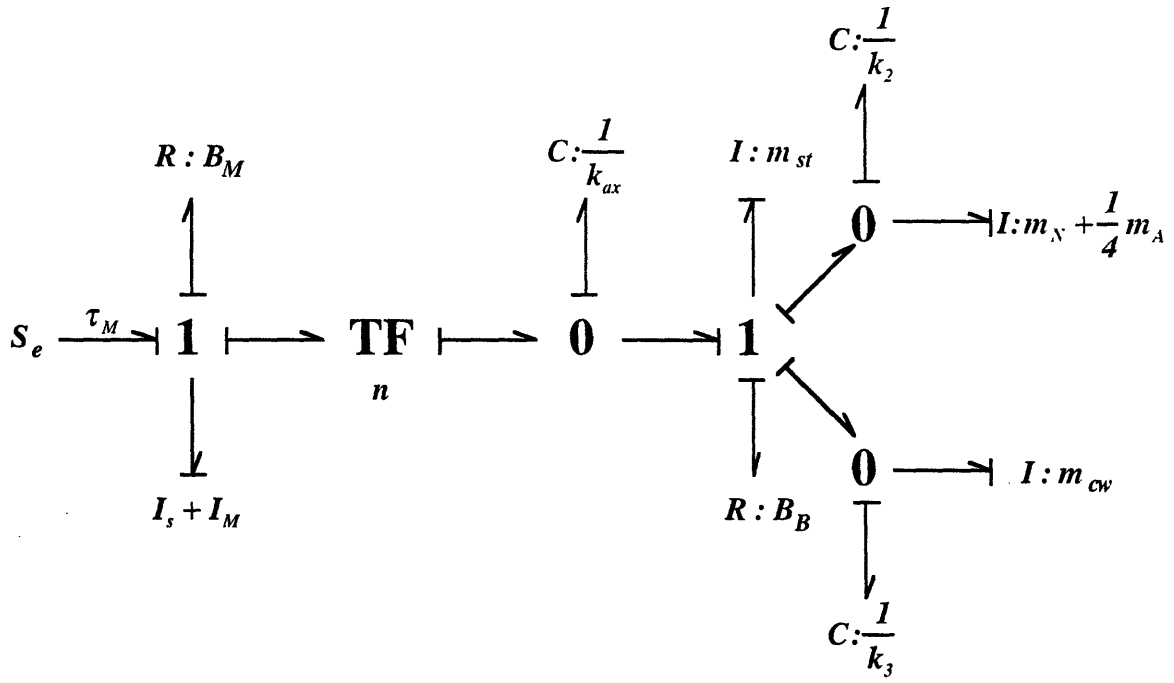

Figure 6-3. Bond graph of the translation subsystem.

Using the power variables (the velocities of the inertial elements and the forces or torques in the spring elements) as the state variables, we obtain a set of seven linear, ordinary differential equations, summarized as follows in state-space form.

$$\frac{d}{dt}\begin{bmatrix} \omega_M \\ f_{k_{ax}} \\ v_{st} \\ f_{k_2} \\ v_N \\ f_{k_3} \\ v_{cw} \end{bmatrix} = \begin{bmatrix} \frac{-B_M}{I_{eq1}} & \frac{-n}{I_{eq1}} & 0 & 0 & 0 & 0 & 0 \\ nk_{ax} & 0 & -k_{ax} & 0 & 0 & 0 & 0 \\ 0 & \frac{1}{m_{st}} & \frac{-B_B}{m_{st}} & \frac{-1}{m_{st}} & 0 & \frac{-1}{m_{st}} & 0 \\ 0 & 0 & k_2 & 0 & -k_2 & 0 & 0 \\ 0 & 0 & 0 & \frac{1}{1.25m_N} & 0 & 0 & 0 \\ 0 & 0 & k_3 & 0 & 0 & 0 & -k_3 \\ 0 & 0 & 0 & 0 & 0 & \frac{1}{m_{cw}} & 0 \end{bmatrix} \begin{bmatrix} \omega_M \\ f_{k_{ax}} \\ v_{st} \\ f_{k_2} \\ v_N \\ f_{k_3} \\ v_{cw} \end{bmatrix} + \begin{bmatrix} \frac{1}{I_{eq1}} \\ 0 \\ 0 \\ 0 \\ 0 \\ 0 \\ 0 \end{bmatrix} [\tau_M] \tag{6-2}$$

where

$$I_{eq1} = I_s + I_M \tag{6-3}$$

6.3.2 Arm and Nailer Rotation (Separately). Let us first ignore the coupling between the arm and the nailer rotations and derive the motion equations of each independently. If the nailer is fixed to the arm such that the nailer cannot rotate with respect to the arm and if the belt is detached, the arm subsystem model in Figure 6-2 is represented in bond graph form as shown in Figure 6-4.

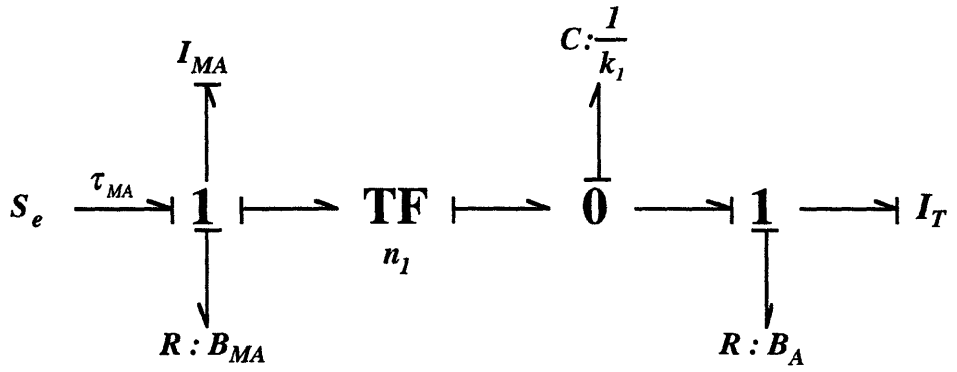

Figure 6-4. Bond graph of the arm subsystem. In the figure, $I_T = I_{AO} + (I_{NG} + m_N L_A^2)$.

Containing two inertial elements and one capacitive element, this subsystem is third order. Using the power variables again, we obtain state equations describing its motion.

$$\frac{d}{dt}\begin{bmatrix} \omega_{MA} \\ \omega_A \\ \tau_{k_1} \end{bmatrix} = \begin{bmatrix} \frac{-B_{MA}}{I_{MA}} & 0 & \frac{-1}{n_1 I_{MA}} \\ 0 & \frac{-B_A}{I_T} & \frac{1}{I_T} \\ \frac{k_1}{n_1} & -k_1 & 0 \end{bmatrix} \begin{bmatrix} \omega_{MA} \\ \omega_A \\ \tau_{k_1} \end{bmatrix} + \begin{bmatrix} \frac{1}{I_{MA}} \\ 0 \\ 0 \end{bmatrix} \begin{bmatrix} \tau_{MA} \end{bmatrix} \qquad (6\text{-}4)$$

The first row describes the motion of the arm-motor armature; the second describes the arm's motion. These motions are linked by the windup in the arm shaft, which is described by the third row.

The model for the nailer subsystem with the arm fixed is described with a similar bond graph (Figure 6-5) and set of state equations.

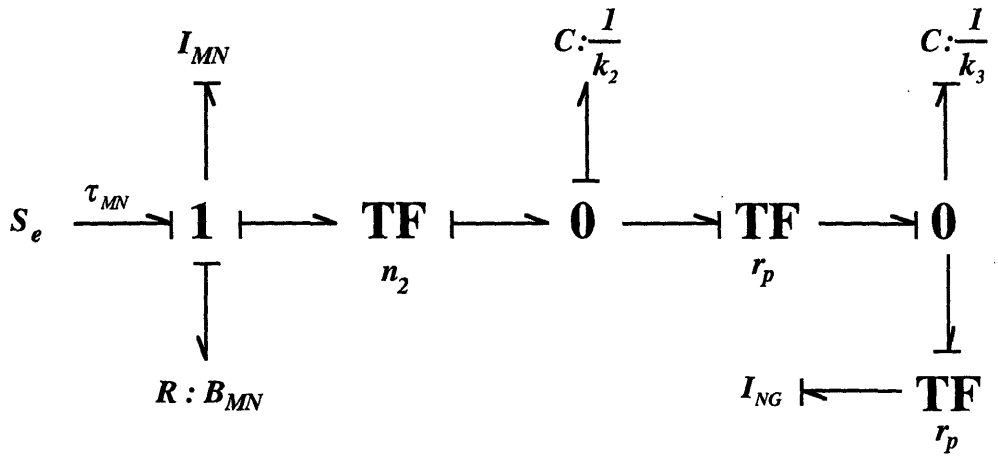

Figure 6-5. Bond graph of the nailer subsystem.

$$\frac{d}{dt}\begin{bmatrix}\omega_{MN}\\ \omega_N\\ \tau_{k_{eq}}\end{bmatrix}=\begin{bmatrix}\frac{-B_{MN}}{I_{MN}} & 0 & \frac{-1}{n_2 I_{MN}}\\ 0 & \frac{-b}{I_N} & \frac{1}{I_{NG}}\\ \frac{k_{eq}}{n_2} & -k_{eq} & 0\end{bmatrix}\begin{bmatrix}\omega_{MN}\\ \omega_N\\ \tau_{k_{eq}}\end{bmatrix}+\begin{bmatrix}\frac{1}{I_{MN}}\\ 0\\ 0\end{bmatrix}\left[\tau_{MN}\right] \tag{6-5}$$

where

$$k_{eq}=\frac{r_p^2 k_2 k_3}{r_p^2 k_3 + k_2} \tag{6-6}$$

6.3.3 Arm and Nailer Dynamic Coupling. If the nail gun's center of mass were located exactly along the rotation axis of the gun, the arm's movement would not cause the nailer to rotate at all. Because the mass center is offset from the axis, however, force interactions between the arm and nailer, occurring at the nailer's pivot point, create moments about the nailer's mass center. As a

result, the nailer experiences angular acceleration as well as translational acceleration.

The equations derived in this sub-section were to be used only in the design of the control system for the arm and nailer rotations. So, for convenience, straight-line recoil mobility of the nailer is ignored. That is, we pretend that the nailer is mounted rigidly to the arm rather than being affixed to the shock absorbing mount. Refer to the free body diagram of the nailer, shown in Figure 6-6.

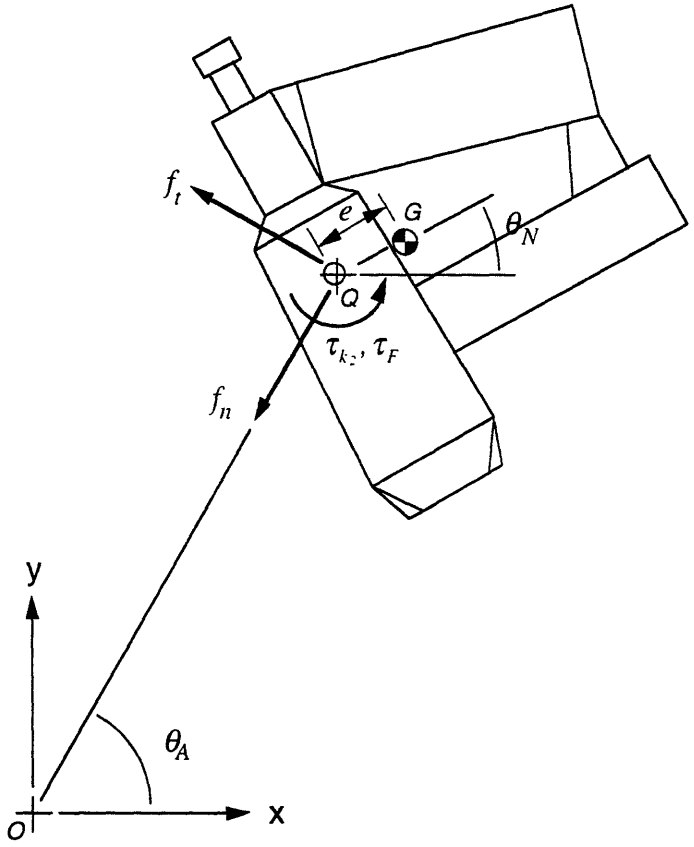

Figure 6-6. Free body diagram of the nailer (ignoring the shock absorbing mount).

Newton's Second Law supplies the equations of motion:

$$\sum F_n: \quad f_n = m_N a_{G_n} \tag{6-7}$$

$$\sum F_t: \quad f_t = m_N a_{G_t} \tag{6-8}$$

$$\sum M_G: \quad \tau_{k_2} + \tau_F - f_t e\cos(\theta_N - \theta_A) - f_n e\sin(\theta_N - \theta_A) = I_{NG}\ddot{\theta}_N \tag{6-9}$$

where

$$\tau_F = b(\dot{\theta}_A - \dot{\theta}_N) \tag{6-10}$$

The absolute acceleration of the nailer's mass center, a_G, is the vector sum of the absolute acceleration of Point Q and the mass center's acceleration relative to Point Q:

$$\bar{a}_G = \bar{a}_Q + \bar{a}_{G/Q} \tag{6-11}$$

And these vectors are composed of centripetal and tangential accelerations, which are expressed in general terms as follows:

$$a_{centripetal} = \dot{\vec{\theta}} \times \dot{\vec{\theta}} \times \vec{r} \tag{6-12}$$

$$a_{tangential} = \ddot{\vec{\theta}} \times \vec{r} \tag{6-13}$$

where $\vec{r}$ is the distance between the point in question and another point about which the body is rotating. Expanding Equation 6-11 and resolving it into its normal and tangential components yields

$$a_{G_n} = L_A\dot{\theta}_A^2 + e\ddot{\theta}_N \sin(\theta_N - \theta_A) + e\dot{\theta}_N^2 \cos(\theta_N - \theta_A) \tag{6-14}$$

$$a_{G_t} = L_A\ddot{\theta}_A + e\ddot{\theta}_N \cos(\theta_N - \theta_A) - e\dot{\theta}_N^2 \sin(\theta_N - \theta_A) \tag{6-15}$$

Substituting these expressions into Equations 6-7 and 6-8 and then substituting the results for f_n and f_t in Equation 6-9 finally renders the following equation:

$$(I_{NG} + m_N e^2)\ddot{\theta}_N + m_N e L_A \cos(\theta_N - \theta_A)\ddot{\theta}_A = m_N e L_A \dot{\theta}_A^2 \sin(\theta_N - \theta_A) + \tau_{k_2} + b(\dot{\theta}_A - \dot{\theta}_N) \quad (6\text{-}16)$$

Now refer to the free body diagram of the arm, shown in Figure 6-7.

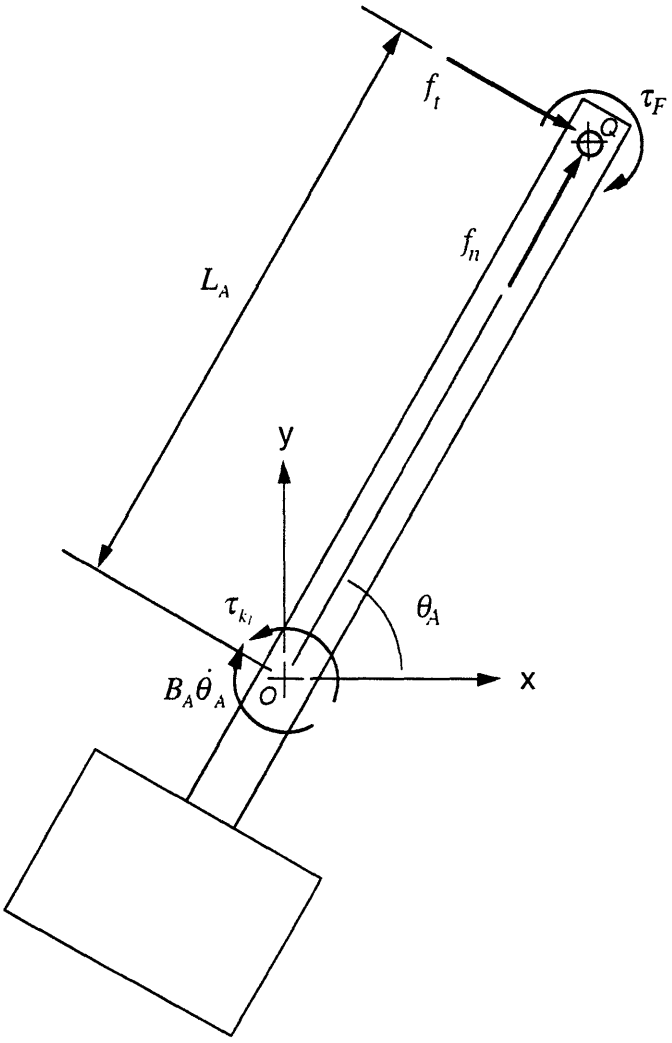

Figure 6-7. Free body diagram of the arm (ignoring the shock absorbing mount).

Summing the moments about Point O gives

$$\sum M_O: \quad \tau_{k_1} - \tau_F - f_t L_A - B_A \dot{\theta}_A = I_{AO} \ddot{\theta}_A \tag{6-17}$$

and substituting the expressions we have for τ_F and f_t yields

$$(I_{AO} + m_N L_A^2)\ddot{\theta}_A + m_N e L_A \cos(\theta_N - \theta_A)\ddot{\theta}_N = m_N e L_A \dot{\theta}_N^2 \sin(\theta_N - \theta_A) + \tau_{k_1} - b(\dot{\theta}_A - \dot{\theta}_N) - B_A \dot{\theta}_A \tag{6-18}$$

Equation 6-16 contains the essence of the nailer's modeled rotation; Equation 6-18 does the same for the arm. By observing the presence of θ_A and θ_N in both equations, one can see that they capture the dynamic interaction between the two bodies.

6.3.4 Linearization. Nonlinear equations can be linearized by expanding them into a Taylor series about a nominal operating point and neglecting second order terms and higher. The following generalized example illustrates this procedure.

Consider a nonlinear system of two equations with two state variables (x) and two inputs (u):

$$\begin{aligned} f_1 &= f(x_1, x_2, u_1, u_2) = 0 \\ f_2 &= f(x_1, x_2, u_1, u_2) = 0 \end{aligned} \tag{6-19}$$

Linearized, the system of equations becomes

$$\begin{aligned} &\frac{\partial f_1}{\partial x_1}(x_1 - x_{1_0}) + \frac{\partial f_1}{\partial x_2}(x_2 - x_{2_0}) + \frac{\partial f_1}{\partial u_1}(u_1 - u_{1_0}) + \frac{\partial f_1}{\partial u_2}(u_2 - u_{2_0}) = 0 \\ &\frac{\partial f_2}{\partial x_1}(x_1 - x_{1_0}) + \frac{\partial f_2}{\partial x_2}(x_2 - x_{2_0}) + \frac{\partial f_2}{\partial u_1}(u_1 - u_{1_0}) + \frac{\partial f_2}{\partial u}(u_2 - u_{2_0}) = 0 \end{aligned} \tag{6-20}$$

where the states and inputs at the operating point are denoted as x_{i_0} and u_{i_0}.

Equations 6-16 and 6-18 are coupled, second order, nonlinear equations. Linearizing them and rewriting the results in matrix form, we obtain

$$\begin{bmatrix} G_{11} & G_{12} \\ G_{21} & G_{22} \end{bmatrix} \begin{bmatrix} \Delta\ddot{\theta}_A \\ \Delta\ddot{\theta}_N \end{bmatrix} = \begin{bmatrix} H_{11} & H_{12} & H_{13} & H_{14} & H_{15} & 0 \\ H_{21} & H_{22} & H_{23} & H_{24} & 0 & H_{26} \end{bmatrix} \begin{bmatrix} \Delta\theta_A \\ \Delta\dot{\theta}_A \\ \Delta\theta_N \\ \Delta\dot{\theta}_N \\ \Delta\tau_{k_1} \\ \Delta\tau_{k_2} \end{bmatrix} \tag{6-21}$$

where Δ denotes the deviation of a variable from its initial value (at the operating point). For example, $\Delta\theta_A = \theta_A - \theta_{A_0}$. The elements of the matrices are defined as follows:

$$G_{11} = I_{AO} + m_N L_A^2 \tag{6-22}$$

$$G_{12} = G_{21} = m_N e L_A \cos\beta \tag{6-23}$$

$$G_{22} = I_{NG} + m_N e^2 \tag{6-24}$$

$$H_{11} = -m_N e L_A (\dot{\theta}_{N_0}^2 \cos\beta + \ddot{\theta}_{N_0} \sin\beta) \tag{6-25}$$

$$H_{12} = -(b + B_A) \tag{6-26}$$

$$H_{13} = m_N e L_A (\dot{\theta}_{N_0}^2 \cos\beta + \ddot{\theta}_{N_0} \sin\beta) \tag{6-27}$$

$$H_{14} = b + 2 m_N e L_A \dot{\theta}_{N_0} \sin\beta \tag{6-28}$$

$$H_{15} = 1 \tag{6-29}$$

$$H_{21} = m_N e L_A (\dot{\theta}_{A_0}^2 \cos\beta - \ddot{\theta}_{A_0} \sin\beta) \tag{6-30}$$

$$H_{22} = b - 2m_N eL_A \dot{\theta}_{A_0} \sin\beta \tag{6-31}$$

$$H_{23} = m_N eL_A(-\dot{\theta}_{A_0}^2 \cos\beta + \ddot{\theta}_{A_0} \sin\beta) \tag{6-32}$$

$$H_{24} = -b \tag{6-33}$$

$$H_{26} = 1 \tag{6-34}$$

where

$$\beta = \theta_{N_0} - \theta_{A_0} \tag{6-35}$$

6.3.5 Rotation State Equations (Linear). The complete linear model of the arm and nailer subsystems (rotational) comes from Equations 6-4, 6-5, and 6-21. Equations 6-4 and 6-5 were derived with the assumption that dynamic interaction between the arm and the nailer does not occur. Yet, we just showed that they do interact. As it turns out, we simply need to replace one row in Equation 6-4 and one in Equation 6-5 to account for this coupling.

First, we solve for the accelerations in Equation 6-21:

$$\begin{bmatrix} \Delta\ddot{\theta}_A \\ \Delta\ddot{\theta}_N \end{bmatrix} = \begin{bmatrix} G_{11} & G_{12} \\ G_{21} & G_{22} \end{bmatrix}^{-1} \begin{bmatrix} H_{11} & H_{12} & H_{13} & H_{14} & H_{15} & 0 \\ H_{21} & H_{22} & H_{23} & H_{24} & 0 & H_{26} \end{bmatrix} \begin{bmatrix} \Delta\theta_A \\ \Delta\dot{\theta}_A \\ \Delta\theta_N \\ \Delta\dot{\theta}_N \\ \Delta\tau_{k_1} \\ \Delta\tau_{k_2} \end{bmatrix} \tag{6-36}$$

This set contains two second order equations. To convert it to state-space form, we rename two of the variables:

$$\Delta\dot{\theta}_A = \Delta\omega_A \tag{6-37}$$

$$\Delta\dot{\theta}_N = \Delta\omega_N \tag{6-38}$$

And, with the inverted matrix of Equation 6-36 written out explicitly, the expression becomes

$$\begin{bmatrix} \Delta\dot{\omega}_A \\ \Delta\dot{\omega}_N \end{bmatrix} = \frac{1}{G_{11}G_{22} - G_{12}^2} \begin{bmatrix} G_{22} & -G_{12} \\ -G_{12} & G_{11} \end{bmatrix} \begin{bmatrix} H_{11} & H_{12} & H_{13} & H_{14} & H_{15} & 0 \\ H_{21} & H_{22} & H_{23} & H_{24} & 0 & H_{26} \end{bmatrix} \begin{bmatrix} \Delta\theta_A \\ \Delta\omega_A \\ \Delta\theta_N \\ \Delta\omega_N \\ \Delta\tau_{k_1} \\ \Delta\tau_{k_2} \end{bmatrix} \tag{6-39}$$

The two second order equations have been recast as a set of four first order equations: one from (6-37), one from (6-38), and two from (6-39).

These linearized equations combine with the first and third rows of Equations 6-4 and 6-5 to complete the linear equations of motion of the arm and nailer subsystems. However, the variables of Equations 6-4 and 6-5 must be expressed as deviations to be consistent with the linearized equations. For clarity, the state equations are rewritten together.

$$\Delta\dot{\theta}_A = \Delta\omega_A \tag{6-40}$$

$$\begin{aligned} \Delta\dot{\omega}_A = \frac{1}{G_{11}G_{22} - G_{12}^2} [&(G_{22}H_{11} - G_{12}H_{21})\Delta\theta_A + (G_{22}H_{12} - G_{12}H_{22})\Delta\omega_A \\ &+ (G_{22}H_{13} - G_{12}H_{23})\Delta\theta_N + (G_{22}H_{14} - G_{12}H_{24})\Delta\omega_N + G_{22}H_{15}\Delta\tau_{k_1} - G_{12}H_{26}] \end{aligned} \tag{6-41}$$

$$\Delta\dot{\theta}_N = \Delta\omega_N \tag{6-42}$$

$$\Delta\dot{\omega}_N = \frac{1}{G_{11}G_{22} - G_{12}^2}[(-G_{12}H_{11} + G_{11}H_{21})\Delta\theta_A + (-G_{12}H_{12} + G_{11}H_{22})\Delta\omega_A + (-G_{12}H_{13} + G_{11}H_{23})\Delta\theta_N + (-G_{12}H_{14} + G_{11}H_{24})\Delta\omega_N - G_{12}H_{15} + G_{11}H_{26}] \quad (6\text{-}43)$$

$$\Delta\dot{\tau}_{k_1} = -k_1\Delta\omega_A + \frac{k_1}{n_1}\Delta\omega_{MA} \quad (6\text{-}44)$$

$$\Delta\dot{\tau}_{k_2} = -k_{eq}\Delta\omega_N + \frac{k_{eq}}{n_2}\Delta\omega_{MN} \quad (6\text{-}45)$$

$$\Delta\dot{\omega}_{MA} = \frac{-1}{n_1 I_{MA}}\Delta\tau_{k_1} - \frac{B_{MA}}{I_{MA}}\Delta\omega_{MA} + \frac{1}{I_{MA}}\Delta\tau_{MA} \quad (6\text{-}46)$$

$$\Delta\dot{\omega}_{MN} = \frac{-1}{n_2 I_{MN}}\Delta\tau_{k_2} - \frac{B_{MN}}{I_{MN}}\Delta\omega_{MN} + \frac{1}{I_{MN}}\Delta\tau_{MN} \quad (6\text{-}47)$$

The system of equations reveals that the combined arm and nailer subsystem is eighth order. This result contradicts Equations 6-4 and 6-5, which suggest that the sum of the two subsystems should be sixth order. The two extra states come from the nonlinearity of the arm and nailer interaction. When the subsystems are independent, their motion is independent of position, but with the coupling, their motion depends on both θ_A and θ_N.

6.3.6 Rotation Equations (Nonlinear). For the sake of simplicity, the nonlinear equations derived previously excluded the shock absorbing motion of the nailer. That motion, however, must be simulated for evaluation of the mechanism's performance.

Refer again to the free body diagram of the nailer, redrawn in Figure 6-8 to reflect the changes in how the nailer interacts with the arm. The figure also includes the external forces from the panel.

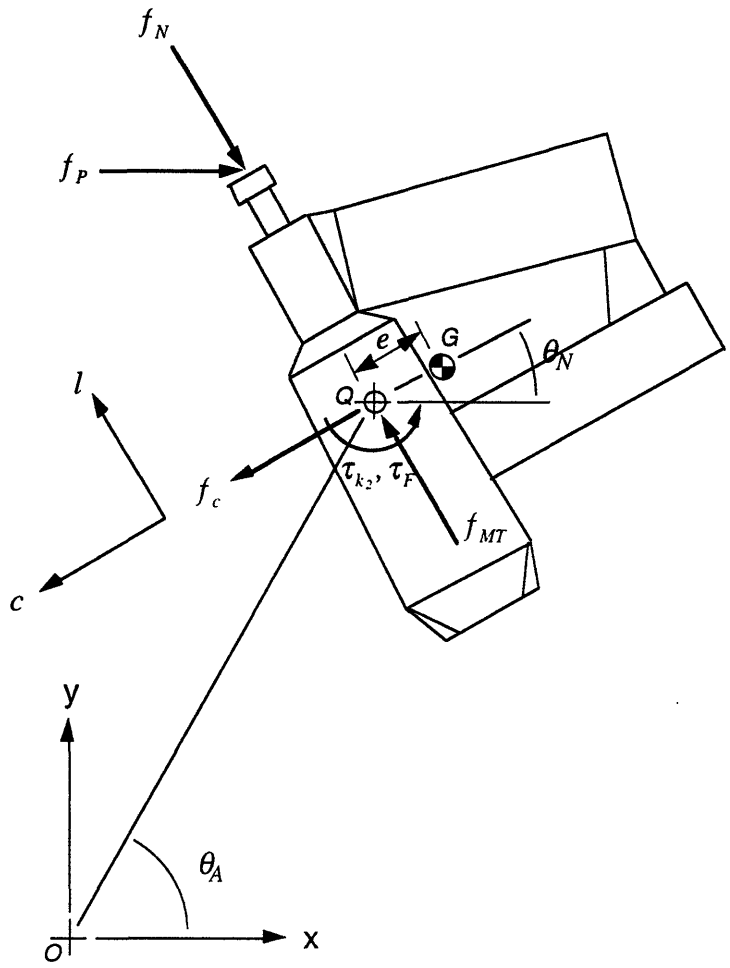

Figure 6-8. Free body diagram of the nailer (including the shock absorbing mount). In the figure, f_{MT} is the force that the shock absorber exerts on the nailer.

Applying Newton's Second Law in the c- and l- directions and about the mass center (Point G), we obtain the following equations:

$$\sum F_c: \quad f_c \pm f_P \cos\theta_N = m_N a_{G_c} \qquad \text{(6-48)}$$

$$\begin{Bmatrix} +: \ \theta_N \text{ in quadrant III or IV} \\ -: \ \theta_N \text{ in quadrant I or II} \end{Bmatrix}$$

$$\sum F_l: \quad f_{MT} - f_N \pm f_P \sin\theta_N = m_N a_{G_l} \qquad \text{(6-49)}$$

$$\left\{\begin{matrix} +: & \theta_N \text{ in quadrant III or IV} \\ -: & \theta_N \text{ in quadrant I or II} \end{matrix}\right\}$$

$$\sum M_G: \quad \tau_{k_2} + \tau_F + f_N e - f_{MT} e \pm f_P L_N \cos\theta_N \mp f_P e \sin\theta_N = I_{NG}\ddot{\theta}_N \tag{6-50}$$

$$\left\{\begin{matrix} +: & \theta_N \text{ in quadrant III or IV} \\ -: & \theta_N \text{ in quadrant I or II} \end{matrix}\right\}$$

where

$$f_{MT} = k_{MT}x + b_{MT}\dot{x} \tag{6-51}$$

and x is the linear deflection of the nailer mount from its free position (in the negative l-direction). (Note: $\mp$ in Equation 6-50 signifies that the sign is opposite the explanation given the brackets.)

Now refer to the free body diagram of the arm, depicted in Figure 6-9.

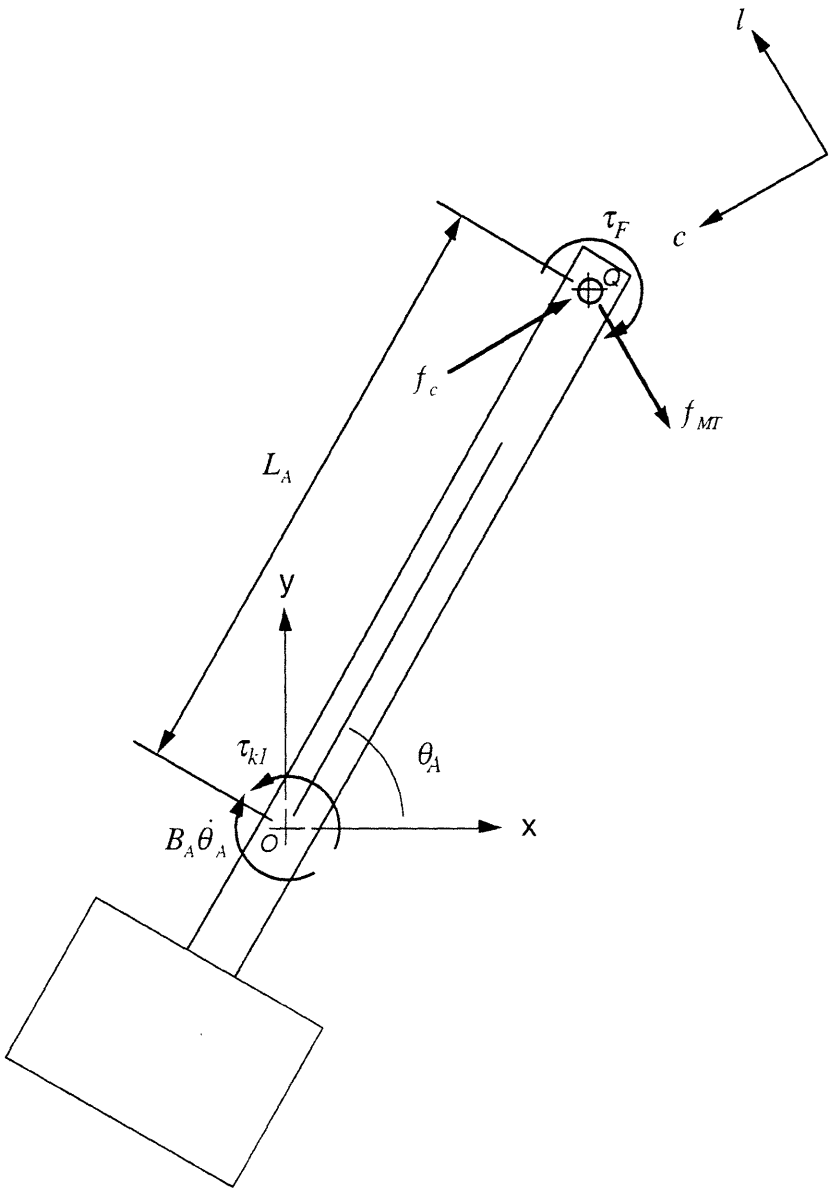

Figure 6-9. Free body diagram of the arm (including the shock absorbing mount).

The relevant dynamic equation is the sum of the moments about the arm's axis of rotation:

$$\sum M_o: \quad \tau_{k_l} - \tau_F - B_A\dot{\theta}_A + f_c L_A \sin(\theta_N - \theta_A) - f_{MT} L_A \cos(\theta_N - \theta_A) = I_{AO}\ddot{\theta}_A \qquad (6\text{-}52)$$

Solving for f_C in Equation 6-48, we can eliminate this unknown in Equation 6-52. In addition, a_{G_c} is the vector sum of the absolute acceleration of Point Q in the c-direction and the nailer mass-center's acceleration with respect to Point Q, also in the c-direction:

$$a_{G_c} = a_{Q_c} + (a_{G/Q})_c \tag{6-53}$$

or

$$a_{G_c} = L_A\dot{\theta}_A^2 cos(\theta_N - \theta_A) - L_A\ddot{\theta}_A sin(\theta_N - \theta_A) + e\dot{\theta}_N^2 \tag{6-54}$$

Making the substitutions and rearranging, we get the following expanded expression:

$$\dot{\omega}_A = \frac{1}{I_{AO} + m_N L_A^2 sin^2(\theta_N - \theta_A)}[-(b + B_A)\omega_A + m_N L_A^2 sin(\theta_N - \theta_A)cos(\theta_N - \theta_A)\omega_A^2$$
$$+b\omega_N + m_N eL_A sin(\theta_N - \theta_A)\omega_N^2 + \tau_{k_1} - k_{MT}L_A cos(\theta_N - \theta_A)x - b_{MT}L_A cos(\theta_N - \theta_A)v$$
$$\pm L_A cos\,\theta_N sin(\theta_N - \theta_A)f_P] \tag{6-55}$$

$$\left\{\begin{matrix} +: & \theta_N \text{ in quadrant I or II} \\ -: & \theta_N \text{ in quadrant III or IV} \end{matrix}\right\}$$

where

$$v = \dot{x} \tag{6-56}$$

Also,

$$\ddot{x} = a_{Q_1} - a_{G_1} \tag{6-57}$$

where

$$a_{Q_I} = L_A\ddot{\theta}_A cos(\theta_N - \theta_A) + L_A\dot{\theta}_A^2 sin(\theta_N - \theta_A) \tag{6-58}$$

Now, substituting for a_{G_I} with expressions from Equations 6-49 and 6-50, we find that

$$\ddot{x} = L_A cos(\theta_N - \theta_A)\ddot{\theta}_A + L_A sin(\theta_N - \theta_A)\dot{\theta}_A^2 - \frac{k_{MT}}{m_N}x - \frac{b_{MT}}{m_N}\dot{x} + \frac{1}{m_N}f_N \pm \frac{1}{m_N}f_P sin\theta_N \tag{6-59}$$

$$\left\{\begin{matrix} +: \ \theta_N \ in \ quadrant \ I \ or \ II \\ -: \ \theta_N \ in \ quadrant \ III \ or \ IV \end{matrix}\right\}$$

Again, the nonlinear equations combine with the first and third rows of Equations 6-4 and 6-5 to form the complete set of motion equations, which is tenth order for this model (the mount adds two states). The set is composed of the ten first order differential equations that follow.

$$\dot{\theta}_A = \omega_A \tag{6-60}$$

$$\dot{\omega}_A = \frac{1}{I_{AO} + m_N L_A^2 sin^2(\theta_N - \theta_A)}[-(b + B_A)\omega_A + m_N L_A^2 sin(\theta_N - \theta_A)cos(\theta_N - \theta_A)\omega_A^2 + b\omega_N + m_N eL_A sin(\theta_N - \theta_A)\omega_N^2 + \tau_{k_1} - k_{MT}L_A cos(\theta_N - \theta_A)x - b_{MT}L_A cos(\theta_N - \theta_A)v \pm L_A cos\theta_N sin(\theta_N - \theta_A)f_P]$$

(6-61)

$$\dot{\theta}_N = \omega_N \tag{6-62}$$

$$\dot{\omega}_N = \frac{1}{I_{NG}}[b\omega_A - b\omega_N + \tau_{k_2} - k_{MT}ex - b_{MT}ev + f_N e + f_P(\pm L_N cos\theta_N \pm e sin\theta_N)] \tag{6-63}$$

$$\dot{\tau}_{k_1} = -k_1\omega_A + \frac{k_1}{n_1}\omega_{MA} \tag{6-64}$$

$$\dot{\tau}_{k_2} = -k_{eq}\omega_N + \frac{k_{eq}}{n_2}\omega_{MN} \tag{6-65}$$

$$\dot{\omega}_{MA} = \frac{-1}{n_1 I_{MA}} \tau_{k_1} - \frac{B_{MA}}{I_{MA}} \omega_{MA} + \frac{1}{I_{MA}} \tau_{MA} \tag{6-66}$$

$$\dot{\omega}_{MN} = \frac{-1}{n_2 I_{MN}} \tau_{k_2} - \frac{B_{MN}}{I_{MN}} \omega_{MN} + \frac{1}{I_{MN}} \tau_{MN} \tag{6-67}$$

$$\dot{x} = v \tag{6-68}$$

$$\dot{v} = L_A \cos(\theta_N - \theta_A)\dot{\omega}_A + L_A \sin(\theta_N - \theta_A)\omega_A^2 - \frac{k_{MT}}{m_N} x - \frac{b_{MT}}{m_N} v + \frac{1}{m_N} f_N \pm \frac{1}{m_N} f_P \sin\theta_N \tag{6-69}$$

(For conciseness, $\dot{\omega}_A$ is left unexpanded in Equation 6-69. Simply substituting for $\dot{\omega}_A$ with the expression in Equation 6-61 puts the equation in terms of state variables only.)

6.4 Implementation

The equations of motion were incorporated in a computer simulation with MATLAB, a commercial software application. Because MATLAB solves systems of equations numerically, the system parameters, such as stiffness and inertia, had to be computed first. Appendix G displays all the system data that was used in the simulation.

For the linear simulation, this information was put into MATLAB in the form of state-space matrices: $\underline{\underline{A}}$ and $\underline{\underline{B}}$. (MATLAB also accepts linear systems in the form of transfer functions.) System responses to standard inputs were then obtained by using built-in MATLAB functions, such as impulse and step.

6.5 Model Verification

In all computer simulation work, models must be tested before they can be used to obtain reliable results. Comparing the simulation output with expected results will usually reveal mistakes and may also uncover computation roundoff errors. More important, it may disclose whether the model itself is valid.

The output of the mechanism simulation was checked in two basic ways: by inspection and by comparison with independent estimates of system oscillation frequencies.

6.5.1 Intuitive Observation. The first question is whether the model moves in a way that makes physical sense. If the mechanism is initially in the position shown in Figure 6-10 and the arm motor gives a sudden positive torque, the arm should accelerate in the positive direction. The torque on the arm also transmits a force to the nailer that creates a positive moment about the nailer's mass center. As a result, the nail gun should rotate at a higher rate during the early part of the response. The simulated response to an impulse in the arm-motor torque, depicted in Figure 6-11, confirms this presumption.

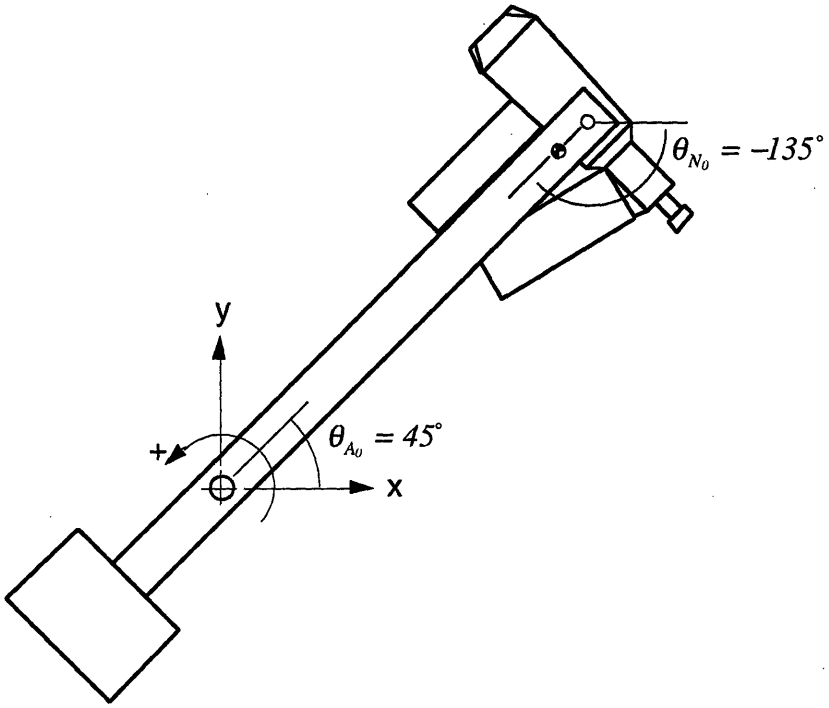

Figure 6-10. An initial configuration used to check the open-loop simulation. Both θ_{A_0} and θ_{N_0} are absolute angles, measured with respect to the x-axis.

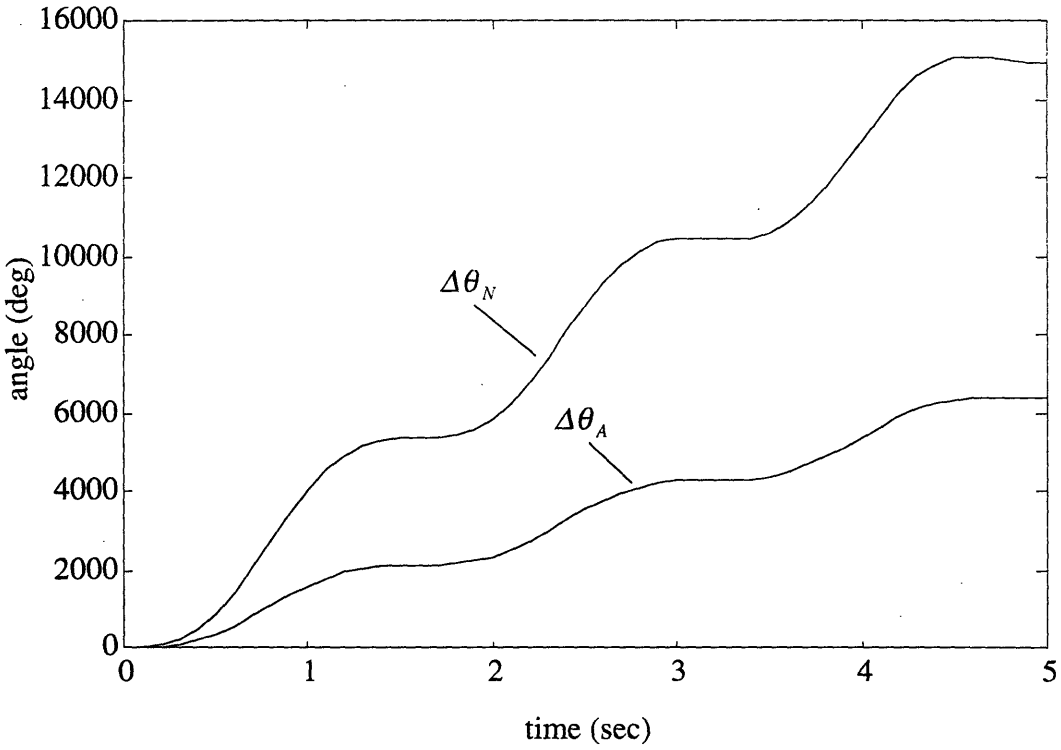

Figure 6-11. Impulse response of the arm and the nailer (linear simulation). For this particular response, the stiffness parameters were arbitrarily set to one.

After the torque ceases, the arm and nailer continue to rotate. The exact motions they should follow are not intuitive, but one thing is clear. With gravity excluded from the simulation, the nailer should eventually settle at an orientation with respect to the arm in which its mass center is at its farthest point from the arm. In other words, $\Delta\theta_N - \Delta\theta_A$ should be an odd multiple of 180°. As shown in Figure 6-12, the relative rotation did not converge to any particular point.

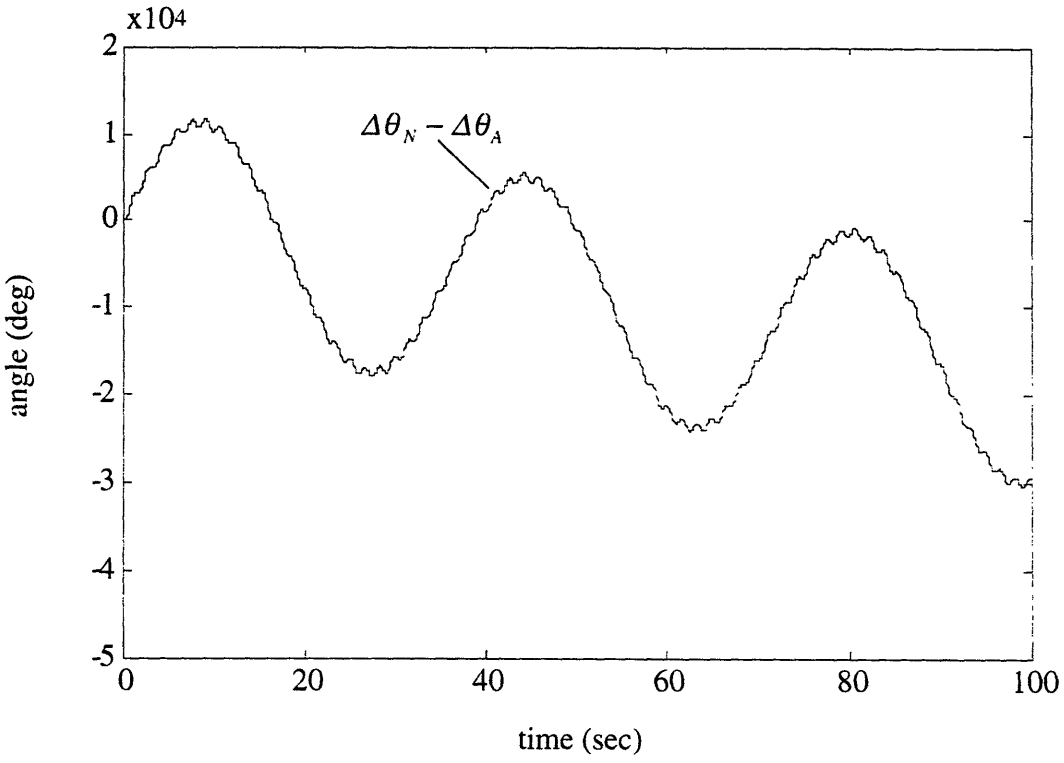

Figure 6-12. Relative displacement of the arm and the nailer after an impulse (linear simulation). This inaccurate response is an example of the linear model's limitations.

This result does not mean that the model is incorrect. It simply confirms the tenet that the linear model is only valid for small

deviations from the initial configuration. The nonlinear model should be used to simulate the motion of the mechanism.

Nonlinear simulation is accomplished in MATLAB by writing the equations (must be first order) in a separate file called a script file and then using a built-in function called `ode` that numerically integrates the equations (Runge-Kutta, 2nd-3rd order or 4th-5th order). The nonlinear model does predict what we expect: the relative position, plotted in Figure 6-13, moves away from its initial value and appears to oscillate about 180°. The large oscillations occur because the modeled damping is very small.

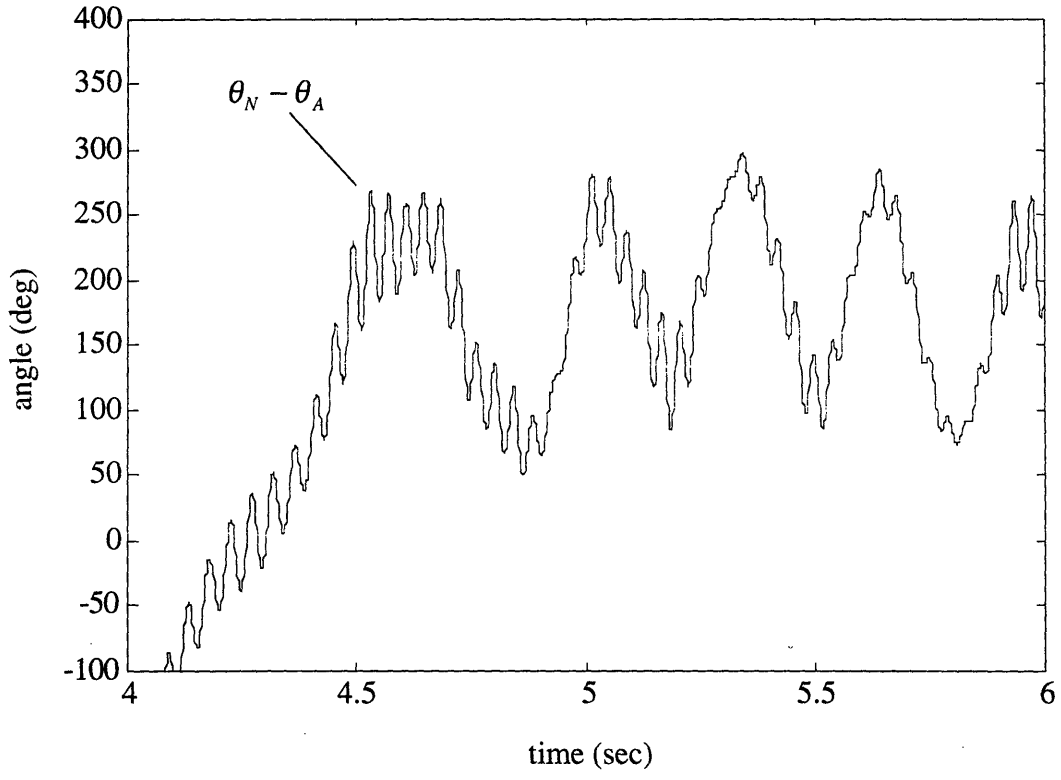

Figure 6-13. Relative displacement of the arm and the nailer after an impulse (nonlinear simulation). The response oscillates about 180°, as we expect.

6.5.2 Oscillation Frequencies. Having an understanding of the system dynamics beforehand helps greatly in verifying and using the simulation. Performing independent estimates of response characteristics helps develop intuition, and it provides a more precise check on the simulation.

The frequencies at which the system oscillates are a function of the stiffness and inertia of the system's components. These natural frequencies can be estimated with very simple models and compared to the output of the simulation. The model in Figure 6-14 captures the dominant vibration characteristics of the arm and nailer subsystems.

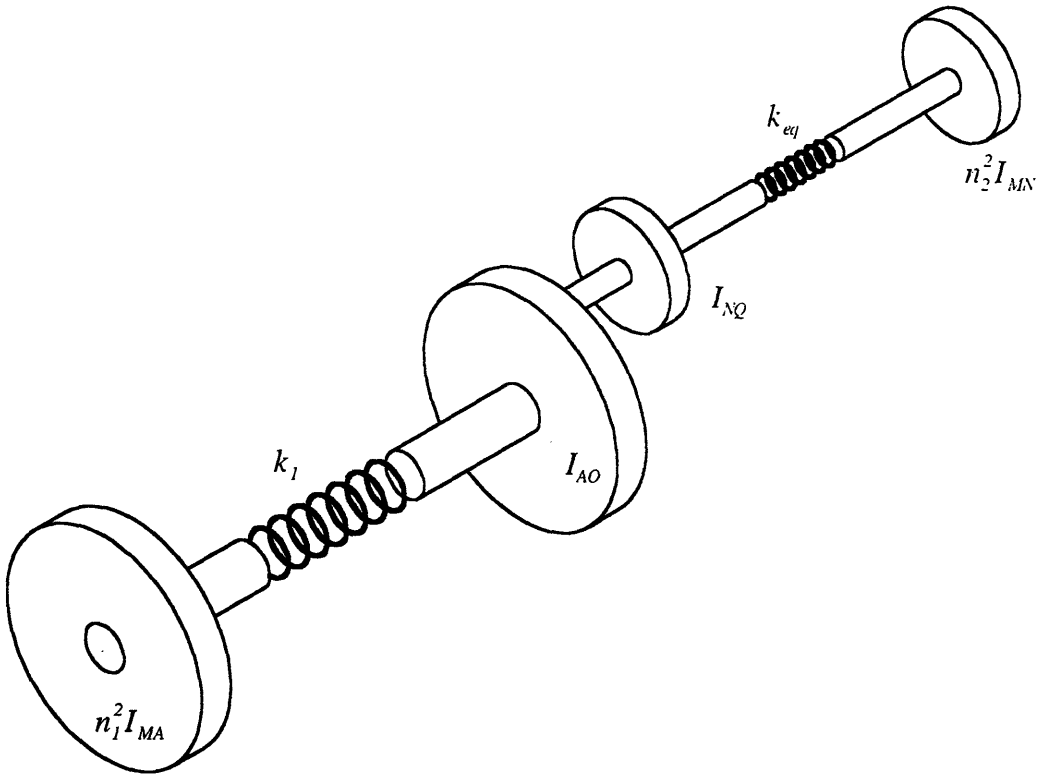

Figure 6-14. Simplified model of the nailing mechanism for estimating natural frequencies of torsional vibration.

If the arm and nailer coupling is ignored, the natural frequency of each subsystem is given by

$$\omega_{arm} = \sqrt{\frac{k_1(I_{AO} + n_1^2 I_{MA})}{n_1^2 I_{MA} I_{AO}}} \tag{6-70}$$

$$\omega_{nailer} = \sqrt{\frac{k_{eq}(I_{NQ} + n_2^2 I_{MN})}{n_2^2 I_{MN} I_{NQ}}} \tag{6-71}$$

Substituting convenient guesses for some of the parameters in these equations, we find

$$\omega_{arm} = 4.0 \ \frac{rad}{sec} \ (0.64 \ Hz) \tag{6-72}$$

$$\omega_{nailer} = 0.16 \ \frac{rad}{sec} \ (0.025 \ Hz) \tag{6-73}$$

In the computer simulation, an impulse input excited the oscillatory response given in Figure 6-15. The arm's rotational vibration, at a frequency of 0.67 Hz (4.2 rad/sec), compares well to our prediction, but the nailer's response contains two frequencies. The first, 0.03 Hz, matches our prediction for the nailer; the second frequency corresponds exactly to the oscillation of the arm. These results make sense because the arm has a strong effect on the nailer's motions whereas the nailer's influence on the arm is relatively weak.

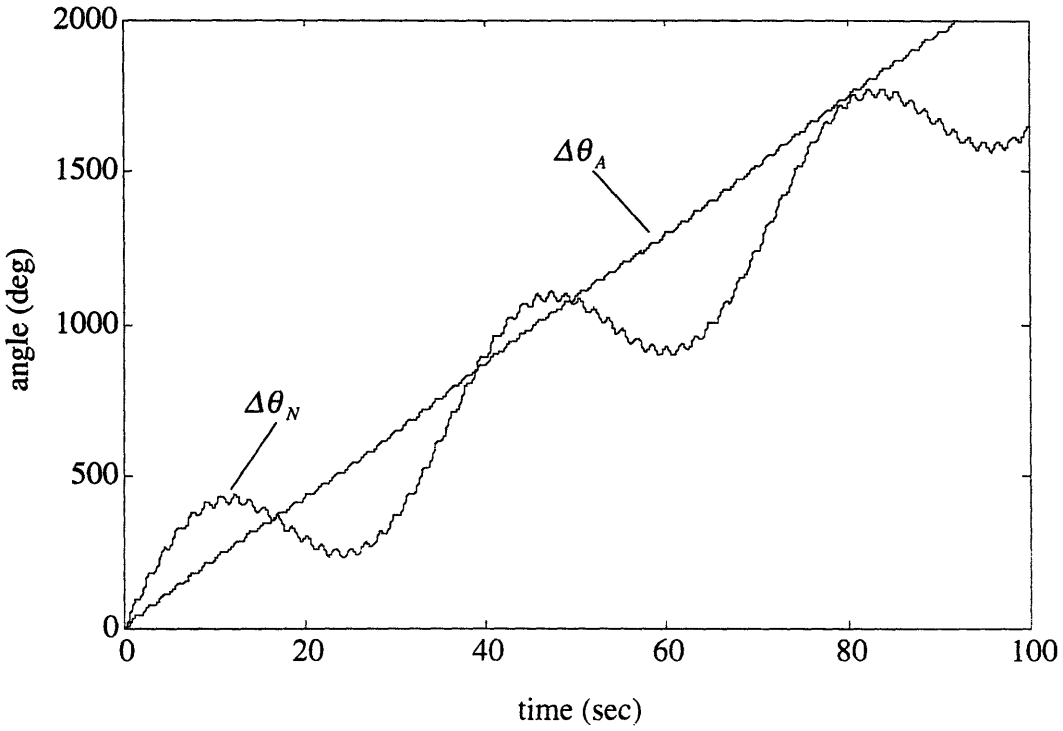

Figure 6-15. Impulse response of the arm and the nailer (linear simulation). Because of dynamic coupling, the nailer oscillates at the arm's natural frequency as well as its own.

Chapter 7
Control System Design

In its broadest interpretation, the term control system denotes everything in a system that acts on the inputs to produce the outputs [Kuo, 1991]. This definition includes electronic hardware and computer software, as well as mechanical elements, such as linkages and gear trains. In this thesis, however, control system refers specifically to the logic that generates the input signals to the nailing mechanism's actuators.

The fundamental goal in designing a control system is to shape a system's characteristics such that the system performs its function and behaves in a controlled, predictable manner. The control system has its own dynamic characteristics that interact with the dynamics of the system to be controlled. The combination of the two effectively forms a new system.

Position, velocity, temperature, and flow rate are examples of typical controlled outputs. The designer usually specifies the control of these variables in terms of response properties, such as vibration, speed, and sensitivity to disturbances. The primary objective of the nailing mechanism's control system is to move the components of the mechanism through a series of positions. The exact trajectory between the points is not important. What is important is that the mechanism settles at the specified points within a certain amount of time. This task requires feedback control, in which the controlled

variable, position in this case, is compared with the control command, and a signal is generated to correct any discrepancy.

This chapter explains the feedback control strategy chosen for the nailing mechanism and justifies the strategy using frequency domain techniques. Such techniques are further employed to tune the controller gains. In addition, a model of the control system is implemented in the computer simulation, which is used to evaluate the nailing mechanism's performance.

7.1 Control Strategy

A variety of closed-loop control schemes exist, ranging from simple feedback to nonlinear and adaptive techniques. Some of the more advanced schemes were developed for tasks that are particularly demanding for robots. For example, impedance control applies to robots that perform delicate operations in contact with their environment [Hogan, 1985]. Other schemes, such as robust control and adaptive control, address problems that arise from modeling errors and variation in loads and system characteristics.

Most of these techniques are rarely used in industry, however [Asada and Slotine, 1986]. Simple position control loops can manage most of today's automated operations and are much easier to implement. Furthermore, some of the more sophisticated schemes will not work for certain classes of systems. For instance, techniques such as feedforward and nonlinear control that attempt to cancel out the dynamics of the open-loop system cannot be applied to some

sensitive systems. One can never cancel the dynamics exactly because the dynamics are never known exactly; modeling errors always exist. With a system that is inherently unstable, such as a non-collocated servo-controlled arm, even a slight error in the model will allow the closed-loop system to go unstable at high gains.

7.1.1 Basic Feedback Control. The simplest and most common family of controllers comprises various combinations of proportional (P), derivative (D), and integral (I) control. By itself, proportional control works by multiplying the error, which is the difference between the command and the system output, by a constant gain. P control, in effect, acts as a simple spring, where the proportional gain is the spring constant. As a result, any disturbance acting on the output, no matter how small, will cause an error that the control system cannot correct. The magnitude of that error, however, can be reduced by increasing the proportional gain.

Derivative control, which conditions the controller's output by differentiating the error signal with respect to time, effectively adds damping to the system. The amount of damping is adjusted with the derivative gain, which amplifies the differentiated signal.

With the addition of integral control, the system attains some ability to reject disturbances. The output of the controller increases in magnitude as the error signal is integrated over time. As a result, a static disturbance, such as a constant applied torque, would be overcome by the controller as the error signal grew.

Figure 7-1 depicts the general feedback control scheme in block diagram form. In the figure, G_C stands for the transfer

function of the controller, and G signifies the transfer function of the open-loop system (the nailing mechanism without the controller). The transfer function converting the output to a signal to be subtracted from the input command is given by H. For PID control,

$$G_C = K_P + \frac{K_I}{s} + K_D s \tag{7-1}$$

The P term is K_P; $\frac{K_I}{s}$ and $K_D s$ are the I and D terms.

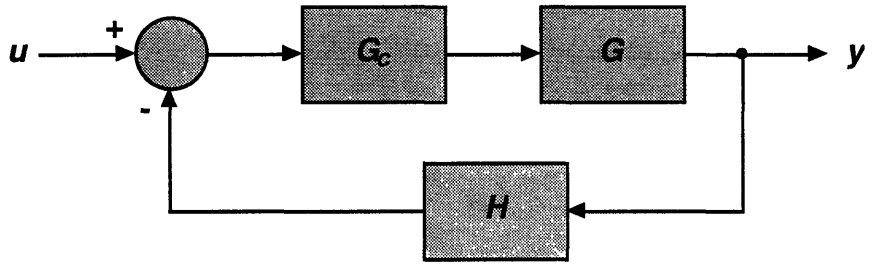

Figure 7-1. Basic feedback-controlled system. The input signal to the open-loop system, G, is given by $G_C(u - Hy)$.

7.1.2 Approach to Controlling the Nailing Mechanism. The control system applied to the nailing mechanism consists of individual controllers for each axis. In each case, the control strategy is proportional plus velocity feedback (PV), which acts in a way similar to PD control. That is, it acts as a damped spring.

Integral control is excluded for several reasons. It increases overshoot in the step response, which is an undesirable effect because it could cause the nailer to contact the panel prematurely.

Integral control often decreases system stability as well. Moreover, the disturbances this system experiences mostly come from the discharge of the nail gun. The mechanism should not try to maintain its position in spite of these disturbances. Rather, it should give when the panel makes contact.

In PV control, the velocity of some point on the mechanism is measured directly and fed back. Figure 7-2 shows this process schematically.

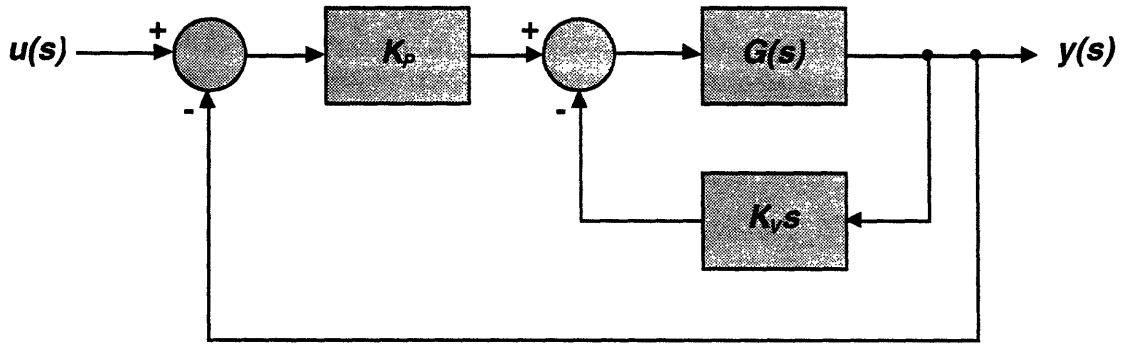

Figure 7-2. Proportional plus velocity feedback (PV) control, with unity feedback.

This diagram can be simplified to a mathematically equivalent diagram with one feedback loop:

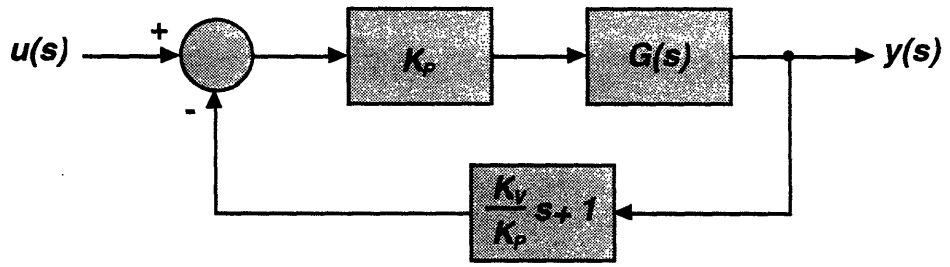

Figure 7-3. Simplified block diagram of PV control. Although the physical relations associated with the blocks are less obvious, the input-output relationships are easier to obtain.

In contrast, the PD controller measures position only and then differentiates the position error signal to achieve the damping effect. Refer to Figure 7-4.

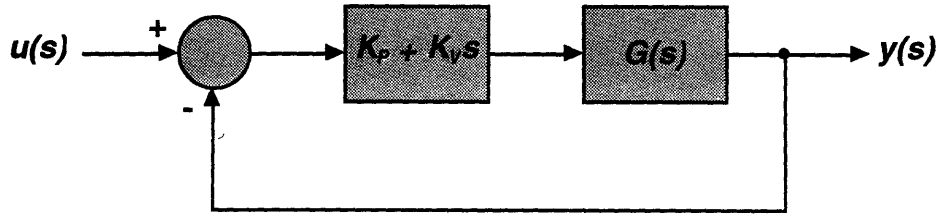

Figure 7-4. PD control, with unity feedback.

The closed-loop transfer functions of the PV and PD controlled systems have identical denominators. However, as the numerator in Equation 7-2 expresses, the derivative term in PD control introduces an additional zero into the system. This zero shortens the rise time of the step response, but it also causes the response to have greater overshoot [Shahian and Hassul, 1993]. For PD control, the closed-loop transfer function, which represents the total system response y to any input u, is

$$\frac{y(s)}{u(s)} = \frac{(K_D s + K_P)G(s)}{(K_D s + K_P)G(s) + 1} \tag{7-2}$$

The closed-loop transfer function of the PV controlled system is

$$\frac{y(s)}{u(s)} = \frac{K_P G(s)}{(K_D s + K_P)G(s) + 1} \tag{7-3}$$

In practice, differentiation results in a noisy signal and causes the system to act unpredictably. For this reason, the PD controller, as it is, is not used in real applications [Shahian and Hassul, 1993]. Instead, a pole is usually added to the derivative term to filter out high frequency noise:

$$G_C = K_P + \frac{K_D s}{T_D s + 1} \tag{7-4}$$

or

$$G_C = \frac{K_P(T_D + K_D/K_P)s + 1}{T_D s + 1} \tag{7-5}$$

This controller is known as a lead compensator.

7.1.3 Sensor Location. To obtain the highest possible accuracy, and to be consistent with the controller model of Figure 7-2, the positions and velocities must be measured directly from the endpoints. For the nailer rotation and translation, the term endpoint refers to the tip of the nail gun. Similarly, the point near the end of the arm where the nailer connects to it, is the endpoint for the arm subsystem.

Because the mechanism is flexible, positions of other points, which may be more convenient to measure, do not maintain a fixed correlation to the endpoints when the mechanism is in motion. In addition, nonlinearities between an alternative point and the

endpoint, such as backlash in transmission elements, will cause steady-state position errors.

However, mounting the sensors away from the actuator generally reduces the controllability of the system [Gervarter, 1970]. In fact, with a PV controller, flexible systems such as the nailing mechanism are unstable when this setup is used. If the sensors are instead mounted directly on the actuator, the system becomes stable under PV control (within a certain range of gains). The following example uses the root locus of both cases to prove this point.

Consider the single, servo-controlled arm modeled in Figure 7-5. In open-loop operation, the angular position of the arm responds to the torque output by the motor according to the following transfer function.

$$\frac{\theta_A(s)}{\tau(s)} = \frac{k/nI_A I_M}{s^2(s^2 + \frac{k}{I_A} + \frac{k}{n^2 I_M})} \tag{7-6}$$

If non-collocated sensor feedback (sensor mounted away from the actuator) is implemented in PV control, the system may be represented as in Figure 7-2, with

$$u(s) = \theta_{ref}(s) \tag{7-7}$$

$$y(s) = \theta_A(s) \tag{7-8}$$

and

$$G(s) = \frac{\theta_A(s)}{\tau_M(s)} \tag{7-9}$$

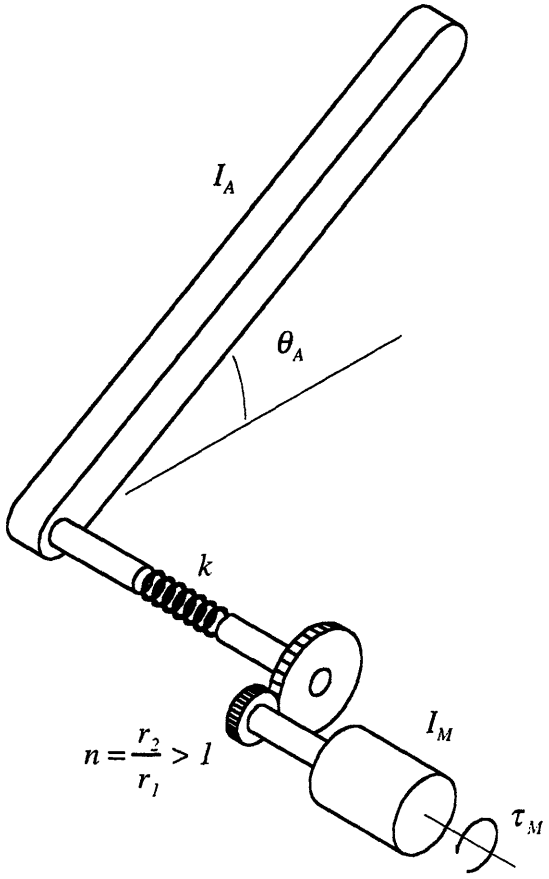

Figure 7-5. Single-axis, robotic-arm servo system.

The resulting closed-loop response to position input commands is given by

$$\frac{\theta_A(s)}{\theta_{ref}(s)} = \frac{K_P G(s)}{K_V G(s)s + K_P G(s) + 1} \tag{7-10}$$

The roots of the characteristic equation, obtained by setting the denominator equal to zero and solving for s, determine the stability of the system. By varying K_P, we produce a locus of roots to this equation, plotted in Figure 7-6. The root locus shows that the system

is unstable for almost all gains (poles in the right half plane indicate instability).

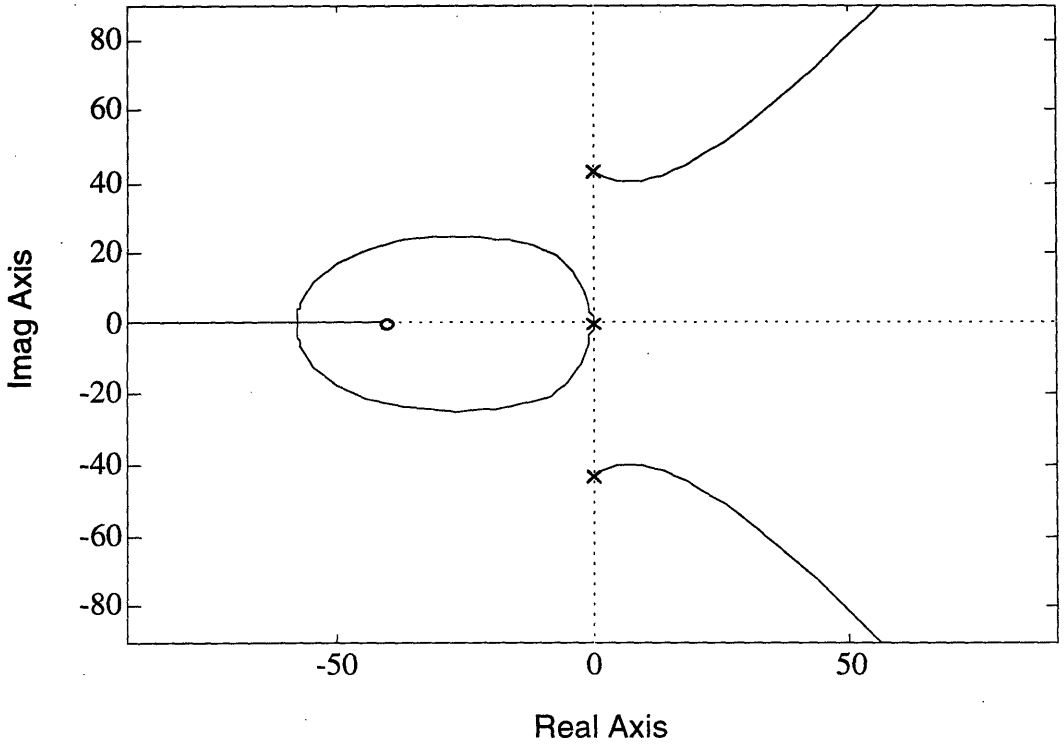

Figure 7-6. Root locus for the non-collocated case. Some poles move into the right half plane immediately, indicating instability for almost all gains.

Now consider the system with collocated feedback, where the sensors are mounted directly to the actuator. The block diagram looks a little different, as shown in Figure 7-7. The closed-loop transfer function, which is more difficult to obtain than in the non-collocated case, differs significantly (refer to Appendix H for the derivation):

$$\frac{\theta_A(s)}{\theta_{ref}(s)} = \frac{K_P k / n I_A I_M}{s^4 + (\frac{k}{I_A} + \frac{k}{n^2 I_M})s^2 + \frac{K_V}{I_M}s^3 + \frac{K_P}{I_M}s^2 + \frac{K_V k}{I_M I_M}s + \frac{K_P k}{I_A I_M}} \qquad (7\text{-}11)$$

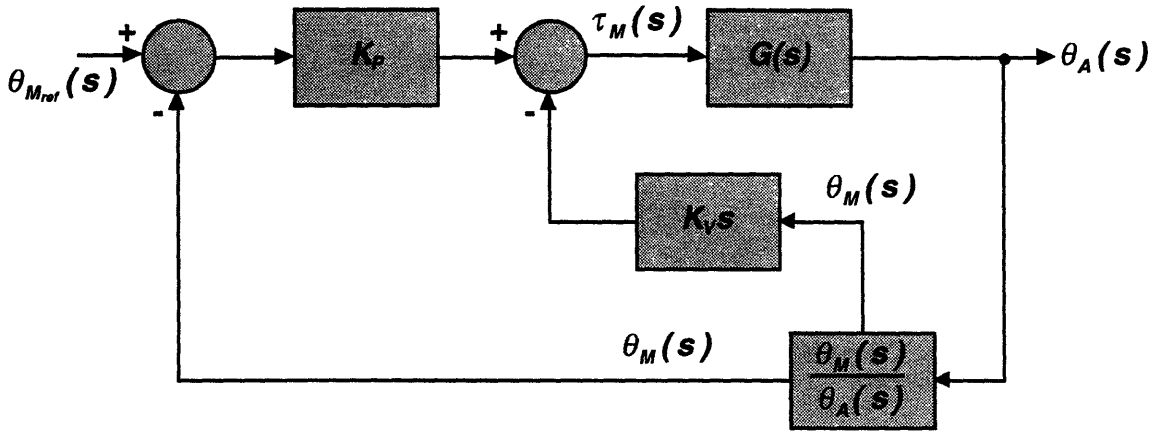

Figure 7-7. Single-arm servo system with collocated PV control. The system measures position and velocity of the motor to control the position of the arm.

This time, the root locus (Figure 7-8) shows that the system is theoretically stable for a large range of gains. (In reality, noise and unmodeled dynamic effects may reduce the range of gains for which the system is stable.)

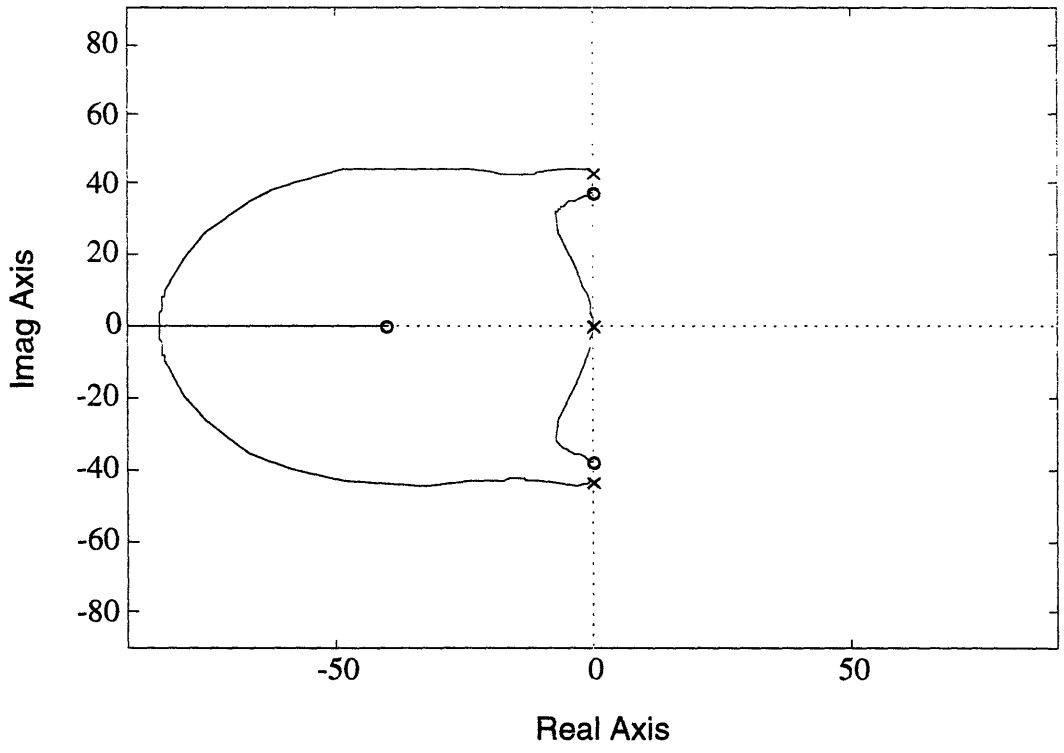

Figure 7-8. Root locus for the collocated case. The poles stay in the left half plane, indicating inherent stability.

7.2 Modeling the PV Controlled Nailing Mechanism

The control system alters the dynamics of the nailing mechanism by using state feedback to influence the input command. To understand how, we must incorporate the controller into the dynamic model of the mechanism.

The block diagram in Figure 7-9 represents the closed-loop translation subsystem. This subsystem is single-input, single-output because the nailing mechanism's translation is not affected significantly by the mechanism's other movements. In the figure, K_{TM} represents the electrical portion of the motor. This subsystem is modeled as a simple gain because its dynamics are assumed to be much faster than the overall system dynamics.

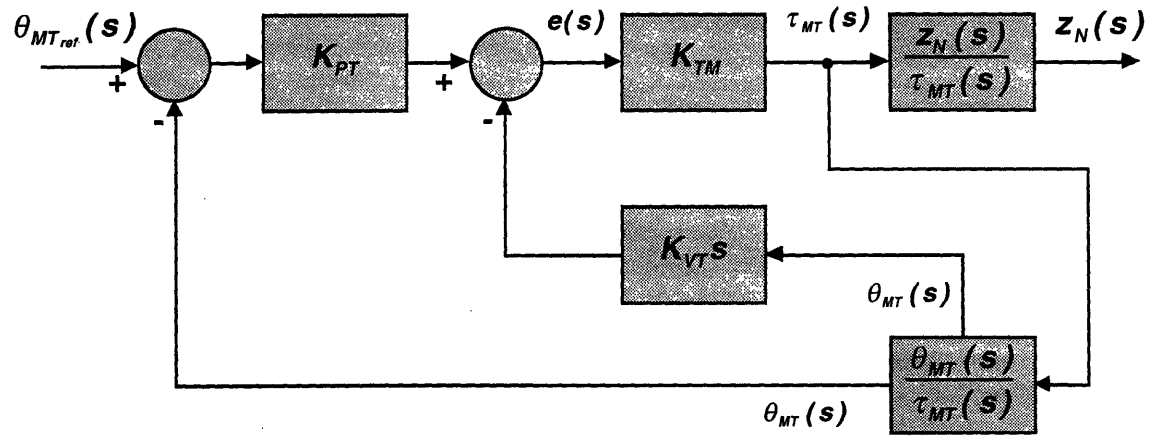

Figure 7-9. The closed-loop translation subsystem. The output variable is the position of the mechanism along the z-axis. Also, the letter T in the variable names refers to translation.

The rotations of the arm and nailer are dynamically coupled according to Equations 6-16 and 6-18. The two axes combine to form the closed-loop subsystem depicted in Figure 7-10. In a sense, the

subsystem is multi-input, multi-output. The command for one axis affects the output of the other axis indirectly through the dynamics of the mechanism. However, the term multi-input, multi-output usually applies to systems where the output of one axis is directly fed back to the input of several axes. Again, simple gains stand for the electrical portions of the motors.

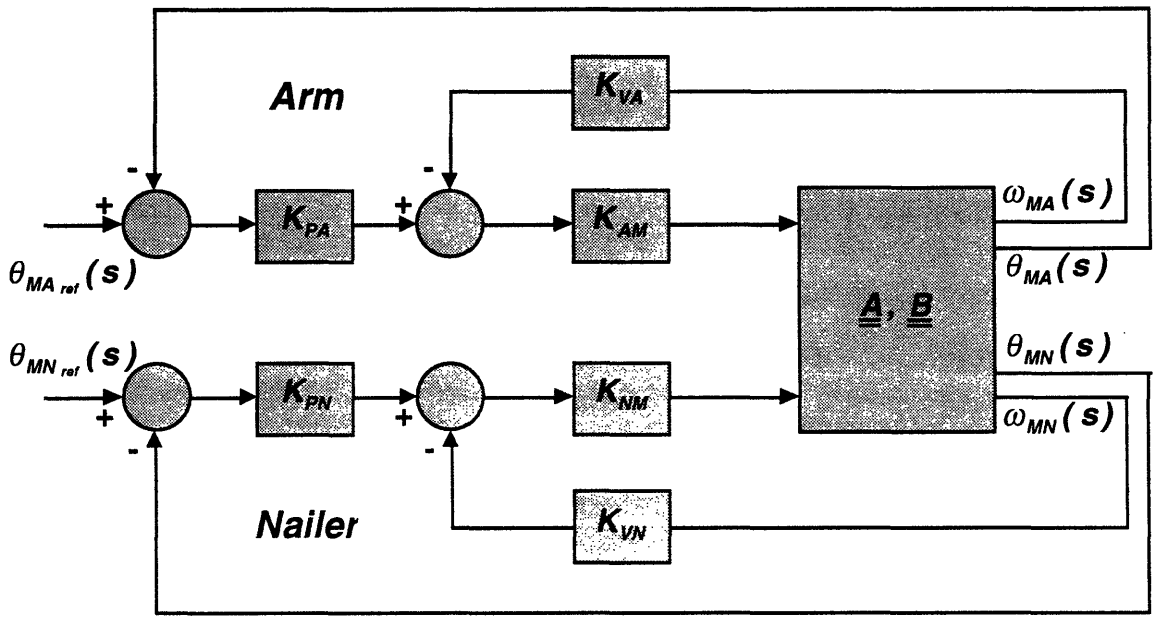

Figure 7-10. The closed-loop arm and nailer subsystems. Each output is affected by both inputs because of dynamic interaction between the arm and the nailer. The letters A and N in the variable names refer to arm and nailer.

Recall from Chapter 6 that the open-loop dynamic equations of the nailing mechanism can be represented in state-space form by the following general equation.

$$\dot{\underline{x}} = \underline{\underline{A}}\underline{x} + \underline{\underline{B}}\underline{u} \tag{7-12}$$

where $\underline{\underline{A}}$ and $\underline{\underline{B}}$ contain the parameters that define the system characteristics. To add the control system to the computer simulation, the dynamic equations are simply modified to reflect the feedback loops. The motor-torque input for each axis becomes a function of the states:

$$\tau_M = K_M[K_P(\theta_{M_{ref}} - \theta_M) - K_V\omega_M] \tag{7-13}$$

In generalized variables, the input is given by

$$\underline{u} = \underline{\underline{K}}\underline{x} + \underline{\underline{R}}\underline{r}$$

where $\underline{r}$ refers to the commanded position (for example, $\theta_{M_{ref}}$), and $\underline{\underline{R}}$ defines how this command influences the input signal. Substitution for u in the general state-space equation yields

$$\dot{\underline{x}} = \underline{\underline{A}}\underline{x} + \underline{\underline{B}}(\underline{\underline{K}}\underline{x} + \underline{\underline{R}}\underline{r}) \tag{7-14}$$

or

$$\dot{\underline{x}} = (\underline{\underline{A}} + \underline{\underline{B}}\underline{\underline{K}})\underline{x} + \underline{\underline{B}}\underline{\underline{R}}\underline{r} \tag{7-15}$$

This equation fits into the general form with $\underline{\underline{A}} + \underline{\underline{B}}\underline{\underline{K}}$ reduced to a single matrix $\underline{\underline{A'}}$ and $\underline{\underline{B}}\underline{\underline{R}}$ to $\underline{\underline{B'}}$. (The vector $\underline{r}$ has replaced $\underline{u}$ as the input.) To obtain the closed-loop responses of the nailing mechanism, the matrices $\underline{\underline{A'}}$ and $\underline{\underline{B'}}$ are entered into MATLAB just as $\underline{\underline{A}}$ and $\underline{\underline{B}}$ were in the open-loop simulation.

7.3 Design

Once the control strategy is specified, designing the control system becomes a matter of tuning the gains to meet the system specifications. The specifications may be stability margins, or they may be performance criteria, such as rise time of the step response, maximum overshoot, or even energy consumption.

Regardless of the specifications, stability must always be addressed. The controller may actually cause the system to go unstable for certain ranges of gains. Numerous stability analysis techniques are available that can be used to acquire insight into the effects that changes in the system have on its response.

7.3.1 Stability. We have already shown that under collocated PV control, a servo-controlled arm with a flexible transmission is stable (Figure 7-8). Therefore, the translation subsystem, which is analogous, is also stable. Refer to the Bode plot of Figure 7-11. This open-loop plot reveals the relative stability of the closed-loop system: the gain margin is 115 dB and the phase margin is 90°.

Gain margin indicates the effect that changing the proportional gain has on the closed-loop stability. When the gain is increased, the magnitude plot shifts upward, maintaining its shape, and the gain margin decreases (the phase plot is unchanged). The gain margin is defined as the amount by which the magnitude plot is below 0 dB at the phase crossover frequency, ω_{pc} (frequency at which the phase plot reaches -180°). If the plot is above 0 dB at ω_{pc}, the system is

unstable for all gains greater than one. Therefore, the 115 dB gain margin means that the translation subsystem is theoretically stable for $0 < K_{PT} < 5.64 \times 10^5$.

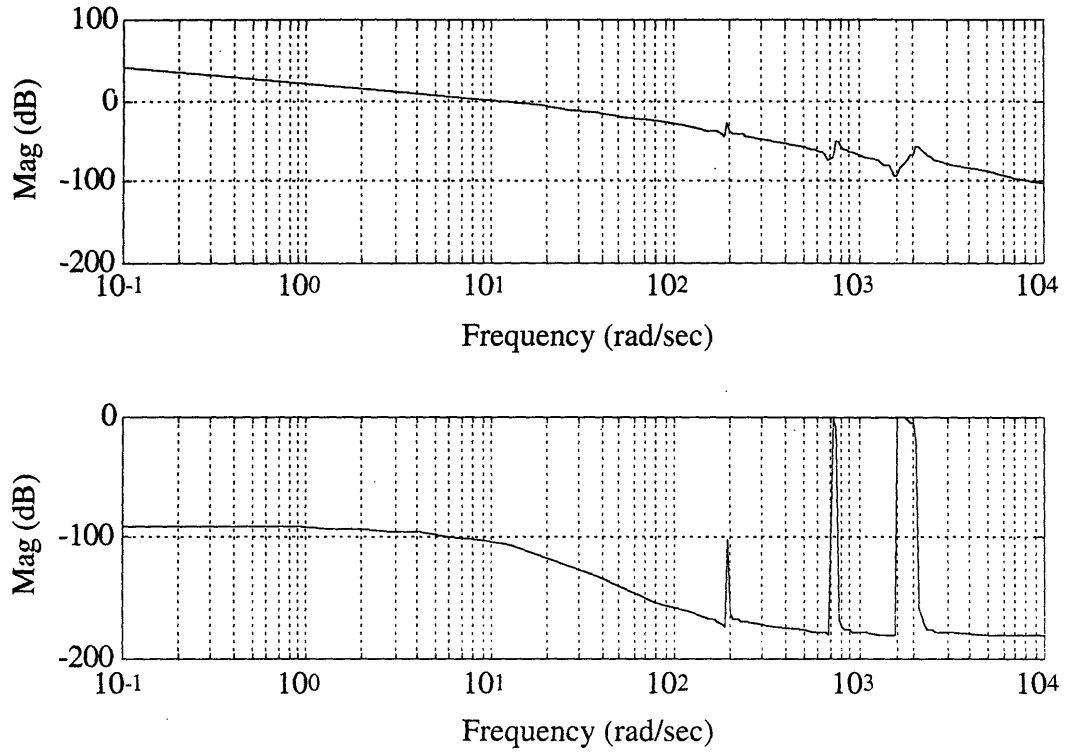

Figure 7-11. Open-loop Bode plot of the translation subsystem ($K_{PT} = 1$).

The phase margin, on the other hand, reveals the effect that changes in system parameters have on stability [Kuo, 1991]. Theoretically, these changes affect the phase plot by the same amount at all frequencies. Phase margin is defined as the amount by which the phase plot is above -180° at the gain crossover frequency, ω_{gc} (frequency at which the magnitude plot crosses the 0 dB line).

As the open-loop Bode plots in Figures 7-12 and 7-13 indicate, the PV controller also stabilizes the coupled rotation axes for a large

range of gains. The gain margin for the arm subsystem is 142 dB, so the closed-loop system is stable for $0 < K_{PA} < 1.3 \times 10^7$. The nailer subsystem's gain margin is 130 dB ($0 < K_{PN} < 3.1 \times 10^6$). In both cases, the phase margin is 90°.

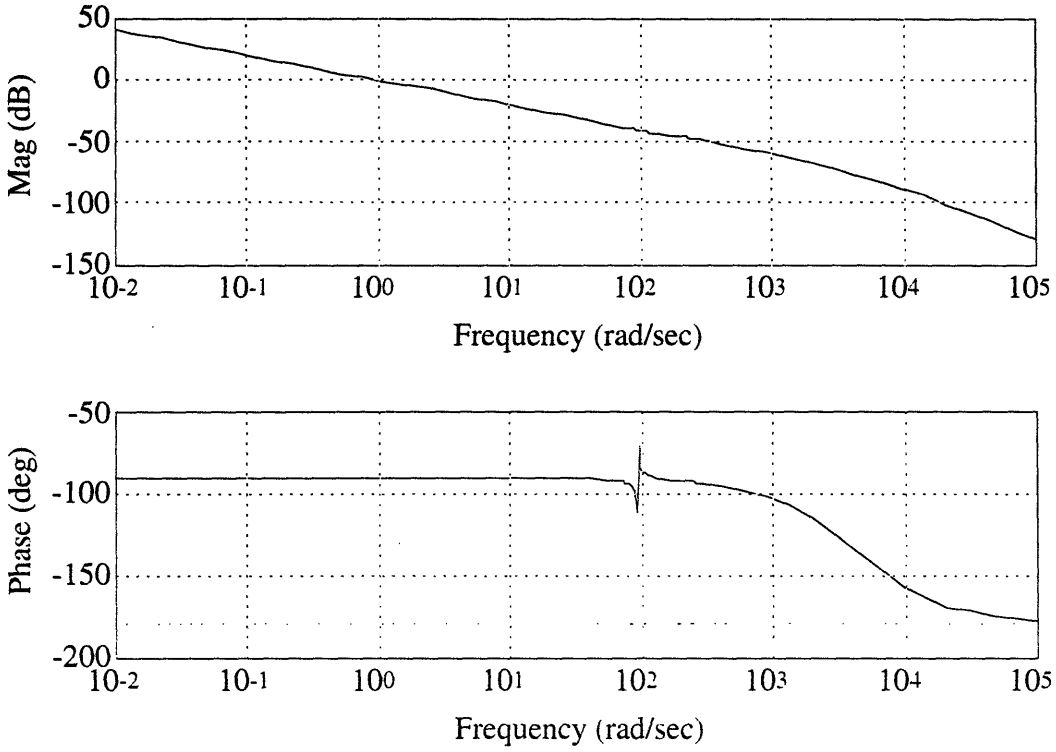

Figure 7-12. Open-loop Bode plot of the arm subsystem ($K_{PA} = 1$).

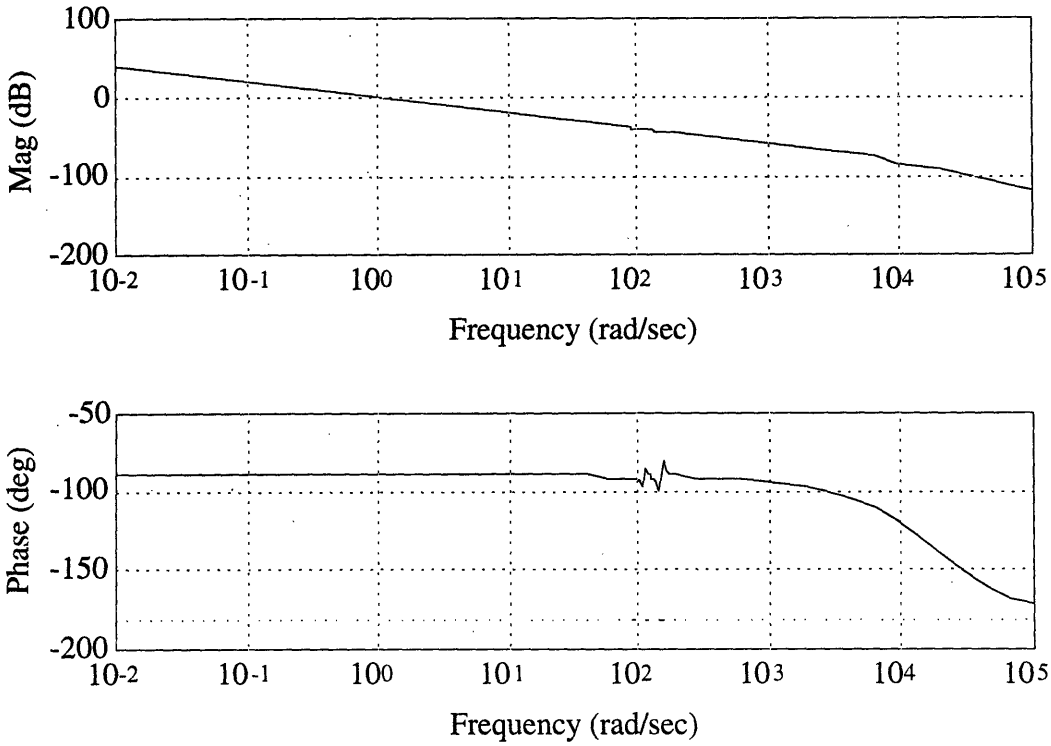

Figure 7-13. Open-loop Bode plot of the nailer subsystem ($K_{PN} = 1$).

7.3.2 Tuning the Gains. The nailing mechanism moves the nail gun from point to point so that it can fasten the end cap to the panel, often while the panel is moving. Timing is critical. Thus, settling time effectively defines the performance of each of the mechanism's subsystems.

However, the gains cannot be chosen analytically to satisfy a specific settling time, as no closed form expression exists for the settling time of high order systems. Tuning the gains iteratively by measuring the settling time from the step response is not practical either.

A more efficient approach is to tune the gains such that the closed-loop bandwidth is maximized. Bandwidth, defined as the

frequency at which the output-to-input magnitude ratio drops by -3 dB from its low frequency value, is inversely proportional to settling time [Kuo, 1991]. In other words, higher bandwidth corresponds to a faster system. Refer to the closed-loop Bode plot of the arm rotation axis (shown in Figure 7-14), in which the proportional and velocity feedback gains have been arbitrarily set to one; the corresponding bandwidth is approximately 0.1 rad/sec. The system acts as a low pass filter, following inputs at low frequency and attenuating higher frequency inputs. The spikes in magnitude and phase near 100 rad/sec (16 Hz) correspond to the natural resonance of the system.

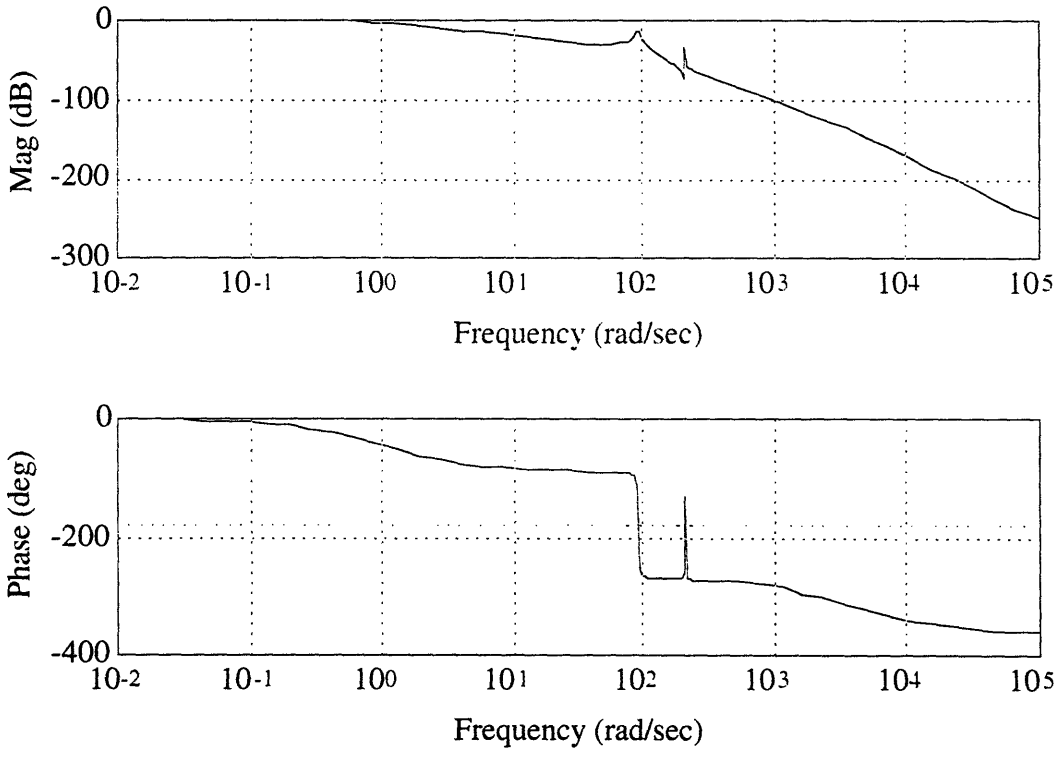

Figure 7-14. Closed-loop Bode plot of the arm subsystem with gains set to one.

In first and second order systems, the open-loop gain crossover frequency is approximately equal to the closed-loop bandwidth if the gain is large [Shahian and Hassul, 1993]. So, perhaps we can use this correlation to find the proper gain settings. Using the information we have from the open- and closed-loop Bode plots for the arm subsystem, we find that

$$\frac{\omega_{gc}}{BW} \approx 14.3 \tag{7-16}$$

To make sure the system filters out inputs near resonance, we attempt to achieve a maximum bandwidth of 90 rad/sec (14.3 Hz). According to the relationship in Equation 7-16, ω_{gc} should be set to 1287 rad/sec. Figure 7-12 then indicates that about 60 dB must be added to the magnitude plot to meet this target. In other words, the proportional gain must be increased to 1000. However, the resulting closed-loop response is not what we are trying to achieve (see Figure 7-15). The bandwidth is fine, but the resonance peak is above the 0 dB line. Inputs at or near the resonance frequencies will be amplified. As a result, the mechanism may behave erratically with this gain setting. We therefore do not use this technique to tune the gains.

We must maximize bandwidth while filtering out the resonance peak. Increasing K_V while keeping K_P constant does not smooth out the closed-loop response; it simply causes the resonance peak to drop, and thus causes the bandwidth to drop significantly. Decreasing K_P while holding K_V constant lowers the resonance peak, but it also reduces the bandwidth. Moreover, although this action

lowers the maximum value of the peak, the vertical rise of the peak changes very little. On the other hand, reducing K_V with K_P reduces the vertical rise, and as a result, allows the bandwidth to be increased without pushing the peak above 0 dB.

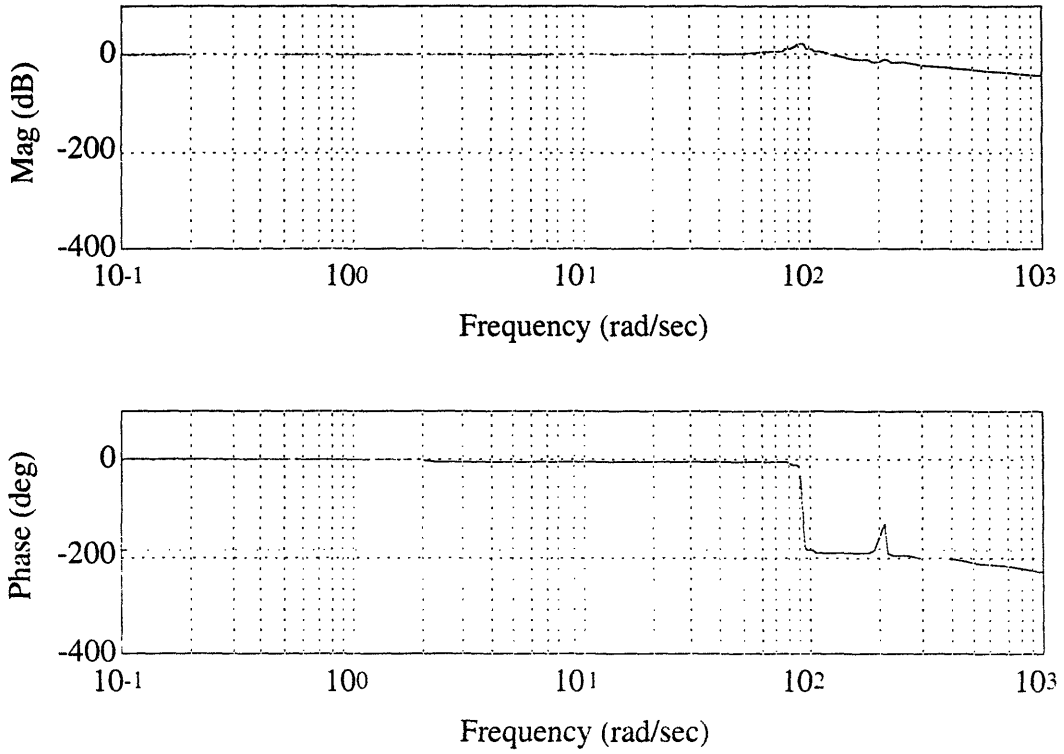

Figure 7-15. Closed-loop Bode plot of the arm subsystem with $K_{PA} = 1000$.

The procedure, then, is to decrease K_P to some value and then decrease K_V in small increments until the resonance peak just reaches 0 dB. Further, the process is repeated until an optimum is reached. The highest bandwidth this procedure achieved for the arm subsystem was about 92 rad/sec (15 Hz); the gains were K_{PA}=1.52 and K_{VA}=0.06. The resulting closed-loop Bode plot appears in Figure 7-16.

In the same manner, the Bode plot was used in tuning the proportional and velocity feedback gains for the nailer's rotation (Figure 7-17) and the mechanism's translation (Figure 7-18). For the nailer, K_{PN}=0.35 and K_{VN}=.01, and for the translation axis, K_{PT}=2.01, and K_{VT}=0.1.

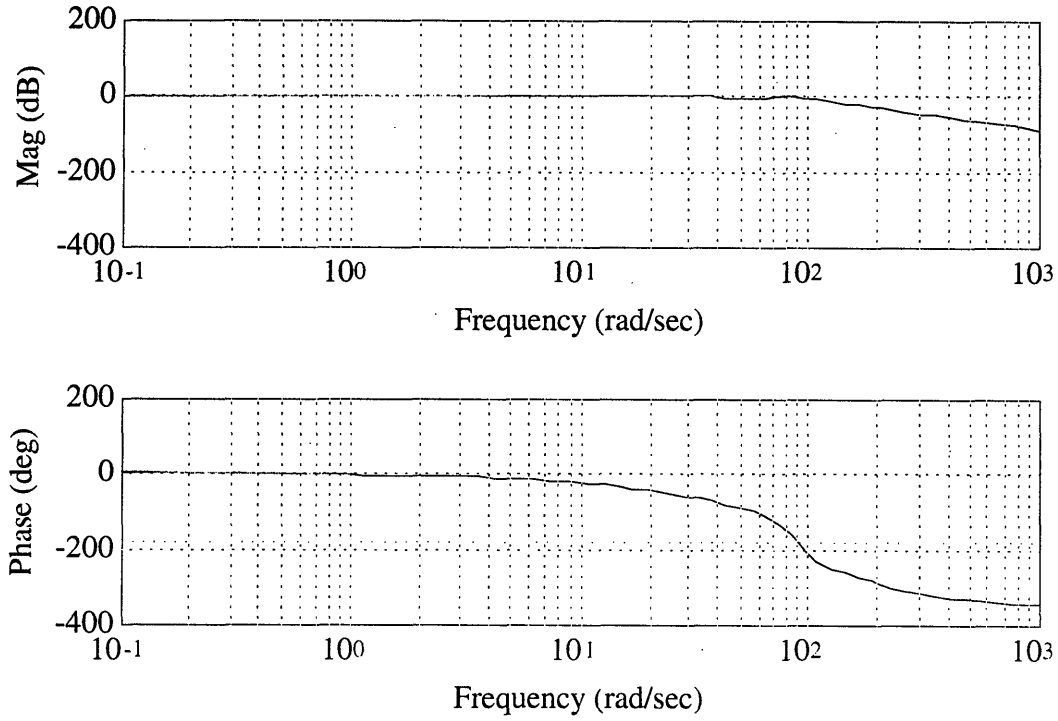

Figure 7-16. Closed-loop Bode plot of the arm subsystem with tuned gains. The bandwidth is 92 rad/sec (15 Hz).

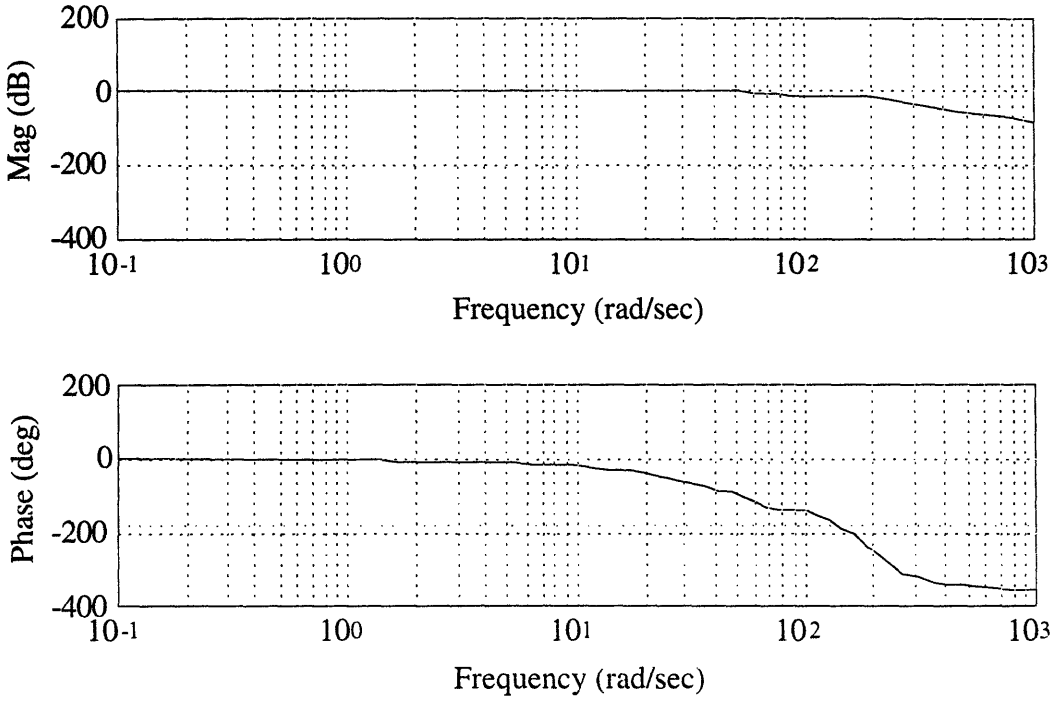

Figure 7-17. Closed-loop Bode plot of the nailer subsystem with tuned gains. The bandwidth is 56 rad/sec (9 Hz).

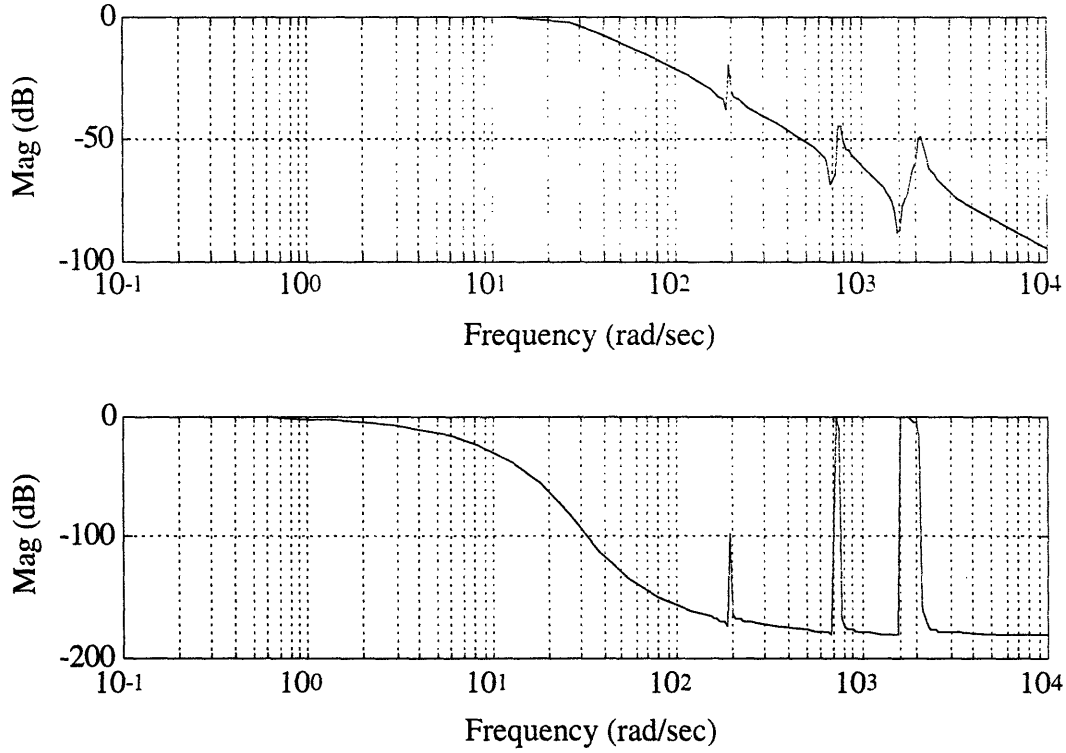

Figure 7-18. Closed-loop Bode plot of the translation subsystem with tuned gains. The bandwidth is 31 rad/sec (5 Hz).

7.4 Performance

System performance is commonly expressed in terms of the step response. It visually exhibits the relative damping of the system, and step response characteristics such as rise time and maximum overshoot provide basic criteria on which the system can be evaluated quickly. Figures 7-19 and 7-20 depict the step responses of the mechanism's axes, which were obtained from the linear simulation. Table 7-1 presents the quantitative response characteristics.

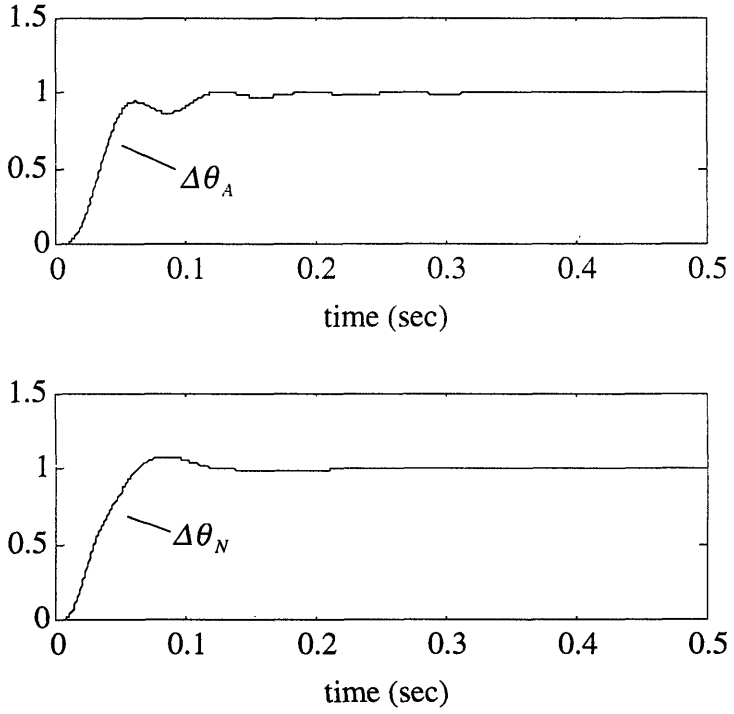

Figure 7-19. Unit step responses of the arm (upper plot) and the nailer. The arm's response is slower than the nailer's, but the arm's response has less overshoot. Minimizing overshoot of the arm is more critical because error in the arm's angular position results in larger error at the nailer tip (Abbe error).

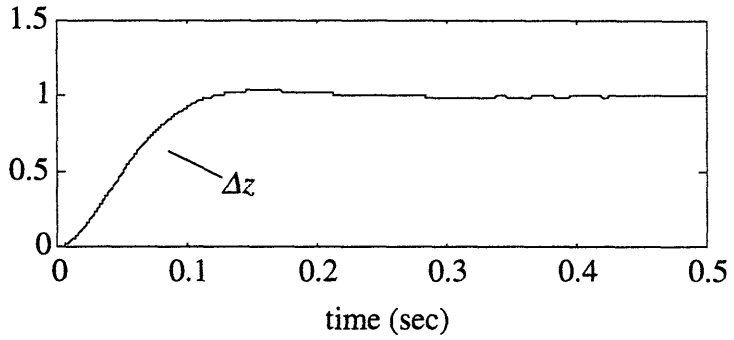

Figure 7-20. Unit step response of the mechanism's translation (z-axis).

Table 7-1
Step Response Characteristics of the Nailing Mechanism

Axis	5% rise time (sec)	max. overshooot (%)	2% settling time (sec)
arm rotation	.11	1.1	.17
nailer rotation	.10	8.3	.12
translation	.10	3.7	.21

7.4.1 Simulated End-Cap Attachment. To predict how the nailing mechanism will actually perform during operation, the sensible approach is to simulate the attachment of an end cap. We accomplish this simulation by giving the nonlinear system model a series of impulses and position commands at appropriate points in time.

Because the firing of a nail occurs over such a short period, this event can be modeled as an impulse input. Appendix I explains the implementation, which is very simple but not intuitive. Changes in reference position are given to the mechanism in the form of ramp

commands. The controlling software supplies a sequence of reference positions produced by interpolating between the initial position and the new target position.

Ultimately, settling time at each position determines the success of the nailing operation. The angled-end panels move toward the mechanism at a constant speed, and if the mechanism does not reach each position on time, the nails will not be driven in the proper place.

The time constraints enforced by these panels depend on the roof pitch. As it decreases, the panel ends become less sharp, leaving less distance between consecutive nail destinations. Therefore, the simulation is run for the panel end with the smallest roof pitch angle, 30°. We also assume that the end faces downward—a scenario that creates slightly tighter constraints than its counterpart.

If the panel is moving at 3.0 inches per second, the mechanism has 0.64 seconds to reach the next nail location after driving the first nail in the same rib. After driving the second nail, the mechanism then has 5.06 seconds to reach the first nail position in the next rib. This process is repeated until all the nails for the end cap have been driven. Figure 7-21 displays the profile of the arm position during one cycle, and Figure 7-22 depicts the corresponding angular position profile of the nailer. In Figure 7-21, the constant-position region denotes the period in which the mechanism translates to the next rib. The arm is not commanded to move again until the mechanism has settled at this new position, at about t=3 seconds.

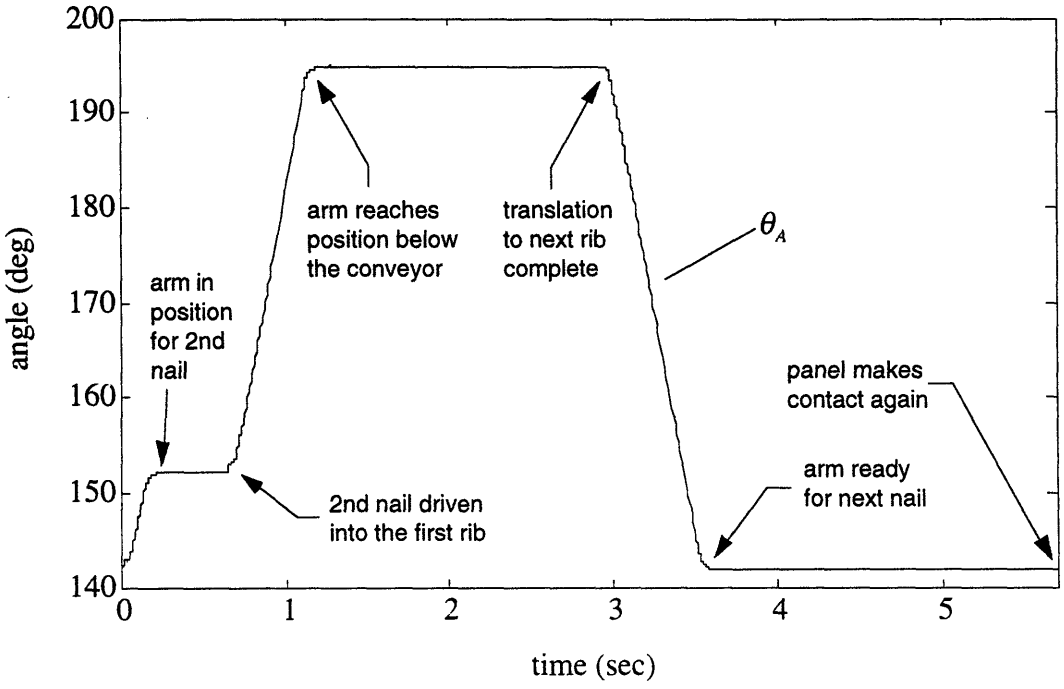

Figure 7-21. Arm position profile during one cycle of the end-cap attachment process.

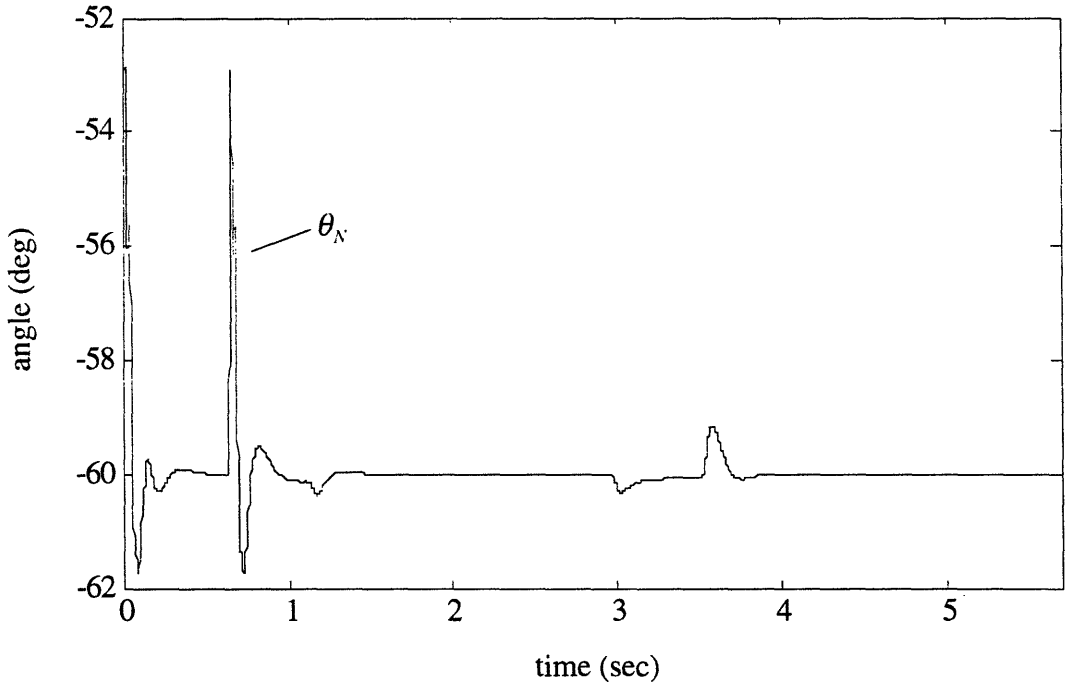

Figure 7-22. Nailer position profile during one cycle of the end-cap attachment process. Discharge of the nailer causes it to deflect about 7°.

The profiles show that theoretically all the actively controlled axes settle at each of their destinations before the next event occurs. In this run, the most critical move occurs between the first and the second nail because the mechanism has less than a second to damp the oscillations induced by the recoil. Figure 7-23, a close-up of the arm and nailer position profiles, shows more clearly the mechanism's response during this period.

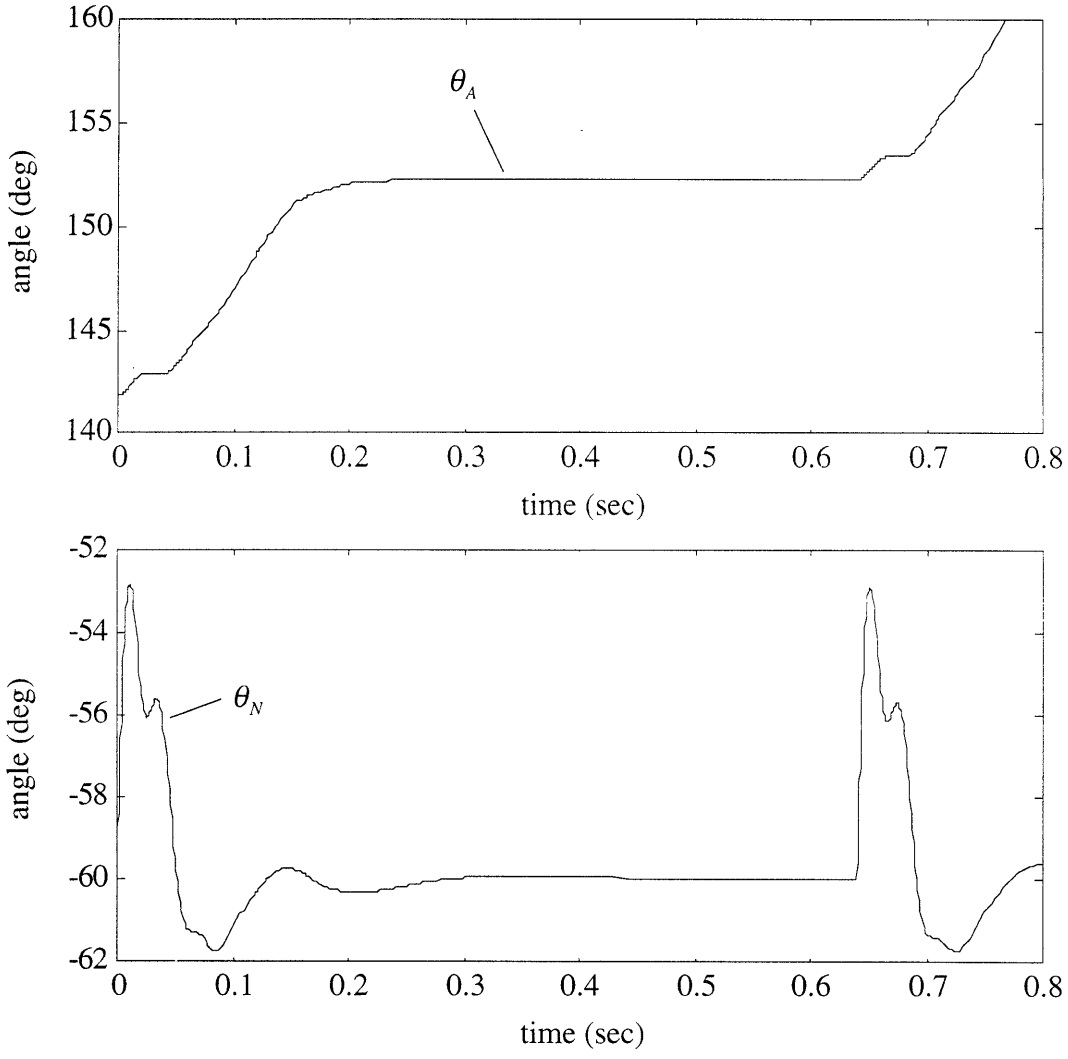

Figure 7-23. Arm and nailer responses to the discharges of the nail gun.

7.4.2 Tuning the Nailer Mount. The shock absorbing mount permits the nailer to rebound along its line of action, and thereby reduces loads on the mechanism. In Chapter 5, we showed how the mount's stiffness could be set to limit the loads on the arm shaft bearings to an acceptable level. However, when the nailer's line of action is directed more towards a right angle with respect to the arm, the recoil creates excessive torsion loads on the arm shaft, up to 500 N-m. This load exceeds what we might expect intuitively, but consider the circumstances:

- large rotational inertia
- high stiffness
- moment arm of nearly two feet
- conservative estimate of recoil as a triangular pulse
- conservative estimate of recoil peak force—maximum capability of nailer

The mount's stiffness must be reduced further to attenuate this torsion. Yet, the mount cannot be tuned to achieve arbitrarily small loads because the nailer must return to its initial position and be at rest before the time of the next event. The motion also should not have any overshoot, which may cause the nailer to bump into the panel before the next nail is supposed to be fired. So, after a process of iteration, we find the right amount of stiffness and damping that limits the loads while providing an acceptable response:

$$k_{mount} = 6.9 \frac{in.}{lb.} \ (1200 \frac{N}{m})$$

$$b_{mount} = 0.57 \ \frac{lb.\cdot sec}{in.} \ \ (100 \ \frac{kg}{sec})$$

Figure 7-24 shows the nailer's axial movement after a nail discharge when the command for the controlled axes is to maintain initial configuration. Figure 7-25 shows the response during the attachment simulation. Also, in both figures, corresponding profiles of torque in the arm shaft appear.

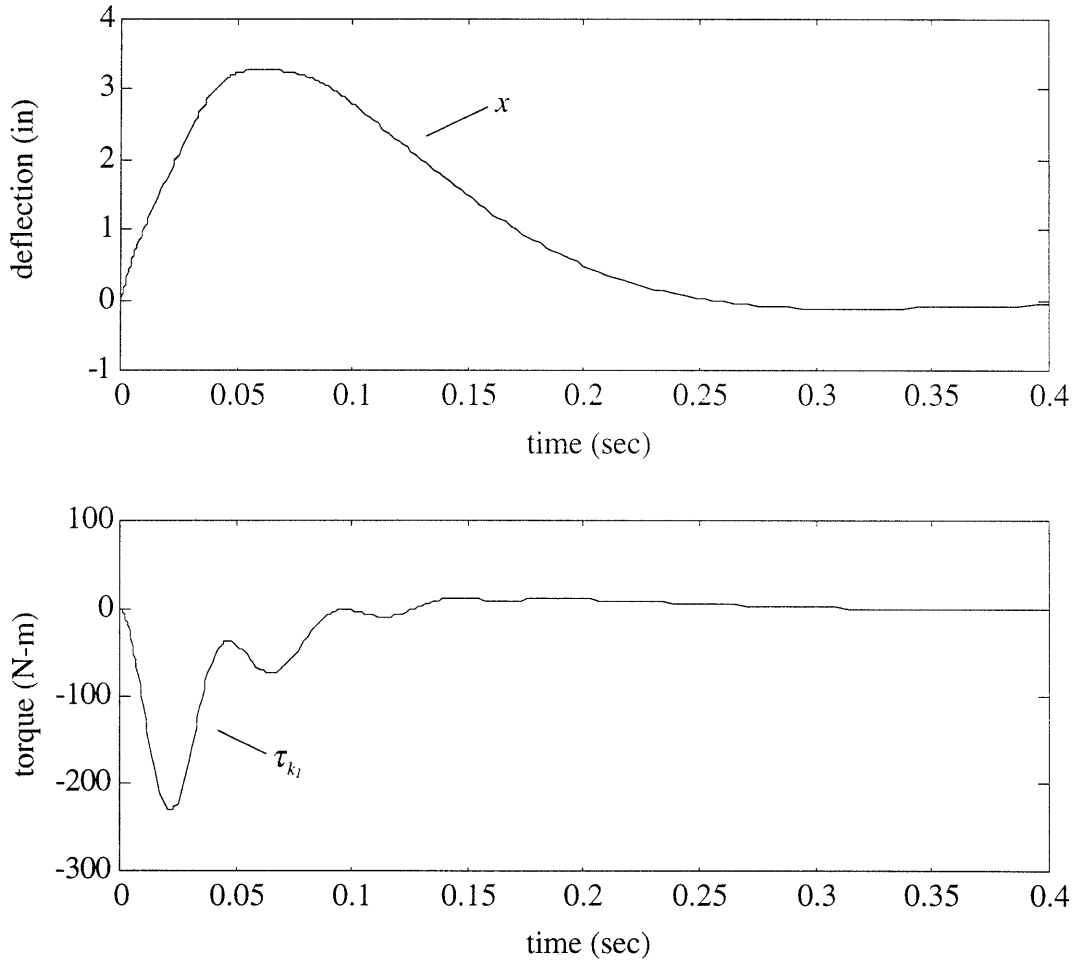

Figure 7-24. Rebound of the nailer and corresponding torque in the arm shaft when a nail is fired (nonlinear simulation). The command for all controlled axes was to hold position.

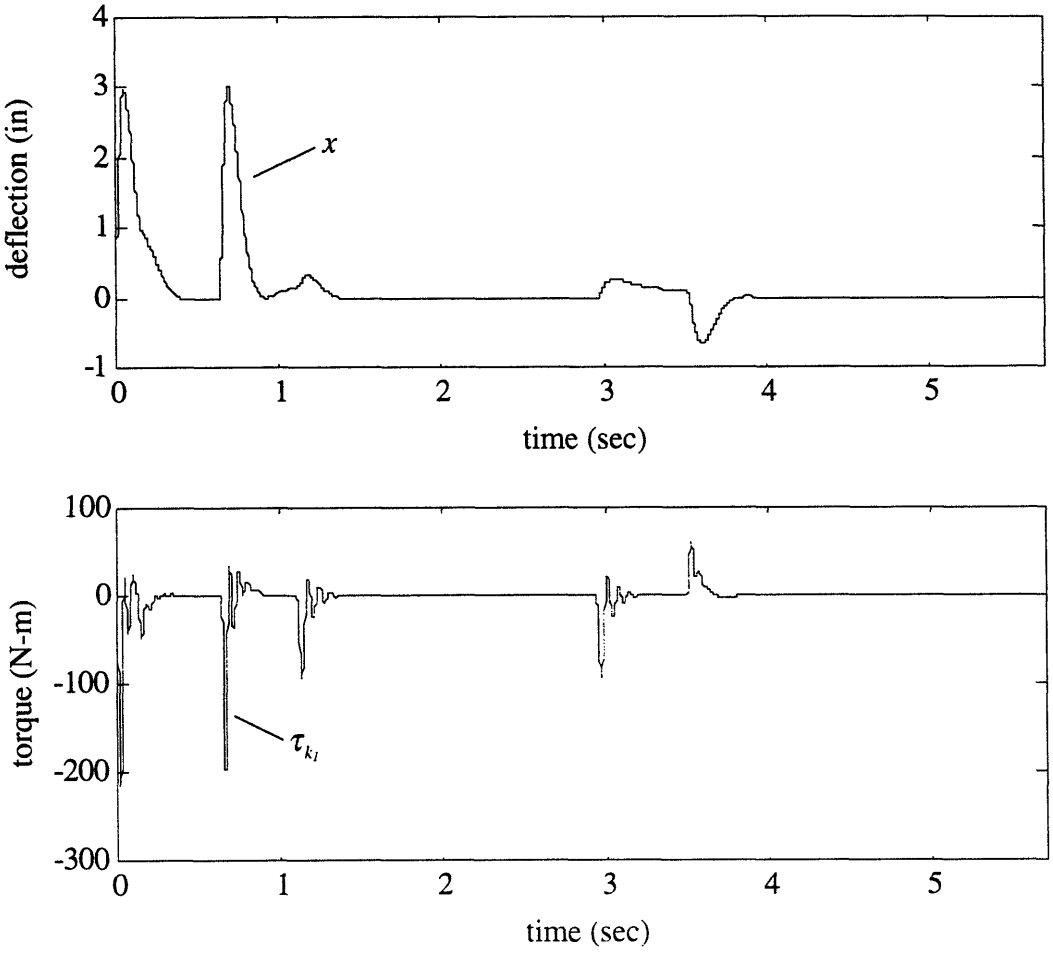

Figure 7-25. Rebound of the nailer and corresponding torque in the arm shaft during an end-cap attachment cycle. The peak arm-shaft torque is lower than it was for the hold-position simulation because the arm does not fight the recoil as much.

7.4.3 Motor Demand. The output-torque profiles of Figures 7-26 and 7-27 reveal the demand on the motors as a function of time. In the nailer motor profile, portions of the plot near the beginning are cut-off outside a certain band that is centered on 0 N-m. (For a closer look, refer to Figure 7-28.) These sections indicate saturation of the motors, which cannot output any more torque.

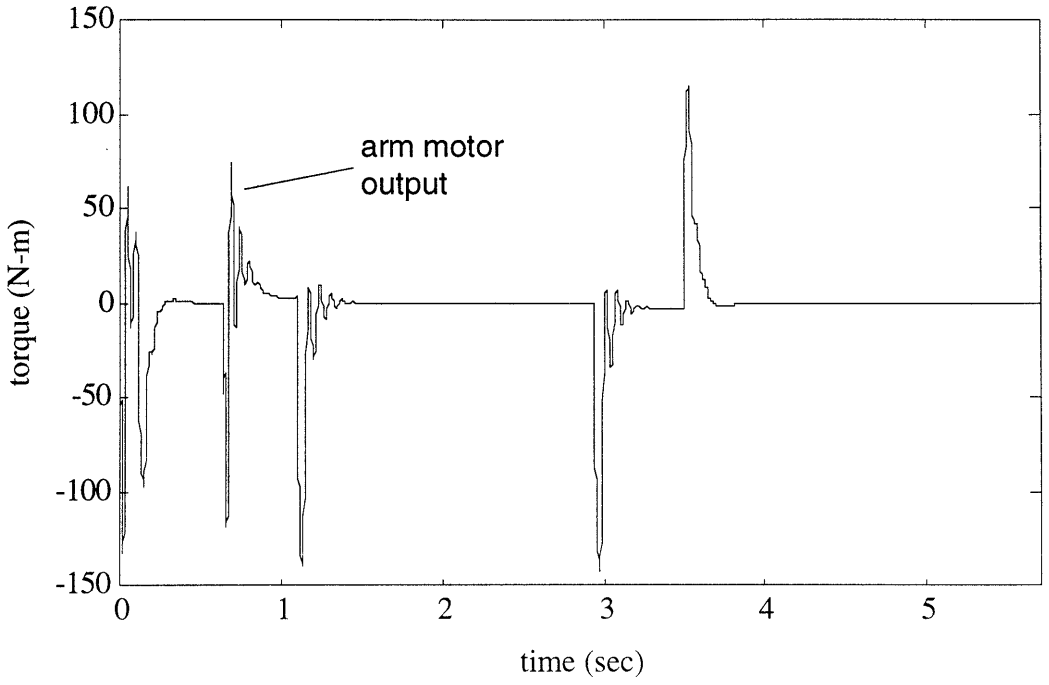

Figure 7-26. Torque demand on the arm motor during the end-cap attachment cycle.

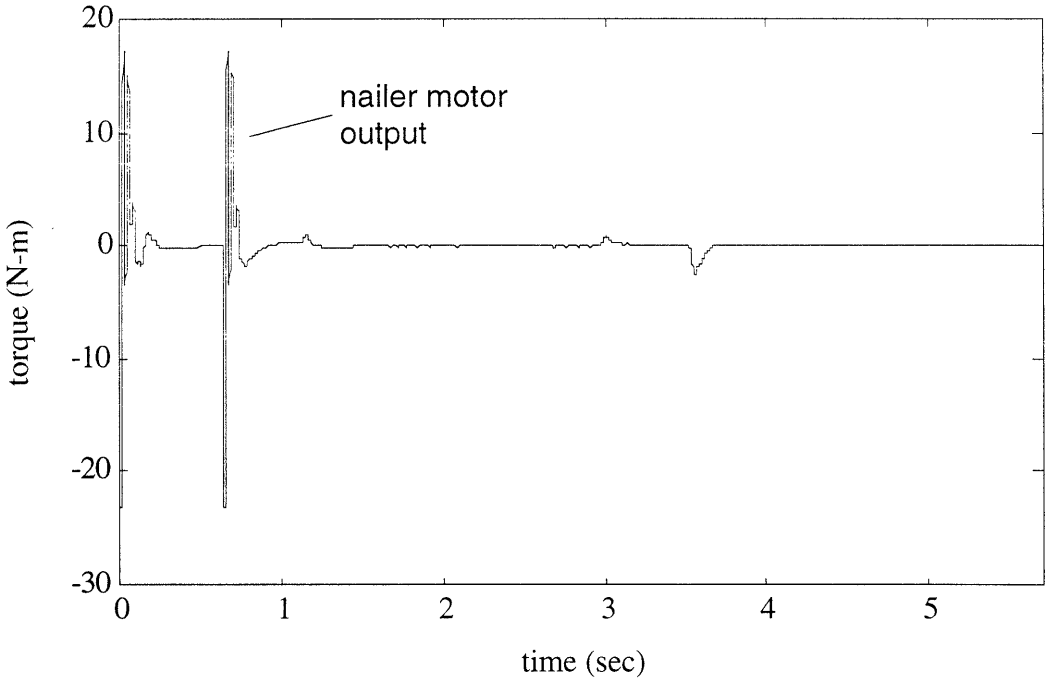

Figure 7-27. Torque demand on the nailer motor during the end-cap attachment cycle.

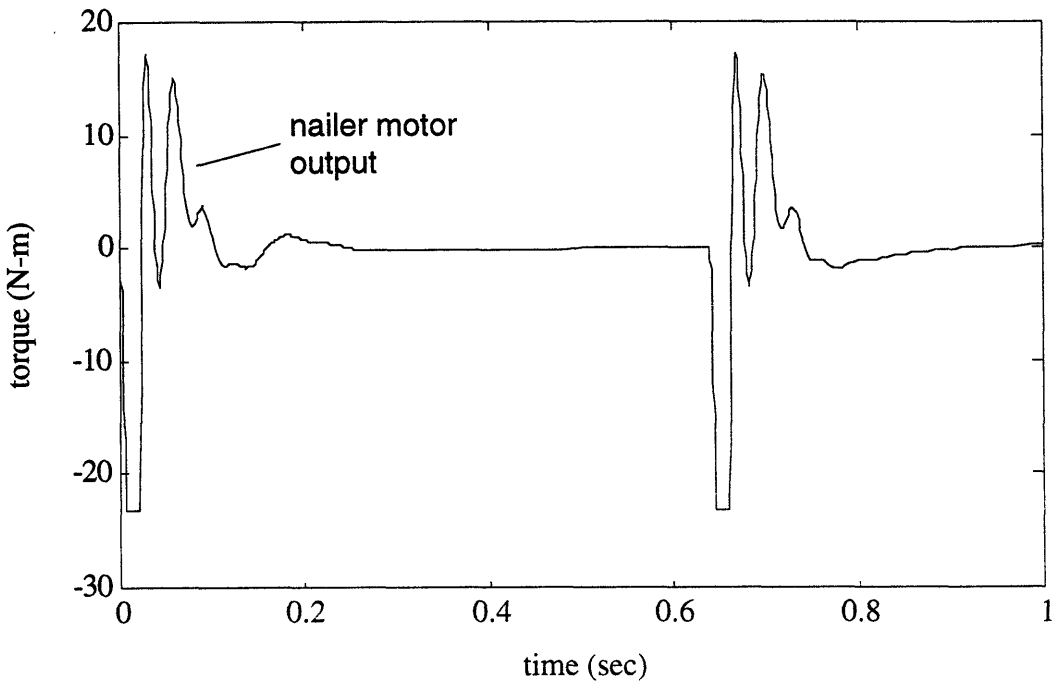

Figure 7-28. Close-up of nailer-motor torque during the firing of nails. The motor reaches its peak output for a very brief moment each time a nail is fired.

Along with peak torque output, motor manufacturers report a lower, continuous torque rating, at which the motor can operate safely on a continuous basis. The motors can only operate above this rating for short periods of time; otherwise, they will overheat. In Figures 7-26 and 7-27, which effectively show the duty cycles of the motors, we see that the motors must output high torques only a small percentage of time while the mechanism is operating. The arm motor exceeds its continuous rating of 77 N-m about 5% of the time. Likewise, the nailer motor exceeds 5.8 N-m about 3% of the time. Furthermore, the nailing mechanism is at rest for more than two minutes after each end-cap attachment procedure.

Chapter 8
Conclusion

Since the Early Industrial Revolution, manufactured housing has been only a dream solution to the problem of inadequate affordable housing. Today, with the increasing demand for energy efficiency and the diminishing supply of old-growth timber, the impetus for developing low-cost, high-quality, engineered housing systems is stronger than ever.

Nearly every house constructed today contains prefabricated components—cabinets, doors, windows, and so on. The inability of many complete housing systems to offer attractive and diverse designs, however, still restrains the success of the factory-built house. Accommodating the variety of tastes of consumers requires novel design of the system and a high degree of flexibility in its manufacture. Nowhere is this requirement more pronounced than for the roof, where complex geometry gives character to the home's outward appearance.

The basis for this thesis is a complete, prefabricated roof system that possesses technical and economic advantages over conventional roofs while promoting individuality. Designers, or even the prospective homeowners, simply present architectural plans (or a sketch) for the roof they want, and a computer converts them into a customized layout of roof panels, which are manufactured directly from the computer-generated information.

8.1 Summary

This thesis described a conceptual layout of an automated fabrication process. The process, which is driven by CAD/CAM software, can produce about 160 12'×4' panels per eight hour shift. That is 7700 square feet of roof per day.

Automated equipment assembles and fastens the OSB components with precision, producing high-quality panels with tolerances much tighter than what is typical in housing construction. This precision ensures snug field assembly, which promotes energy efficiency. In addition, the fabrication process applies a precise amount of insulation to each panel, eliminating thermal defects that are common in conventional roofing.

Using a composite material of low value wood in place of old-growth lumber, the MIT roof system consumes 60% less wood fiber than traditional roofing. The panel production line, in keeping with this sound practice of efficient material usage, minimizes waste of the OSB stock. The process first splices the OSB sheets end to end with a scarf joint and then cuts the components exactly to length, drastically reducing the production of scrap. Although the equipment that end-joints the OSB is expensive, the environmental payoff and the savings in material cost justify its use. Furthermore, the stock supply can be reduced to one standard size—a result that simplifies purchasing, stock inventory, and material handling.

Focusing on a challenging section of the fabrication process, this thesis also presented design and analysis of the end cap station. A design concept for a three-axis mechanical manipulator (with an

extra axis for moving it out of the way) was introduced. In a step-by-step narration, the thesis explained how an operator uses this device to position and to orient an end cap at the end of a panel subassembly, which consists of the ribs and the bottom face. Once the end cap is in place, the panel is conveyed to a three-degree-of-freedom robotic device that drives two nails into each rib. The discussion continued further to the detailed design of this nailing mechanism, which employs a commercial, hand-held nail gun mounted at the end of a servo-controlled arm.

Analysis of the loads on the nailer provided the design and selection criteria for the arm shaft and arm shaft bearings. Specifically, the analysis of radial loads on the arm shaft, based on simple beam models, verified that the bearings would not be overloaded. With the help of dynamic simulation, the peak torsion loads on the shaft during operation were determined to be about 214 N-m (158 ft.-lb.). This estimate became the basis for selecting the size and material of an arm shaft that has a fatigue life of five years.

Implemented on MATLAB, the computer simulation was also used in the design of the control system. For the most critical axis, the arm, we achieved a bandwidth of 15 Hz. The nailer and the translation subsystems have bandwidths of 9 Hz and 5 Hz.

Ultimately, the nonlinear computer model was used to simulate an end cap attachment for the worst-case panel moving at 3.0 in./sec. The simulation showed that the system settles at each specified point on time.

8.2 Recommendations

In submitting a comprehensive, conceptual layout, this thesis laid the foundation for developing the means to mass-produce the roof panels cost-effectively. This report also offered specific design solutions for crucial assembly equipment. Much significant and challenging design work lies ahead, however. Several basic issues remain unresolved as well.

Here, we attempt to supply direction for future work by raising several important issues not previously discussed, as well as recalling some of the details that were left open. Recommendations specific to the end cap station come first, and other points follow.

8.2.1 End Cap Mechanisms Design. Although the nail-gun mount's primary functional parameters were specified, its form design has not yet been explored. Several configurations, using elements such as mechanical springs or air pistons, exist that could satisfy the criteria, but other issues are involved in the design problem as well. First, the mount should be designed to be as generic as possible so that it may work with any nailer model. Perhaps it could be equipped with a standard connector that mates with a custom-fit, but very simple, plate attached to the nailer. The mount should further be designed for quick release and re-attachment; ideally, the pneumatic and electrical connections would be built into the mount such that the nailer could be snapped on in one motion.

The specifics of the nailer tip modification, just as important, have not been crystallized either. The tip must dig into the end cap so that side loads on the mechanism are eliminated, but this action must not damage the end cap or cause the nailer to get stuck. Furthermore, this modified tip precludes the use of the built-in contact trip exactly as it is.

The effective stroke of the contact trip must be shortened so that interaction between the nailer tip and the end cap does not take away the accuracy of the nailer. Modifying the trip in this way, however, makes the nailer more dangerous. Great care must be taken to ensure that the nailer cannot be touched by anyone while it is operating, and that it does not fire when an end cap is not in contact with it. When the mechanism is not nailing an end cap, the air supply should be cut off automatically.

The end cap manipulator, presented as a conceptual a sketch in Chapter 3, plays a critical role in the overall fabrication process, although it may appear almost trivial. According to the analysis presented in Appendix A, end cap attachment is the bottleneck, and the procedure depends on an operator being able to use the manipulator efficiently. The designer also faces confining physical constraints. The manipulator must hold the end caps in many orientations without obstructing the nailing mechanism. Also, the manipulator must position each end cap such that a gap as small as possible is left between the end cap and the bottom face. Otherwise, insulation will leak out of the panel as it is being filled. This requirement is not so easy to meet because of the boundary formed by the tops of the conveyor rollers.

8.2.2 Other Issues. In Chapter 2, we argued for end-jointing as a way to prevent heavy scrap production. With jointing equipment already commercially available, the method appears to be an elegant solution. However, managing the two rib preparation lines will be a challenge because the ribs are cut to different lengths.

The high cost of radio frequency (RF) curing lessens the strength of the solution as well. At the time of this writing, no alternative adhesive is available that will both meet ASTM fire endurance codes (E84 and E119) and cure quickly enough to achieve cycle time goals. Polyurethane reactive hot melt adhesives, which obtain a virtual cross-link in curing, show promise, however. We suspect that the RF curing equipment will not be necessary in the near future.

Finally, production scheduling strongly affects the performance of the fabrication process. The order in which the panels are produced should be optimized for minimum cycle time and scrap production, also taking into account the stacking requirements for shipping and field assembly. The CAD/CAM software used to plan the panel layouts and drive the fabrication process could be enhanced for this purpose.

References

Aragon, J., Engineer at Ark-Seal International, Inc. (Denver: 15 January 1993), phone interview.

Asada, H., and J.-J. E. Slotine, Robot Analysis and Control, (New York: John Wiley & Sons, 1986).

Bender, R., Engineer at Indspec Chemical Corporation (Pittsburgh: 23 February 1993), phone interview.

Cerkanic, L., Engineer at Henkel Adhesives Corp. (CA: 8 April 1993), phone interview.

Crandall S. H., D. C. Karnopp, E. F. Kurtz, and D. C. Pridmore-Brown, Dynamics of Mechanical and Electromechanical Systems (Malabar, FL: Krieger Publishing Company, 1968).

Crowley, J., Research Associate at MIT (Cambridge, MA: 19 November 1992), meeting.

Crowley, J., L. Glicksman, A. Sharon, and L. Morse-Fortier, Proposal for: Innovative Housing Construction Technology, unpublished proposal (Cambridge, MA: Massachusetts Institute of Technology, 1992).

Crowley, J., L. Glicksman, A. Sharon, and L. Morse-Fortier, Proposal for: Innovative Housing Construction Technology, unpublished proposal (Cambridge, MA: Massachusetts Institute of Technology, 1993).

Crowley, J., J. Dentz, L. Gibson, L. Glicksman, L. Morse-Fortier, M. Parent, and T. Tonyan, Innovative Materials and Construction Systems for Energy-Efficient Building Envelopes, unpublished

report (Cambridge, MA: Massachusetts Institute of Technology, 1992).

Farmer, G., Engineer at Foam Enterprises, Inc. (Minneapolis: 8 June 1993), phone interview.

Fish, G. S., editor, The Story of Housing (New York: MacMillan, 1979).

Gervarter, W. B., "Basic Relations for Control of Flexible Vehicles," AIAA Journal (April 1970).

Herbert, G., The Dream of the Factory-Made House: Walter Gropius and Konrad Wachsmann (Cambridge, MA: MIT Press, 1984).

Hogan, N., "Impedance Control: An Approach to Manipulation: Part 1—Theory," ASME Journal of Dynamic Systems, Measurement, and Control, vol. 107 (March 1985).

Karnopp, D. C., D. L. Margolis, and R. C. Rosenberg, System Dynamics: A Unified Approach, 2nd ed. (New York: John Wiley & Sons, 1990).

Knutson, K., Division Sales Manager at Mann-Russell Electronics (Tacoma, WA: 29 July 1991), letter to the MIT Building Technology Group.

Kuo, B. C., Automatic Control Systems, 6th ed. (Englewood Cliffs, NJ: Prentice-Hall, 1991).

Kuta, M., Engineer at Ark-Seal International, Inc. (Denver: 21 May 1993), phone interview.

Marshall, P., Sales Representative at Servo Systems Co. (Montville, NJ: 15 April 1993), phone interview.

Mason, J. B., History of Housing in the U.S. 1930-1980 (Houston: Gulf Publishing Company, 1982).

McCullough, B., Engineer at Georgia-Pacific Corp. (Atlanta: 23 February 1993), phone interview.

Moore, S., Engineer at the Dow Chemical Company (OH: 8 June 1993), phone interview.

Morse-Fortier, L. J., Assistant Professor of Building Technology at MIT (Cambridge, MA: 20 January 1993), meeting.

Park, J. S., and S. W. Kim, "Optimum Speed Reduction Ratio for DC Servo Drive Systems," International Journal of Machine Tools & Manufacture, vol. 29, no. 2 (1989), pp. 207-216 .

"Reactive Hot Melt Adhesives," brochure (Mendota, IL: Black Bros. Co., 1992).

Rowe, P. G., Modernity and Housing (Cambridge, MA: The MIT Press, 1993).

Shahian, B., and M. Hassul, Control System Design Using MATLAB (Englewood Cliffs, NJ: Prentice-Hall, 1993).

Slocum, A. H., Associate Professor of Mechanical Engineering at MIT (Cambridge, MA: 31 January 1994), meeting.

Slocum, A. H., Precision Machine Design (Englewood Cliffs, NJ: Prentice-Hall, 1992).

Somerville Lumber Co. (Somerville, MA: 27 October 1992), phone interview.

Thomson, W. T., Theory of Vibration With Applications, 3rd ed. (Englewood Cliffs, NJ: Prentice-Hall, 1988).

Valley, G., Engineer at Stanley-Bostitch, Inc. (Indianapolis: 1 February 1994), phone interview.

Vick, C., Engineer at the U. S. Forest Products Laboratory (Madison, WI: 23 February 1993), phone interview.

Ward, S. D., Flexible Manufacturing of Ribbed Roofing Panels: Process Layout and Rib Orientation, mechanical engineering M.S. thesis at MIT (Cambridge, MA: Massachusetts Institute of Technology, 1994).

Ward, S. D., Reasearch Assistant at MIT (Cambridge, MA: 5 March 1993), meeting.

Appendix A
Fabrication Process Timing Analysis

Described in Chapter 2, the roof panel fabrication process has a cycle time of about 180 seconds. In other words, when the line is operating continuously, it completes a panel once every period of 180 seconds. This estimate was made by breaking the process down into basic tasks, estimating the time to complete each task, and planning the sequence of the tasks. In the analysis, we assumed that all the panels were rectangular, full width, and twelve feet long.

The fabrication process has inherent divisions that separate sets of operations working in parallel. These divisions force the repetitions of the sets to occur at the same frequency. The time to complete one may be shorter than the time to complete the next, but the process cannot continue until each of these subprocesses has been completed. For instance, at the end of the rib preparation subsystem (Figure 2-10), finished ribs must wait in a buffer for the overhead transport mechanism (OTM), which also takes part in assembly of the panels.

The parallel subprocesses in this line include rib preparation, face and end-cap preparation, OTM operation (which includes rib transport, fastening of the ribs to the bottom face, and attachment of the leading end cap), trailing end-cap attachment, foam block and insulation application, and top-face attachment. To find the overall cycle time, which is defined by the longest of these subprocesses, time estimates in each subprocess are itemized and totalled (except

for the face and end-cap preparation, which we know by inspection is shorter than the rib preparation). As the totals in Table A-1 indicate, the OTM operation requires the most time.

Table A-1
Subprocess Cycle-time Estimates

Subprocess	Individual Cycle Time (sec)
(1) Rib preparation	109
(2) OTM operation	180
(3) Trailing end-cap attachment	126
(4) Foam and insulation	153
(5) Top-face attachment	68

The steps for Subprocesses 3, 4, and 5 appear in Tables A-2, A-3, and A-4. Also, the manual part of end-cap attachment, which is a sub-subprocess of both the OTM operation and the trailing end-cap attachment, is detailed in Table A-5. The task sequences of rib preparation and OTM operation, however, are more complex, having parallel operations within them. We present these sequences in the bar graphs that appear at the end of this appendix. Note that Subprocess 1 is divided into two phases, each one for a pair of ribs. The reason is that the factory has only two rib lines in which to make the four ribs for a full-width panel.

Table A-2
Steps in Trailing End-cap Attachment (Subprocess 3)

Step	t (sec)
Operator manually positions end cap	66
End-cap nailing process	40
Panel conveyed to insulation station (28 ft. at 1.5 ft./sec)	20
Total	126

Table A-3
Steps in Foam and Insulation Application (Subprocess 4)

Step	t (sec)
Foam block deposited	8
Foam block cures	5
Insulation sprayed into the panel	120
Panel conveyed to the top-face attachment station (28 ft.)	20
Total	153

Table A-4
Steps in Top-face Attachment (Subprocess 5)

Step	t (sec)
Glue applied to the ribs	30
Top-face lifter presses top face onto the ribs	3
Top face stapled to the ribs	15
Panel conveyed to end of line (28 ft.)	20
Total	68

Table A-5
Detailed Steps of Manual End-cap Positioning

Step	t (sec)
The Operator (Op) gets an end cap, carries it to the end cap station, and sets it down	15
Pulls the manipulator down from its stowed position	4
Adjusts the end cap holder	6
Picks up the end cap and slides it onto the holder	10
Adjusts the swing of the manipulator	3
Lines up the end of the end cap with a reference edge	5
Turns the suction holders on	2
Moves the end cap up to the panel and locks the swing	7
Adjusts pitch of the end cap	4
Fine-adjusts the end cap along its length	4
Presses the end cap against the ribs	4
Presses a start button	2
Total	66

The graphs for rib preparation and OTM operation each start at time equals zero; this choice makes reading the graphs easier. However, the timelines for the two graphs are not coordinated, so the timing of events in the two subprocesses cannot be compared directly by selecting a single point in time. The purpose of the charts, rather, is to derive individual cycle times.

For the OTM operation, cycle time is simply the time that elapses from the first step to the final step: 180 seconds. The rib-preparation cycle time, however, is less obvious. The time to prepare a set of ribs is longer than the cycle time because the line starts making ribs for the next panel before it has completed the first set. In addition, at time equals zero, we have assumed that OSB strips from the previous cycle are left in the end jointer. To find the cycle time, we must observe when Step 1 of Phase A begins for the next panel. That point, at time equals 109 seconds, marks where the cycle begins to repeat.

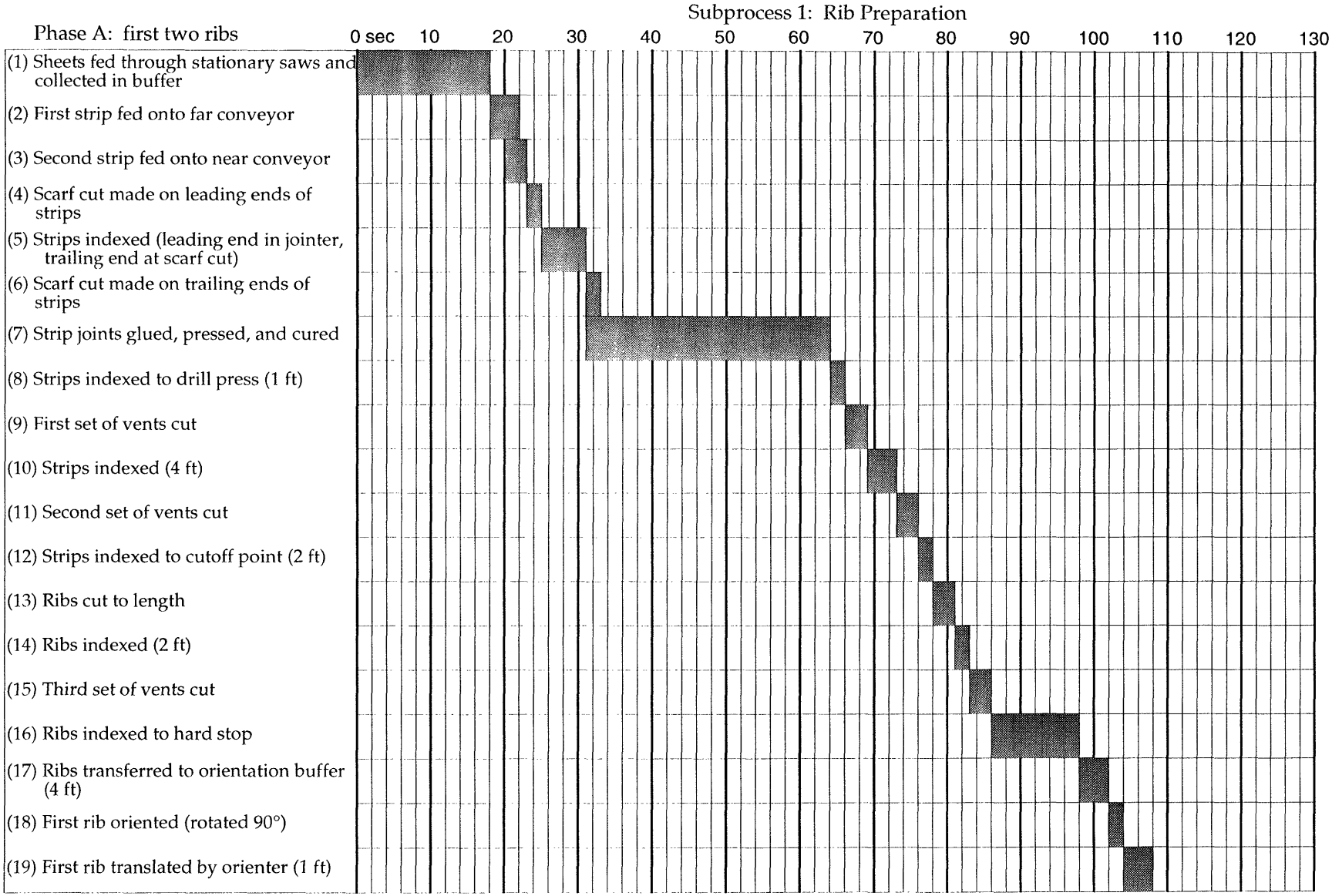
Subprocess 1: Rib Preparation
Phase A: first two ribs
0 sec
10
20
30
40
50
60
70
80
90
100
110
120
130
(1) Sheets fed through stationary saws and collected in buffer
(2) First strip fed onto far conveyor
(3) Second strip fed onto near conveyor
(4) Scarf cut made on leading ends of strips
(5) Strips indexed (leading end in jointer, trailing end at scarf cut)
(6) Scarf cut made on trailing ends of strips
(7) Strip joints glued, pressed, and cured
(8) Strips indexed to drill press (1 ft)
(9) First set of vents cut
(10) Strips indexed (4 ft)
(11) Second set of vents cut
(12) Strips indexed to cutoff point (2 ft)
(13) Ribs cut to length
(14) Ribs indexed (2 ft)
(15) Third set of vents cut
(16) Ribs indexed to hard stop
(17) Ribs transferred to orientation buffer (4 ft)
(18) First rib oriented (rotated 90°)
(19) First rib translated by orienter (1 ft)

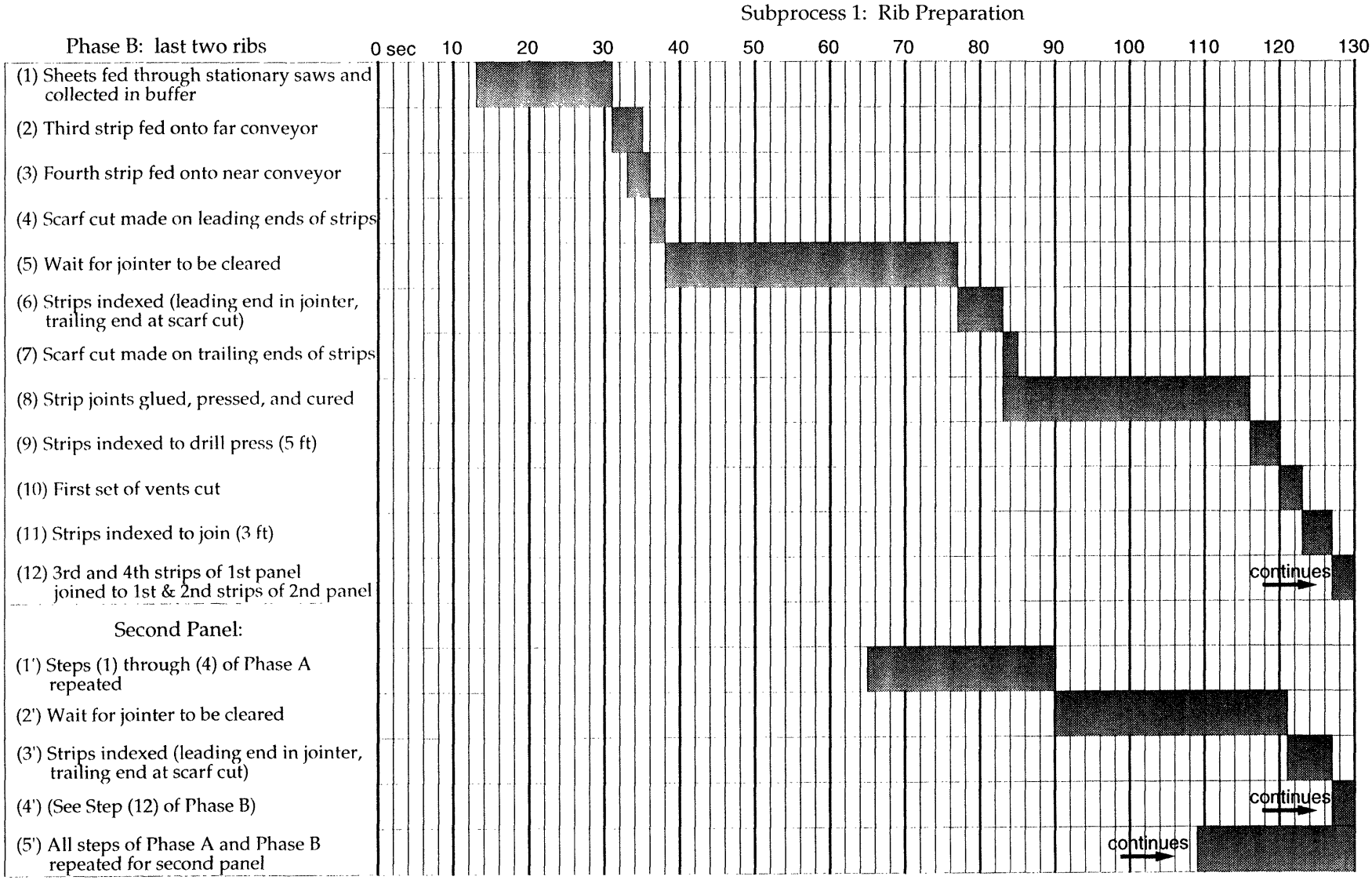
Subprocess 1: Rib Preparation
Phase B: last two ribs
0 sec
10
20
30
40
50
60
70
80
90
100
110
120
130
(1) Sheets fed through stationary saws and collected in buffer
(2) Third strip fed onto far conveyor
(3) Fourth strip fed onto near conveyor
(4) Scarf cut made on leading ends of strips
(5) Wait for jointer to be cleared
(6) Strips indexed (leading end in jointer, trailing end at scarf cut)
(7) Scarf cut made on trailing ends of strips
(8) Strip joints glued, pressed, and cured
(9) Strips indexed to drill press (5 ft)
(10) First set of vents cut
(11) Strips indexed to join (3 ft)
(12) 3rd and 4th strips of 1st panel joined to 1st & 2nd strips of 2nd panel
continues
Second Panel:
(1') Steps (1) through (4) of Phase A repeated
(2') Wait for jointer to be cleared
(3') Strips indexed (leading end in jointer, trailing end at scarf cut)
continues
(4') (See Step (12) of Phase B)
(5') All steps of Phase A and Phase B repeated for second panel
continues

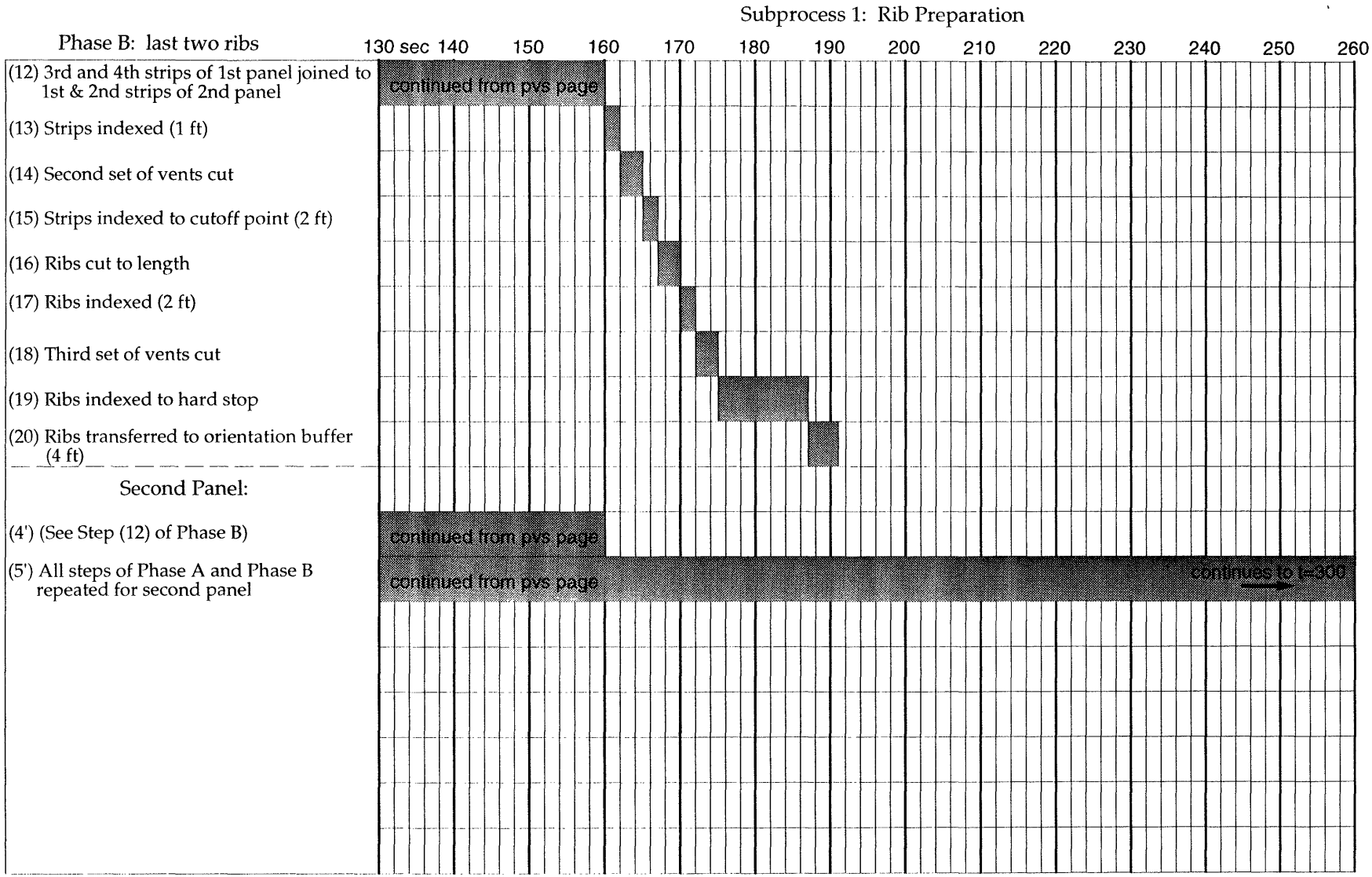
Subprocess 1: Rib Preparation
Phase B: last two ribs
130 sec
140
150
160
170
180
190
200
210
220
230
240
250
260
(12) 3rd and 4th strips of 1st panel joined to 1st & 2nd strips of 2nd panel
continued from pvs page
(13) Strips indexed (1 ft)
(14) Second set of vents cut
(15) Strips indexed to cutoff point (2 ft)
(16) Ribs cut to length
(17) Ribs indexed (2 ft)
(18) Third set of vents cut
(19) Ribs indexed to hard stop
(20) Ribs transferred to orientation buffer (4 ft)
Second Panel:
(4') (See Step (12) of Phase B)
continued from pvs page
(5') All steps of Phase A and Phase B repeated for second panel
continued from pvs page
continues to t=300

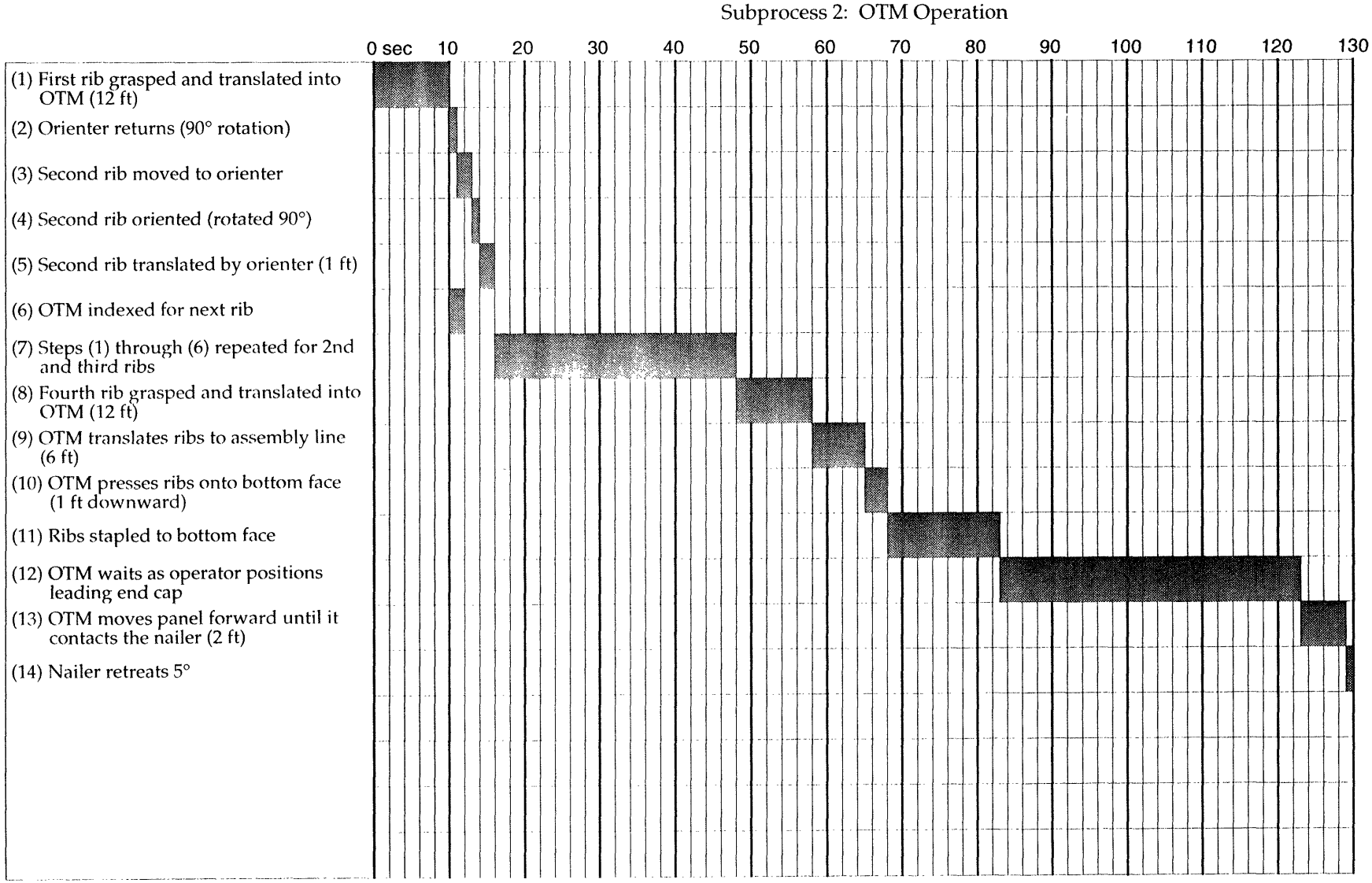
Subprocess 2: OTM Operation
0 sec
10
20
30
40
50
60
70
80
90
100
110
120
130
(1) First rib grasped and translated into OTM (12 ft)
(2) Orienter returns (90° rotation)
(3) Second rib moved to orienter
(4) Second rib oriented (rotated 90°)
(5) Second rib translated by orienter (1 ft)
(6) OTM indexed for next rib
(7) Steps (1) through (6) repeated for 2nd and third ribs
(8) Fourth rib grasped and translated into OTM (12 ft)
(9) OTM translates ribs to assembly line (6 ft)
(10) OTM presses ribs onto bottom face (1 ft downward)
(11) Ribs stapled to bottom face
(12) OTM waits as operator positions leading end cap
(13) OTM moves panel forward until it contacts the nailer (2 ft)
(14) Nailer retreats 5°

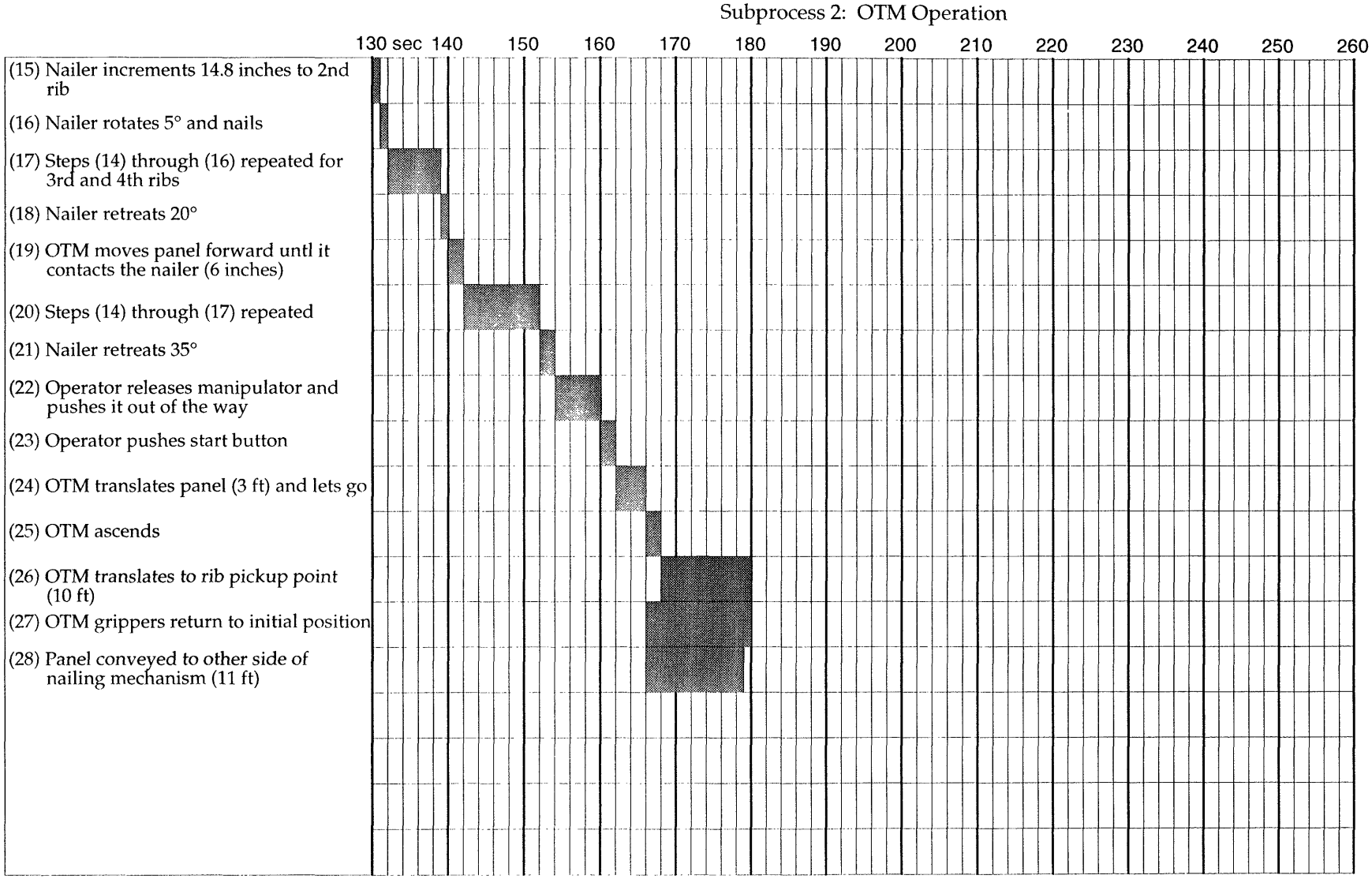
Subprocess 2: OTM Operation
130 sec
140
150
160
170
180
190
200
210
220
230
240
250
260
(15) Nailer increments 14.8 inches to 2nd rib
(16) Nailer rotates 5° and nails
(17) Steps (14) through (16) repeated for 3rd and 4th ribs
(18) Nailer retreats 20°
(19) OTM moves panel forward untl it contacts the nailer (6 inches)
(20) Steps (14) through (17) repeated
(21) Nailer retreats 35°
(22) Operator releases manipulator and pushes it out of the way
(23) Operator pushes start button
(24) OTM translates panel (3 ft) and lets go
(25) OTM ascends
(26) OTM translates to rib pickup point (10 ft)
(27) OTM grippers return to initial position
(28) Panel conveyed to other side of nailing mechanism (11 ft)

Appendix B
Nailing Mechanism Design Drawings

Drawings included:
(1) Nailing mechanism assembly
(2) Nailer mount shaft
(3) Nailer motor block
(4) Nailer motor shaft
(5) Nailer motor plate
(6) Nailer channel
(7) Arm
(8) Arm shaft
(9) Pillow block base
(10) Arm motor shaft
(11) Arm motor block
(12) Arm motor plate
(13) Arm channel
(14) Base plate
(15) Counterweight

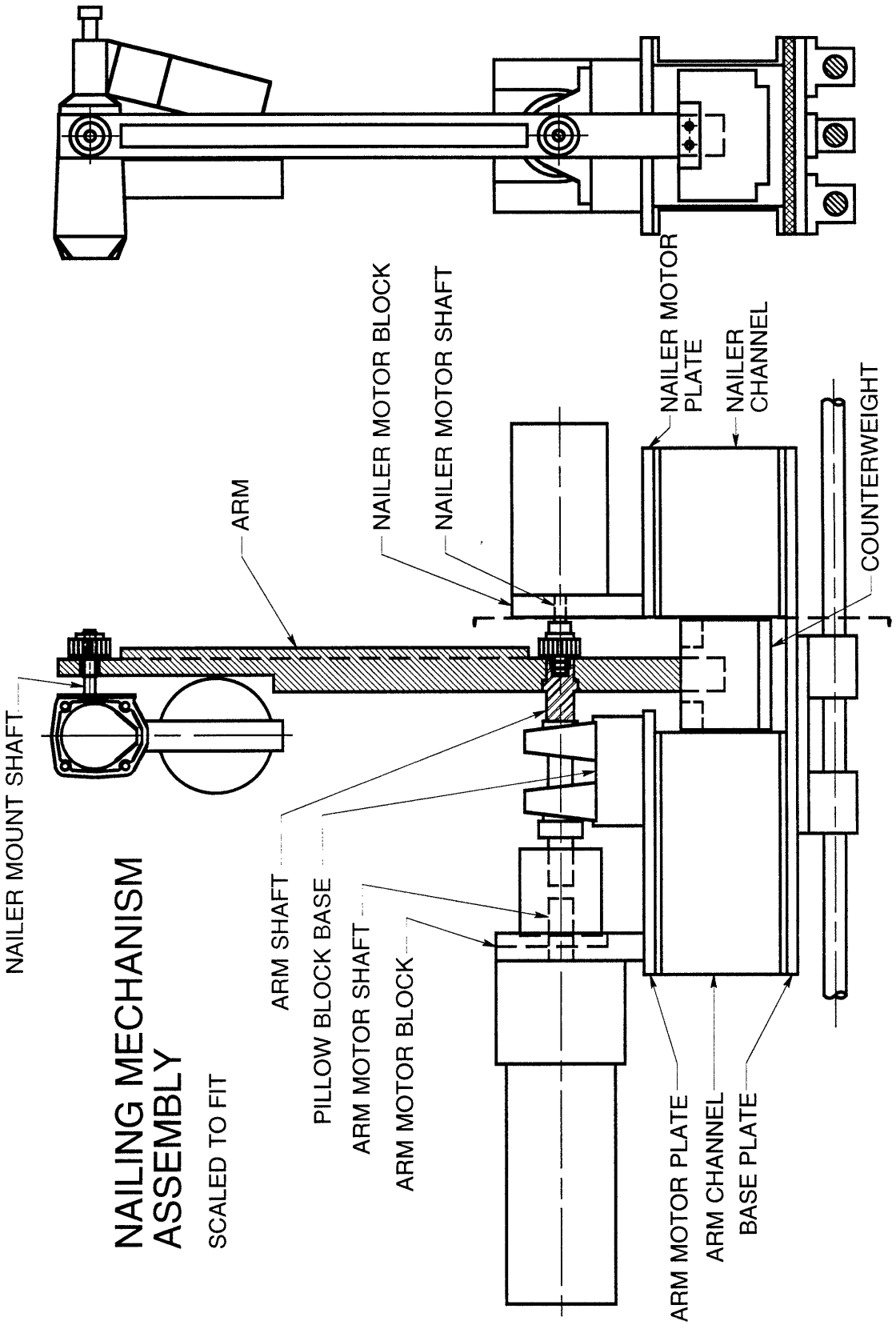
NAILING MECHANISM ASSEMBLY
SCALED TO FIT
NAILER MOUNT SHAFT
ARM
NAILER MOTOR BLOCK
NAILER MOTOR SHAFT
NAILER MOTOR PLATE
NAILER CHANNEL
COUNTERWEIGHT
ARM SHAFT
PILLOW BLOCK BASE
ARM MOTOR SHAFT
ARM MOTOR BLOCK
ARM MOTOR PLATE
ARM CHANNEL
BASE PLATE

NAILER MOUNT SHAFT

MATERIAL: AISI 1050 COLD-DRAWN STEEL

QUANTITY: 1 SCALED TO FIT

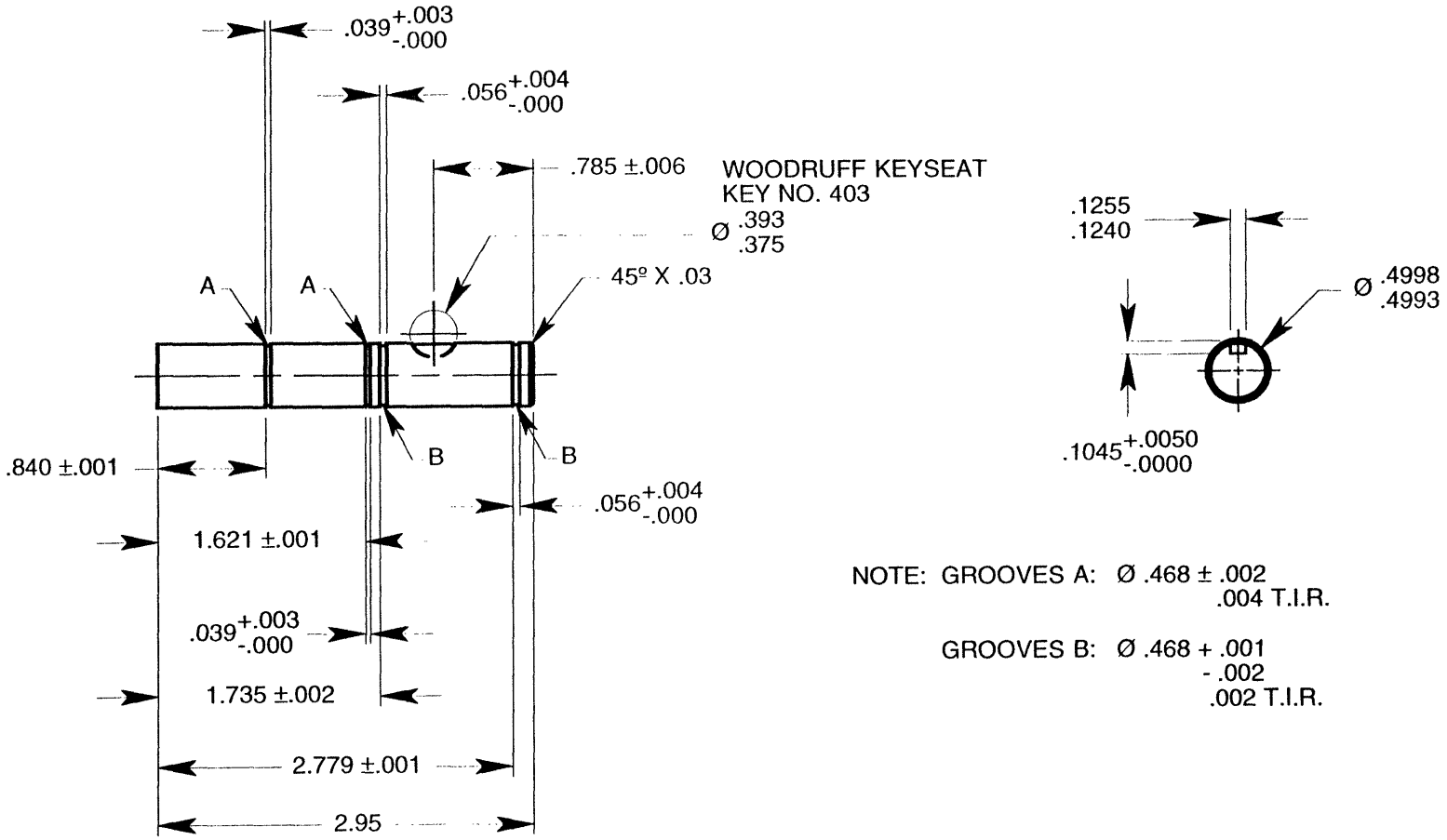

NOTE: GROOVES A: Ø .468 ± .002
.004 T.I.R.

GROOVES B: Ø .468 + .001
- .002
.002 T.I.R.

NAILER MOTOR BLOCK

MATERIAL: LOW CARBON STEEL
QUANTITY: 1 SCALED TO FIT
45° X .03 CHAMFER ON ALL CORNERS

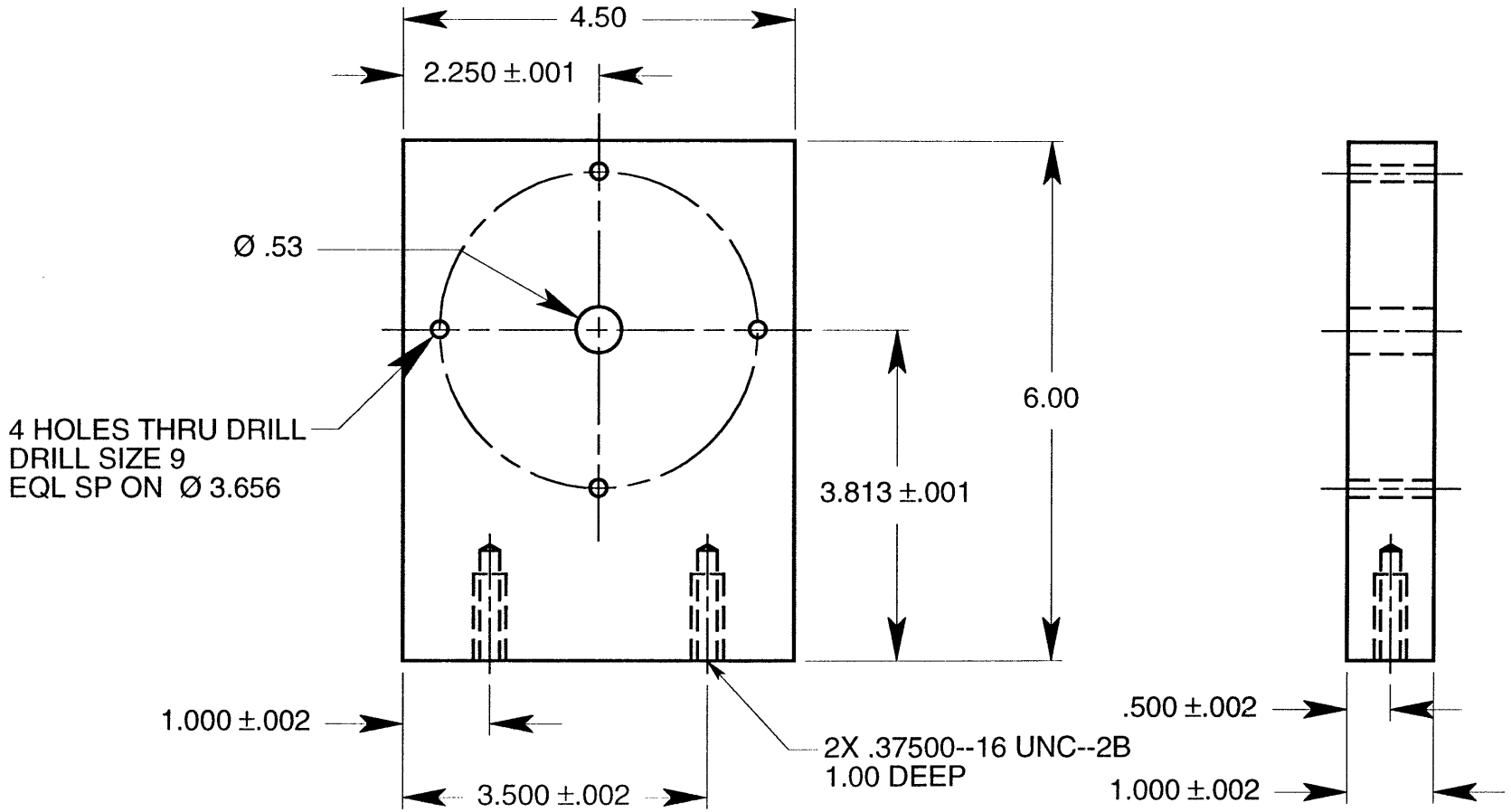

NAILER MOTOR SHAFT

MATERIAL: AISI 1050 COLD-DRAWN STEEL

SCALED TO FIT

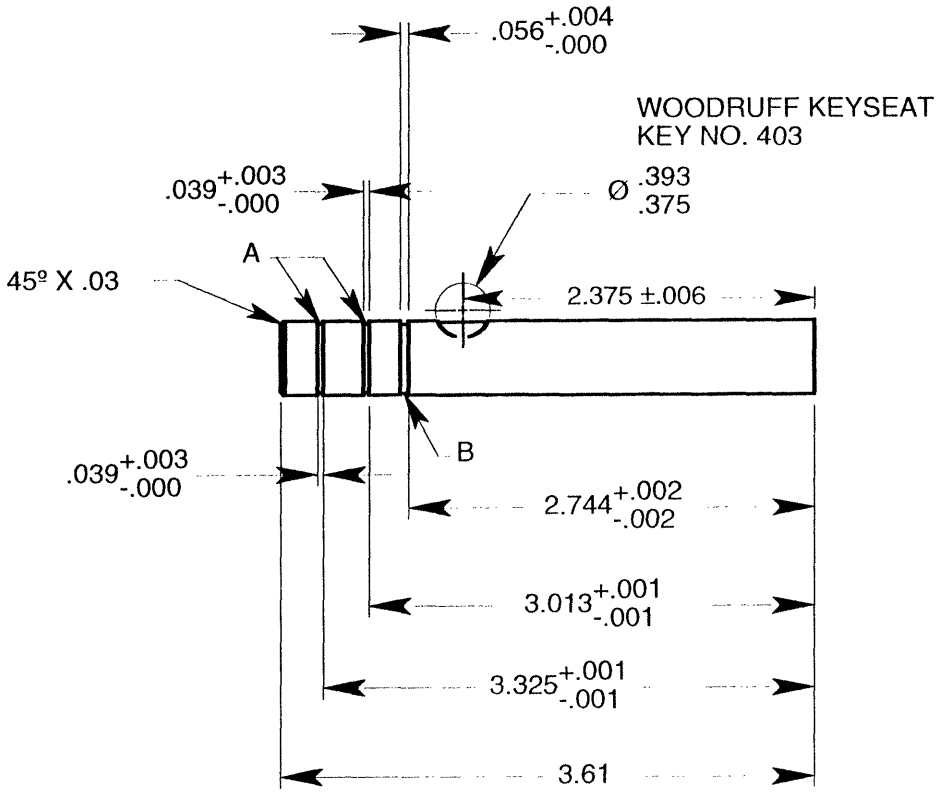

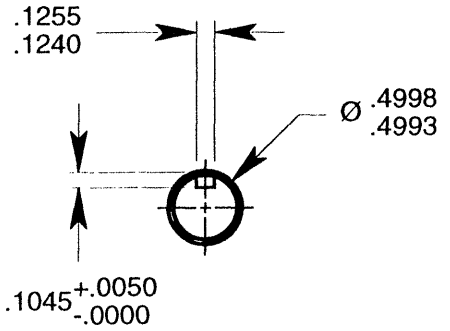

NOTE: GROOVES A: Ø .468 ± .002
.004 T.I.R.

GROOVE B: Ø .468 + .001
- .002
.002 T.I.R.

NAILER MOTOR PLATE

MATERIAL: GENERAL PURPOSE ALUMINUM

QUANTITY: 1 SCALED TO FIT

45° X .03 CHAMFER ON ALL CORNERS

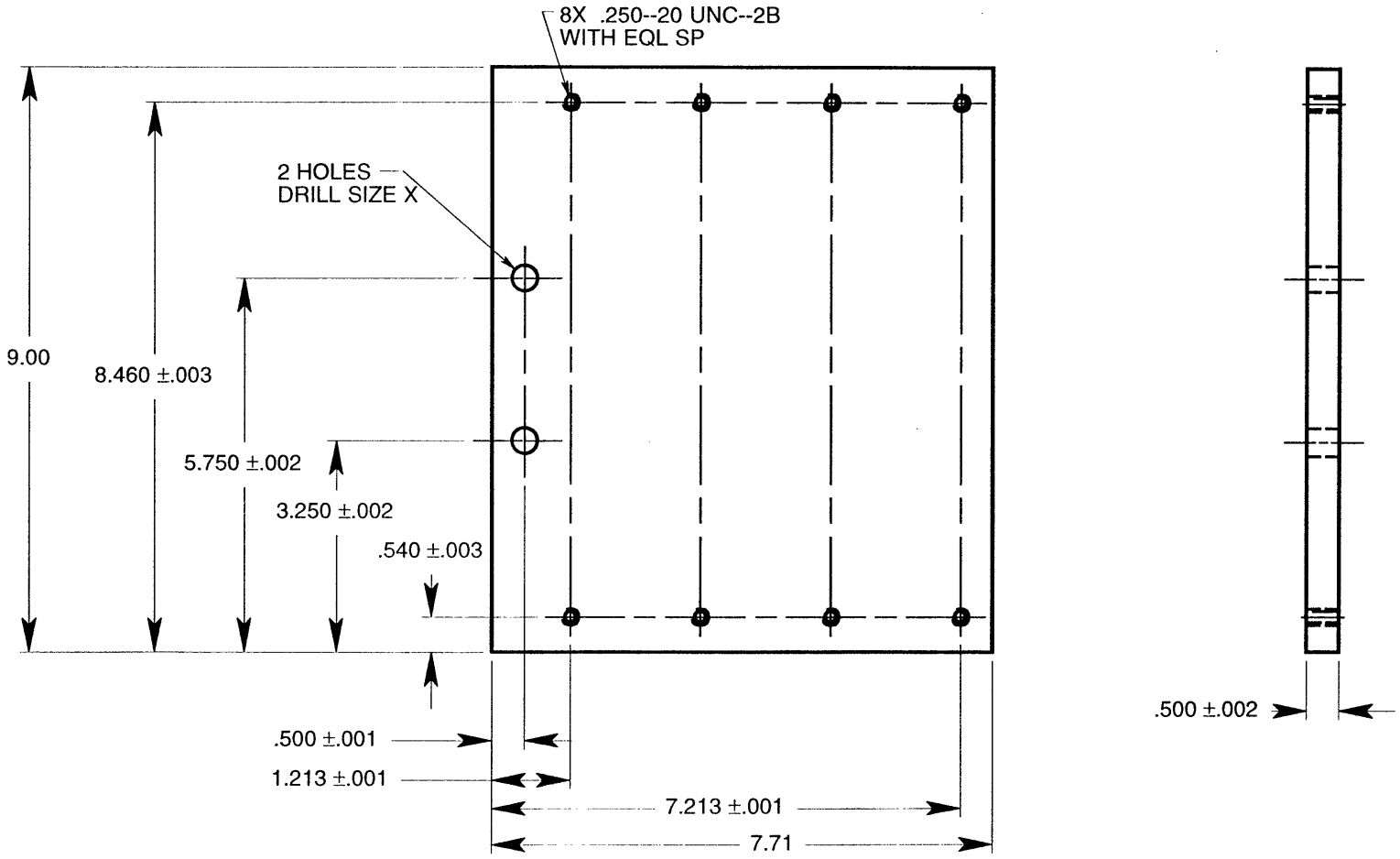

NAILER CHANNEL

MATERIAL: STOCK ALUMINUM CHANNEL 6 X .170
(RYERSON, ALUMINUM ASSOCIATION, 6061-T6)

MILL DEPTH TO SPEC

QUANTITY: 2

SCALED TO FIT

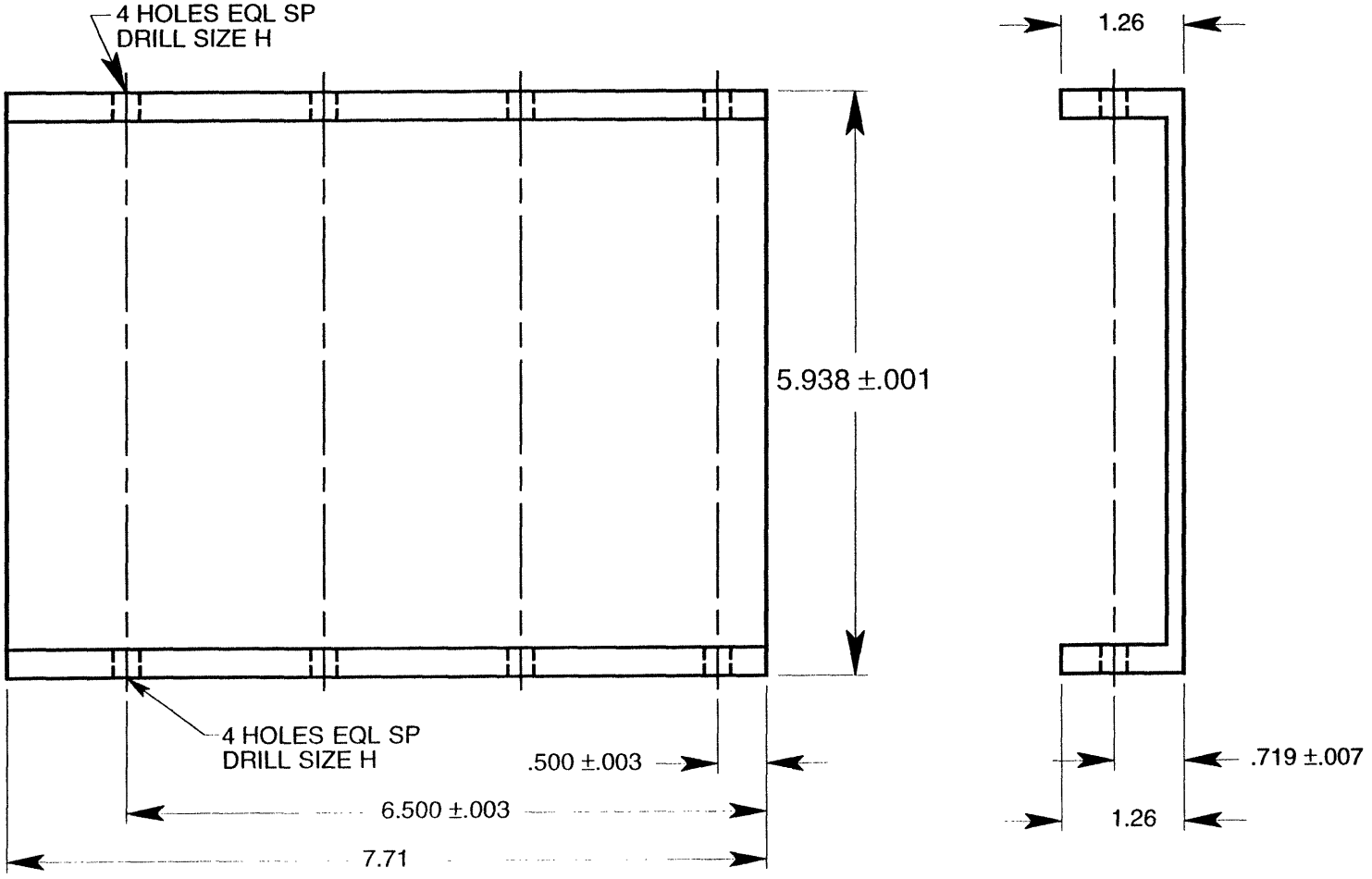

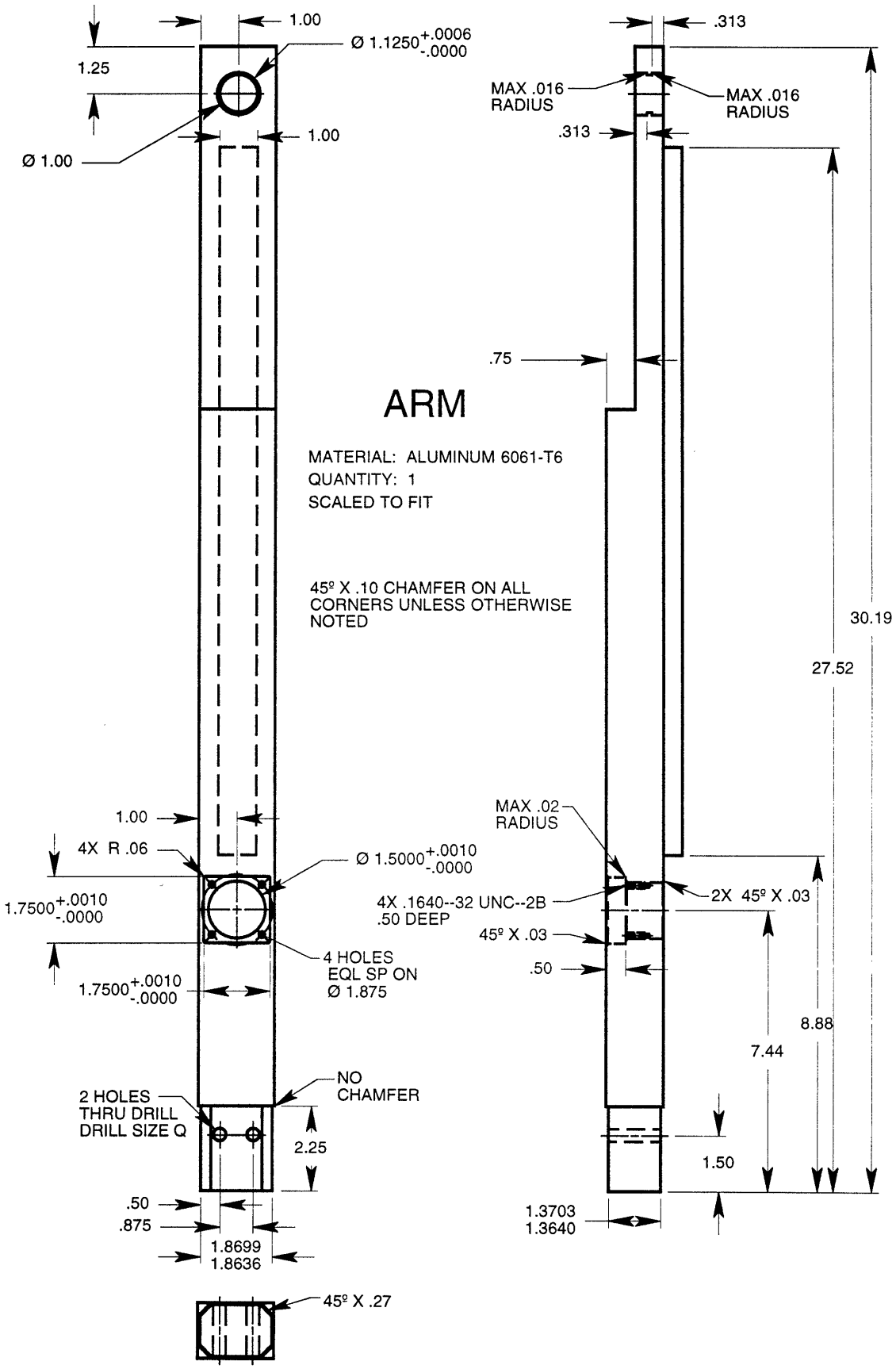
1.00
Ø 1.1250 +.0006 -.0000
1.25
Ø 1.00
1.00
.313
MAX .016 RADIUS
MAX .016 RADIUS
.313
.75
ARM
MATERIAL: ALUMINUM 6061-T6
QUANTITY: 1
SCALED TO FIT
45º X .10 CHAMFER ON ALL CORNERS UNLESS OTHERWISE NOTED
30.19
27.52
1.00
4X R .06
Ø 1.5000 +.0010 -.0000
1.7500 +.0010 -.0000
4 HOLES EQL SP ON Ø 1.875
1.7500 +.0010 -.0000
MAX .02 RADIUS
4X .1640--32 UNC--2B .50 DEEP
2X 45º X .03
45º X .03
.50
8.88
7.44
NO CHAMFER
2 HOLES THRU DRILL DRILL SIZE Q
2.25
1.50
.50
.875
1.8699
1.8636
1.3703
1.3640
45º X .27

ARM SHAFT

MATERIAL: AISI 1050 COLD-DRAWN STEEL
SQUARE STOCK

QUANTITY: 1 SCALED TO FIT

ALL CHAMFERS 45° X .03
UNLESS OTHERWISE NOTED

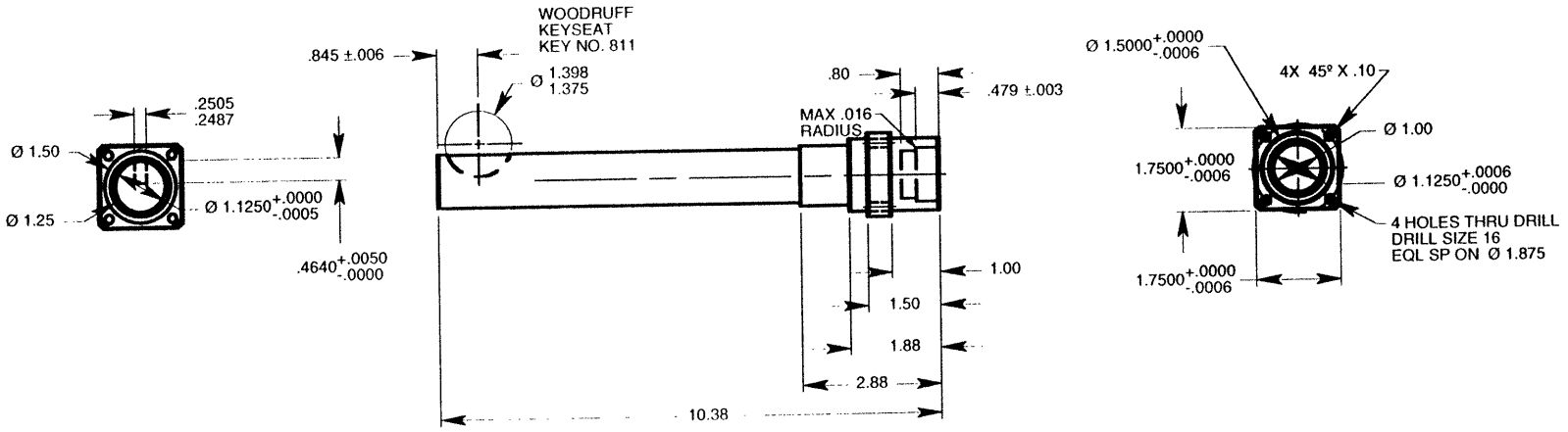

PILLOW BLOCK BASE

MATERIAL: GENERAL PURPOSE ALUMINUM
QUANTITY: 1 SCALED TO FIT
45° X .03 CHAMFER ON ALL CORNERS
UNLESS OTHERWISE NOTED

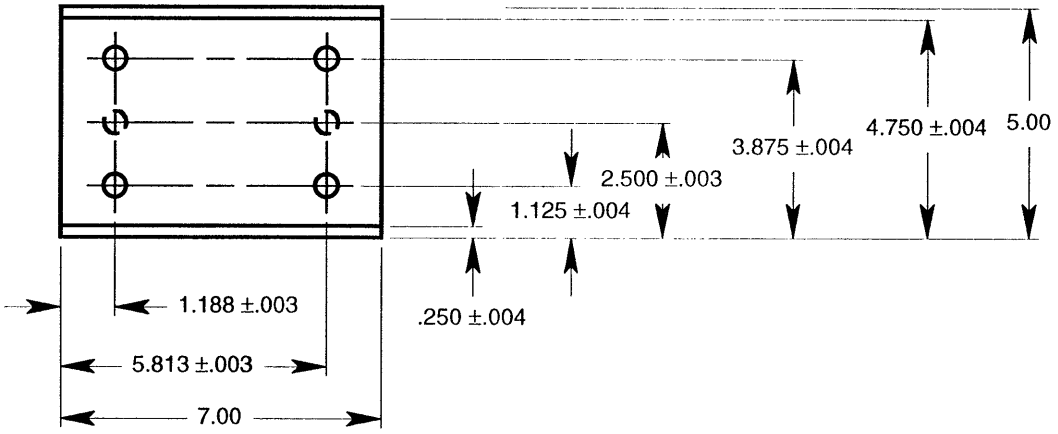

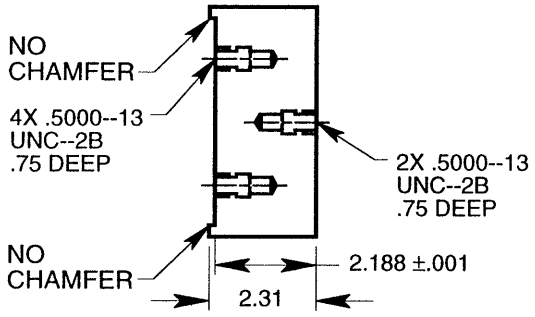

ARM MOTOR SHAFT

MATERIAL: AISI 1050 COLD-DRAWN STEEL

FULL SCALE

WOODRUFF KEYSEAT
KEY NO. 811

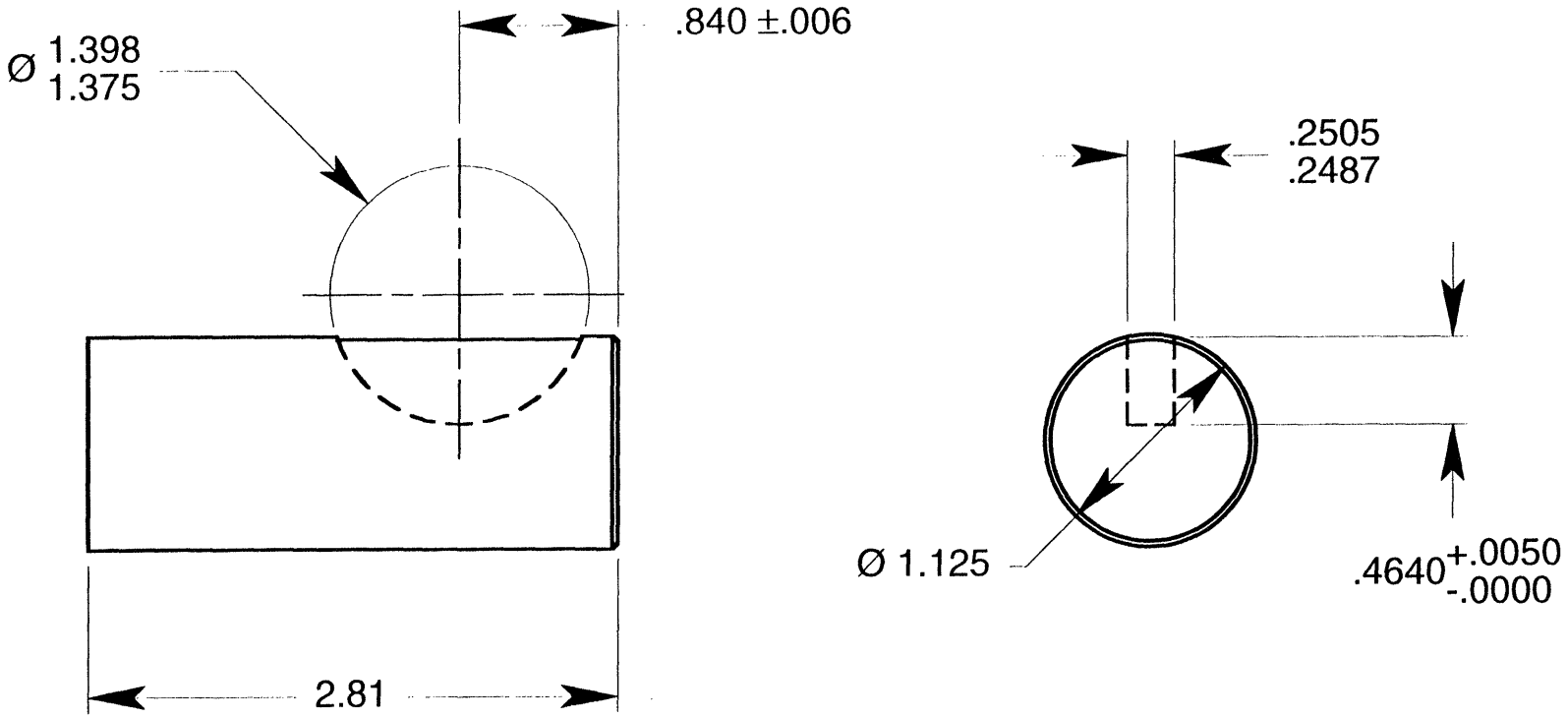

ARM MOTOR BLOCK

MATERIAL: LOW CARBON STEEL
QUANTITY: 1 SCALED TO FIT
45° X .03 CHAMFER ON ALL CORNERS

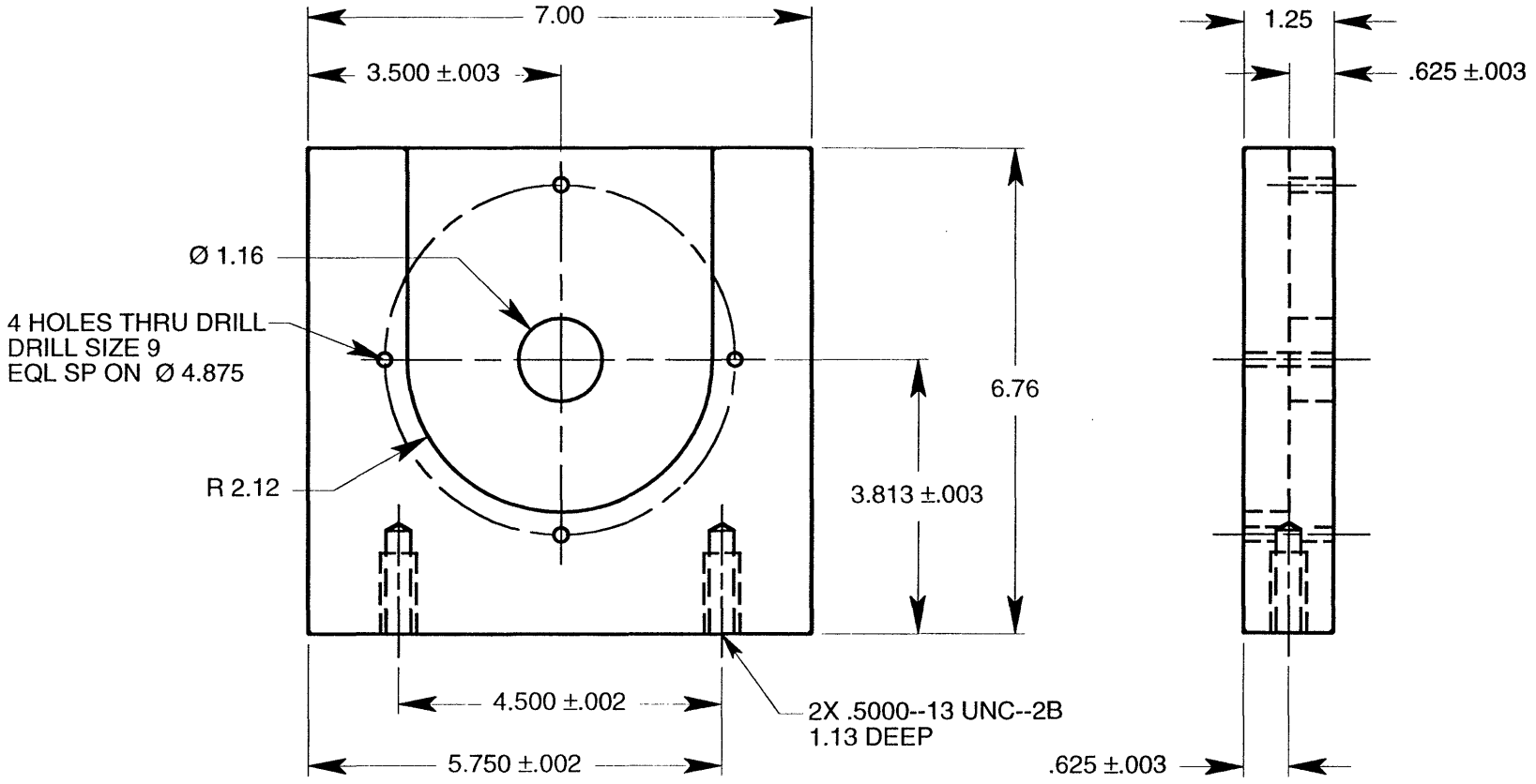

ARM MOTOR PLATE

MATERIAL: GENERAL PURPOSE ALUMINUM

QUANTITY: 1 SCALED TO FIT

45° X .03 CHAMFER ON ALL CORNERS

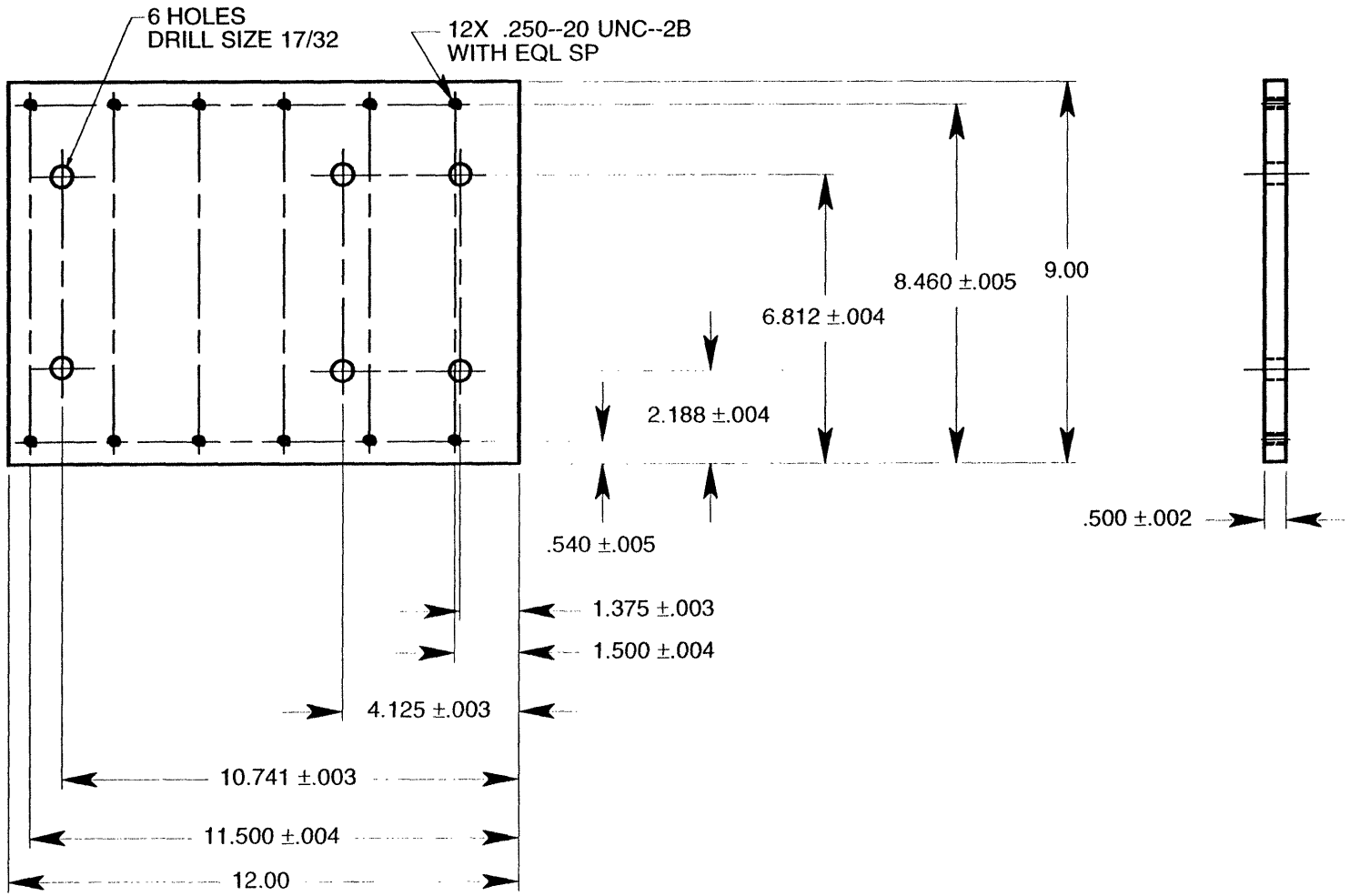

ARM CHANNEL

MATERIAL: STOCK ALUMINUM CHANNEL 6 X .170
(RYERSON, ALUMINUM ASSOCIATION, 6061-T6)
MILL DEPTH TO SPEC
QUANTITY: 2 SCALED TO FIT

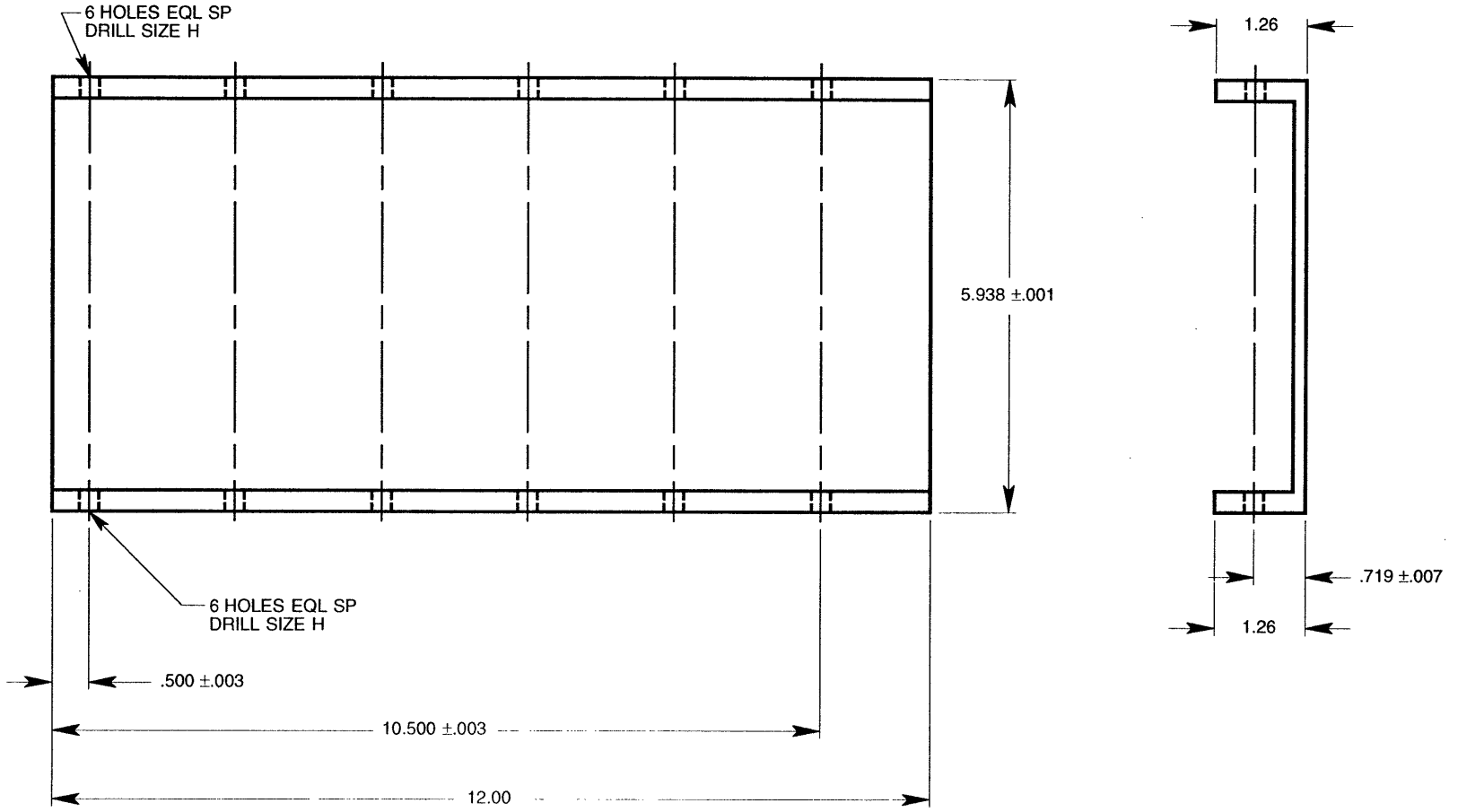

BASE PLATE

MATERIAL: GENERAL PURPOSE ALUMINUM
QUANTITY: 1 SCALED TO FIT
45º X .03 CHAMFER ON ALL CORNERS

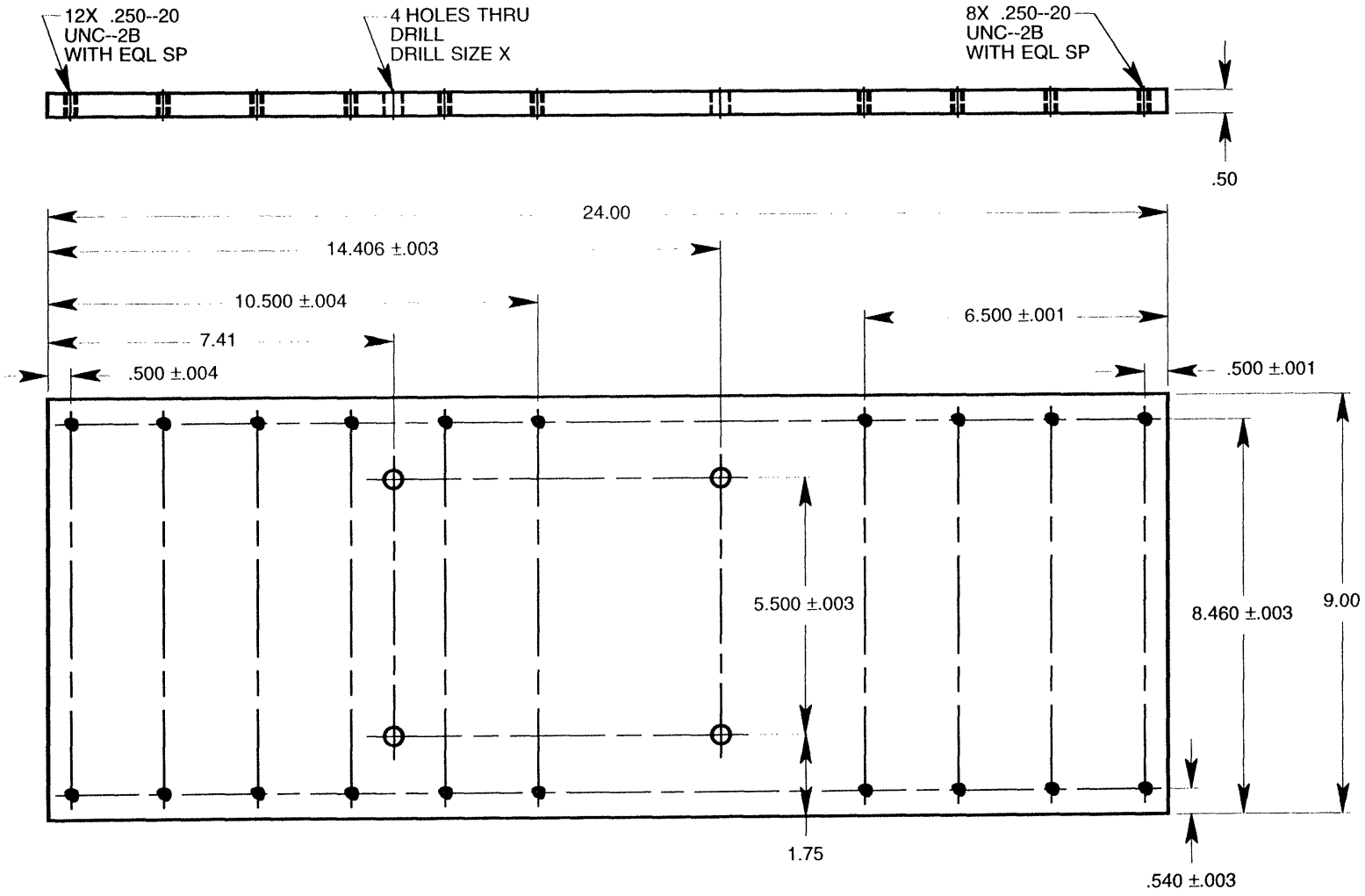

COUNTERWEIGHT

MATERIAL: LOW CARBON STEEL
QUANTITY: 1 SCALED TO FIT
NOTE: ALL RADII .25

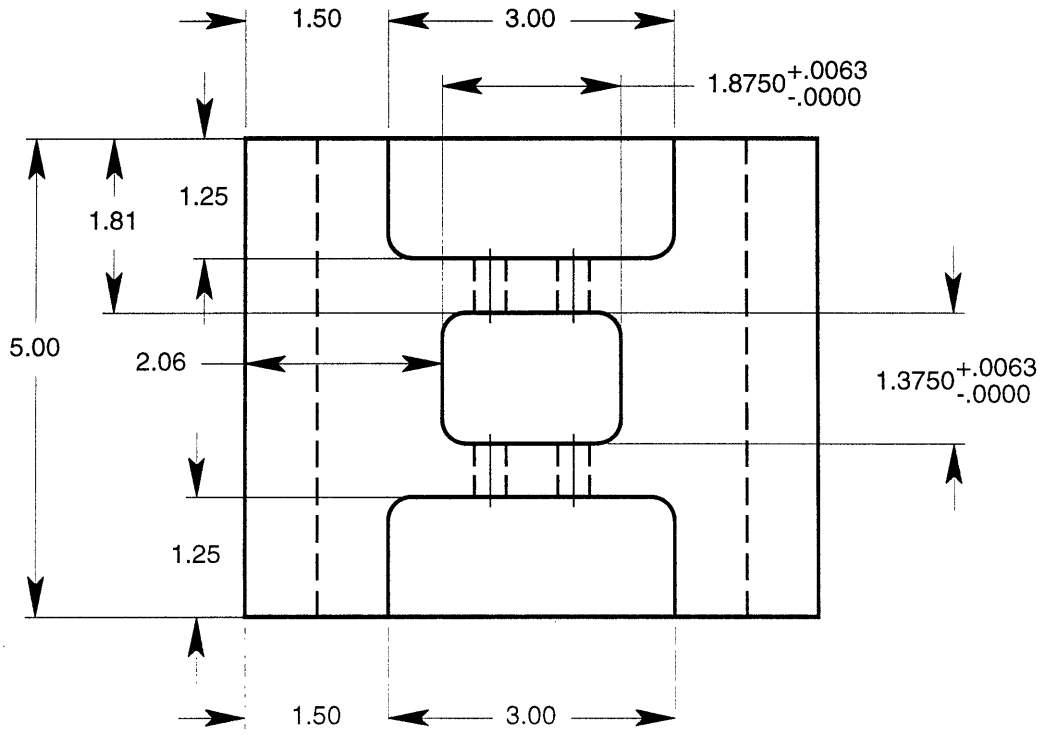

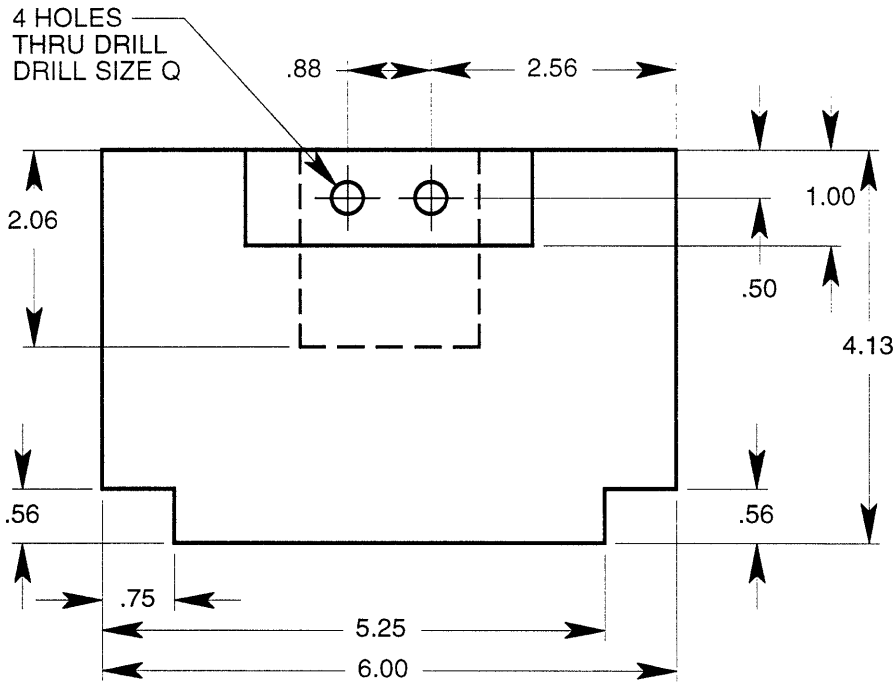

Appendix C
Purchased Parts List

Qty	Description	Vendor	Part number
2	Flex-E-Grip timing pulley	Berg	50TP8-12
1	Flex-E-Grip timing belt (0.75" wide)	Berg	50TB-102
3	Ball bearings (1/2" bore, ABEC-1)	MRC	R-8FF
1	Single flex, composite disc coupling	Zero-Max	6A45
2	Pillow block with SC ball bearings (1 1/8" bore)	Dodge	123808
2	Al C channel (6061-T6, 6 x 0.17, Al Assoc., 25 ft. length)	Ryerson	
1	Linear guide assembly (ball screw, double shaft system)	Thomson	2EB-16-FTB-T
3	External retaining rings (basic, 0.5" bore)	Waldes Truarc	5100-50
3	External retaining rings (heavy duty, 0.5" bore)	Waldes Truarc	5160-50
1	Internal retaining rings (basic, 1.125" housing)	Waldes Truarc	N5000-112
1	DC servo gearmotor w/ encoder, tach, and brake (100:1)	PMI Motion Tech.	JR12M4CH/GH12-100
1	DC servo gearmotor w/ encoder and tach (20:1)	PMI Motion Tech.	U9M4T/GH9-20
1	DC servo motor	PMI Motion Tech.	JR12M4CH
1	Hand-held coil nailer	Stanley-Bostitch	N50C-1
1	Timing belt tensioner	Brecoflex	

Appendix D
Side-to-Side Vibration of the Nailing Mechanism's Arm

Movements of the nailing mechanism and various disturbances will cause the arm to vibrate. Its shortest dimension is its 1.5 inch width, so the vibration direction most likely to cause problems is side to side. This vibration is also the most critical because the mechanism needs accuracy the most along this axis (the z-axis).

At lower frequencies, vibration amplitudes are greater—and vice versa. Thus, to ensure that side-to-side vibration will not be a problem, we must make sure that the arm's fundamental frequency is not too low. We obtain an estimate by modeling the arm and nailer as a massless, cantilever beam with a lumped mass at the end (Figure D-1). Because the arm's mass center would be a distance of $L/2$ away from the base and because moment of inertia is proportional to distance squared, we add a quarter of the actual arm's mass to the lumped mass in our model.

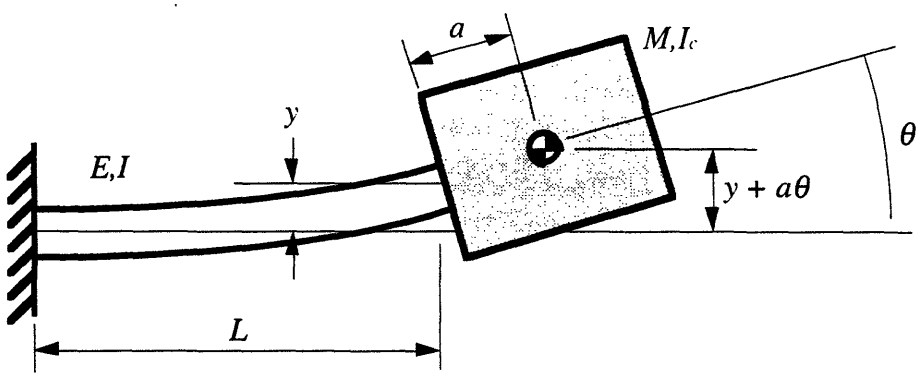

Figure D-1. Cantilever beam vibration model. The model has two degrees of freedom: θ and y [Crandall and others, 1968].

The equations of motion for this system, in which friction has been ignored, are given by the following matrix equation:

$$\underline{\underline{K}}\,\underline{y} = -\underline{\underline{M}}\,\underline{\ddot{y}} \tag{D-1}$$

where $\underline{\underline{K}}$ and $\underline{\underline{M}}$ are the stiffness and mass matrices. For this model, they are

$$\underline{\underline{K}} = \begin{bmatrix} \frac{12EI}{L^3} & \frac{-6EI}{L^2} \\ \frac{-6EI}{L^2} & \frac{4EI}{L} \end{bmatrix} \tag{D-2}$$

and

$$\underline{\underline{M}} = \begin{bmatrix} M & Ma \\ Ma & I_c + Ma^2 \end{bmatrix} \tag{D-3}$$

The vector $\underline{y}$ contains the displacements of the model:

$$\underline{y} = \begin{bmatrix} y \\ \theta \end{bmatrix} \tag{D-4}$$

The solutions to this equation are of the form $A\cos(\omega t)$, so if we substitute this expression for $\underline{y}$ into Equation D-1, we realize that the following equation must be satisfied:

$$det(\underline{\underline{K}} - \omega^2 \underline{\underline{M}}) = 0 \tag{D-5}$$

We then solve this expression for ω^2, the square of the model's natural frequencies.

$$\omega^2 = \frac{4EI}{2MI_cL^3}(3I_c + 3Ma^2 + L^2M + 3LMa) \pm \frac{1}{2MI_c}\sqrt{\frac{16E^2I^2}{L^6}(3I_c + 3Ma^2 + L^2M + 3LMa)^2 - \frac{48MI_cE^2I^2}{L^4}} \quad \text{(D-6)}$$

At last, the fundamental (lowest) frequency is found by substituting the values from Table D-1 into the version of Equation D-6 that has the negative sign. We find that

$$\omega_n \approx 170 \frac{rad}{sec} \ (28\ Hz) \quad \text{(D-7)}$$

Table D-1
Parameter Values for the Arm and Nailer Model

Parameter	Value
L	1.79 ft.
a	0.125 ft.
E	1.44e9 lb./ft.^{2}
I	3.39e-6 ft.^{4}
M	0.248 slug
I_c	0.0211 slug-ft.^{2}

Appendix E
One-Dimensional Stiffness Matrix Derivation

To understand how the stiffness matrix for a system is found, observe the following example. Figure E-1 depicts a one-dimensional mass-spring system. If the system is static, the position and force at each node can be found by solving the matrix equation

$$\underline{f} = \underline{\underline{K}}\,\underline{x} \tag{E-1}$$

where $\underline{f}$ and $\underline{x}$ are vectors composed of the individual forces and displacements. $\underline{\underline{K}}$ is known as the stiffness matrix.

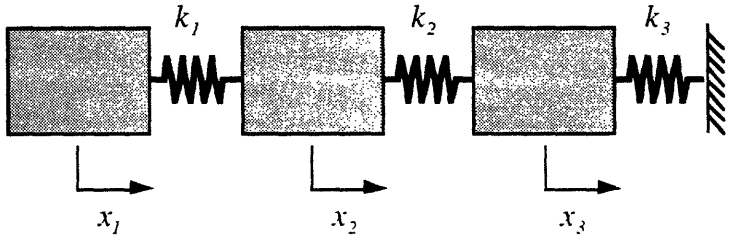

Figure E-1. Model of a mass-spring system with three degrees of freedom.

We can assemble the elements of the stiffness matrix as follows [Thomson, 1988]:

(1) Set the displacement of the first node equal to one while setting all the others equal to zero.

(2) Solve for the external forces that would have to be exerted on the nodes to maintain this configuration.

(3) The ith force on the jth node equals the i,jth element of the stiffness matrix. For example, if we let $x_2 = 1$ and $x_1 = x_3 = 0$, the force at node 1, f_1, is $-k_1$. Likewise, $f_2 = k_1 + k_2$ and $f_3 = -k_2$. Therefore, the second column of the stiffness matrix is

$$\underline{k}_2 = \begin{bmatrix} -k_1 \\ k_1 + k_2 \\ -k_2 \end{bmatrix} \tag{E-2}$$

The complete stiffness matrix for the system is

$$\underline{\underline{K}} = \begin{bmatrix} k_1 & -k_1 & 0 \\ -k_1 & k_1 + k_2 & -k_2 \\ 0 & -k_2 & k_2 + k_3 \end{bmatrix} \tag{E-3}$$

Appendix F
Derivation of the Partial Stiffness Matrices

In Chapter 5, we used $\underline{\underline{K}}_N$ and $\underline{\underline{K}}_P$ to help us estimate the maximum radial loads that the arm shaft bearings would experience as a result of the nail gun discharging and the panel colliding with the nailing mechanism. These matrices describe the stiffness characteristics of the nailing mechanism in two extreme configurations. Here, we show how the matrices are derived from simple models with beam elements by going through the steps for $\underline{\underline{K}}_N$. In the derivation, we assume that the beam elements are connected to one another rigidly, such that the corners always have a 90° vertex, and we assume that the axial displacements of the beams are small compared to the lateral (bending) displacements.

The procedure is an extension of the one illustrated in Appendix BLANK, where one by one, the nodes are given unit displacements. The differences here are that the displacements occur in more than one dimension and that angular displacements are considered in addition to linear displacements. For each displacement, we look at the contortion of the structure that must occur to maintain all the other displacements equal to zero, and then draw free body diagrams of the corners to ensure static equilibrium.

First consider the structure of Figure 5-4, repeated here in Figure F-1. The relevant displacements are the free-end linear deflections of the two horizontal beams (u_1 and u_2) and the angular deflections of both corners(θ_1 and θ_2). To help us with the

derivation, we also pretend that there is a corresponding set of applied forces and moments on the structure. In this case, the equation of static equilibrium is

$$\begin{bmatrix} f_N \\ f_2 \\ M_1 \\ M_2 \end{bmatrix} = \begin{bmatrix} k_{11} & k_{12} & k_{13} & k_{14} \\ k_{21} & k_{22} & k_{23} & k_{24} \\ k_{31} & k_{32} & k_{33} & k_{34} \\ k_{41} & k_{42} & k_{43} & k_{44} \end{bmatrix} \begin{bmatrix} u_1 \\ u_2 \\ \theta_1 \\ \theta_2 \end{bmatrix} \tag{F-1}$$

However, in reality, f_N is the only applied force on the structure, so f_2, M_1 , and M_2 are set equal to zero in the end.

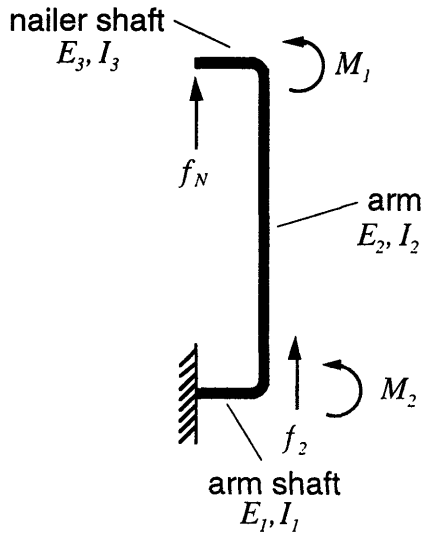

Figure F-1. Beam model of the nailing mechanism with the nailer tip pointing along arm's long axis.

Starting with u_1, we now derive $\underline{\underline{K}}_N$:

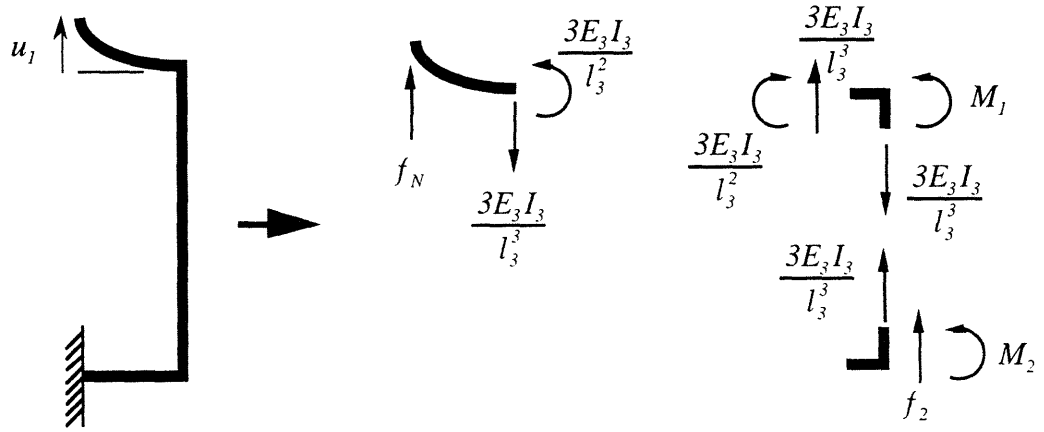

$$f_N = \frac{3E_3I_3}{l_3^3}u_1 \tag{F-2}$$

$$f_2 = \frac{-3E_3I_3}{l_3^3}u_1 \tag{F-3}$$

$$M_1 = \frac{3E_3I_3}{l_3^2}u_1 \tag{F-4}$$

$$M_2 = 0 \cdot u_1 \tag{F-5}$$

u_2:

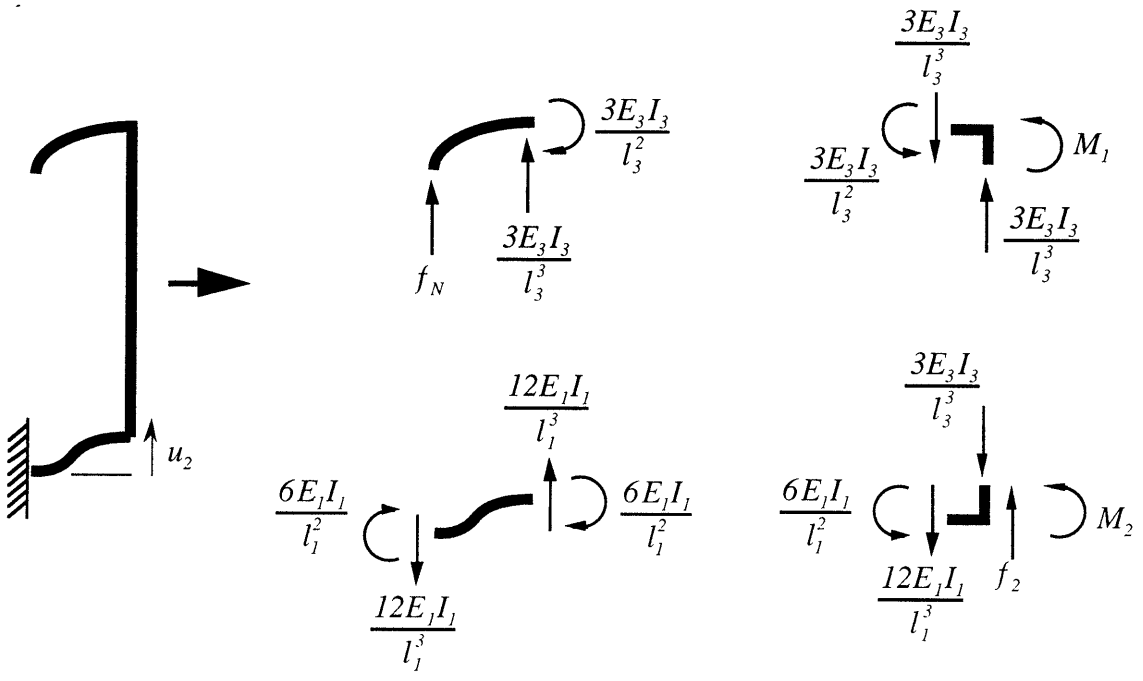

$$f_N = \frac{-3E_3I_3}{l_3^3}u_2 \tag{F-6}$$

$$f_2 = \frac{3E_3I_3}{l_3^3} + \frac{12E_1I_1}{l_1^3}u_2 \tag{F-7}$$

$$M_1 = \frac{-3E_3I_3}{l_3^2}u_2 \tag{F-8}$$

$$M_2 = \frac{-6E_1I_1}{l_1^2}u_2 \tag{F-9}$$

θ_1:

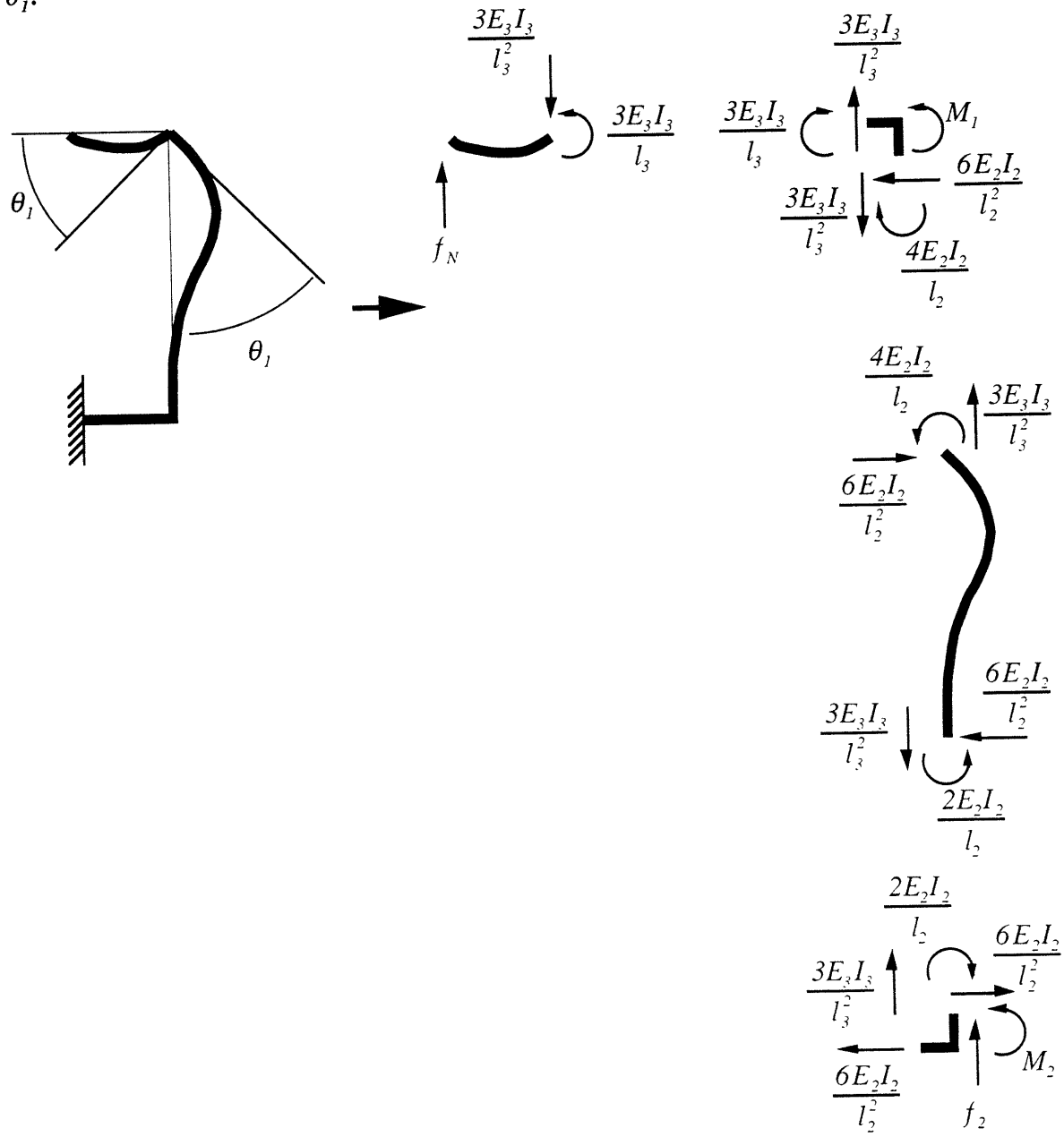

$$f_N = \frac{3E_3I_3}{l_3^2}\theta_1 \qquad \text{(F-10)}$$

$$f_2 = \frac{-3E_3I_3}{l_3^2}\theta_1 \qquad \text{(F-11)}$$

$$M_1 = (\frac{3E_3I_3}{l_3} + \frac{4E_2I_2}{l_2})\theta_1 \qquad \text{(F-12)}$$

$$M_2 = \frac{2E_2I_2}{l_2}\theta_1 \qquad \text{(F-13)}$$

θ_2:

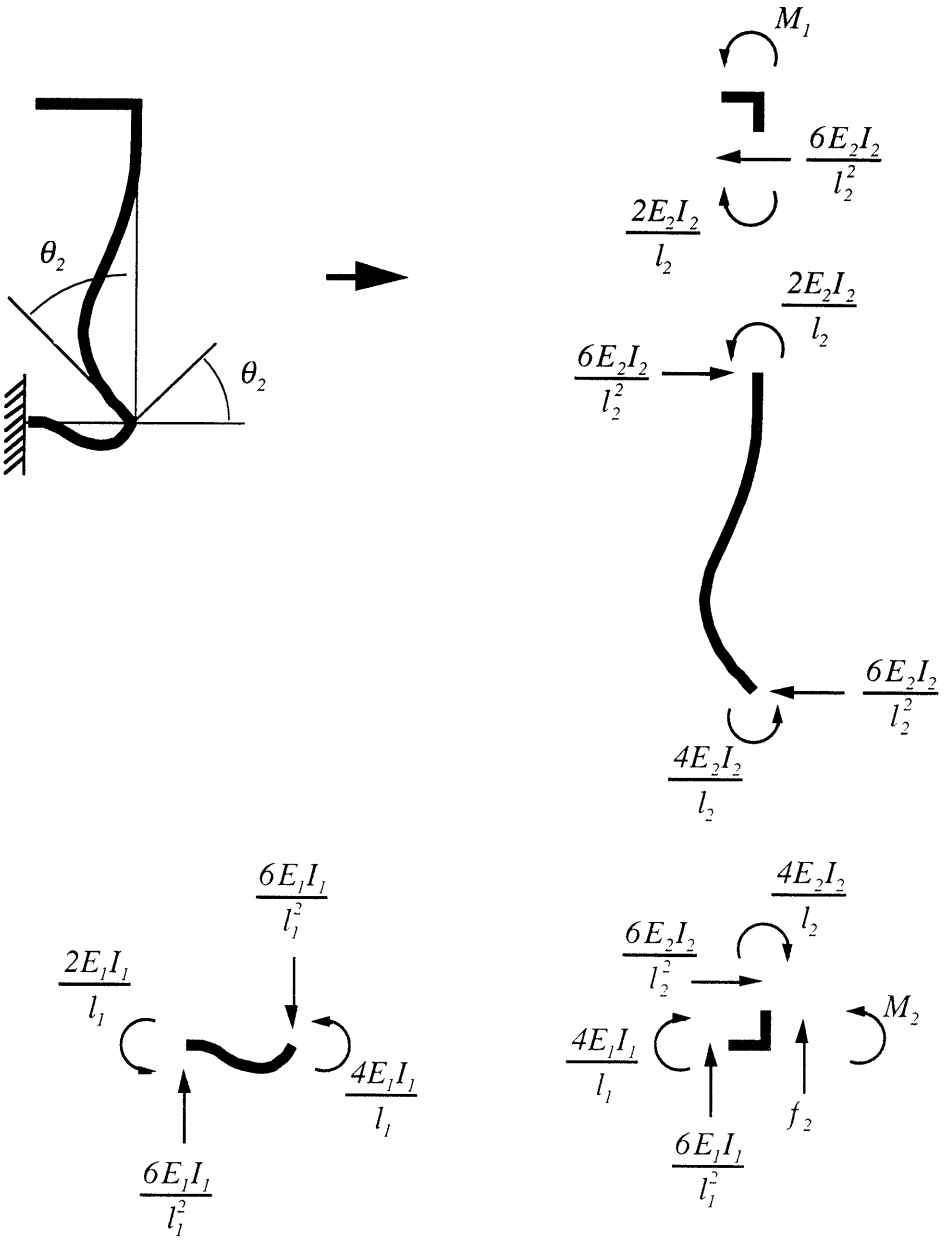

$$f_N = 0 \cdot \theta_2 \tag{F-14}$$

$$f_2 = \frac{-6E_1I_1}{l_1^2}\theta_2 \tag{F-15}$$

$$M_1 = \frac{2E_2I_2}{l_2}\theta_2 \tag{F-16}$$

$$M_2 = (\frac{4E_2I_2}{l_2} + \frac{4E_1I_1}{l_1})\theta_2 \tag{F-17}$$

Combining the equations derived for each displacement, we get the following stiffness matrix:

$$\underline{\underline{K}}_N = \begin{bmatrix} \frac{3E_3I_3}{l_3^3} & \frac{-3E_3I_3}{l_3^3} & \frac{3E_3I_3}{l_3^2} & 0 \\ \frac{-3E_3I_3}{l_3^3} & \frac{3E_3I_3}{l_3^3} + \frac{12E_1I_1}{l_1^3} & \frac{-3E_3I_3}{l_3^2} & \frac{-6E_1I_1}{l_1^2} \\ \frac{3E_3I_3}{l_3^2} & \frac{-3E_3I_3}{l_3^2} & \frac{3E_3I_3}{l_3} + \frac{4E_2I_2}{l_2} & \frac{2E_2I_2}{l_2} \\ 0 & \frac{-6E_1I_1}{l_1^2} & \frac{2E_2I_2}{l_2} & \frac{4E_2I_2}{l_2} + \frac{4E_1I_1}{l_1} \end{bmatrix} \quad \text{(F-18)}$$

Now consider the structure of Figure 5-5, repeated here in Figure F-2. This model, which is used for deriving $\underline{\underline{K}}_P$, has one linear degree of freedom and six angular degrees of freedom. The derivation, not presented here, follows exactly the same procedure as for $\underline{\underline{K}}_N$.

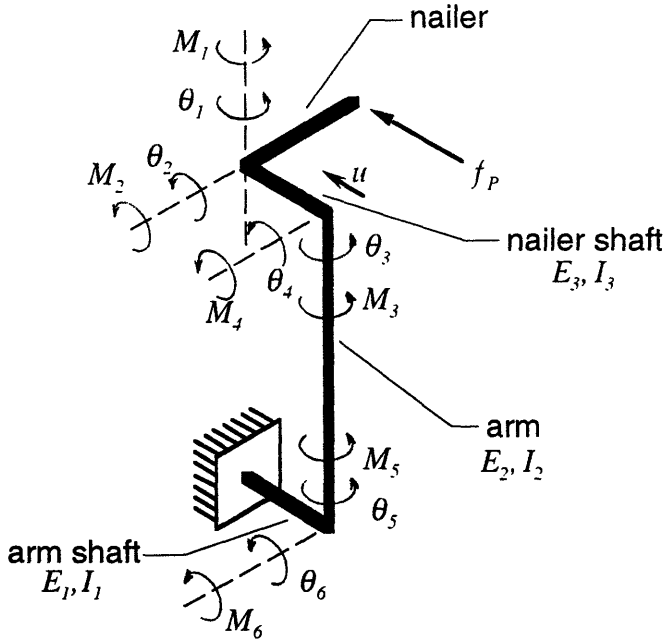

Figure F-2. Beam model of the nailing mechanism with the nailer tip pointing perpendicular to the arm's long axis.

$$\underline{\underline{K}}_P = \begin{bmatrix} \frac{12E_2I_2}{l_2^3} & 0 & 0 & 0 & \frac{-6E_2I_2}{l_2^2} & 0 & \frac{-6E_2I_2}{l_2^2} \\ 0 & \frac{4E_3I_3}{l_3} & 0 & \frac{2E_3I_3}{l_3} & 0 & 0 & 0 \\ 0 & 0 & \frac{4E_3I_3}{l_3} & 0 & \frac{2E_3I_3}{l_3} & 0 & 0 \\ 0 & \frac{2E_3I_3}{l_3} & 0 & \frac{GI_p}{l_2} + \frac{4E_3I_3}{l_3} & 0 & \frac{-GI_p}{l_2} & 0 \\ \frac{-6E_2I_2}{l_2^2} & 0 & \frac{2E_3I_3}{l_3} & 0 & \frac{4E_2I_2}{l_2} + \frac{4E_3I_3}{l_3} & 0 & \frac{2E_2I_2}{l_2} \\ 0 & 0 & 0 & \frac{-GI_p}{l_2} & 0 & \frac{GI_p}{l_2} + \frac{4E_1I_1}{l_1} & 0 \\ \frac{-6E_2I_2}{l_2^2} & 0 & 0 & 0 & \frac{2E_2I_2}{l_2} & 0 & \frac{4E_1I_1}{l_1} + \frac{4E_2I_2}{l_2} \end{bmatrix} \quad \text{(F-19)}$$

Appendix G
Simulation Data

Arm and Nailer Subsystems	Parameter	Value
	IAO (kg*m^2)	0.77
	ING (kg*m^2)	0.028
	mn (kg)	3.6
	La (m)	0.55
	Ln (m)	0.15
	e (m)	0.04
	IMA (kg*m^2)	2.36E-04
	IMN (kg*m^2)	5.93E-05
	n1	100
	n2	20
	k1 (N*m)	14500
	keq (N*m)	703
	rp (m)	0.025
	b (N*m*sec)	5.40E-04
	BA (N*m*sec)	8.70E-04
	BMA (N*m*sec)	1.87E-04
	BMN (N*m*sec)	5.63E-05
Translation Subsystem	**Parameter**	**Value**
	leq1 (kg*m^2)	1.17E-03
	n (m/rad)	4.04E-03
	kax (N/m)	1.33E+08
	k2 (N/m)	1.94E+05
	k3 (N*m)	7.47E+06
	ms (kg)	56
	mn (kg)	3.6
	mcw (kg)	14
	BM (N*m*sec)	6.15E-04
	BB (N*sec/m)	15

Appendix H
Derivation of the Closed-Loop Transfer Function for a Collocated, Single-Axis Servo System

The control strategy for each axis in the nailing mechanism is collocated, proportional plus velocity feedback (PV) control. In this scheme, the position and velocity of the actuator (rather than the output) are measured, amplified, and fed back to the input. Figure H-1 depicts this scheme in block-diagram form for a single-axis servo system. This collocated system is stable for all gains, as the root locus of Figure 7-8 showed.

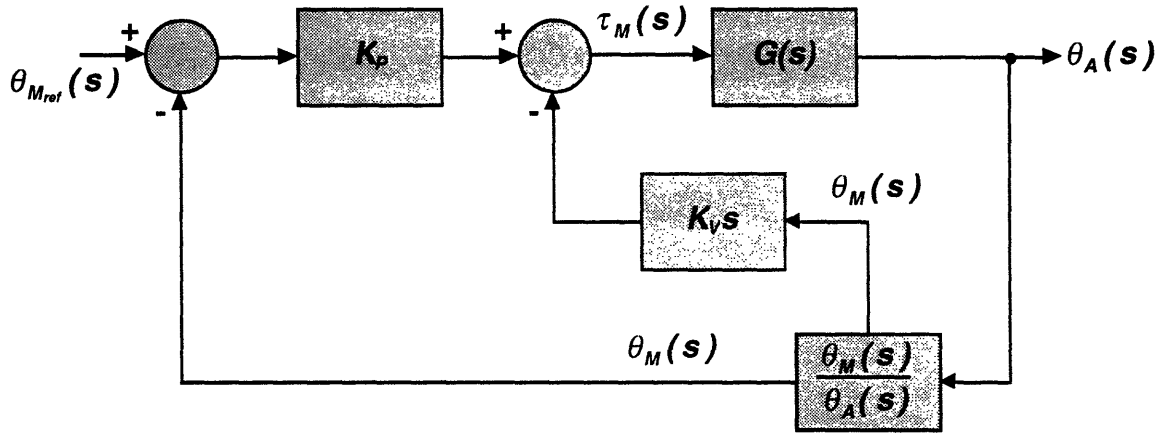

Figure H-1. Single-axis servo system with collocated PV control. The system measures position and velocity of the actuator to control the position of the output.

The closed-loop transfer function of the system embodies the relationship between the input command and the output response. Using the block diagram, we derive this transfer function for the single-arm system of Figure 7-5, repeated here in Figure H-2.

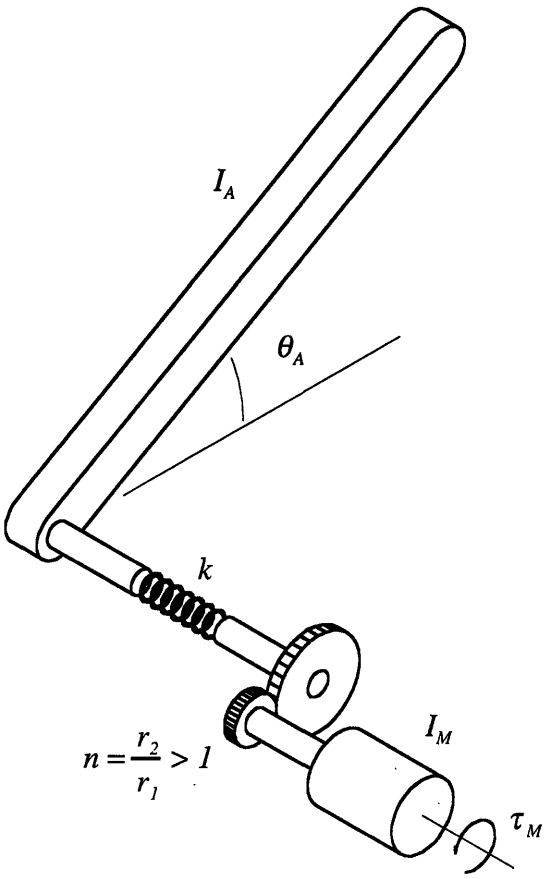

Figure H-2. Robotic-arm servo system.

First, we draw the equivalent block diagram shown in Figure H-3, which makes the input-output relationship easier to obtain.

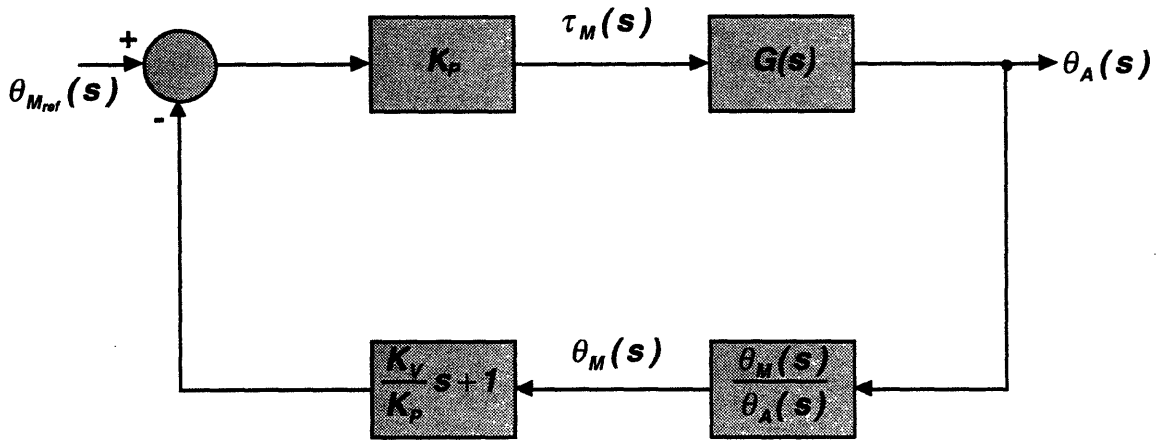

Figure H-3. Mathematically equivalent block diagram.

In terms of the parameters of Figure H-3, the unexpanded closed-loop transfer function is given by the following:

$$\frac{\theta_A(s)}{\theta_{M_{ref}}(s)} = \frac{K_P}{1 + G(s)(K_V s + K_P)\dfrac{\theta_M(s)}{\theta_A(s)}} \tag{H-1}$$

Rewriting $\dfrac{\theta_M(s)}{\theta_A(s)}$ in the following form allows us to expand this expression:

$$\frac{\theta_M(s)}{\theta_A(s)} = \frac{1}{s} \cdot \frac{\omega_M(s)}{\tau(s)} \cdot \frac{\tau(s)}{\theta_A(s)} \tag{H-2}$$

Part of Equation (H-2) comes from the open-loop dynamics of the arm system:

$$\frac{\tau(s)}{\theta_A(s)} = \frac{s^2\left(s^2 + \dfrac{k}{I_A} + \dfrac{k}{n^2 I_M}\right)}{k/nI_A I_M} \tag{H-3}$$

To get $\frac{\omega_M(s)}{\tau(s)}$, we must start with one of the dynamic state equations for the arm:

$$\dot{\omega}_M = \frac{-1}{nI_M}\tau_k + \frac{1}{I_M}\tau_M \tag{H-4}$$

where τ_k, a state variable, is the torque in the arm shaft. Another state equation allows us to write τ_k as a function of the arm's acceleration:

$$\tau_k = I_A\dot{\omega}_A \tag{H-5}$$

Substituting (H-5) into (H-4), we obtain

$$\dot{\omega}_M = -\frac{I_A}{nI_M}\dot{\omega}_A + \frac{1}{I_M}\tau_M \tag{H-6}$$

The third and final state equation of the arm system is

$$\frac{1}{k}\dot{\tau}_k = \frac{1}{n}\omega_M - \omega_A \tag{H-7}$$

Rearranging this expression and taking its derivative with respect to time, we get

$$\dot{\omega}_A = \frac{1}{n}\dot{\omega}_M - \frac{1}{k}\ddot{\tau}_k \tag{H-8}$$

and we already know $\dot{\omega}_A$ as a function τ_k from (H-5). Now, we solve for τ_k in (H-4),

$$\tau_k = n\tau_M - nI_M\dot{\omega}_M \tag{H-9}$$

and take two time derivatives:

$$\ddot{\tau}_k = n\ddot{\tau}_M - nI_M\ddot{\omega}_M \tag{H-10}$$

Substituting (H-10) and (H-9) into (H-8) (with $\dot{\omega}_A = \frac{\tau_k}{I_A}$) reveals that

$$\frac{n}{I_A}(\tau_M - I_M\dot{\omega}_M) + \frac{n}{k}(\ddot{\tau}_M - I_M\ddot{\omega}_M) = \frac{1}{n}\dot{\omega}_M \tag{H-11}$$

Taking the Laplace transform of this expression and rearranging, we obtain the other part of Equation H-2 for which we are looking:

$$\frac{\omega_M(s)}{\tau(s)} = \frac{\frac{1}{I_M}s^2 + \frac{k}{I_M I_A}}{s(s^2 + \frac{k}{I_A} + \frac{k}{n^2 I_M})} \tag{H-12}$$

Expansion of (H-2) reveals the transfer function:

$$\frac{\theta_M(s)}{\theta_A(s)} = \frac{nI_A}{k}(s^2 + \frac{k}{I_A}) \tag{H-13}$$

Finally, if we substitute (H-13) into (H-1) and simplify, we get what we are seeking: the closed-loop transfer function.

$$\frac{\theta_A(s)}{\theta_{ref}(s)} = \frac{K_P k / n I_A I_M}{s^4 + (\frac{k}{I_A} + \frac{k}{n^2 I_M})s^2 + \frac{K_V}{I_M}s^3 + \frac{K_P}{I_M}s^2 + \frac{K_V k}{I_M I_M}s + \frac{K_P k}{I_A I_M}} \qquad \text{(H-14)}$$

Appendix I
Simulating an Impulse Input

When the nail gun drives a nail into an end cap, the mechanism experiences a large forcing function from the recoil. Recall from Chapter 5 that the peak force on the nailer is up to 7000 lb. This forcing function was modeled in the simulation as an impulse of magnitude 2.8 lb.-sec (13 N-sec), which is an estimate found by treating the forcing function as a triangular pulse and integrating the pulse over the 800 microsecond duration.

Implementation of the impulse in the computer simulation deserves special attention, as the method is not obvious. Theoretically, an impulse is an input of infinite magnitude that occurs over an infinitesimal period of time. So how do you simulate that? If the model is linear, simulating an impulse in MATLAB is nothing to the user. He or she simply uses the built-in function appropriately titled impulse. However, when doing nonlinear simulation in MATLAB, one must provide the inputs in the form of a table of data. One might try simulating the impulse by setting the first entry in the table to some large number and all the other entries to zero. This approach, however, only works in practice if the time step used in the integration routine is very small. The reason is that this input effectively acts as either a trapezoidal or a square pulse, depending on whether the input is interpolated. The larger the step size, the longer the input stays at its maximum value, and the less it looks like an impulse.

The easiest and most accurate way to simulate the impulse comes with some analytical manipulation, starting with the impulse definition. The impulse is defined by its integral over time:

$$\int_{-\infty}^{+\infty} u \cdot dt = 1 \tag{I-1}$$

For a linear system,

$$\dot{\underline{x}} = \underline{\underline{A}}\,\underline{x} + \underline{\underline{B}}\,\underline{u} \tag{I-2}$$

where

$\underline{x} \equiv$ *the state vector*

$\underline{u} \equiv$ *the input vector*

$\underline{\underline{A}}, \underline{\underline{B}} \equiv$ *matrices embodying the physical parameters of the system*

Integrating over all time,

$$\underline{x} = \underline{\underline{A}} \int_{-\infty}^{+\infty} \underline{x} \cdot dt + \underline{\underline{B}} \int_{-\infty}^{+\infty} \underline{u} \cdot dt \tag{I-3}$$

Substituting (I-1) in this expression, we then write

$$\underline{x} = \underline{\underline{A}} \int_{-\infty}^{+\infty} \underline{x} \cdot dt + \underline{\underline{B}} \tag{I-4}$$

We assume that from $t = -\infty$ to $t = 0$, $x = 0$, and that the impulse occurs at $t = 0$. We can now evaluate the integral of Equation I-4 from $t = 0$ to some arbitrary time t. Because the impulse acts over an

infinitesimal duration, the state vector $\underline{x}$ at time zero captures the state of the system at the end of the impulse. From that time on, the response is transient; external inputs no longer act on the system. Therefore, we can find the effective impulse response by simulating the response of the system to zero input with these state vector values as the initial conditions. The integral in Equation I-4 evaluated from $t = 0^-$ to $t = 0^+$ is equal to zero. Thus,

$$\underline{x}(0) = \underline{\underline{B}} \tag{I-5}$$

Although we derived this result assuming the system is linear, the result is also valid in the nonlinear simulation. Using this trick, we can simulate the firing of the nail gun . The response of the arm as predicted by the nonlinear model appears in Figure I-1.

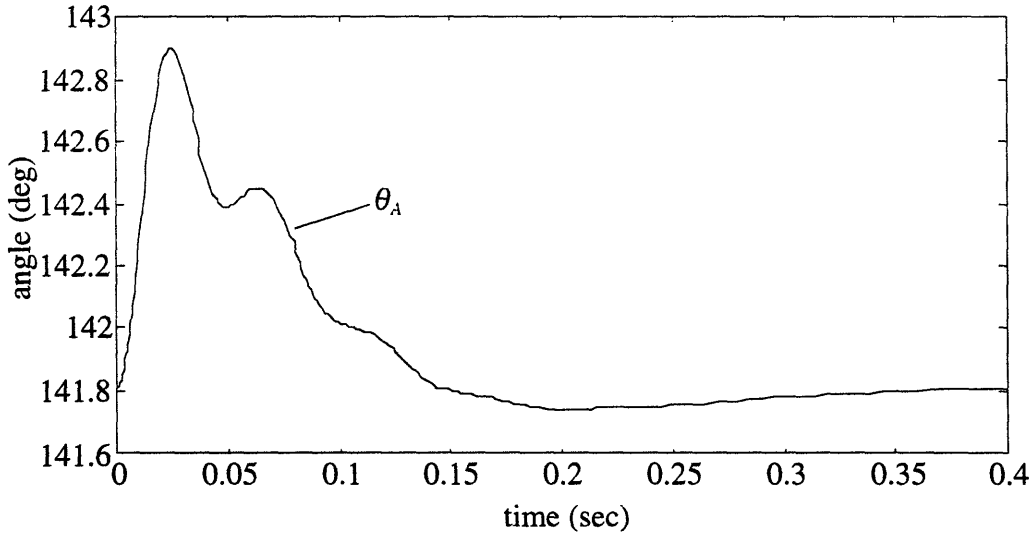

Figure I-1. Response of the nailing mechanism's arm to a discharge of the nail gun. The command given to the control system was to maintain the initial configuration.